SAPIENZA
UNIVERSITÀ DI ROMA

# Object-oriented modeling of micro-ORC systems for low-grade waste heat recovery applications


**Faculty of Civil and Industrial Engineering**

**Department of Astronautical, Electrical and Energy Engineering**
**Ph.D. Degree in Energy and Environment**

**Ramin Moradi**

**Matricola 1792546**

supervisor

Prof. Emanuele Habib

Cotutors

Prof. Enrico Bocci

Prof. Luca Cioccolanti


May 2021

## Thesis Committee

Prof. Dario Ambrosini

Prof. Luisa Ferroni

Prof. Coriolano Salvini

## External Reviewers

Prof. Khamid Mahkamov

Prof. Electo Eduardo Silva Lora

## Abstract

Organic Rankine Cycle (ORC) systems are one of the most suitable technologies to produce electricity from low-temperature sources. A comprehensive understanding of these systems is necessary for their further deployment especially in micro scales, in which the intrinsic issues such as low isentropic efficiency and unreliability arise more severely.

In this thesis, the components of a non-regenerative, micro-scale ORC unit are modeled empirically using the experimental data. The components models are used as functions in the system-level solver. The system solver uses a novel approach, in which no assumption is made for the modeling and only the components specifications and the real system boundaries that an operator has during the system run are put as inputs. This assumption-free, object-oriented model follows the two fundamental conservation laws of thermodynamics that are the conservation of energy and the conservation of mass. The developed mass-sensitive model is a robust solver that leads to a full understanding of the system limitations and losses using the empirical models of the main system components.

In addition to the system modeling, the thesis theoretically studies the impact of the expander lubricant oil on the system performance using the empirical lubricant-refrigerant miscibility model and a data reconciliation method. The impact of the expander's lubricant is found significantly effective on the performances of the heat exchangers, the expander, and the overall system especially in micro-scales, despite its influence has been mostly neglected in the literature so far.

Since the use of micro-scale ORC systems for low-temperature waste heat recovery (WHR) applications is investigated, a novel kind of expander for such systems has been here analyzed using computational fluid dynamics (CFD). The regenerative flow turbine (RFT) is found particularly interesting due to its good and reliable performance in very low-pressure ratios making the machine suitable as an alternative expansion.

Finally, a biomass-fed integrated system is studied in detail. The integrated system consists of a dual-fluidized-bed gasifier, a hot gas conditioning unit, a steam-injected-micro gas turbine, and an ORC as the bottom cycle. This system-level study shows the performance of the integrated system when full conservation of energy and mass is applied. The results show that the overall system efficiency improvement by the ORC is limited to 1-2 % using the wet gas turbine compared to 5-8% without the steam injection. Nevertheless, the produced thermal power in the condenser of the ORC unit shows the ability of the integrated system to meet higher users' thermal demands in small-scale CHP applications.

**Keywords:** mass-sensitive modeling, experimental modeling, micro ORC, off-design, lubricant, regenerative flow turbine, system integration, low-grade WHR

*"To live is to risk it all, otherwise you're just an inert chunk of randomly assembled molecules drifting wherever the universe blows you"*

Rick Sanchez, a misanthropic scientist in Rick & Morty TV series

## Acknowledgments

I can resemble my Ph.D. with my mountain climbing experiences in Iran, looking to the snow-covered crest when you are in the foothills making you think it would be a *mission impossible*, then standing up there looking at the breathtaking landscape, exhausted but stronger, never remembering the point zero that all started.

Among all people supporting me during the journey, I would like to appreciate my tutors' support when needed. I spent most of the working days with Prof. Enrico Bocci in his office; thank you for your unconditional support and the piled-up bond. Many thanks to Prof. Luca Cioccolanti for providing me the test bench, following the work process closely, being available whenever needed. Finally, my supervisor Prof. Emanuele Habib who trusted in my work and pushed me on the way up to the crest.

To the members of the evaluation committee, internal and external reviewers, thank you for your time and energy devoted to reading the manuscript and providing me useful insights to fortify my work. I also acknowledge the funds provided to me by the Sapienza University of Rome that made my study possible at the first point.

Thanks to Comit Srl for its support in the design and set up of the new test rig. Thanks also to S.TRA.TE.G.I.E. Srl (www.strategiesrl.com) for the development of the initial test bench.

Colleagues aside, my heart to my family, supporting me unconditionally, joining the cheers but also being there when I was down when my knees were shaking on the way. Special thanks to my mum, my unique person in the world. To my father for the wise advice and supports; to my beloved sister Marjan for her sympathy and heartwarming presence, and to my young brother Amir for sharing moments and fun even when we were 4,060 km far away! Thank you all for supporting me to challenge myself to spend the time out of home, out of my beloved country.

Finally, I want to thank myself for the hard work, for staying on-track and motivated, and for not being surrendered when the odds were against me.

Ramin Moradi

# 1. Contents

# List of Figures

# List of Tables

# Chapter 1

# 1. Introduction

*"Only everyone knows everything, and everyone is yet to be born"*

Bozorgmehr, ancient Iranian politician

## 1.1 ORC technology overview

The concept of organic Rankine cycle (ORC) technology is rather old going back to the 19th century [1]. Large-scale commercial plants have been installed worldwide with an estimated capacity of 2.7 GW, of which a considerable share is represented by geothermal ORC plants (about 75%), while waste heat recovery (WHR) plants are the majority when the number of plants is considered [2].

In the last two decades, many efforts have been put into the development of power generation systems able to exploit the high amount of waste heat to improve the efficiency of existing industrial facilities thus reducing their fossil fuel consumption and greenhouse gas emissions. A large amount of waste heat is available in oil refineries, glass industries, and steel mills. Moreover, strict environmental standards in some applications like car engines have pushed interests to increase the efficiency of the engines using light, reliable, and economic WHR technologies ending in an emission reduction of vehicles. In addition, the ongoing evolution of stand-alone, low-temperature power generation systems is accelerating due to the increasing electricity demand and lack of infrastructure in many countries. The

share of the installed ORC capacity for different WHR applications in 2017 is represented in Figure 1-1.

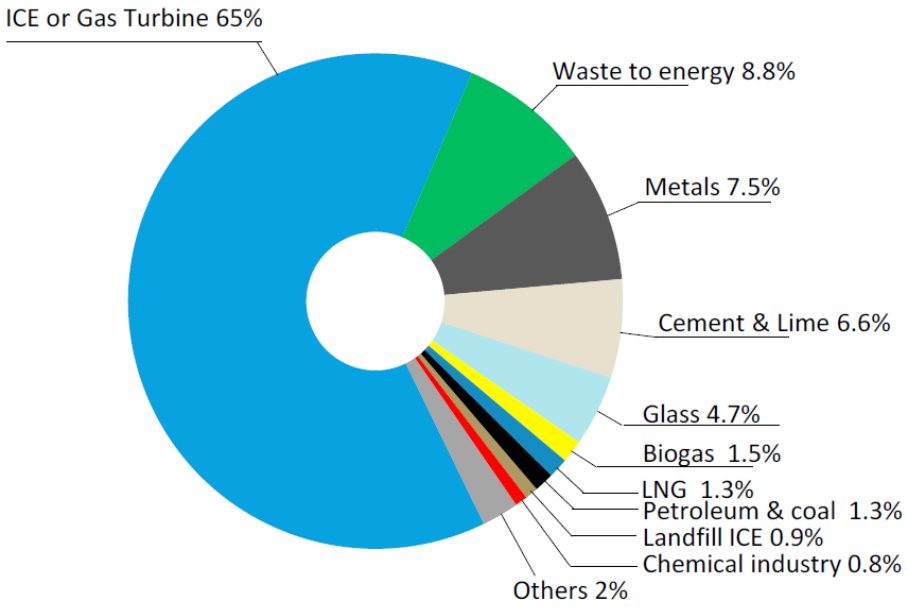


Figure 1-1. Installed capacity share of different WHR-ORC applications in 2017 adopted from [2]

The amount and density (quantity) and the temperature (quality) of the waste heat are important factors to plan suitable strategies to exploit the waste heat. They mainly depend on the type of the industry and application, and national or even regional energy structure and energy policy. For instance, it is estimated that 20% to 50% of industrial energy consumption is wasted in the USA. The number can be better understood knowing that one-third of the total energy consumption in the USA is related to the industries meaning almost one-third of the fossil-fuel-related greenhouse gas emissions, which can be significantly reduced as it is estimated that between 18% and 30% of this waste heat can be utilized [3]. Another example is the UK industrial sector that consumes about 17% of the overall energy of the country and produces almost 32% of the UK heat-related $CO_2$ emissions. It is estimated that

72% of this energy is consumed in industrial thermal processes of which 20% is estimated as the potential to be reused by WHR technologies, which approximately means 2.5% of the UK total energy consumption [4].

It should be noted that WHR is a general term including the use of waste heat for process heating, space heating, or electricity production. WHR systems may use the technically and economically usable part of the waste heat in three ways: i) direct use without upgrading, ii) direct use after upgrading [5], and iii) electricity generation [6]. The latter adds value to the thermal waste, but it is technically more challenging. Using the waste heat for heating purposes is technically easier. In this thesis, only electricity production is considered when WHR is mentioned.

Regarding the waste heat quality, that is the most effective parameter on the WHR technology choice, the waste heat temperature can be from around 30 °C up to about 1600 °C as presented in Figure 1-2 that represents a non-exhaustive list of waste heat sources from low to high-temperature applications with common technologies to exploit it. In general, industrial processes reject heat at different temperatures determining the quality of the waste heat as high (>400°C), medium (100-400°C), and low (<100°C) [4].

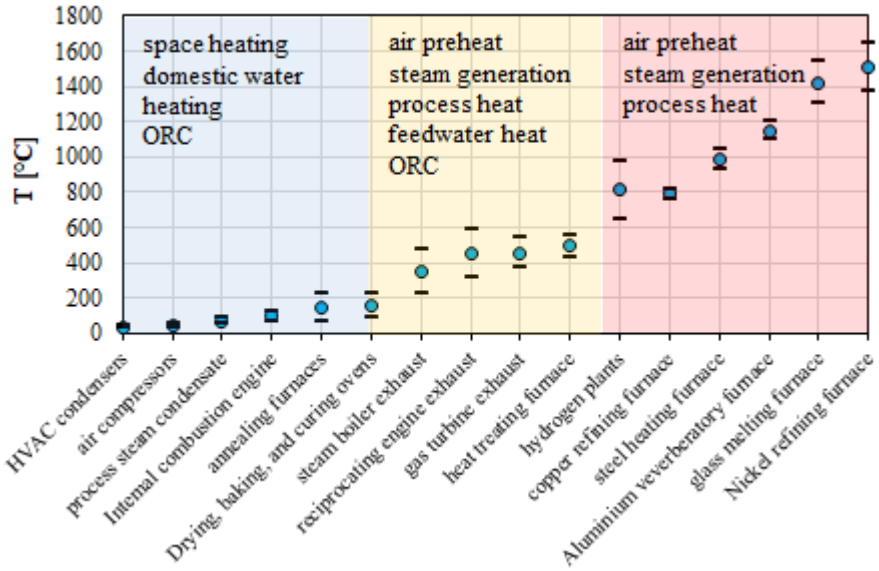


Figure 1-2. Examples of waste heat applications and their temperature range (data are adapted from a table reported in [3])

According to Haddad et al. [7], the significant share of the global waste heat is at low temperatures as shown in Figure 1-3, which makes the WHR more challenging to be efficient and economic.

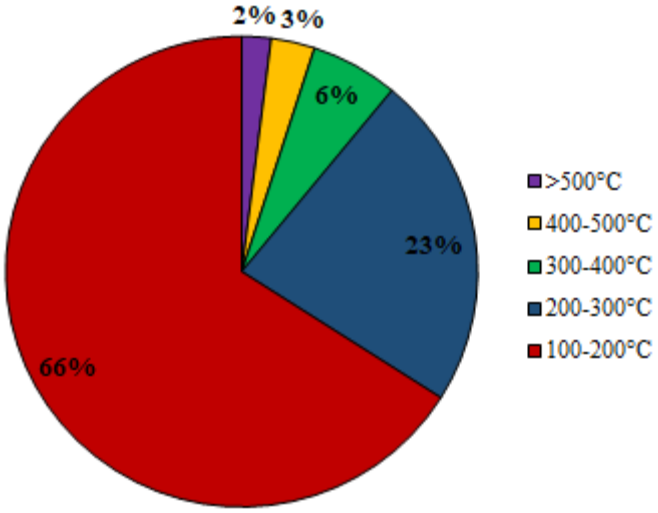


Figure 1-3. The available waste heat categorized based on the temperature

In the case of low and medium-grade waste heat, direct electrical conversion devices like thermo-electric generators, or those operating according to Kalina cycle or organic Rankine cycle (ORC) is used [4]. Due to their simplicity and reliability [8], ORC systems have proven to be suitable for low to medium-grade WHR applications. In addition, ORC systems have recently attracted attention from industry and academia to convert into electricity low-temperature thermal energy from renewables such as solar [9], biomass [10], and geothermal [11]. For example, it is recognized as one of the most promising technology for residential combined heat and power (CHP) systems [12]. An ORC system is a power generation system operating as a Rankine cycle, but using an organic working fluid with a low-boiling point instead of steam. This, in general, allows having a pressure of the fluid higher than atmospheric pressure in the condenser avoiding air leakages into the system. ORC systems are particularly interesting for their reliability, flexibility, safety, and applicability for low-temperature power generation [13]. At medium (50-300 kWe) and large scales (>300 kWe), ORCs are a mature and reliable technology as reported in [14]. However, further efforts are still needed to make these systems competitive and reliable at the micro (<10 kWe) to small (10-50 kWe) scales.

The range of the power output and heat source temperature of the ORC systems for different applications are represented in Figure 1-4. Besides, the range of the experiments on the low-temperature, micro-scale ORC unit in this study is highlighted in Figure 1-4 indicating the very off-the-map working condition of the experiments compared to common ORC systems.

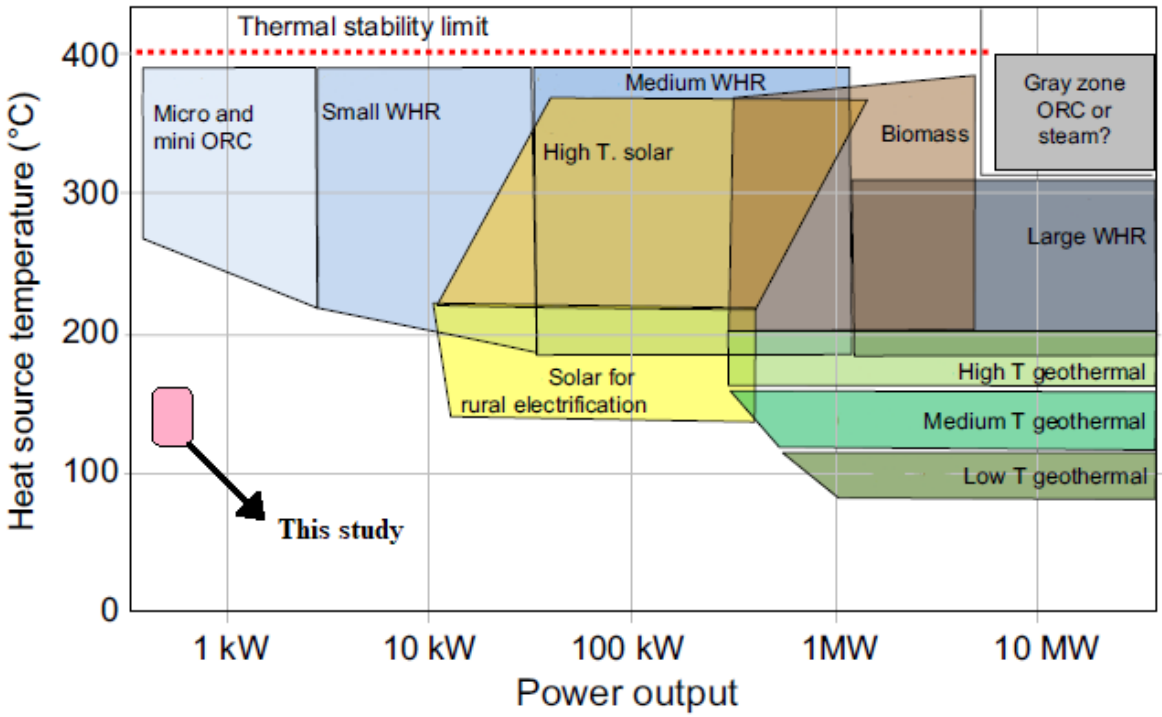


Figure 1-4. Heat source temperature with power output for different ORC applications (the figure is the modified copy presented in [15])

Considering the studied ORC unit being at micro-scales, it is designed as a non-regenerative cycle to avoid further complexity for a relatively low gain in performance [16,17]. Besides, a sub-critical system equipped with a scroll expander is taken in this work for its good performance, low-cost, and widespread use in low-temperature ORC systems [18]. Moreover, an innovative turbine is studied numerically as a low-cost candidate for low-grade WHR applications.

The working fluid selection affects the performance of the system significantly. Several criteria are considered for a suitable working fluid: availability, flammability, toxicity, material compatibility with lubricants and metals, system performance, cost, thermal stability, and environmental impacts. The latter obeys up-to-date environmental standards for Global Warming Potential (GWP) and Ozone Depletion Potential (ODP) resulting in some widespread fluids being out of

the market. Considering the criteria above, a list of candidate fluids can be prepared, which have minimum requirements.

Then, the firsthand criteria to reduce the list again is the fluid critical temperature if a subcritical system is intended, which dictates the system maximum pressure as well. Figure 1-5 Shows the common working fluid for ORC systems classified for low, medium, and high-temperature sources based on their critical temperature [19].

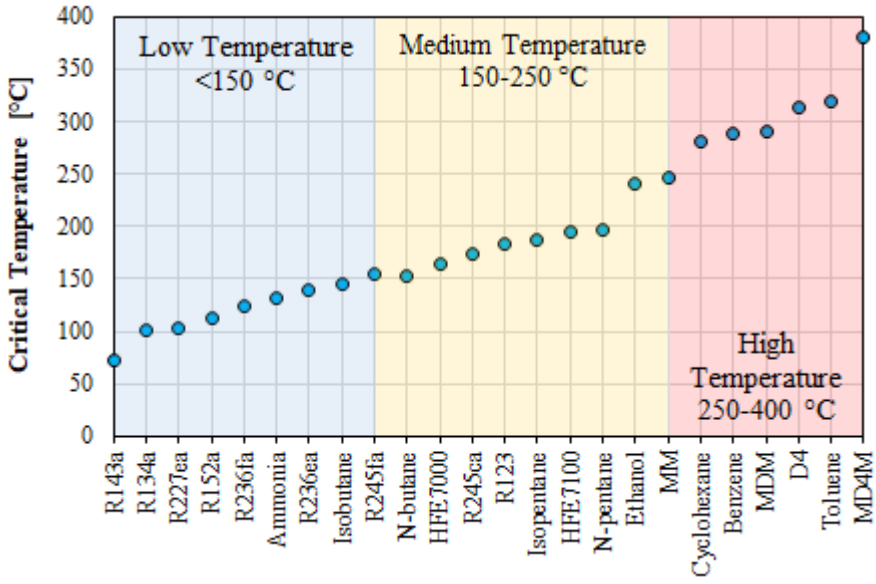


Figure 1-5. Fluid list for ORC systems categorized based on heat source temperature and fluid critical temperature

In this work, R134a is considered for the experimental study since it is suited for range of the low temperature heat source (120-150°C) and it has the other aforementioned criteria except the low GWP. Furthermore, R134a is one of the most studied working fluids in the literature with a good availability of heat transfer, void fraction, and lubricant-refrigerant miscibility models that are essential for the research objectives of the thesis.

In addition to R134a, R245fa, which has similar general characteristics of R134a but a higher critical temperature [20], is considered for simulations of an innovative turbine, the regenerative flow turbine, introduced in this thesis for the first time, owing to the higher temperature application of the turbine.

ORC systems were studied from different aspects and with different objectives in the literature. Figure 1-6 shows a graphical summary of core research areas of the ORC technology with their relative distribution [21]. Most studies focused on the application of the ORC systems, while turbines were the most common expansion machines in the studies. Optimization of the system was the goal of most studies using control models. In this work, the main goal is the realistic off-design performance of the system using a scroll expander in a non-regenerative system to present an assumption-free simulation tool using an object-oriented modeling approach. Therefore, the goals of the thesis rely on areas that were not studied much in the literature as is discussed in more detail in the following section.

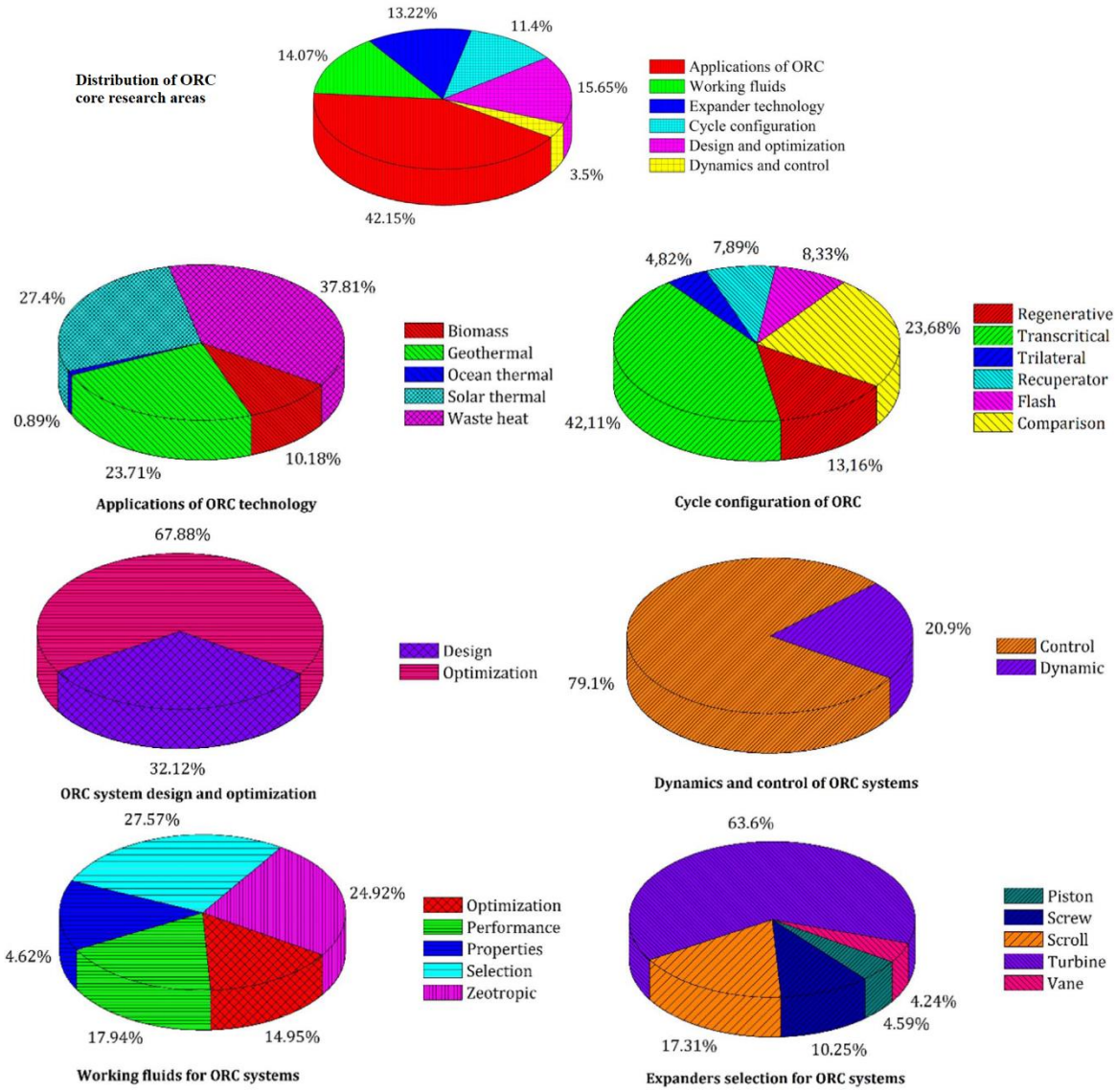


Figure 1-6. The main research area of the ORC systems classified using different parameters up to 2018 (the figure is the modified copy presented in [21])

## 1.2 **Off-design system performance and modeling**

Even if an ORC system is well designed for a specific heat source and heat sink characteristics, the instabilities of the heat source and the heat sink propel the system and its components to operate in a condition that is out of the design point especially in micro scale applications. Such a condition is not only due to the heat source and sink fluctuations, but also electricity load or even refrigerant mass

reduction due to leakages can change the system boundary conditions. This is called *off-design* condition and it usually results in system efficiency degradation at best, or pump cavitation or turbine damage at worst cases because the components specifications are not optimal for the new working conditions. Therefore, understanding the system off-design characteristics is necessary to realize a system for reliable on-site performance, control logic development, and ORC system integration with other energy systems, especially in the low temperatures to exploit the large WHR potential. An extreme example is the automotive exhaust WHR system, in which the heat source condition varies significantly because of the fluctuations of the exhaust gas temperatures and mass flow rate as shown in Figure 1-7, and the heat sink temperature due to the seasonality.

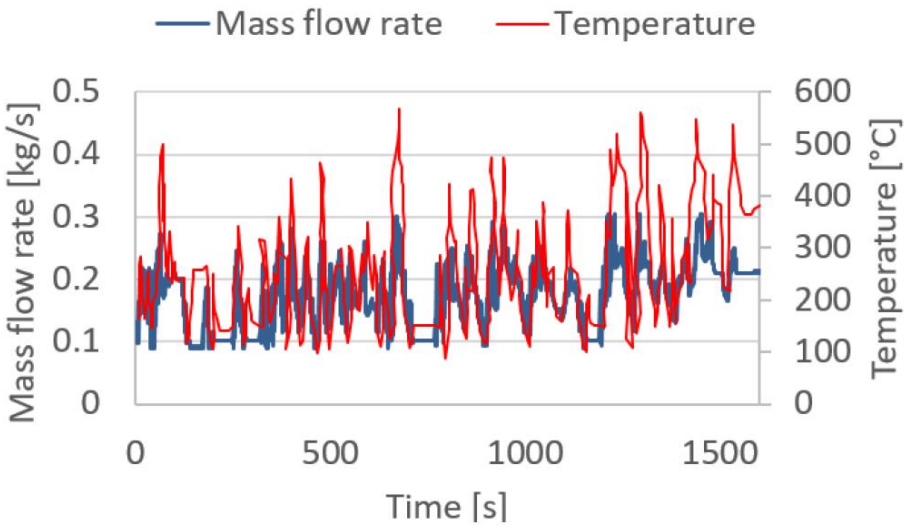


Figure 1-7. Example of exhaust gas fluctuations of an internal combustion engine adapted from [22]

It can be stated that any ORC system works in off-design conditions to some extents, but at small sizes, the system is more sensitive since the expander usually operates with low superheating degrees, the pump operates in low subcooling degrees, turbines work close to their choked condition and their performance can be

penalized significantly with a marginal change in mass flow rate. At such scales, the system efficiency is intrinsically low even at the design point because of the low Carnot efficiency, thus any deterioration can penalize the overall performance at relatively considerable rates. Therefore, off-design modeling has considerably higher research value in micro-scales compared to the design studies. Thus, the off-design model of the main system's components is essential. To this end, the scroll expander and the regenerative flow turbine are modeled in off-design conditions. The first is a popular and efficient volumetric expander, and the latter is a novel turbine with peculiar characteristics suitable for low-grade WHR systems with significant fluctuations of the heat source.

From the modeling point of view, off-design models are on the opposite road of design models. A designer is willing to determine the specifications of a system to reach a set of predefined performances and thermodynamic states, while an *off-designer* tends to find out the performances and thermodynamic states of a known system as presented in Figure 1-8. The approach of the thesis is therefore off-design modeling of the ORC unit.

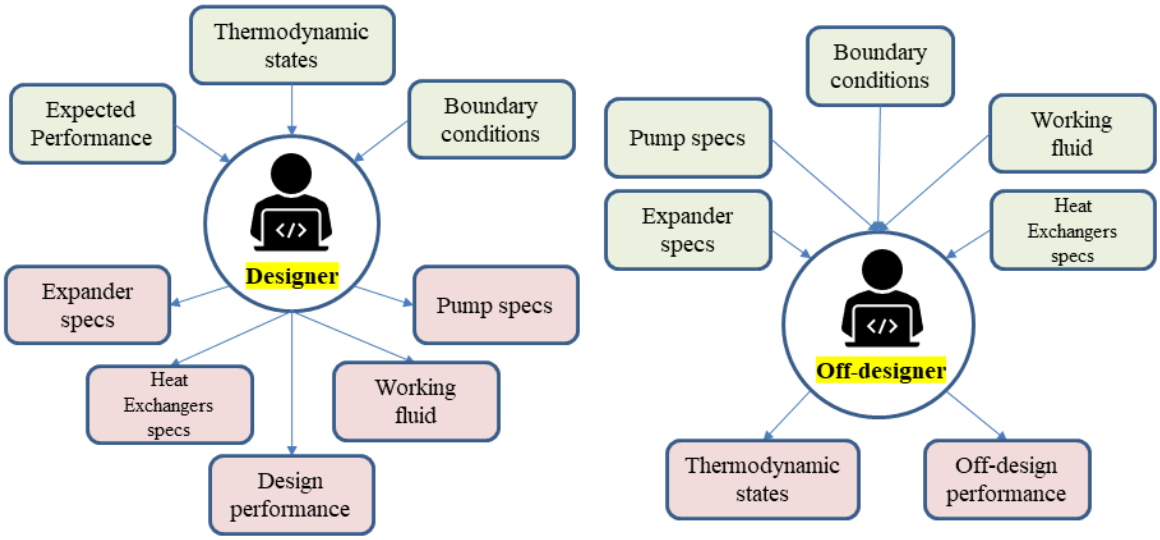


Figure 1-8. Design and off-design modeling approaches

Considering the extensive number of papers dealing with off-design modeling of ORC systems, they can be categorized based on the modeling approaches to deal with time, or the ways to simulate the system components. The first categorize the models into dynamic and steady-state ones. Dynamic models consider the components' time-inertia to respond to the variations of the system boundary conditions; hence they are more comprehensive compared to the steady-state models. Therefore, dynamic models are more suited for controlling programs especially if a component exists with considerably different time-dependent characteristics that affect the system performance, reliability, or durability. An example is solar ORC units, in which the thermal inertia of the heat transfer medium in the solar collector dictates the refrigerant pump speed response function to maintain a preset superheating degree in the evaporator. On the other hand, steady-state models are useful for the system reliability assessment to be used in the controlling logic to define the system boundaries, which guarantee a range of the system performance, and to protect the pump and the expander machine for long-term operations.

Moreover, the way that the components are modeled is important and mainly three methods were used in the literature namely constant-efficiency, the polynomial-regression, and semi-empirical models [23]. Moreover, deterministic models and CFD simulations are other tools to simulate the components with high accuracy and extrapolability. However, they are not suitable for system-level simulations due to their high computational cost.

Constant-efficiency models are very simple and computationally fast but with poor accuracy for off-design modeling and can be used for complex system integration to simulate the integrated system for a large set of boundary conditions such as hourly solar ORC simulations for one year. The results of such models are reliable

if the system always operates close to its design condition. Moreover, they can be used as a working fluid screening method for a system. Examples are constant isentropic efficiency and volumetric efficiency of volumetric expanders and pumps, and constant overall heat transfer coefficients of heat exchangers.

The polynomial-regression models describe the components based on the experimental data as a function of the effective parameters. Such models are more accurate than single-coefficient models to predict each component in the range of the experimental data used for the regression model. However, they can easily give wrong or even unphysical results if they are extrapolated in a system-level simulation.

The semi-empirical models require experimental data to tune physically meaningful correlations that simulate a component. Therefore, they can represent the limited physics of a component when a comprehensive knowledge about the phenomenon is unknown or too complicated. These models can predict the component performance more robustly with good accuracy and can be extrapolated to a limited extent making them suitable for the system off-design modeling [23]. Therefore, the semi-empirical modeling approach is used here to simulate the components of the ORC test bench. A non-exhaustive list of the modeling approaches in the literature up to 2018 are reported in [23].

Component modeling aside, system modeling can be performed in different ways using different tools that can be categorized as code-based tools such as MATLAB®, Python™, and EES®, and library-based tools like Simulink®, Cycle-Tempo®, and Aspen Plus®. A very common approach for off-design modeling is taking one or more assumptions in the model to identify the cycle thermodynamic state at some points such as subcooling degree at the condenser outlet, superheating degree at the evaporator outlet, and evaporator inlet pressure. For example, Freeman et al. [24] assumed zero subcooling at the condenser and 5 K superheating at the

evaporator in a small-scale solar ORC system. Besides, the temperature pinch in the evaporator and condenser was assumed 5 K, and the temperature difference between the evaporation temperature and the thermal storage temperature was assumed 10 K. Similarly, Villarini et al. [25] modeled two different solar ORC systems for one year assuming a superheating degree of 5 K and a minimum temperature difference between the hot fluid inlet temperature to the evaporator and the working fluid temperature. Hu et al. [26], instead, considered 5 K superheating degree and fixed condensing pressure to simulate an ORC system for geothermal applications in off-design conditions. Eventually, Ibarra et al. [27] considered the evaporation pressure and the condensation temperature as inputs to their off-design model of an ORC system and also assumed a maximum cycle temperature as a limit of the system. Hence, the most common assumptions are a superheating degree in the range of 5-10 K and a fixed subcooling degree [28].

Therefore, assumption-based, off-design models cannot be fully deterministic. For instance, if a subcooling degree is assumed, one of the most important aspects of the off-design models remains in the shadows: the probability of the pump cavitation. Therefore, relatively few works aim to present fully deterministic models that are discussed in the following.

## 1.3 **Mass-sensitive system modeling**

An assumption-free, off-design model means the model must predict the performance of the system using the real system boundary conditions that an operator encounters during the system operation. They are the hot stream and cold stream inlet conditions in the evaporator and condenser respectively, the expander

shaft speed[1], refrigerant pump speed, and initial refrigerant mass charge. The latter adds the conservation of mass for each component resulting in the refrigerant mass distribution in the system. The sum of the calculated mass of the components must be equal to the initial system mass charge. This method is called mass-sensitive or charge-sensitive modeling in the literature that has been adopted by relatively few studies to present an assumption-free model. Indeed, the refrigerant mass charge is an important factor in the environmental issues and costs of ORC systems. Moreover, the mass charge affects the evaporator superheating and subcooling degree thus it is influential on the overall system performance as well.

To better explain a mass-sensitive model, let us consider a simple system consisting of an evaporator, a condenser, a pump, an expander, pipes, and fittings without a liquid receiver between condenser and pump. The mass charge calculations of the expander, pump, pipes, and fittings are straightforward using their volume and density. They are known with a high accuracy since these components include single-phase fluid only. In the case of the heat exchangers that are usually flooded in small-scale systems meaning three-phases exist simultaneously, the mass calculation strongly depends on the zone length of each phase. In other words, the heat exchanger mass model is strongly coupled with their hydro-thermal models. Therefore, the model can use a try and error approach to find some system thermodynamic states, usually evaporator or condenser pressure, until the calculated system's mass charge is close enough to the initial mass charge. In this way, the mass conservation and the energy conservation are used to perform assumption-free system modeling.

[1] Shaft speed is adjusted using the electric or mechanical load. Hence, one may consider electric or mechanical load as the boundary condition instead of the shaft speed.

However, the liquid receiver is an inevitable component protecting the pump from cavitation when the system mass charge distribution is changing between the components. Furthermore, the extra system mass charge is absorbed in the liquid receiver resulting in different liquid levels in the liquid receiver as the system working conditions change especially in off-design conditions. The liquid receiver includes some level of liquid and the rest is filled with gas. Moreover, any non-condensable gas in the system is trapped at the top of the liquid receiver reducing the system's available volume. Therefore, the liquid receiver mass charge generally depends on the system working conditions as in the heat exchangers.

Among the mass-sensitive studies on ORC systems in the literature, four works had a liquid receiver in their system and the models to calculate the liquid level are presented in different forms. It should be noted that to perform the mass-sensitive model of the system, mass charge models of each component must be known; thus, an accurate liquid receiver mass model is crucial. The mass sensitive studies are presented in Table 1-1 that include five steady-state models and one dynamic model, two of which did not consider a liquid receiver in their system. In some studies reported in Table 1-1, the liquid receiver was assumed filled with the liquid if the condenser outlet fluid is subcooled, and it was considered emptied of liquid [28,29] or with some level of liquid if the condenser outlet is two-phase flow [30,31]. These assumptions are controversial for several reasons that are discussed thoroughly in Chapter 4, Mass-sensitive modeling of the ORC system. Therefore, the mass-sensitive modeling conducted in the thesis considers experimentally and numerically verified liquid levels in the liquid receiver unlike what was considered in the literature so far.

Table 1-1. The list of mass-sensitive modeling of ORC systems in the literature (sorted by the publication year)

| Authors | System description | Summary | Liquid receiver model |
|---|---|---|---|
| Yousefzadeh and Uzgoren (2015) [30] | 10 $kW_{el}$, non-regenerative ORC, R134a, screw expander, shell & tube HE, liquid receiver | A dynamic model with steady-state validation using experimental adopted from the literature. | The liquid was considered at the same thermodynamic state as the condenser outlet. The liquid receiver is filled if the condenser outlet is subcooled or saturated liquid and it is partially filled if the fluid is two-phase. The liquid level and outlet enthalpy were modeled as the following: $$h_{out} = \begin{cases} h_{tank} & h_{tank} \le h_l \\ h_l & h_{tank} > h_l \end{cases}$$ $$Level_{l,tank} = \frac{(1-x)\rho_{tank} \cdot \forall_{tank}}{\rho_l \cdot A_{base,tank}}$$ |
| Ziviani et al. (2016) [31] | Two experimental systems:<br>11 $kW_{el}$ ORC, R134a, screw expander, centrifugal pump, BPHE, liquid receiver<br>5 $kW_{el}$ ORC, R134a, scroll expander, diaphragm pump, BPHE, liquid receiver | Steady-state model. The code can use mass-sensitive or subcooling-sensitive methods. System results were validated with experimental data. | The liquid receiver is filled if the condenser outlet is subcooled or saturated liquid and it is partially filled if the fluid is two-phase: $$Level_{l,tank} = \left(\frac{h_{v,sat} - h_{in}}{h_{v,sat} - h_{l,sat}}\right)\frac{\rho_{in}}{\rho_{l,sat}} = \frac{m_{l,sat} \cdot v_{l,sat}}{m_{tot} \cdot v_{in}} = \frac{\forall_l}{\forall_{tot}} = \frac{\forall_l}{(D_{in}/2)^2 \cdot h_{effective}}$$ |

| Authors | System description | Summary | Liquid receiver model |
|---|---|---|---|
| Liu et al. (2017) [32] | Numerical study of 3 $kW_{el}$ ORC, R123, scroll expander, shell & tube condenser, find-tube evaporator | Steady-state model. The impact of the refrigerant mass charge on the part-load conditions is presented. Pump speed was found to reach preset power, thus it was not a fully assumption-free model.<br><br>No experimental validation. | The liquid receiver was not considered in the ORC system. |
| Santos et al. (2018) [33] | 1.5 $kW_{el}$ ORC for CHP, R245fa, scroll expander, vane pump | Steady-state model in Fortran using empirical and semi-empirical models. The refrigerant mass charge model was not validated. The pressure and temperature results of the model were validated experimentally. | The liquid receiver was not considered in the ORC system. |
| Dickes et al. (2018) [28] | 2 $kW_{el}$ regenerative ORC, R245fa, scroll expander, diaphragm pump, BPHEs, liquid receiver | Steady-state model in MATLAB® using semi-empirical models. Four heat transfer coefficients and five void fraction models were used to find the best combination to calculate the BPHE thermal load and system initial mass charge. The best set for BPHE thermal load was found different from the set with the least system mass error. The gain of the accuracy of the system mass was found more important than losing the accuracy of the BPHE thermal loads for overall system performance modeling accuracy. | The liquid receiver is filled if the condenser outlet is subcooled and is emptied if the fluid is saturated. It can hold a liquid level only if the condenser outlet is saturated liquid. The liquid receiver mass charge is modeled as the following:<br>$$m_{LR} = \begin{cases} \forall_{LR} \cdot \rho_{in,LR} & h_{in,LR} < h(x=0, P=P_{in,LR}) \\ \forall_{LR}[L_{LR} \cdot \rho_l + (1-L_{LR})\rho_v] & x_{in,LR} = 0 \\ \forall_{LR} \cdot \rho_v & 0 < x_{in,LR} \leq 1 \\ \forall_{LR} \cdot \rho_{in,LR} & h_{in,LR} > h(x=1, P=P_{in,LR}) \end{cases}$$ |

| Authors | System description | Summary | Liquid receiver model |
|---|---|---|---|
| Dickes (2019) [29] | 2 $kW_{el}$ regenerative ORC, R245fa, scroll expander, diaphragm pump, BPHEs, liquid receiver | Steady-state model in MATLAB® using semi-empirical models. The only study that the refrigerant mass of each component was measured during the system run. System results were validated experimentally. | The same as the above row. |

Regarding the modeling of the ORC system, the mass charge model of the liquid receiver is used in the mass-sensitive modeling of the system. Furthermore, the scroll expander model is the improved version of the widely accepted semi-empirical model in the literature using both the polytropic expansion process instead of assuming isentropic expansion and the expander geometrical parameters as fixed inputs to the model instead of finding them from the results of the model. Finally, the impact of the expander lubricant oil is simulated using the lubricant-refrigerant mixture model considering the refrigerant miscibility models. Therefore, the novelty of the thesis regarding only the ORC system modeling is represented in Figure 1-9 with the relevant reference works that studied the system in the four areas.

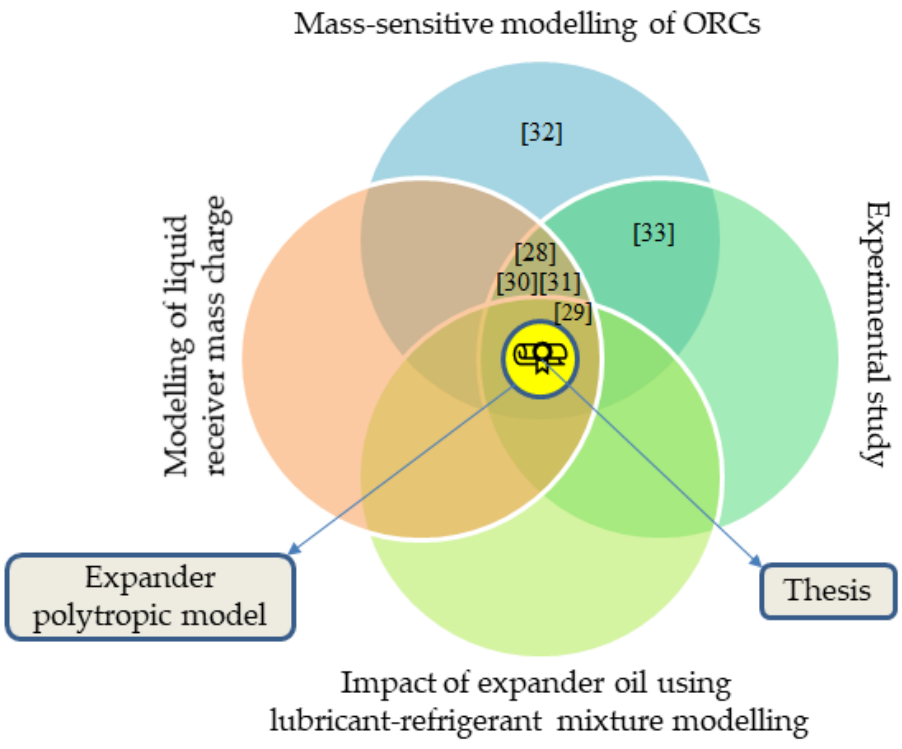


Figure 1-9. State-of-the-art and the goal of the thesis regarding the modeling of ORC systems only (the numbers in the brackets refer to the references reported in Table 1-1)

## 1.4 **Thesis objectives and novelties**

The main goal of the thesis is to present a reliable modeling tool to simulate micro-scale ORC systems and its main components in off-design conditions for low-grade WHR applications. To this end, the thesis offers the following original contribution to the current literature:

- Assumption-free modeling of a micro-scale ORC system taking the system boundaries as the inputs without making any assumption regarding the system's state using the mass-sensitive method. In addition to relatively few similar works in the literature, the proposed system-solver algorithm is unique.
- The liquid receiver is found partially filled even when the condenser outlet is subcooled unlike what was assumed in the existing models in the literature. This finding is verified using numerical and experimental approaches.
- The scroll expander is modeled using the polytropic expansion process instead of the common and simplified isentropic model in the literature. In this model, the expander geometrical parameters are fixed inputs to the model instead of estimating them using the model.
- The impact of the expander lubricant oil on the performance of the plate heat exchangers and the scroll expander in micro-scale ORC systems is studied using the lubricant-refrigerant miscibility models.
- The performances of a regenerative flow turbine (RFT) for micro-scale ORC systems suited for low-grade WHR applications is studied using CFD. The merits and drawbacks of this novel expander machine are addressed to facilitate its future re-engineering for such applications.
- A small-scale, integrated CHP system consists of a dual-fluidized-bed gasifier, a steam-injected micro gas turbine, and a micro-scale ORC as the bottoming cycle is simulated considering the realistic requirements and

limitations of the process. The proposed configuration considers the main practical issues of the system integration. The gasifier model is improved considering full energy and balance of the reactor and the combustor and the auxiliary fuel. Finally, a proper gas conditioning unit is proposed and modeled to meet the practical requirements of the syngas-fueled micro gas turbine.

The thesis is organized in different chapters to assess the different aspects regarding micro-scale ORC systems to facilitate their widespread use for low-grade WHR applications. The thesis includes different aspects of the micro-scale ORC system from detailed modeling of each component to the system integration level. The main thesis objectives and the related reference works to each field are represented in Figure 1-10.


Figure 1-10. The main objectives of the thesis

# Chapter 2

# 2. Experimental investigations

*"If you can't measure it, you can't improve it"*

Lord Kelvin, British mathematical physicist

## 2.1 Introduction

To model the main components of the ORC system and to validate the models of the components and of the system itself, an experimental study is performed on a non-regenerative, micro-scale ORC system. Hence, the experimental test bench and the procedure are presented in this chapter followed by the analysis of the obtained experimental database to represent the performance of the components and the system using the raw experimental data. The experimental database is used in the next chapter to model the different components of the system and to reconcile the raw data using the lubricant oil-refrigerant mixture properties.

## 2.2 Test bench description

The ORC unit is a non-regenerative system consisted of three loops: a diathermic oil loop that provides the hot source, the working fluid loop using R134a, and the water circuit that is the heat sink of the system. The hot circuit is heated by five electrical heaters, and the cold sink is cooled down using a chiller. The flow rate of the organic fluid and the oil are adjusted using pump inverters, while the water flow rate provided by the chiller pump was fixed in all measurements. The P&ID of

the ORC system studied in this work is shown in Figure 2-1, and a photo of the system is presented in Figure 2-2.

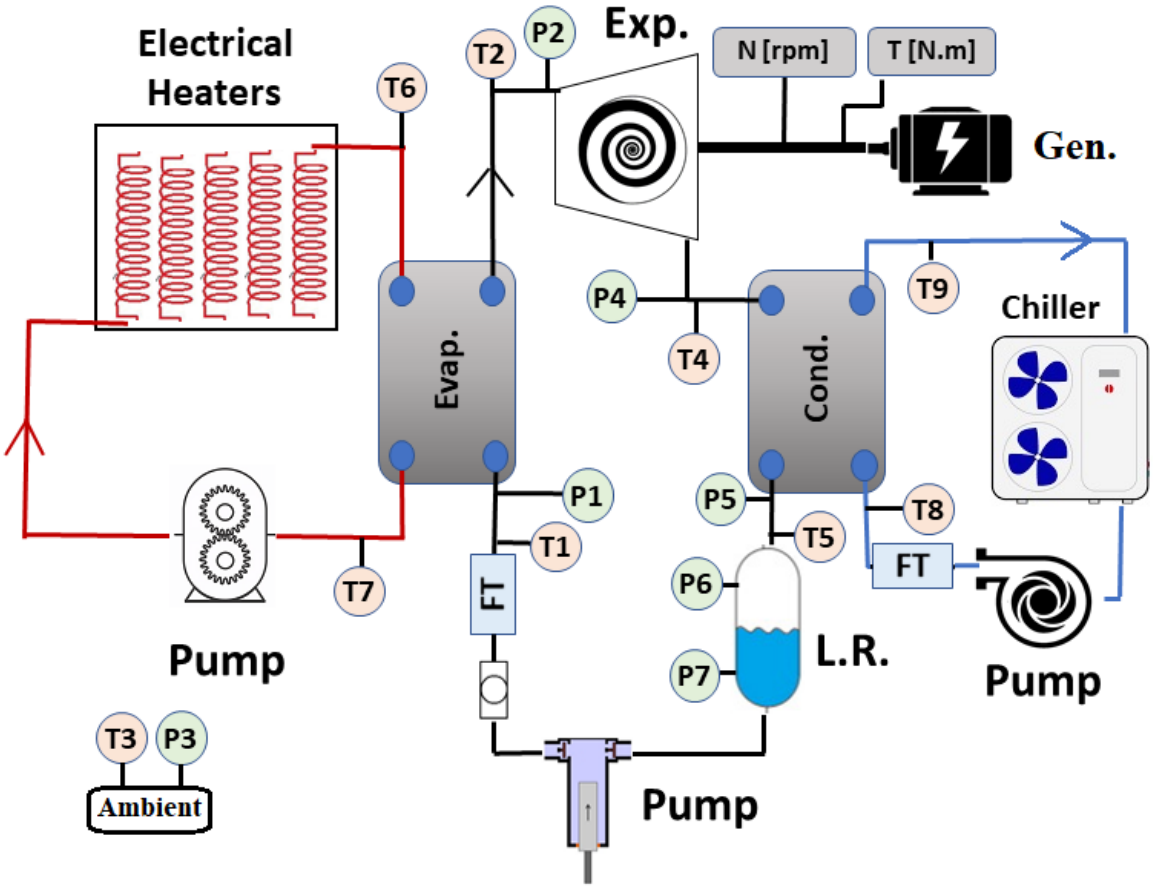


Figure 2-1. P&ID of the ORC test bench

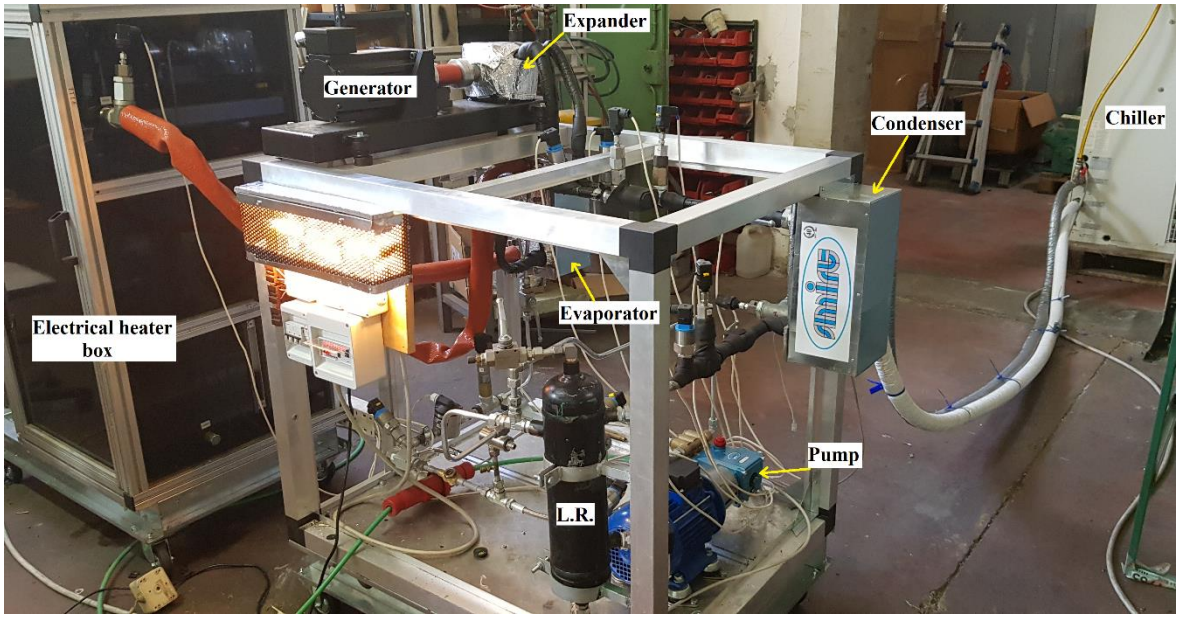


Figure 2-2. Photo of the ORC test bench

The electric load consists of three single-phase resistors (spotlights) connected in star configuration that can be adjusted using dimmer switches as illustrated in Figure 2-3.

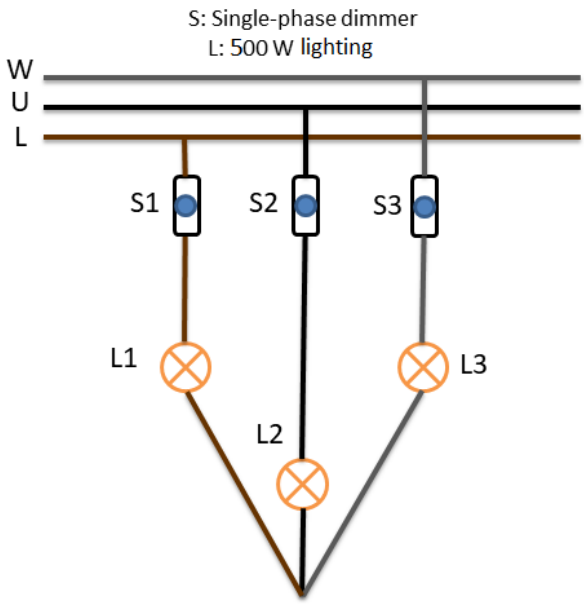


Figure 2-3. The electric load

The system is equipped with an automatic and programmable data acquisition system using a PLC board. The control program is written in a way that the system works at an almost fixed hot source temperature specified by the operator, and no specific control logic[1] is adopted in the control program to let the system operates in various conditions providing the system an off-design performance map.

The measured data of the steady-state performance are recorded with a time interval of 1s for 10 minutes (600 data points) and then the average of the recorded data is used. To determine whether the system is at the steady-state condition, the methodology used by Woodland et al. [34] and Ziviani et al. [35] is used. More precisely, the average of the first 30 data points is compared with the average of the last 30 data points meaning two sample data with 9 minutes delay. If the average of the two groups shows a negligible deviation, the system is considered at a steady state. For the sake of this analysis, relative deviations <1% for the pump discharge pressure, <5% for the expander discharge temperature, and <2.5% for the expander shaft speed are considered suitable.

The tests are performed in a way that its performance can be captured in different working conditions representing the off-design performance of the system, in which the electric generator operates at lower speeds (<1,500 rpm). This approach reduces the total number of the test numbers compared to the matrix-based test campaign maintaining the proper off-design investigation of the system as well. Considering the characteristics of the test bench, 84 useful data points are recorded.

[1] For example, to force the system to reach a preset degree of superheating by variation of the refrigerant pump speed

The description of the main components of the ORC test bench is reported in Table 2-1, and the characteristics of the sensors are reported in Table 2-2.

Table 2-1. Characteristics of main components of the ORC unit

| | | |
|---|---|---|
| Heat source medium (Texatherm HT22) | Density (at 20 °C) [kg/l] | 0.8851 |
| | Operating temperature range [°C] | -45 - 290 |
| | Kinematic viscosity [cSt] | 22 at 40 °C<br>3.75 at 100 °C |
| Electrical heaters (5 numbers) | Resistor power [$kW_{el}$] | 4.5 |
| Diathermic oil pump (gear pump) | Maximum flow rate [lpm] | 23.5 |
| | Maximum motor speed [rpm] | 1,400 |
| Evaporator/condenser | Number of plates | 50/60 |
| | Dimension (L*W) [$mm^2$] | 304*124 |
| | Heat transfer area of one plate [$m^2$] | 0.03 |
| | Space between two plates [mm] | 2.4 |
| Organic fluid pump (piston pump) | Maximum flow rate [lpm] | 13.26 |
| | Maximum motor speed [rpm] | 1,430 |
| | Nominal efficiency [%] | 85 |
| Scroll compressor | Model | Sanden TRS090 |
| | Nominal fluid | R134a |
| | Swept volume [cc/rev] | 85.7 |

| | | |
|---|---|---|
| | BVR [-] | 1.9 |
| | Oil charge (PAG) [cc] | 130+20 |
| | Maximum continuous speed [rpm] | 10,000 |
| Electric generator (3-phase brushless servomotor) | Nominal speed [rpm] | 1500 |
| | Nominal power [kW] | 1.59 |
| | Nominal Voltage [V] | 334 |
| | Maximum torque [N.m] | 10 |
| Liquid receiver | Internal Volume [l] | 3 |
| | Maximum pressure [bar] | 22.5 |

Table 2-2. Characteristics of the sensors of the ORC system

| Parameter | Model | Resolution | Accuracy | Output signal |
|---|---|---|---|---|
| Temperature | PT100 resistance | 0.1 °C | ±(0.15+0.002∗T) [°C] | 4-20 mA |
| Pressure | PMC131(A11E1A2T & A11E1A2R) | 2 mbar | <0.5% of sensor upper limit | 4-20 mA |
| Flow rate | Gear flow meter, Cobold, DOM-S15HR31 | 702 pulse/l | 1% of the read value | 4-20 mA |
| Torque | DataFlex 16/30 | 360 pulse/rev | 0.1% of the read value | -10 to +10 V |
| Shaft speed | DataFlex 16/30 | 360 pulse/rev | 1 deg. | 0-10 V |

The following points are noteworthy regarding the experimental procedure and database:

- The operation of the system is adjusted using refrigerant and oil pump speeds, oil and water inlet temperatures to the evaporator and condenser, and the electric load (five degrees of freedom). The water flow rate is constant.
- Electric power consumption of the organic fluid pump and electric power produced by the generator is measured using electric data loggers.
- Water flow rate is measured using domestic counters. The average value of 10 measurements is used for each data set.
- The oil flow rate is calculated using the oil pump specifications and an empirical model adopted from the literature.
- The range of the operating conditions of the system is limited due to the electric generator's maximum speed, and the system maximum pressure.
- Considering the electric generator speed, the scroll expander always performs in off-design conditions considering their typical shaft speeds presented in the literature.

To better illuminate the experimental constraints, the following points that appeared during the tests are noteworthy:

- The maximum pressure is limited due to the pressure sensors that can measure up to 16 bar. In addition, the scroll expander nominal working pressure is around 14 bar and cannot be extended much.
- Two pressure sensors were installed on the liquid receiver body to measure the liquid level. Their maximum threshold is 6 bar.

- The maximum thermal power is limited to around 22 kW using 5 electric heaters. However, experimental data showed that around 10-20% of the available thermal power is wasted during the heat transfer from the resistors to diathermic oil.

- The maximum refrigerant flow rate is limited due to the maximum pressure of the cycle.

- The maximum scroll expander speed is limited firstly due to the electric generator that can work at a maximum of 1,500 rpm. Then it is limited based on the refrigerant flow rate delivered to the expander, which in its turn, is limited due to the maximum pressure of the system as described in the point above.

- The water flow rate is fixed because the chiller turns off if the flow rate is reduced. Therefore, the subcooling degree cannot be adjusted at the condenser outlet using the water flow rate, but it is affected by the initial mass charge of the system.

## 2.3 **Raw data analysis**

The ORC system and its performances are investigated in this section using the raw experimental data. The recorded data are post-processed in MATLAB© using the pure refrigerant properties adopted from CoolProp ad-hoc. For the diathermic oil thermo-physical properties, they are calculated using the provided table by the supplier that is correlated and presented in the equations in Appendix (A). The range of important parameters in the experiments is reported in Table 2-3.

Table 2-3. The range of the experimental data

| $\dot{m}_{ref}$ [kg/h] | $N_{exp}$ [rpm] | $P_{su,exp}$ [bar] | $P_{su,p}$ [bar] | $T_{in,HF,ev}$ [°C] | $T_{in,,CFcd}$ [°C] | SH [K] | SC [K] |
|---|---|---|---|---|---|---|---|
| 195-176 | 753-1416 | 11.2-15.4 | 4.7-7.1 | 119.7-150.7 | 8.7-19.6 | 2-24 | 3.7-7.9 |

### 2.3.1 Data reduction

The performance of the ORC system and its main components are expressed in common and relevant parameters of such systems. The theoretical mass flow rate of the volumetric pumps is calculated using Eq. (2-1). This equation is used to calculate the theoretical mass flow rate of the diathermic oil and the refrigerant in the evaporator.

$$\dot{m}_{th,i} = \frac{N_i \cdot SV_i \cdot \rho_{su,i}}{60} \tag{2-1}$$

where $N$ is the pump speed [rpm], $SV$ is the pump swept volume [m$^3$/rev] and $\rho_i$ is the fluid density [kg/m$^3$].

However, the real flow rate of the volumetric pumps is always less than their theoretical flow rates due to internal leakages. Hence, the volumetric efficiency of a pump depends on the working conditions of the pump especially its rotational speed and operating temperature. The latter affects the fluid viscosity and the physical condition of the internal sealings. The ratio of the pump measured mass flow rate over the theoretical mass flow rate is the pump volumetric efficiency.

$$\eta_{vol,p} = \frac{\dot{m}_{meas}}{\dot{m}_{th}} \tag{2-2}$$

Expander isentropic and mechanical efficiencies are presented in Eqs. (2-3) and (2-4) respectively.

$$\eta_{is,exp} = \frac{\dot{W}_{th,act}}{\dot{W}_{th,is}} \times 100 = \frac{h_{su,exp} - h_{dis,exp}}{h_{su,exp} - h_{dis,is,exp}} \times 100 \quad (2\text{-}3)$$

$$\eta_{mech,exp} = \frac{\dot{W}_{sh}}{\dot{W}_{th,act}} \times 100 = \frac{\dot{W}_{sh}}{\dot{m}(h_{su,exp} - h_{dis,exp})} \times 100 \quad (2\text{-}4)$$

The expander produced shaft power is calculated using Eq. (2-5):

$$\dot{W}_{sh} = 2\pi\tau \cdot N_{exp}/60 \quad (2\text{-}5)$$

The scroll expander volumetric efficiency also called the filling factor, is the ratio of the measured volumetric flow rate over the theoretical volumetric flow rate. Unlike pump efficiency, its value is usually above unity indicating the internal leakages.

$$FF_{exp} = \frac{\dot{V}_{meas}}{\dot{V}_{th}} = \frac{\dot{m}_{ref}/\rho_{su,exp}}{N_{exp} \cdot SV_{comp}/(60BVR)} \quad (2\text{-}6)$$

where BVR is the expander Built-in-ratio adopted from the manufacturer datasheet to calculate the expander swept volume using the scroll compressor suction displacement ($SV_{comp}$). Finally, the system performance is expressed using the net and gross electric efficiencies:

$$\eta_{el,net} = \frac{\dot{W}_{el,net}}{\dot{Q}_{ev}} \times 100 = \frac{\dot{W}_{el,exp} - \dot{W}_{el,p}}{\dot{m}\left(h_{out,ev,HF} - h_{in.ev,HF}\right)} \times 100 \quad (2\text{-}7)$$

$$\eta_{el,gross} = \frac{\dot{W}_{el,exp}}{\dot{Q}_{ev}} \times 100 = \frac{\dot{W}_{el,exp}}{\dot{m}\left(h_{out,ev,HF} - h_{in.ev,HF}\right)} \times 100 \quad (2\text{-}8)$$

The gross efficiency is also used here since the refrigerant pump selected for the tests operates in off-design conditions resulting in low isentropic efficiencies, which leads to negative net electric efficiency for some points. To better understand the

impact of the pump, the back-work-ratio is presented that is defined as the following:

$$BWR = \frac{\dot{W}_{el,p}}{\dot{W}_{el,exp}} \tag{2-9}$$

### 2.3.2 Oil pump

The flow rate of the diathermic oil in the evaporator was not measured; instead, an evaluation of its values is performed using the empirical models adapted from the literature. Regarding the gear pump and the diathermic oil in the hot circuit, the volumetric efficiency depends on the pump speed and the viscosity of the oil, which depends on the working temperature of the oil. The real mass flow rate of the hot stream that directly associates with the performance and modeling of the evaporator and the ORC unit must be known. Therefore, an empirical model of the gear pump volumetric efficiency suggested by Michael et al. [36] is adopted here. This model was obtained from experimental tests of 16 external flow gear pumps. The volumetric efficiency is correlated to the Stribeck non-dimensional number, also known as non-dimensional viscosity that was first introduced in 1901 [37] to represent the bearing friction curves and is defined as the following:

$$\bar{\mu} = \frac{\mu \cdot \omega}{\Delta P} = \frac{2\pi}{60} \times \frac{\mu \cdot N}{\Delta P} \tag{2-10}$$

where $\mu$ is the fluid viscosity [Pa.s], $\omega$ the shaft speed [rad/s], and $\Delta P$ is the pressure difference [Pa]. The volumetric efficiency is then calculated using the suggested correlation:

$$\eta_v = 1 - \frac{6.8 \times 10^{-9}}{\bar{\mu}} - \frac{2 \times 10^{-5}}{\sqrt{\bar{\mu}}} \tag{2-11}$$

The volumetric efficiency of the gear pump is shown in Figure 2-4 at a given pressure and pump speed and varying the working temperature from 20 °C to 150 °C.

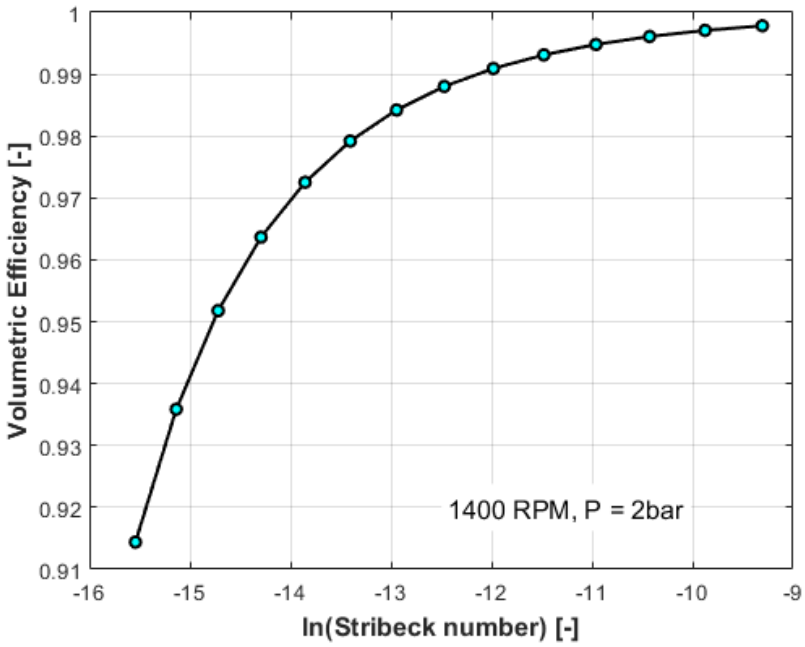


Figure 2-4. Volumetric efficiency of the oil gear pump for a given pump speed and pressure and different oil temperatures (20 °C -150 °C)

Looking at Figure 2-4 and considering the operating temperature of the oil pump in the range of 120-150 °C, its volumetric efficiency can be penalized significantly if the provided pressure is 2 bar. Therefore, an estimation of the pressure drop that the gear pump must overcome is calculated to have an estimation of the volumetric efficiency. Hence, the pressure drop is considered of two main components of pressure drop in pipes and fittings, and in the evaporator.

To calculate the pressure drop in the pipes and fittings of the oil circuit, the well-known Darcy-Weisbach friction factor is estimated using the implicit correlation for turbulent liquid flows in conduits suggested by Colebrook and White [38]:

$$\frac{1}{\sqrt{f}} = -2\ln\left(\frac{\varepsilon/D}{3.7} + \frac{2.51}{Re\sqrt{f}}\right) \quad (2\text{-}12)$$

The pressure drop in the pipes and fittings (fitting are considered using equivalent pipe length of each fitting) is calculated using Eq. (2-13):

$$\Delta P_{pipe} = \frac{1}{2} f \cdot \rho \cdot v^2 \frac{L}{D} \quad (2\text{-}13)$$

The pressure drop correlation deduced for mineral oil flow in a PHE presented by Bogaert & Bolcs [39] is used to calculate the Fanning friction factor of the oil flow in the evaporator. This correlation is presented in Eq. (2-14). It is used as Eq. (2-15) to calculate the pressure drop in the evaporator.

$$f = \frac{11.215}{Re^{0.248}} \quad (2\text{-}14)$$

$$\Delta P_{ev} = 2f \cdot \rho \cdot v^2 \frac{L}{D} \quad (2\text{-}15)$$

Therefore, the pressure drop of the oil circuit is calculated as the sum of Eqs. (2-13) and (2-15) to calculate the non-dimensional viscosity for all experimental data points. The resulted volumetric efficiency of the oil pump for the experimental database is shown in Figure 2-5 confirming the reliable performance of the oil pump in the temperature range of the tests.

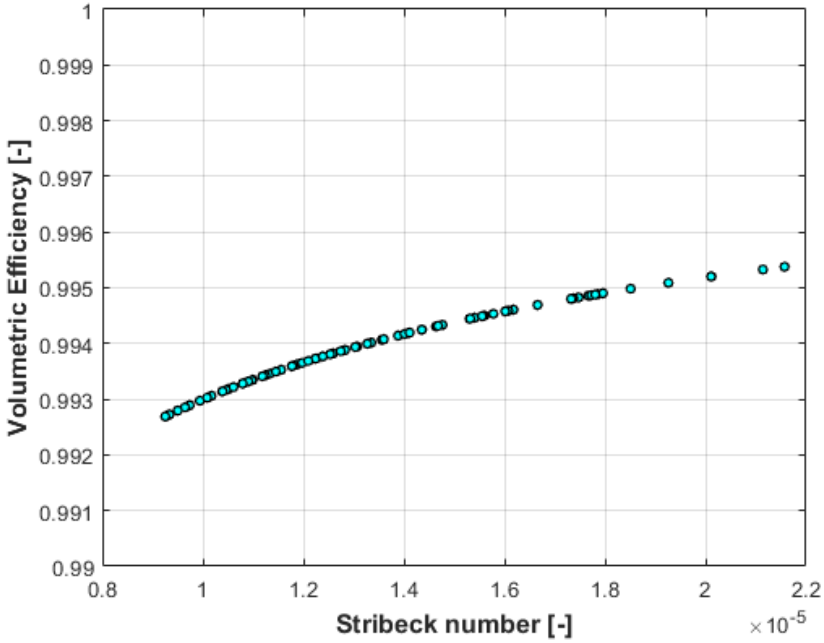


Figure 2-5. volumetric efficiency of the oil pump for all experimental data points

### 2.3.3 Experimental data cloud

The tests are performed in different working conditions to provide adequate data points for evaluation of the off-design performance of the system. To this end, the system is run at different flow rates as far as the system boundaries are met. The top boundary is whether the available power in the evaporator is not enough to superheat the organic fluid or the electric generator's maximum rotation speed is reached. The low boundaries are related to a minimum superheating degree of 2 K and the low electric power produced at low flow rates which is below the minimum electric load thus causing an unstable operation of the system. Instead of creating a matrix of the experiments that makes the work very exhaustive and time-consuming, the data are taken in a way that the system is tested in working conditions that were not tried before. Figure 2-6 presents the experimental data cloud representing the range of the experimental database.

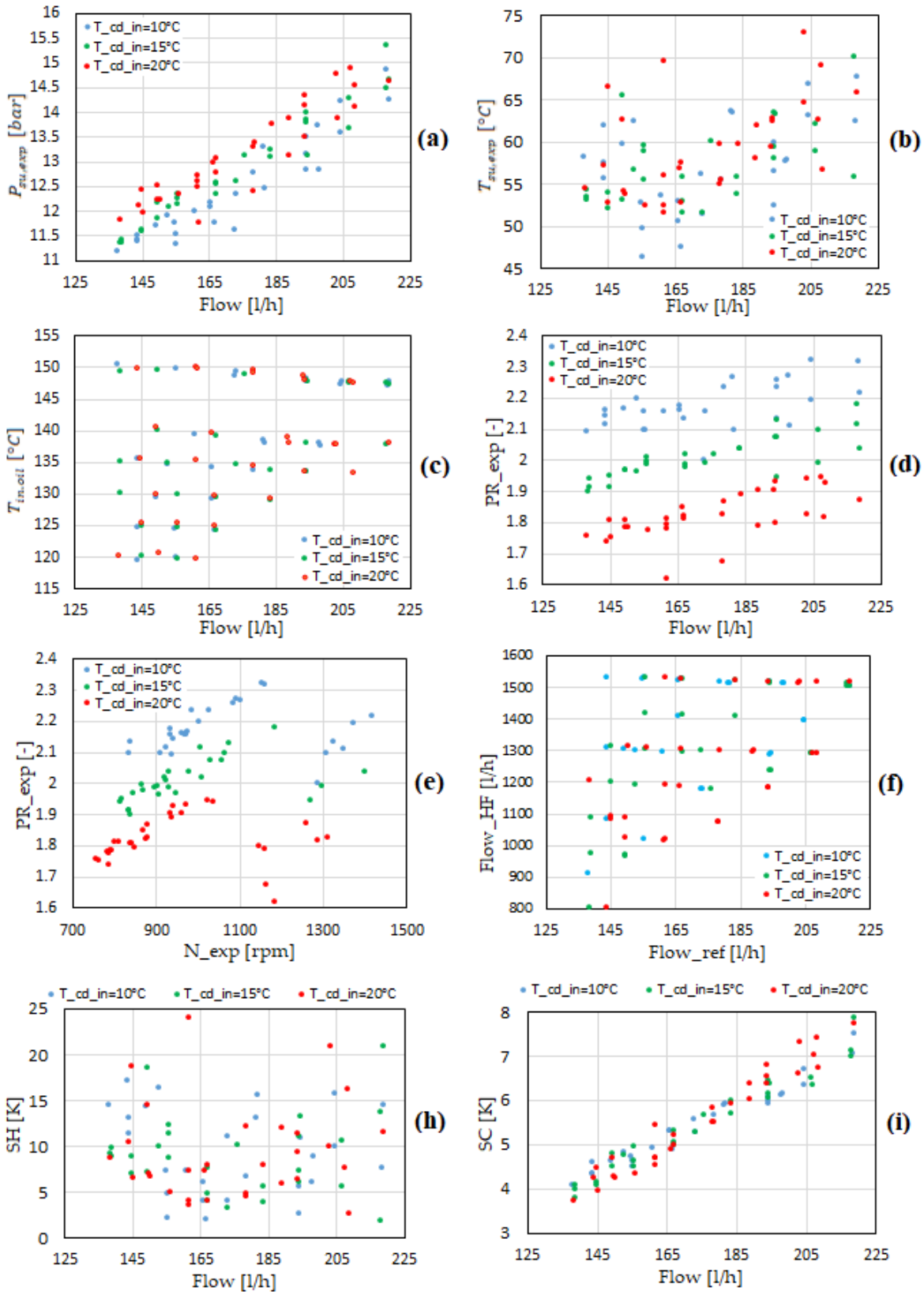


Figure 2-6. Range of the parameters constituting the experimental database

### 2.3.4 Heat exchangers

Before studying the performances of the ORC system, the reliability of the measured data must be evaluated using the relevant methods depending on the sensitivity of a phenomenon to the measurement accuracy. Some measures are mandatory for any experiments such as calibration of the instruments or selecting the instruments with enough precision before the construction of any test bench, while some other methods can be considered extreme in some cases making the system costly such as implementing double sensor configuration for each point. Furthermore, one effective method is to assess the measured data using the conservation laws in each component of the system as much as the measurements allow us. This step is to assure that the measured data are presenting sound values without any egregious errors.

Ideally, the thermal load of the two streams of any heat exchanger must be equal; however, in practice, the thermal load of the hot stream is always higher than the one of the cold stream due to thermal losses to the ambient. The thermal balance plots of the evaporator and condenser are illustrated in Figure 2-7. The uncertainty of the measurements of the thermal loads is considered using two types of uncertainty as presented in Appendix (B). The possible causes of the deviation in the thermal load are:

- Heat loss of the PHEs to the ambient.
- Miscalculation of the thermodynamic properties of R134a in the gas phase due to the presence of the lubricant oil.

The aforesaid phenomena are considered in the next chapter and elaborated on using the modeling techniques.

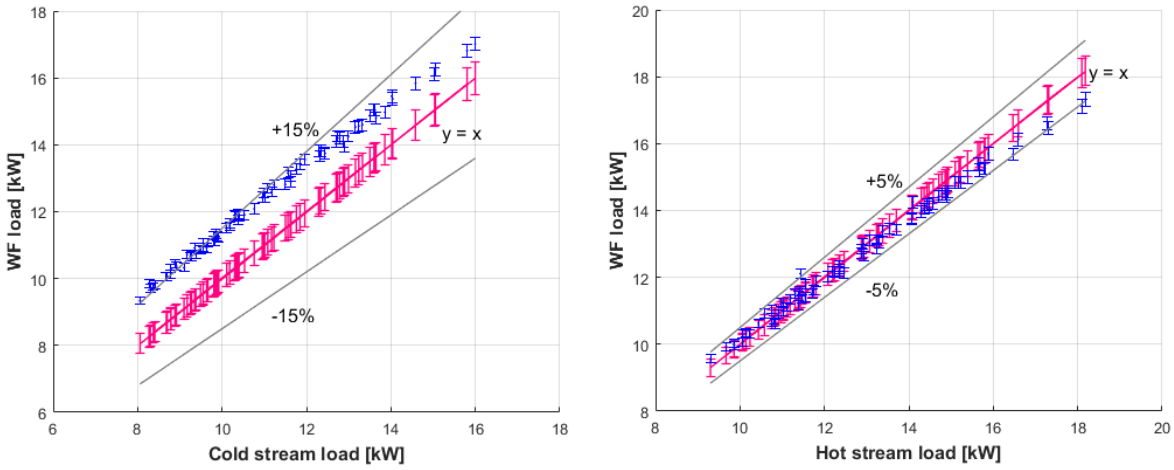


Figure 2-7. Thermal balance between the hot and cold streams of the condenser (left) and the evaporator (right)

### 2.3.5 The refrigerant pump

In the steam Rankine cycle, the power consumption of the pump is negligible compared to the power produced by the turbine and can be neglected in the calculation of the net system power [40]. Despite its importance, the real pump performance in the ORC system was reported in relatively few studies in the literature as reported in Figure 2-8. It can be concluded from Figure 2-8 that the average efficiency of 35% is reasonable for pumps in ORC systems unlike numerical studies or engine design, in which the pump efficiency is taken 65-85% [41]. The low pump performance is more critical in micro-scale ORC systems as even negative net power was reported by Yamada et al [42]. The negative net power is observed in the experiments in this work as well.

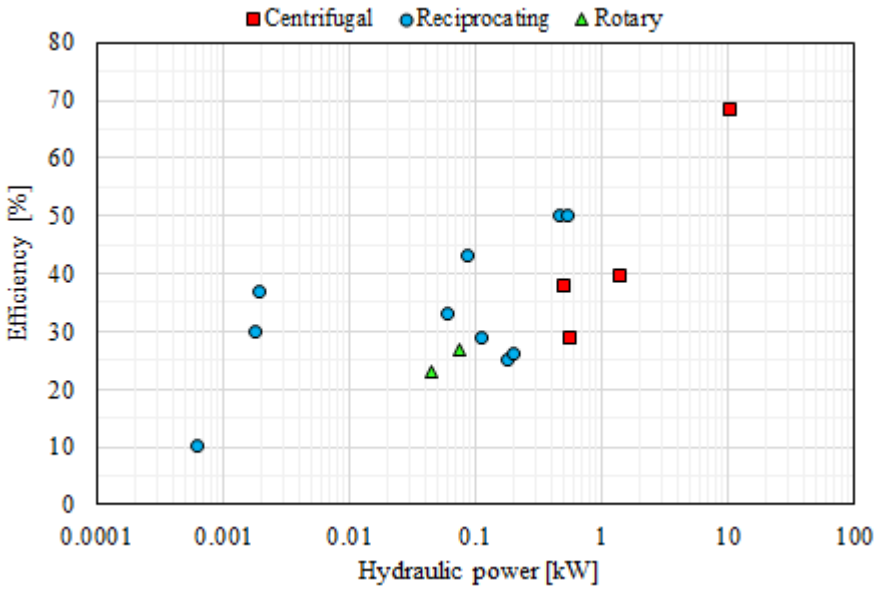


Figure 2-8. Reported pump maximum efficiency and hydraulic power in the literature up to 2017 adapted from [40]

The advantage of the selected pump in this work is its ability to provide a wide range of pressure and flow rate to study the expander machine in its off-design conditions. However, considering the maximum pressure of the system, it operates in off-design conditions leading to a significant drop in its isentropic efficiency and the net system efficiency accordingly.

This effect is observed in the experiments in this work as shown in Figure 2-9, in which the calculated isentropic efficiency of the pump is considerably lower than the nominal value of 85% stated by the manufacturer.

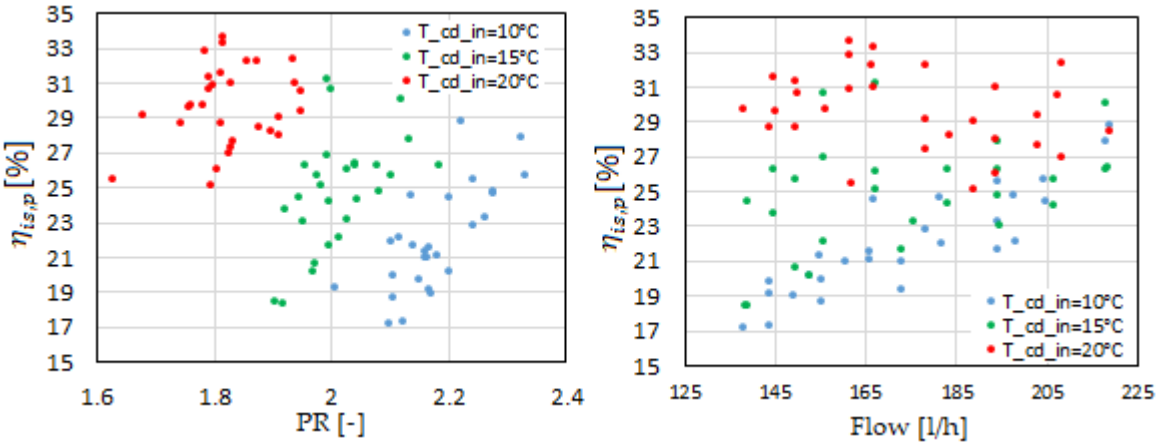


Figure 2-9. The refrigerant pump isentropic efficiency by PR and flow rate

Instead, pump volumetric efficiency shows high values as presented in Figure 2-10. Despite being penalized in higher flow rates (and so higher rotational speeds) due to an increment in the internal leakages, the good volumetric efficiency shows the high quality of the pump sealings during the tests.

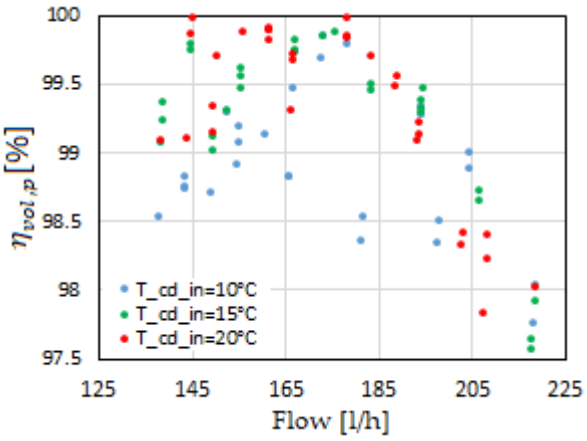


Figure 2-10. Refrigerant pump volumetric efficiency by flow rate

### 2.3.6 Pump cavitation

An important issue that was observed during the experiments is the pump cavitation. Cavitation is referred to as a phenomenon that the liquid evaporates due to the local low-pressure field, which is accounted as a detrimental and unwanted effect. Its first effect is the reduction in pump flow rate, then it may be in the company of noise and vibration. In the most severe condition, it can damage the pump check valve, plunger, and sealings by the implosion of bubbles or by making the sealings work without liquid and being overheated.

Pumps working with refrigerants are more prone to cavitation risk compared to water since their latent heat of vaporization and evaporation temperature is lower [43]. In the ORC literature, the subcooling degree is often used instead of NPSH. Yang et al. [43] reported cavitation in their piston pump for subcooling degree below 20°C. For plunger pumps, Dumont et al. [44] and Chang et al. [45] reported 10°C and 11°C subcooling degrees respectively to avoid cavitation.

The pump of the ORC test bench is originally designed for water, and the minimum suction pressure to avoid cavitation is reported by the manufacturer. Hence, let us first consider that the same curve is valid for R134a as well and adapt the manufacturer's specified unsafe and dangerous zones of water for R134a by considering the same NPSH. The results of this adaption suggest that the pump works in the dangerous zone at zero subcooling degrees as presented in Figure 2-11, and it operates in unsafe conditions at subcooling degrees of 1-4 K. The minimum subcooling degree in the experimental data is 3.75 K that means the pump operates in safe conditions based on Figure 2-11. However, the validity of the adaption procedure cannot be evaluated since no data with lower subcooling degrees are recorded to determine the unsafe and dangerous zones for R134a. Nonetheless, Landelle et al. [40] concluded that the NPSH required by their diaphragm pumps

tested with R134a follows the manufacturer limits for water; hence, the adaption is trustable.

Furthermore, they reported that the minimum NPSH (or subcooling) increases by the pump shaft speed, but it is independent of the pump pressure ratio. Based on the manufacturer specifications of the pump in this work, the NPSH is not sensitive to the pump speed in the tested temperature range for water. The author cannot confirm or reject it for R134a as further study of the pump cavitation characteristics is out of the scope of the thesis and requires a separate test campaign to obtain the pump NPSH for the specific working fluid in different temperatures and shaft speeds.

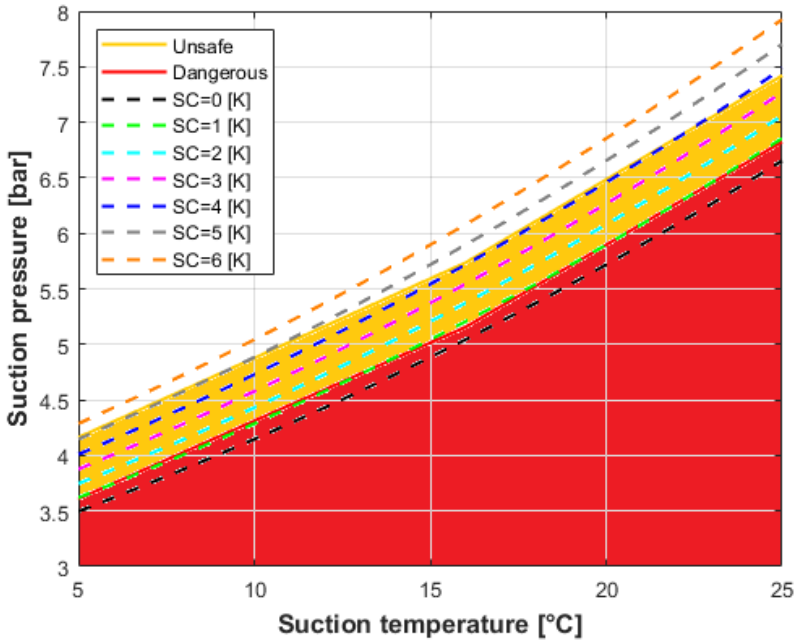


Figure 2-11. The minimum suction pressure to avoid cavitation at the pump suction in different suction temperatures for R134a was adapted from the specifications provided for water by the manufacturer.

It is noteworthy that the cavitation was observed in the plunger pump during the preliminary tests that damages the pump and the sealings were changed. The cavitation was finally resolved by adopting the following implications:

- Removing the filter at the pump suction and removing the unnecessary bends and fittings in the piping from the condenser outlet to the liquid receiver, and from the liquid receiver to the pump.
- Increasing the pump suction pipe size from its nominal size of 0.5 inches to 0.75 inches.
- Installing a vent line from the other pump suction port to the top of the liquid receiver to let the gas formed due to the reciprocating movement of the plungers to escape from the pump chamber as shown in Figure 2-12.
- Finally, the most effective action is to increase the system mass charge[1].

Indeed, the latter implication increases the system pressure in idle mode; therefore, the condenser pressure increases resulting in higher temperature pinch in the condenser and having higher subcooling degrees resulting in higher NPSH at the pump suction and avoiding any cavitation in the range of the experimental data. This approach can resolve the cavitation issue, but the subcooling cannot be adjusted as possible in other implications that are explained in the following.

[1] It was done by letting the cavitation in the pump resulting in bubbles in the sight glass installed at the pump discharge line. Then, the valve at the pump discharge is closed and the pump is run in low speeds, while the refrigerant mass charge is increased until the bubbles disappeared in the sight glass. This approach should be taken fast and with caution to avoid the pump failures.

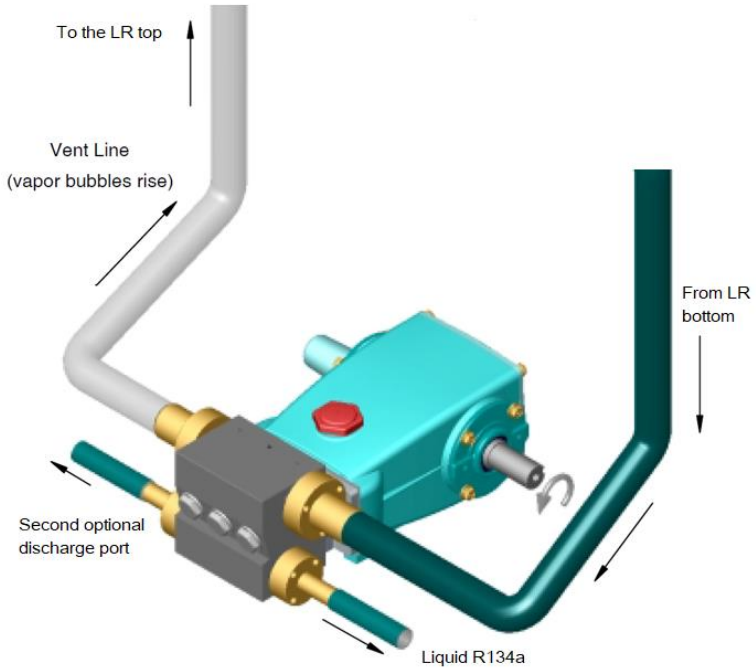


Figure 2-12. The pump vent line[1] suggested by the manufacturer to avoid the cavitation

Further solutions to avoid the cavitation that can help future studies are presented briefly in the following, which is a non-exhaustive summary of the relevant literature.

- Cold stream flow rate

As discussed, the key parameter to avoid pump cavitation is having enough subcooling degree in the condenser meaning a large enough NPSH at the pump suction. One solution is to decrease the cold stream flow rate to have a larger temperature glide that leads to higher pressure in the condenser and higher subcooling degree as shown in Figure 2-13 for an exemplary case. Therefore, if the cold stream mass flow rate is adjusted, the condenser pressure, the subcooling, and

[1] The CAD is provided by the manufacturer.

the pump NPSH can be adjusted. In the case of the studied test bench, the water flow rate was fixed and could not be reduced by other means like a regulator valve due to the requirements of the chiller.

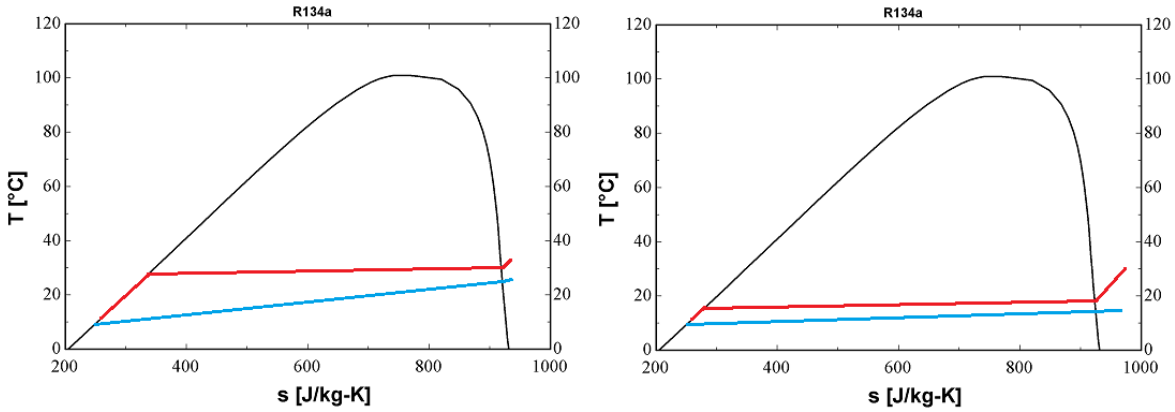


Figure 2-13. Impact of the cold stream flow rate and the temperature glide on the refrigerant subcooling degree in a condenser

- Sub-cooler HE

The use of a sub-cooler heat exchanger is another solution that increases the subcooling degree at the pump suction. Declaye [46] reported the pump cavitation issue in his Ph.D. thesis and recommended an NPSH of 4 m for his pump tested with R245fa. Having a level difference of 1.2 m between the liquid receiver outlet the pump suction, he suggested 6 K subcooling to maintain the NPSH of 4 m. Therefore, he used a sub-cooler heat exchanger in the system layout to control the subcooling degree at the pump suction independently from the condenser pressure. The sub-cooler heat exchanger is adopted also by Dumont et al. [44], and Galindo et al. [47].

The sub-cooler HE is also proposed for the ORC system as the alternative solution if the aforesaid implications failed. Considering the chiller requirement of having a

constant flow rate, the layout presented in Figure 2-14 is considered that increases the subcooling and adjusts the condenser flow rate at the same time using two regulator valves. This solution was not needed at the end and was not implemented but can be a guideline for similar case studies.

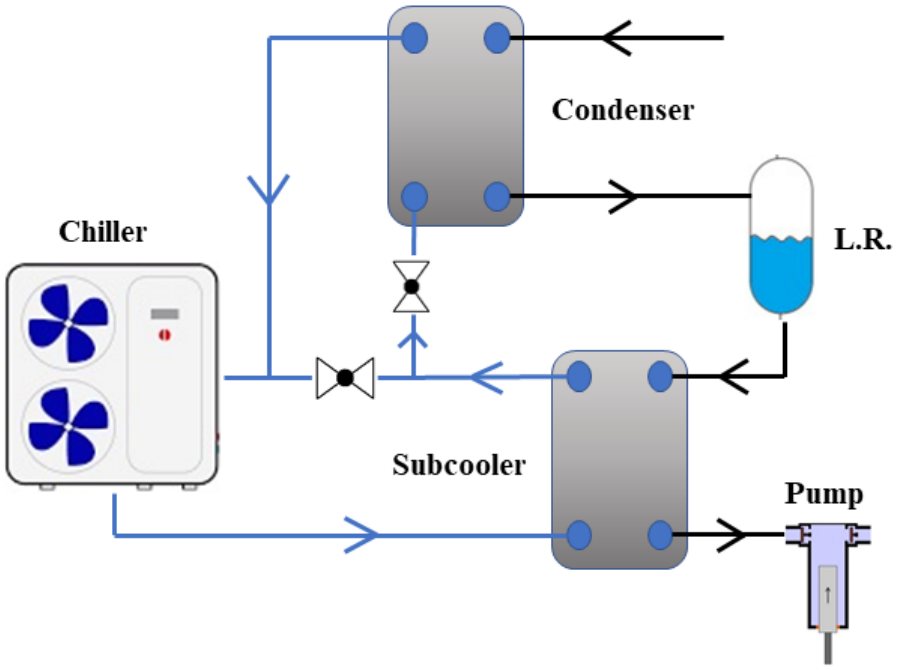


Figure 2-14. Proposal of the sub-cooler layout for the studied ORC test bench

- Pre-feed pump

A pre-feed pump can be another solution, in which a low-NPSH pump is added before the main pump as Miao et al. [48] used a centrifugal pump to feed a piston pump. This option is costly and adds complexity to the system and is not feasible unless for academic purposes.

- Gravity-fed pump

The pump suction NPSH can be increased also by increasing the level of the liquid receiver compared to the pump suction. This gravity-fed solution can be adapted to

some extent, but it is unlikely to be useful to resolve the cavitation since the available space for a system is limited.

In addition, increasing the pump suction line size and reducing the operating pump speed can help to reduce the cavitation possibility.

### 2.3.7 Scroll expander

The isentropic efficiency of the scroll expander is shown in Figure 2-15. Most data are in the range of 40-55% in the range of the pressure ratio around the expander BVR. Therefore, the under-expansion and over-expansion losses may not affect the isentropic efficiency much. However, the isentropic efficiency is slightly reduced in higher expander rotational speeds corresponding to higher pressure ratios, in which the under-expansion losses occur.

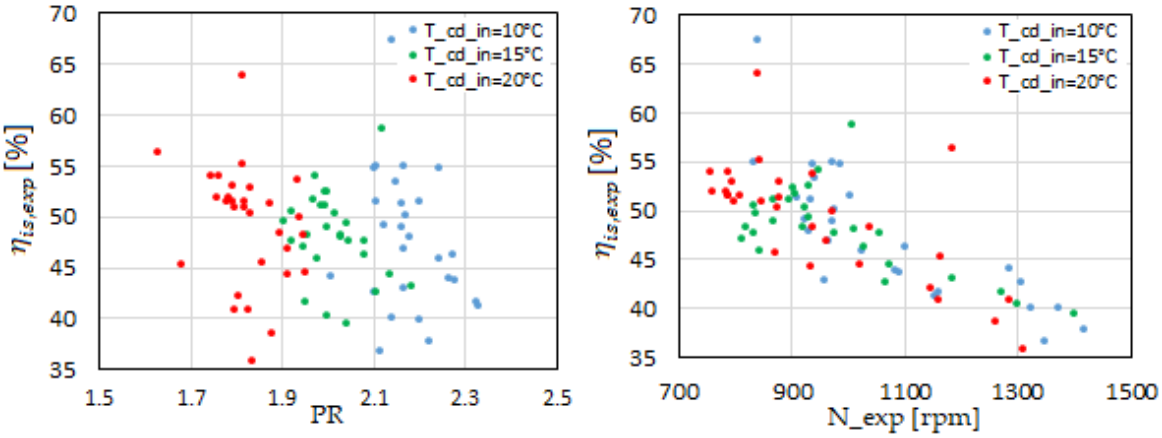


Figure 2-15. Scroll expander isentropic efficiency by PR and shaft speed

The expander shaft power is presented in Figure 2-16 showing the scroll expander produced up to a maximum of 500 W approximately in a range of relatively low shaft speeds. Higher shaft power is produced at higher shaft speeds, while the

isentropic efficiency is penalized as mentioned. In addition, the shaft power increases slightly in higher pressure ratios.

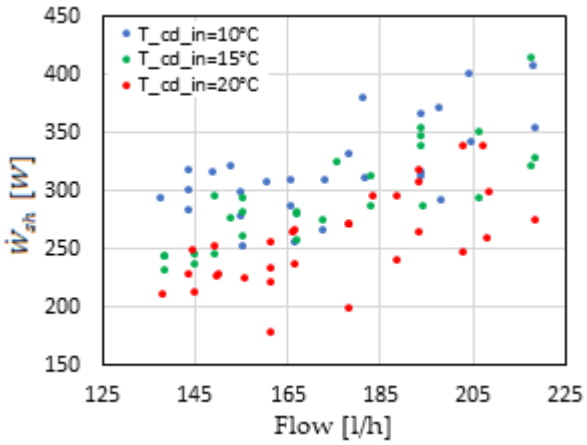


Figure 2-16. Scroll expander shaft power by flow rate

Similar to volumetric pumps, the volumetric efficiency of the volumetric expanders directly associated with the internal leakages. It is well-known that the filling factor (*FF*) is strongly dependent on the expander rotational speed and weakly on the inlet pressure of the expander and the same is observed here. The expander filling factor in this work shows a similar trend as it changes significantly with the shaft speed, and a weak dependency is visible with the pressure ratio as shown in Figure 2-17. Relatively high values of the filling factor in low shaft speeds indicate significant leakages when the expander operates at very low speeds.

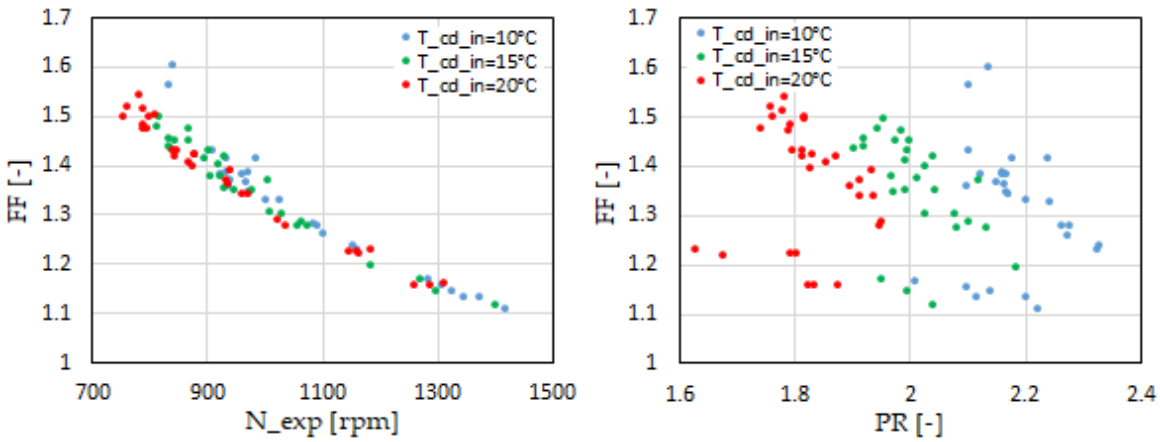


Figure 2-17. Scroll expander filling factor by shaft speed and PR

It is expected that the *FF* is always higher than unity due to internal leakages in the expander. Moreover, *FF*<1 means the measured flow rate is less than the theoretical flow rate of the expander that is unlikely to assume that the expander is producing power, but it is not filled by the gas. This effect was observed in several studies of scroll expanders and was stated as "under-filling" of the suction chamber [20,35]. However, the author believes that *FF*<1 is because the suction density of the expander is calculated using the temperature and pressure measured at the suction pipe, while the real suction density of the expander may differ considerably due to the pressure drop at the suction of the expander from the suction pipe to the suction port of the scroll revolute. Therefore, a conclusion of under-filling should be deduced with caution.

### 2.3.8 System performance

The net electric efficiency and net electric power of the ORC system are presented in Figure 2-18. The low, and in few cases, negative values are because of the low isentropic efficiency of the refrigerant pump working in off-design conditions as mentioned before. Therefore, the net electric efficiency of the ORC system is

penalized. Indeed, the ORC system had been designed to study the performance of the scroll expander and the high system efficiency was not concerned. Thus, the pump was adopted considering its ability to generate a wide range of pressure and flow rates to supply the expander machine in different working conditions.

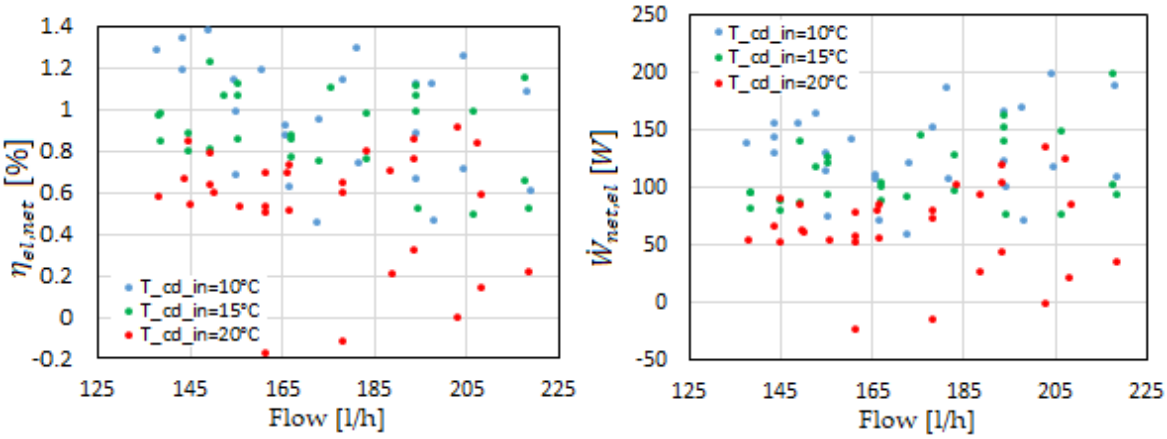


Figure 2-18. ORC system net electric efficiency (left) and net electric power (right)

To better understand the destructive impact of the low isentropic efficiency of the pump on the net efficiency of the system, the back-work-ratio (BWR) is presented in Figure 2-19 confirming the disproportionate pump selection for the range of the power generated by the ORC system. BWR increases as the heat source temperature and fluid critical temperature decrease [49]. Furthermore, BWR is estimated to be about two and four times higher for R245fa and R134a respectively compared to water [45].

Indeed, this effect reveals the non-negligible impact of the pump power consumption in micro-to-small size power systems unlike what one may be able to assume in steam power generation systems. Hence, it is worthy to present the gross system electric efficiency as well to have an estimation of the net electric efficiency if a well-sized pump was used.

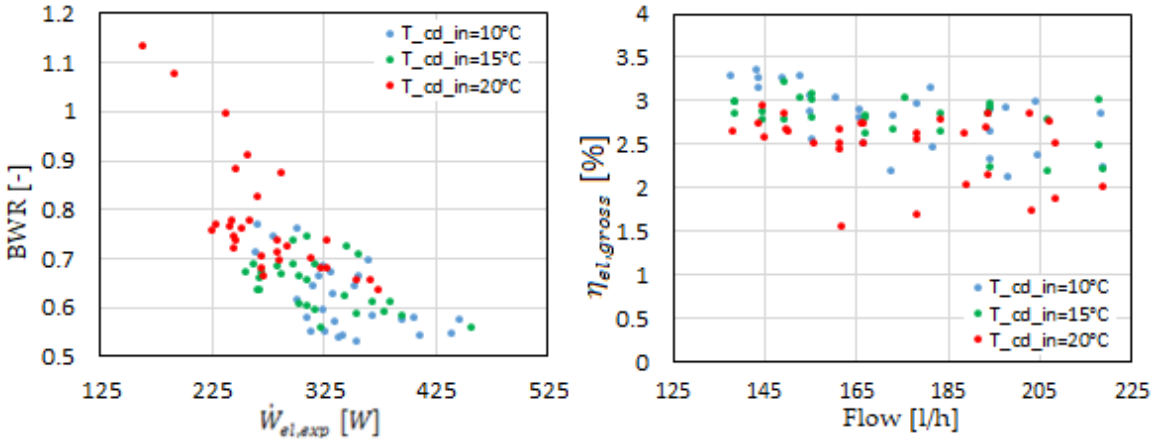


Figure 2-19. Pump back-work-ratio by expander produced electric power (left), and ORC system gross efficiency by the flow rate (right)

## 2.4 **Summary and conclusions**

The description of the micro-scale ORC test bench and the measurement sensors are presented in this chapter. The experimental campaign aimed to record the experimental data in different working conditions. Hence, no controlling code was implemented during the tests to obtain the system off-design performance experimentally. Overall, 84 useful steady-state data points are recorded, and they are reported in Table A5. The issues regarding the pump cavitation that was observed during the tests are presented with the suggested measures to resolve them. The raw experimental data are analyzed to assess the performance of the main components of the system and the overall system performance accordingly. The refrigerant pump has not been operated efficiently; thus, the system's net electric performances are penalized significantly having even some points with negative net electric power. However, the good system performance was not the aim of the experimental campaign, but the possibility to test the different components, especially the scroll expander in different working conditions was targeted.

The recorded data are used for the next chapters to simulate the system's main components, which are used in the mass-sensitive system modeling. Moreover, the physical inconsistency observed in the evaporator and the condenser test results is the foundation for investigating

the impact of the expander lubricant oil on the performance of the evaporator, condenser, and the expander in a separated chapter.

## 2.5 **Nomenclature**

| | |
|---|---|
| $\dot{m}$ | mass flow rate [kg/s] |
| $\dot{V}$ | volumetric flow rate [m³/s] |
| $\dot{W}$ | power (work) [W] |
| $\dot{Q}$ | power (heat) [W] |
| N | shaft speed [rpm] |
| P | pressure [Pa] |
| f | friction factor [-] |
| D | diameter [m] |
| L | length [m] |
| h | enthalpy [J/kg] |

*Greek symbols*

| | |
|---|---|
| $\omega$ | shaft frequency [Hz] |
| $\eta$ | efficiency [%] |
| $\tau$ | torque [N.m] |
| $\mu$ | dynamic viscosity [Pa s] |
| $\bar{\mu}$ | non-dimensional viscosity [-] |
| $\rho$ | density [kg/m³] |
| $v$ | velocity [m/s] |
| ε | surface roughness [m] |

*Subscripts and superscripts*

| | |
|---|---|
| su | suction |
| dis | discharge |
| meas | measured |
| th | theoretical |
| act | actual |
| is | isentropic |
| exp | expander |
| p | pump |
| ev | evaporator |
| mech | mechanical |
| sh | shaft |
| el | electrical |
| v | volumetric |
| HF | hot fluid |

*Acronyms*

| | |
|---|---|
| SV | Swept Volume [m³/rev] |
| BWR | Back Work Ratio [-] |
| Re | Reynolds number [-] |
| NPSH | Net Positive Suction Head [-] |

# Chapter 3

# 3. Modeling of the ORC system components

*"A theory has only the alternative of being right or wrong. A model has a third possibility: it may be right, but irrelevant"*

Manfred Eigen, German biophysical chemist

## 3.1 Introduction

In this chapter, the main components of the ORC system are modeled using the experimental data. The semi-empirical models of the system components are then used in the system-level modeling of the ORC unit. The models are performed to consider the main characteristics of each component considering the computation speed and accuracy at the same time. All measurement uncertainties are calculated based on the equations in Appendix (B).

## 3.2 Heat exchangers

To have a reliable off-design model of an ORC system, the heat exchangers (HEs) must be modeled accurately. The HEs of the ORC unit tested in this work are brazed plate heat exchangers (BPHEs) that are modeled using hydraulic and thermal geometry-independent empirical correlations. In the following, the common methods and implications of the modeling of PHEs are discussed briefly, then the hydro-thermal modeling of the evaporator and condenser of the ORC system are presented.

### 3.2.1 Hydro-thermal modeling methods of PHEs

PHEs were usually modeled using three empirical methods in the literature. The first is to correlate the thermal load of a PHE to the effective parameters or flow non-dimensional numbers using data fitting methods. For instance, the effective parameters in the case of an evaporator can be the mass flow rate and inlet thermodynamic state of the hot and cold streams, saturation pressure of the cold stream, and the degree of superheating. This model needs a series of experimental data of a specific PHE to correlate its thermal load to the effective parameters. The use of such models should be performed cautiously for the working conditions outside the range of the database, and extrapolation of the results would result in even unphysical performance. Moreover, this method gives no information regarding the heat transfer coefficient (HTC) in different zones in both streams of the PHE, the accurate length of the two-phase zone, the dependency of the temperature distribution of both streams to the convective heat transfer coefficients, which leads to a poor prediction of temperature pinch inside the PHE in off-design conditions. Finally, the calculation of the working fluid mass presented in the PHE would be no better than a blind estimation. Therefore, this model is more useful for engineering estimation of the performance of PHEs having an overall view of the performance of a system.

The other two models are aimed to give a resolution of the thermal performance of the PHE using a spatial discretization of its length. The common methods are moving boundary (also known as moving zone) and finite volume methods that are categorized based on the adopted spatial modeling method. In addition, the models can be categorized based on the calculation method of HTC. Therefore, the general aspects of these models are discussed briefly in the following.

#### 3.2.1.1 Spatial resolution methods

The HTC of both streams in different working conditions and different heat transfer zones need to be known to have the resolution of thermal performance, and an estimation of the working fluid mass in a PHE. Because of the presence of different heat transfer mechanisms in PHEs and different thermal and hydraulic characteristics accordingly, a model must be able to distinguish boundaries of zones using relevant hydro-thermal models. The spatial model usually distinguishes the boundaries of different heat transfer zones along the length of the PHE and the distribution of the properties is assumed uniform along the width of the PHE. The common spatial methods are described briefly hereunder.

The moving boundary method divides the heat exchanger into several zones depending on the heat transfer mechanisms at work. This method is used in this work and is described in detail in the following subsections. The other method is the finite volume, in which the length of the heat exchanger is divided into several nodes at the beginning of the solver, then using the heat transfer models, the outlet state of the fluid can be obtained for each cell that is the input state of the next cell. The solver marches cell by cell until it reaches the last cell, and the state of the fluid(s) is checked at each cell to call the relevant hydro-thermal model to calculate the transferred heat between the hot and cold cells.

In general, the finite volume method is more accurate than the moving zone method especially in the calculation of the working fluid mass, but they are more computationally time-consuming. However, by performing node independency analysis, computation time may reduce considerably. Furthermore, their improvement in the thermal and hydraulic calculation accuracies depends on whether the adopted hydro-thermal correlations were local models or average ones.

#### 3.2.1.2 Convective heat transfer coefficient calculations

No matter which of the aforesaid spatial methods are used, the local HTC is to calculated using the relevant correlations. The available models in the literature for PHEs are empirical correlations that can be categorized into geometry-dependent and geometry-independent models. The first group requires the manufacturing geometrical specification of the plate, usually the chevron angle, the corrugation pitch, and the corrugation depth. Such data are not provided in the data sheets by manufacturers and one must obtain them to use these models. Therefore, the tested PHE must be cut to know the manufacturing details resulting in a waste of money and material. The final correlation then finds a correlation between the flow non-dimensional numbers and plate geometries encompassing several empirical coefficients.

The most popular geometry-dependent HTC correlations for PHEs are reported in Appendix (D). The quoted state-of-the-art correlations cover a rather wide range of working conditions, fluid types, and plate geometries with the expense of losing accuracy. Therefore, one should consider the use of a specific model consistent with the specific working condition, plate geometry, and working fluid if it was available in the literature rather than using the generalized models. In this work, these models are not used, and only geometry-independent models are considered.

In geometry-independent models, the HTC is correlated to the non-dimensional numbers of the flow (i.e. Re, Pr, etc.) and the empirical coefficients are needed to tune the correlation for the specific heat exchanger and the specific range of the working conditions. Their main advantage is that they can be applied using the common specification of the PHEs provided in datasheets. However, they have common limitations of an empirical correlation such as being limited to the range of the working conditions and flow hydro-thermal regimes of the database.

In the case of ORC systems, further issues arise regarding the HTC correlations available in the literature that can affect their accuracy. The boiling correlations were mostly obtained for low saturation pressures since they were intended to be used in refrigeration applications not power generation systems. The number of single-phase correlations is limited for the gas phase. Moreover, the number of condensing data points in the database is limited compared to the boiling database. Therefore, hydro-thermal models of flows in tubes must be adopted sometimes then tuned using experimental data to adapt for PHE modeling. Finally, some new refrigerants have not been studied with specific heat transfer mechanisms or plate geometries, while their use in the system-level studies is necessary to reveal their pros and cons. The hydro-thermal modeling of the evaporator and condenser of the ORC system studied in this work is presented in the following.

### 3.2.2 Modeling of the PHEs of the ORC system

In this work, several geometry-independent models for single-phase, boiling, and condensing flows are used to find out the most accurate combination for the thermal modeling of the evaporator and the condenser of the ORC unit. Hence, hydraulic modeling of the PHEs of the ORC test bench is elaborated in the following subsection, then the developed hydraulic models are used in the thermal modeling of the evaporator and condenser of the ORC system. A separate discussion is presented because the hydraulic and thermal models are decoupled as discussed in the following.

#### 3.2.2.1 Hydraulic modeling of the PHEs

The pressure drop in the evaporator and the condenser of the ORC unit is modeled in the refrigerant stream using the retuned empirical correlations, while it is

neglected in the hot fluid stream in the evaporator and the cold fluid stream in the condenser. Hydraulic modeling of the PHEs is performed mainly to assess their thermal performance more correctly. Pressure drop especially influences the calculated degree of subcooling in the condenser and the superheating in the evaporator.

In addition, solving a PHE using moving boundary or finite volume methods requires the resolution of the pressure distribution inside the PHE. Indeed, a specific calculation of the total pressure drop can result from an infinite combination of the pressure distribution inside the channel, which in its turn, affects its thermal modeling. If a pressure drop correlation that depends on the local thermal resolution is adopted, the thermal and hydraulic correlations become coupled and an iterative solver is needed for each zone/cell of the PHE consequently. Therefore, because the mechanistic hydraulic modeling of the PHEs is not of significant importance to this work, an estimation of the pressure drop distribution is obtained using the relevant empirical models to have the hydraulic resolution independently from the thermal solver and make them decoupled.

The pressure drop modeling is performed using experimental data of the PHEs of the ORC unit. All pressure sensors of PHEs are located at the same level of their ports except the inlet pressure sensor of the evaporator that is 64 cm below the evaporator inlet; thus, the inlet pressure is less than the measured pressure due to the pressure of the liquid column in the pipe, which is calculated and considered in the database.

Two geometry-independent pressure drop models are presented hereunder. These models are dependent on the flow characteristics and thermodynamic properties of the fluid. The first model presented in Eq. (3-1) is the simplest one presented in [29] to estimate the overall pressure drop first, then its distribution is considered

according to the enthalpy change of the fluid. The mass flow rate was used in the reference, but mass flux is adopted here.

$$\Delta P_{tot} = a \cdot G^{b} \tag{3-1}$$

where $G$ is the mass flux [kg.m$^{-2}$.s$^{-1}$], $a$[1] and $b$ are empirical coefficients that are to be obtained using the optimization algorithm by minimizing the objective function (f) defined as the sum of the square of the relative deviation between the calculated pressure drop and the measured values as presented in Eq. (3-2):

$$f = \sum_{i=1}^{n} \left( \frac{\Delta P_{cal,i} - \Delta P_{meas,i}}{\Delta P_{meas,i}} \right)^{2} \tag{3-2}$$

This correlation gives the total pressure drop, and to have its spatial distribution, it is assumed proportional to the transferred thermal energy in each zone:

$$P_i = P_{in} - \frac{h_i - h_{in}}{h_{out} - h_{in}} \Delta P_{tot} \tag{3-3}$$

Despite being simple, this model requires the enthalpy at zone/cell boundary and the outlet enthalpy of the channel to calculate the pressure distribution. In other words, the hydraulic solution depends on the thermal solution and the two are coupled and an external iterative solver loop is needed, which makes the model complicated and computationally heavy.

The next model is inspired from [50] suggested for single-phase flows in PHEs and used for boiling pressure drop modeling in PHEs by Desideri et al. [51] as in Eq. (3-4).

[1] This coefficient must be dimensional to make the units of Eq. (3-1) consistent.

$$\Delta P_i = a \frac{G^2}{2\rho_i} \tag{3-4}$$

where G is the mass flux [kg/m$^2$.s], $\rho_i$ is the average zone/cell density [kg/m$^3$], and $a$ is the empirical coefficient to be found by minimization of the objective function presented in Eq. (3-2).

The results of the model and the pressure distribution in the evaporator for one data point are presented in Figure 3-1. It is evident that the Root Mean Square Error (RMSE) of the results is low showing excellent agreement between the model results and the experimental data. The pressure distribution shows that the significant share of the total pressure drop is accounted for in the superheated gas zone despite the marginal enthalpy change in this zone. Indeed, it is expected that the pressure drop increases as the vapor quality goes up resulting in higher fluid velocity in the channel. The resolution of the pressure drop may be different especially in the two-phase zone if the finite volume solver is used to track the variations of the fluid properties with vapor quality and void fraction. In this work, only the moving boundary method is used, and a physical estimation of the pressure drop is adequate.

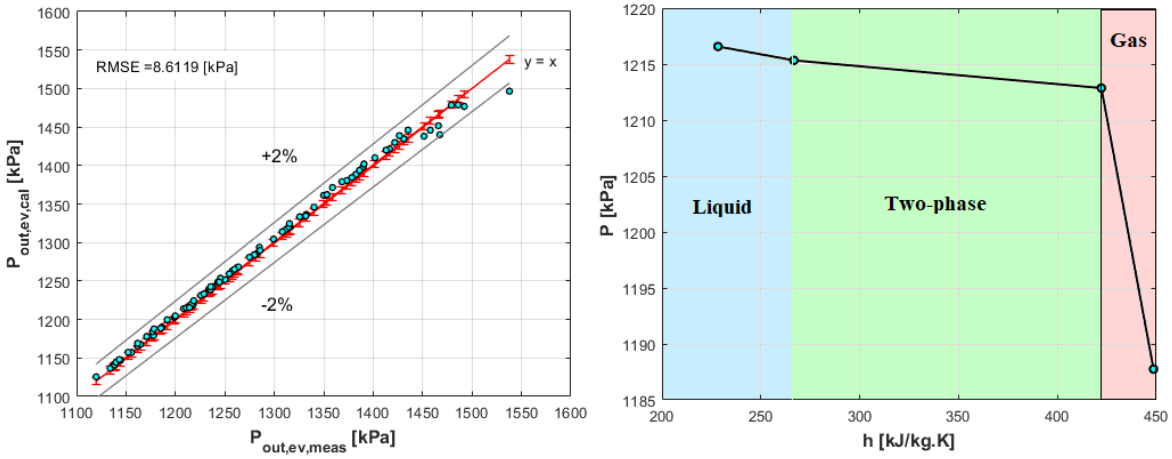


Figure 3-1. Calculated and measured pressure drop of the evaporator (left), and pressure distribution in the evaporator (right)

The results for the condenser are presented in Figure 3-2 showing slightly higher accuracy (lower RMSE) compared to the evaporator results. The lower accuracy of the results of the evaporator is due to the higher deviation of the evaporator experimental data around the mean value. The Inlet pressure of the evaporator is directly prone to the pulses of the plunger pump, and its saturation pressure is affected by the variations of the heat source temperature as well. Instead, the plunger pump pulses were almost damped at the condenser inlet and the water inlet temperature was much more stable due to the high mass flow rate of the cooling circuit.

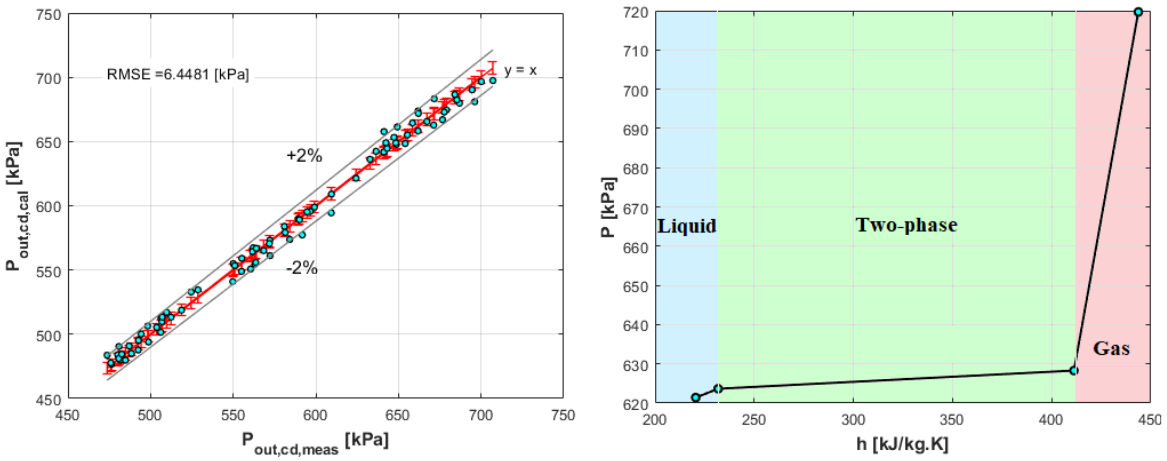


Figure 3-2. Calculated and measured pressure drop of the condenser (left), and pressure distribution in the condenser (right)

Finally, it should be noted that this approach should be taken with caution for general models of the heat exchangers especially if the pressure distribution resolution is important particularly; but for the modeling purposes in this work, a compromise between the accuracy and computational speed is taken. The obtained empirical coefficients for the evaporator and condenser are reported in Table A1.

#### 3.2.2.2 Thermal modeling of the PHEs

The moving boundary method is used in this work for spatial modeling of the PHEs. In this method, the area of the plate (usually the length is the variable parameter and the distribution along the width of the plate is considered uniform) is divided into three zones, if existed, namely fully liquid zone, two-phase zone, and the full gas zone. For instance, in the case of an evaporator, the superheating zone, the boiling zone, and the subcooled zone of the cold stream can be distinguished. If the other stream changes the phase, three zones are expected there as well. Therefore, in the ultimate case of a general flow in an HE that both streams change the phase, five zones can exist as shown in Figure 3-3.

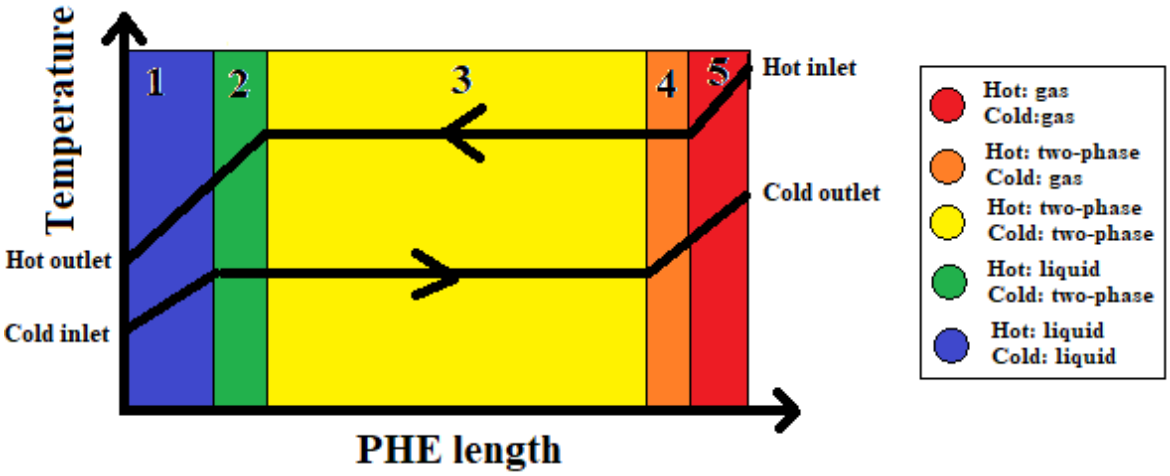


Figure 3-3. A possible distribution of heat transfer zones in a heat exchanger when both streams change the phase

Regarding the studied ORC unit, only the refrigerant stream changes the phase, and the hot stream in the evaporator and the cold stream in the condenser are in the single-phase liquid, so three zones are presented. Therefore, the zones are known easily using the liquid and gas saturation enthalpies of the refrigerant, and so the amount of heat that must be transferred in each zone is calculated. The calculated thermal load of the refrigerant stream is assumed to be fully transferred to the other stream in both the evaporator and the condenser. In this way, the boundaries of the zones are known.

The next step is calculating the HTC in the hot and cold streams using the relevant correlations for each heat transfer zone to obtain the overall HTC of the zone. The pressure drop in each zone is calculated decoupled from the thermal resolution and before the thermal solver using the method and the correlation elaborated in the previous subsection.

Several geometry-independent, single-phase, boiling, and condensation HTC correlations are tried out to find the best combination that can predict the

experimental data of the evaporator and the condenser of the ORC unit. The four single-phase correlations are Dittus-Boelter correlation [52], its modified correlation suggested by Sieder-Tate [53] considering the variations of the viscosity of the fluid due to the difference between the wall temperature and the bulk temperature, Bogaert-Bolcs [39] correlation, and the correlation suggested by Kays and Crawford [54]. Except for the Bogaert-Bolcs model that was suggested for mineral oil in a PHE and is the accepted correlation among the Swedish manufacturers [55], the rest were obtained for turbulent flows in tubes. These correlations are reported in Appendix (D).

To fit the models with the experimental data of the evaporator and the condenser, some effective coefficients are tuned by minimization of the objective function using the optimization methods (Genetic Algorithm). The objective function is the calculated area of the PHE needed to have thermal performance as the experimental data. The sum of the calculated areas of the three zones must be equal to the total heat transfer area of the plate. Therefore, the objective function is defined as the following:

$$f = \sum_{i=1}^{n} \left( \frac{A_{cal,i} - A}{A} \right)^2 \tag{3-5}$$

where $n$ is the number of experimental points (84 no. in this work), $A$ is the heat transfer area of the plate taken from the manufacturer datasheet, and $A_{cal,i}$ is the calculated area of the plate:

$$A_{cal} = A_L + A_{tp} + A_V \tag{3-6}$$

where the area of each zone is calculated using the thermal load needed for the zone calculated from the refrigerant stream, the overall heat transfer coefficient (U) calculated using the HTC of each stream, and the logarithmic mean temperature difference using the following equations:

$$\dot{Q}_i = \dot{m}_{ref,i} \cdot \Delta h_i \tag{3-7}$$

$$U_i = \frac{1}{\frac{1}{CHTC_{C,i}} + \frac{1}{CHTC_{H,i}} + \frac{t}{\lambda_{plate}}} \tag{3-8}$$

where subscripts *C* and *H* refer to cold and hot streams in each zone calculated from the HTC of the zone that is obtained from the relevant correlations, $t$ is the plate thickness, and $\lambda_{plate}$ is the plate material conductivity. Then, the heat transfer area needed for zone "$i$" is calculated using Eq. (3-9).

$$A_i = \frac{Q_i}{U_i \cdot \Delta T_{lm,i}} \tag{3-9}$$

After the optimization is performed for each combination of the HTC models to find the coefficients of the correlations, an iterative solver is adopted to calculate the hydro-thermal performance of the PHE in off-design conditions. The iterative solver calculates the pressure drop in each zone independently from the thermal model first, then the outlet enthalpy of the PHE is guessed. The required area for the guessed thermal performance is calculated and compared with the available heat transfer area of the PHE and if the residual is small enough, the guessed value is transferred to the output of the solver as the final solution. The flowchart of the iterative solver is illustrated in Figure 3-4.

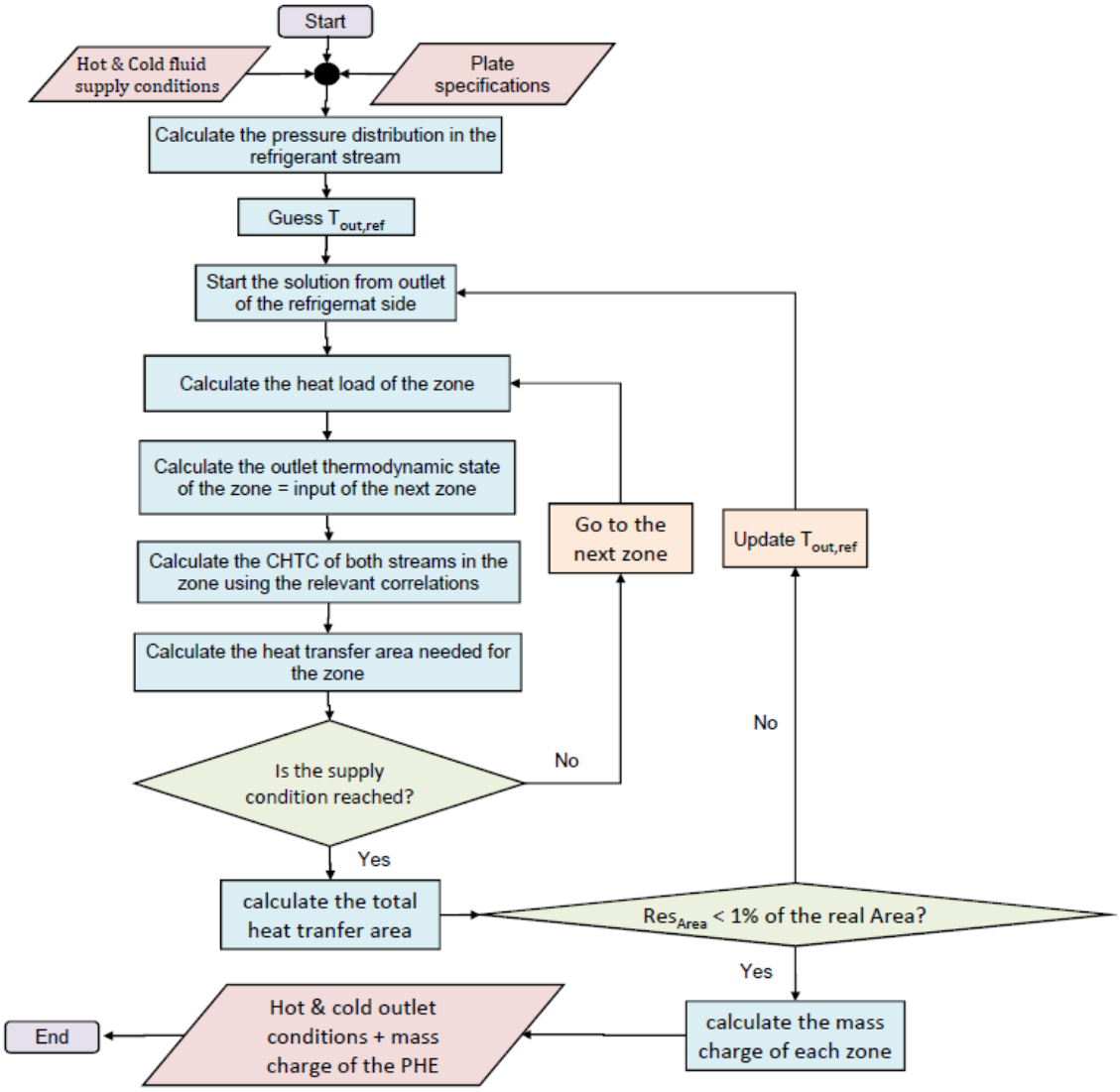


Figure 3-4. Flowchart of the PHE iterative solver using geometry independent HTC models

The results of the optimization are presented in the following for the evaporator and the condenser of the ORC unit using R134a as the working fluid, diathermic oil (H22) as the hot fluid, and water as the cooling medium.

- Condenser:

Four single-phase HTC correlations are combined with the two condensation HTC correlations: Claesson [56] and Kuo [57] models. Claesson correlation was suggested for condensing R134a in PHEs, and the other one for condensing R410 in

PHEs. The best results are obtained using Kays and Crawford single-phase and Claesson condensation correlations. One coefficient is found for water stream correlation, two for liquid and gas single-phase R134a, and one for the condensation correlation (4 in total). The obtained coefficients for the HTC models are reported in Table A2.

The results of the selected model are shown in Figure 3-5, neglecting few points[1] with a very low-temperature pinch that made the modeling difficult to obtain good accuracy for all points. The predicted performance of the condenser shows the excellent agreement of the model with the experimental data. The outlet temperature of the refrigerant reached close to the inlet temperature of the water due to the relatively high mass flow rate of water and the big size of the condenser. Moreover, the high HTC calculated in the two-phase zone can be recognized noticing the relatively large temperature change in the water stream.

[1] 7 points are not presented for the condenser modeling results since the very low temperature pinch required a set of the empirical coefficients for the HTC models that are different from the coefficients of the model that can predict most of the data with good accuracy.

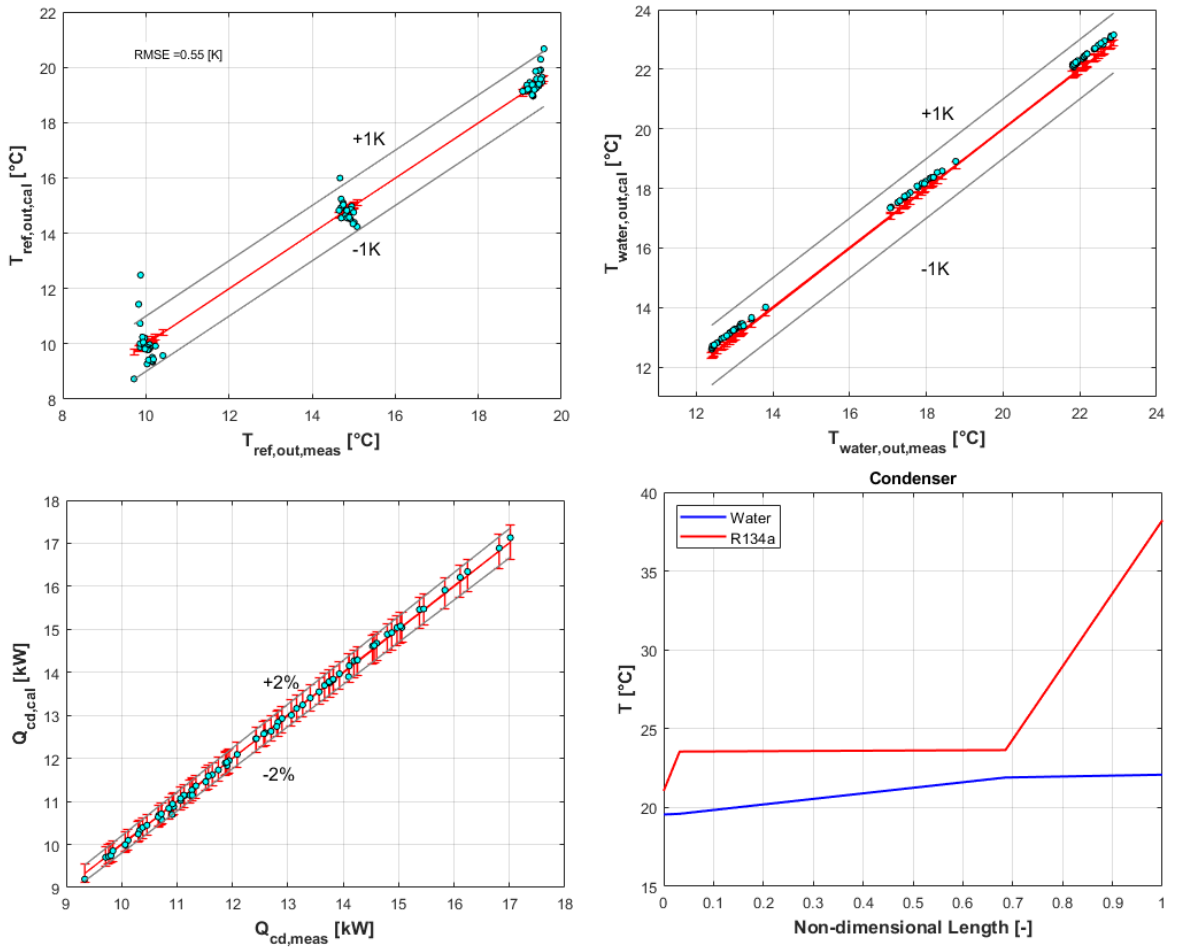


Figure 3-5. Results of the condenser hydro-thermal model vs experimental data

- Evaporator:

Similar to the condenser modeling, four single-phase and three boiling HTC models are considered. The single-phase correlations are the same as for the condenser, and the boiling correlations are Hsieh et al. I [58], Hsieh et al. II [59], Desideri et al. [51], and Yan et al. [60]. Hsieh I correlation was obtained for subcooled boiling of R134a in vertical PHEs, Hsieh II correlation for R410 boiling in PHEs, Desideri's correlation for R245fa and R1233ZD in PHEs, and Yan's one for R134a in PHEs. Due to the presence of more variables effective on the performance of the evaporator and wider range of the working conditions, the coefficient of the boiling HTC correlation

is found for each single data point, then it is correlated to the Re and Pr numbers of the oil and R134a streams using the regression data fitting method.

The best combination of the models is found using Kays and Crawford model for liquid and gas single-phase HTC of R134a using coefficients of the original model, Bogaert-Bolcs model for single-phase oil flow using coefficients of the original model, and Yan's model for boiling HTC with one coefficient correlated to the flow characteristics of the oil and the refrigerant streams. The original coefficients of the aforesaid single-phase correlations and the correlated coefficient of Yan's model are reported in Table A3. The results of the selected model are shown in Figure 3-6. The predicted performance of the evaporator shows good agreement between the model and the experimental data.

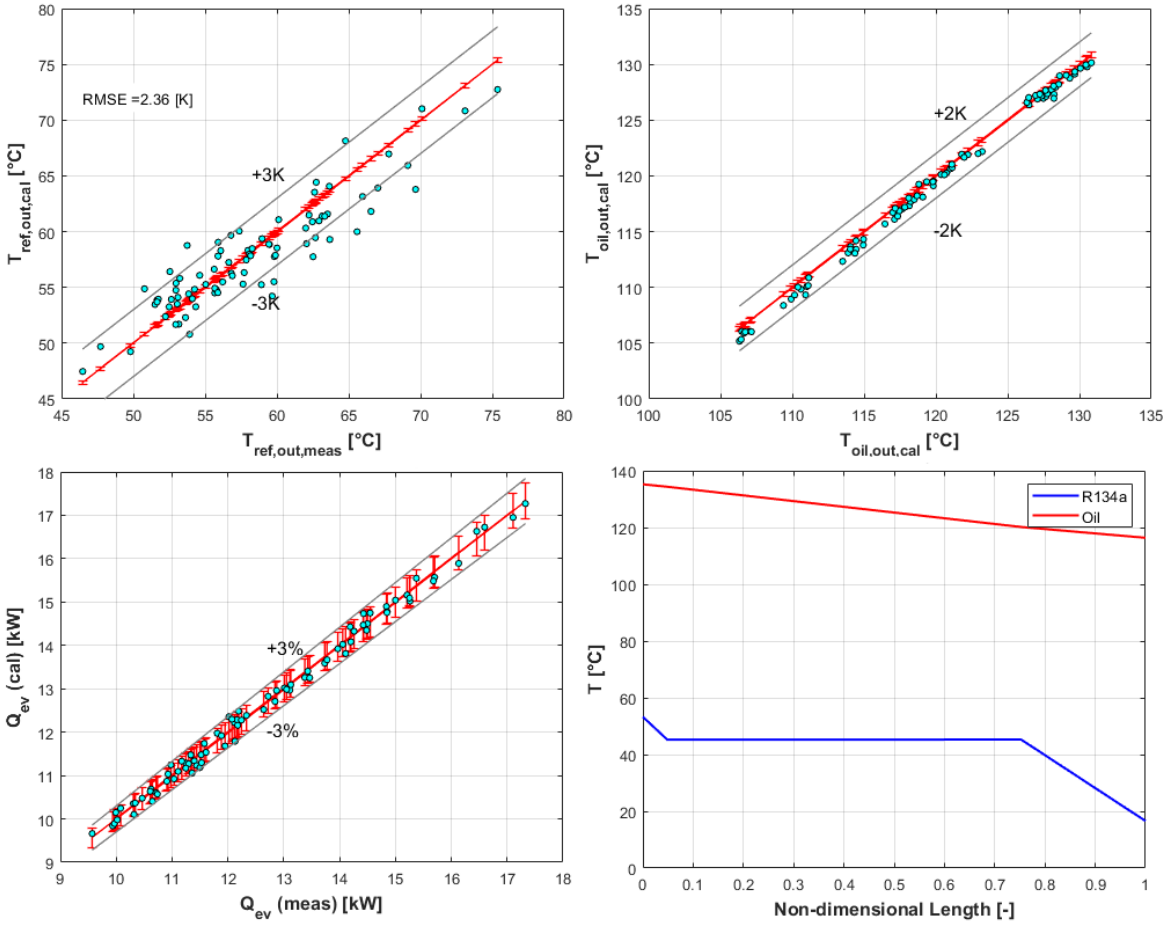


Figure 3-6. Results of the evaporator hydro-thermal model vs experimental data

One reason for less accuracy of the evaporator model compared to the condenser model is the higher heat loss from the evaporator to the ambient compared to the condenser due to the significantly higher temperature of the evaporator. The heat loss is occurred not only from the evaporator body to the ambient but also in the hot fluid pipe since the temperature sensors had a distance from the evaporator inlet and outlet ports. Another reason goes back to the higher fluctuations of the evaporator inlet and outlet pressure due to the direct effect of the plunger pump pulses and variations of the heat source temperature as discussed in the hydraulic modeling subsection. Nonetheless, the accuracy of the model for both the evaporator and condenser of the ORC unit is good enough to rate their performance properly.

In addition, the degree of superheating and subcooling in the evaporator and condenser are important parameters to determine the range of the working conditions for the safe operation of the expander and the pump especially if a turbo-machine is used. Hence, the proposed hydro-thermal models of the PHEs should be evaluated using superheating and subcooling degrees since they depend on the accuracy of both thermal and hydraulic models simultaneously.

The degree of superheating and subcooling[1] are presented in Figure 3-7. It is evident that the deviation between the measured and the calculated values grows in some points for both the evaporator and the condenser, yet most data are predicted with good accuracy. The importance of the superheating and subcooling results is due to their dependency on both the calculated outlet temperature and pressure; hence, a simultaneous effect of errors of both the thermal and hydraulic models may pile up for some data points. Therefore, accurate hydraulic modeling is important when the model is used for the design of the system especially in the case of direct HEs as in micro-scale ORC systems.

[1] As mentioned in the condenser modeling section, 5 points are not presented for the condenser mdelling

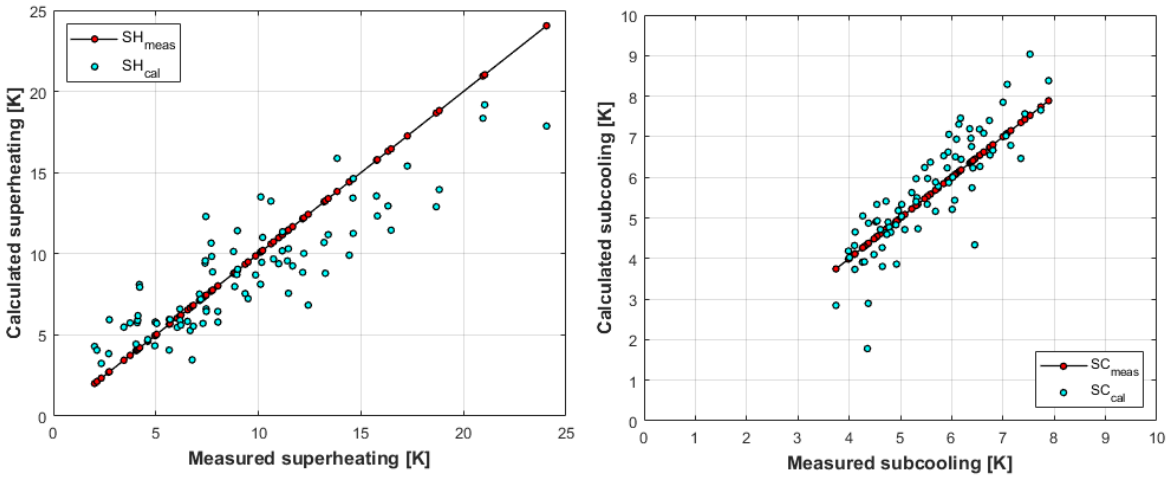


Figure 3-7. measured and calculated superheating in the evaporator (left) and subcooling in the condenser (right)

## 3.3 **Refrigerant pump**

The volumetric efficiency, the isentropic efficiency, and the electromechanical efficiency of the plunger pump are modeled using experimental data. The empirical coefficients of the models are tuned using the experimental data; hence, extrapolation of the models should be done with caution.

### 3.3.1 Volumetric efficiency

The measured flow rate of the pump is used to calculate its volumetric efficiency as Eq. (3-10):

$$\eta_{vol} = \frac{\dot{V}_{meas}}{\dot{V}_{th}} \times 100 = \frac{\dot{V}_{meas}}{\frac{N \cdot SV}{60}} \times 100 \tag{3-10}$$

where subscripts "*meas*" and "*th*" refer to the measured and theoretical values respectively, $N$ is the pump speed [rpm], and $SV$ is the swept volume of the oil pump [$m^3$/rev]. The real flow rate of the volumetric pumps is always less than their

theoretical values due to internal leakages. The internal leakage flow depends on several parameters such as the rotational speed, fluid viscosity (usually depends strongly on the working temperature), and the provided pressure by the pump. Equation (3-10) can be rewritten using the leakage flow rate:

$$\eta_{vol} = \frac{\dot{m}_{act}}{\dot{m}_{th}} \times 100 = \frac{\dot{m}_{th} - \dot{m}_{lk}}{\dot{m}_{th}} \times 100 = (1 - \frac{\dot{m}_{lk}}{\dot{m}_{th}}) \times 100 \quad (3\text{-}11)$$

where subscripts "*act*" and "*lk*" refer to the actual and leakage respectively. The leakage mass flow rate of the pump is modeled using the adiabatic flow in a nozzle, in which the leakage flow travels from the pump discharge pressure to the suction pressure through small clearance gaps. The leakage mass flow rate in the nozzle throttle can be deduced as the following:

$$\dot{m}_{lk} = \rho_{lk} \cdot A_{lk} \cdot lk = \rho_{su} \cdot A_{lk} \cdot v_{lk} \quad (3\text{-}12)$$

where the subscript "*su*" refers to the suction. The fluid velocity in the throttle can be calculated using Bernoulli's equation:

$$v_{lk} = \sqrt{\frac{2(P_{ex} - P_{su})}{\rho_{su}}} = \sqrt{\frac{2\Delta P}{\rho_{su}}} \quad (3\text{-}13)$$

Combining Eqs. (3-12) and (3-13), the leakage mass flow rate is derived as Eq. (3-14):

$$\dot{m}_{lk} = A_{lk}\sqrt{2\rho_{su} \cdot \Delta P} \quad (3\text{-}14)$$

The throttle area ($A_{thr}$) represents the average leak area of the pump that is modeled in this work using the non-dimensional viscosity as the following:

$$\frac{A_{lk}}{A_{bore}} = a \cdot \bar{\mu} = a\left(\frac{\mu \cdot \omega}{\Delta P}\right) \quad (3\text{-}15)$$

where $A_{bore}$ is the bore area of the piston chamber taken from the pump specification sheet, $\omega$ the shaft speed [rad/s]. The empirical coefficient "$a$" is to be

obtained using the minimization of the objective function ($f$) presented in Eq. (3-16) for each data point:

$$f_i = \left( \frac{\eta_{vol,i,cal} - \eta_{vol,i,exp}}{\eta_{vol,i,exp}} \right)^2 \tag{3-16}$$

The coefficient "$a$" is obtained for each data point, then it is correlated to two non-dimensional numbers of the pump namely the suction Prandtl number ($Pr_{su}$) and reduced pump speed ($N_r$) using the regression data fitting method.

$$a = f(Pr_{su}, N_r) \tag{3-17}$$

$$Pr_{su} = \frac{\mu_{su} \cdot C_{p,su}}{\lambda_{su}} \tag{3-18}$$

$$N_r = \frac{N}{N_{max}} \tag{3-19}$$

where $N_{max}$ is the maximum pump speed declared in the pump specification sheet (1,500 rpm).

The calculated volumetric efficiency is shown versus the experimental volumetric efficiency in Figure 3-8 showing the good accuracy of the model. The volumetric efficiency model is needed to know the real mass flow rate of the pump for different working conditions. The calculated mass flow rate of the pump using the pump speed as the input is plotted in Figure 3-8 confirming the accuracy of the model for the range of the working condition of the pump as the experimental data.

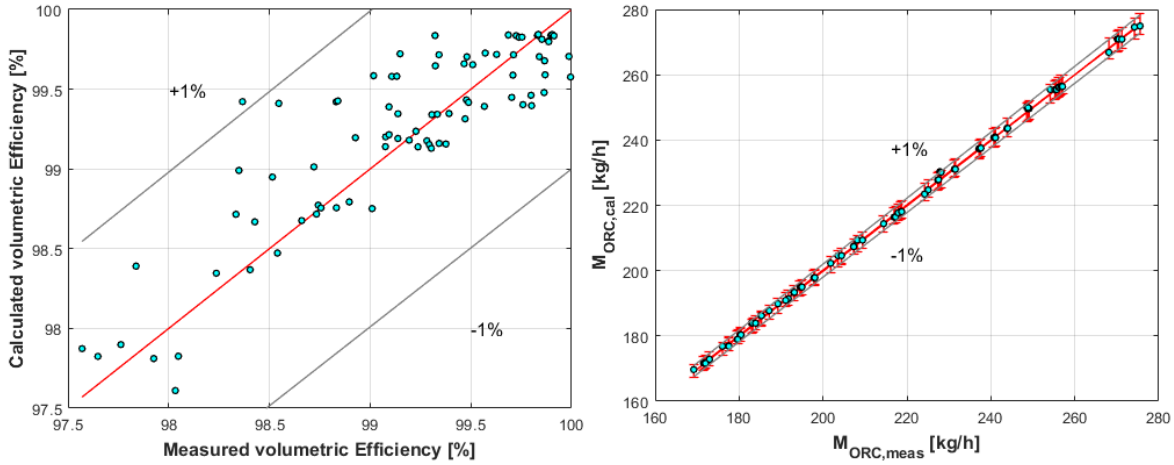


Figure 3-8. Measured and calculated pump volumetric efficiency (left) and pump mass flow rate (right)

### 3.3.2 Isentropic efficiency

Similar to the pump volumetric efficiency model, its isentropic efficiency is modeled empirically. It is defined using Eq. (3-20), in which the actual work of the pump is considered the sum of the reversible work and the shaft loss work, and the shaft loss work is correlated to the loss torque:

$$\eta_{is} = \frac{\dot{W}_{is}}{\dot{W}_{act}} \times 100 = \frac{\dot{W}_{is}}{\dot{W}_{is} + \dot{W}_{loss}} \times 100 \tag{3-20}$$

$$\dot{W}_{loss} = \frac{2\pi}{60} \times N \cdot \tau_{loss} \tag{3-21}$$

where $N$ is the pump speed [rpm] and $\tau_{loss}$ is the loss torque that is the empirical coefficient. The sensitivity analysis showed that the experimentally calculated isentropic efficiency can be correlated to the pump suction Prandtl number; thus, its non-dimensional form is adopted:

$$\frac{\tau_{loss}}{\Delta P \cdot {A_{bore}}^{1.5}} = a \cdot Pr_{su} \tag{3-22}$$

where "$a$" is the empirical coefficient that is correlated to the suction Prandtl number ($Pr_{su}$) and reduced pump speed ($N_r$) using the minimization of the difference between the simulated isentropic efficiency and the experimentally measured values like Eq. (3-16). The calculated isentropic efficiency using the model is depicted in Figure 3-9 showing good accuracy for most data points. Moreover, the predicted pump outlet temperature is plotted showing excellent accuracy.

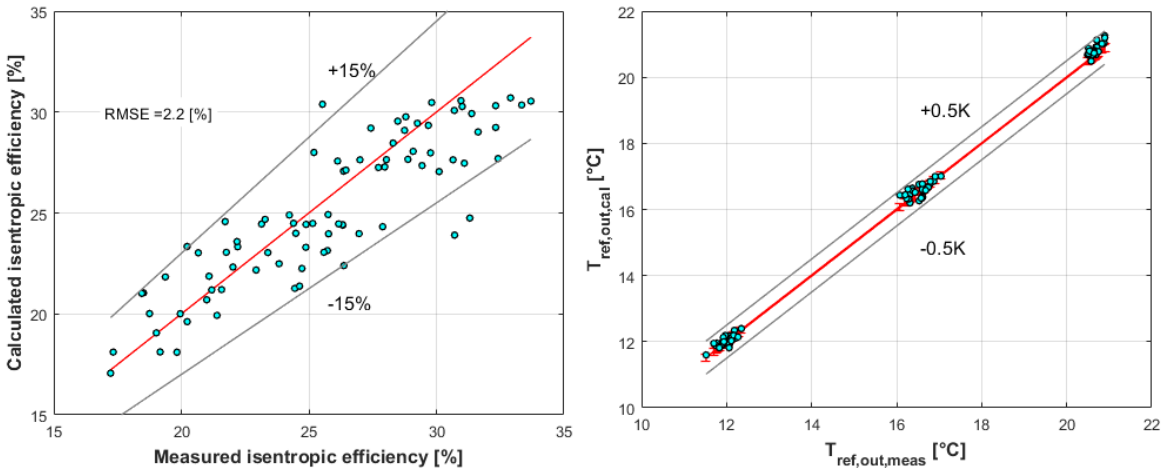


Figure 3-9. Measured and calculated pump isentropic efficiency and discharge temperatures

### 3.3.3 Electro-mechanical efficiency

The electric power consumption of the pump is higher than its thermodynamic power due to mechanical losses in the shaft coupling and bearings and electric losses in the electric motor. Considering the sum of the mechanical and electrical losses, the electro-mechanical efficiency is defined as the following:

$$\eta_{el-mech} = \frac{\dot{m}(h_{ex} - h_{su})}{\dot{W}_{el,meas}} \times 100 \tag{3-23}$$

where the denominator is the measured pump electric power consumption (active power). The pump electric power consumption is correlated to the pump reversible work using Eq. (3-24):

$$\dot{W}_{el} = a \cdot \dot{W}_{rev}{}^{b} \tag{3-24}$$

$$\dot{W}_{rev} = \dot{m}\frac{\Delta P}{\rho_{su}} = \dot{m}\frac{P_{ex} - P_{su}}{\rho_{su}} \tag{3-25}$$

where "$a$" and "$b$" are the empirical coefficients found by minimization of the objective function for electro-mechanical efficiency like Eq. (3-16). Therefore, the pump electric power consumption is calculated using Eq. (3-26):

$$\dot{W}_{el} = 30.6\dot{W}_{rev}{}^{0.53} \tag{3-26}$$

The pump electric power consumption and its electro-mechanical efficiency calculated using the presented empirical models are presented in Figure 3-10 showing good agreement between the suggested model and the experimental data.

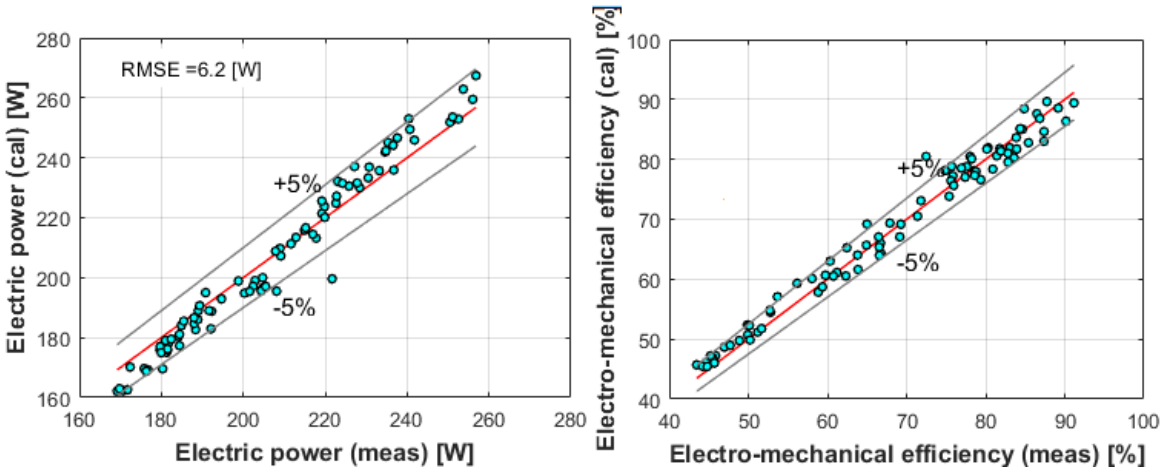


Figure 3-10. Measured and calculated pump electric power and electro-mechanical efficiency

## 3.4 **Scroll expander**

In small-scale ORCs, the expansion machine is the key element in all the aforesaid terms. They are generally categorized into two major types: dynamic machines and volumetric expanders [61]. Due to the inherent technical characteristics, dynamic machines are not usually suited for micro-to-small scales (up to 50 kW), and volumetric machines are preferred [62]. Common examples are vane expanders, piston expanders, screw expanders, and scroll expanders. The latter got a high score among different types of volumetric expanders in multi-criteria rankings studies according to [63,64]. Since the end of the eighties, small compressors were adapted to scroll expanders to obtain reliable and low-cost systems for power generation at small sizes [65]. Song et al. [66] reviewed scroll expanders tested in ORC systems. They categorized the literature based on the type of the scroll expander and quoted six open drive expanders modified from automotive compressors with shaft power in the range 101-2,558 W and efficiency of 10-70%. In addition, five open drive expanders adapted from air compressors were presented with shaft power of 187-2,100 W and efficiency of 42-77.5%. Popularity of the scroll expanders in the literature is also understandable from the review study on four volumetric expanders, namely vane, piston, screw, and scroll, in which the number of the studies on scroll expanders were readily higher than the others [63]. For example, 35 works were listed regarding experimental studies on scroll expanders compared to 16 experimental works on screw expanders. Hence, studying the behaviour of such kind of expander at different working conditions is of paramount importance to assess the off-design performances of ORC systems and their actual reliability.

To predict the performance of the scroll expanders in wider operating ranges, different modeling approaches have been used in the last years besides the experimental studies. They range from simple models such as single-coefficient models [17], quadratic polynomial empirical models [67], to more advanced finite element methods (FEM) [68], and computational fluid dynamic (CFD) models

[69,70], which consider the geometrical evolution of the expander revolute. The simple models are well suited for system-level simulations, but they suffer from low accuracy especially in the working conditions out of the range of the experimental data thus resulting in a lack of extrapolability. On the contrary, the advanced models are very accurate and the evolution of the thermodynamic states of the fluid can be captured during the expansion process. However, they are not suitable for system-level studies and their results are valid for the specific machine geometry [71].

In between, the semi-empirical models, also called grey-box models, represent a good compromise between the model accuracy, the calculation speed, and the model extrapolability. Therefore, they are considered the best choice for system-level optimization analyses. In general, these models require a set of experimental data to tune the coefficients of a series of sub-models that are physically relevant to the expansion process. In the literature, the most widely accepted semi-empirical model of scroll expanders was inspired from the model applied by Winandy et al. [72] to the scroll compressors and then adopted to an open-drive, oil-free scroll expander in an experimental study by Lemort et al. [73]. They adapted an air compressor to the expander in a non-regenerative ORC unit working with R123. The expander shaft speed was set to different values (1,771, 2,296, and 2,660 rpm) and the maximum obtained shaft power and overall isentropic efficiency were 1.82 kW and 68% respectively. For the sake of the present analysis, this model is hereafter called the benchmark model since it showed a good compromise between the accuracy and the computational speed and subsequently was adopted in several studies on scroll expanders [74–76] and scroll compressors [77], and also to other types of volumetric machines such as screw expanders [78].

The benchmark model was then modified by Ziviani et al. [35] by adding the discharge pressure drop and by splitting the loss power into bearing losses and sealing frictional losses. In addition, the artificial neural network technique was

used in their work to further improve the model accuracy. Quoilin et al. [74] used the benchmark model to integrate the model of a hermetic scroll expander with the obtained built-in-volume ratio (BVR) of 4.005 to simulate an ORC system. Their system model showed that reducing the expander speed to a certain point in fixed mass flow rates could increase the net system efficiency due to an increase of the expander suction pressure, while further reductions penalized the expander efficiency significantly and consequently the net system efficiency was reduced too. The benchmark model was also applied to a lubricated hermetic scroll expander with the obtained BVR of 3 working with R245fa in [75]. The model was validated with good accuracy showing the versatility of the model in the case of lubricated expanders. In a more recent work [76], an open-drive scroll expander with the obtained BVR of 3.5 was tested with R245fa and R1233zd(E) in a non-regenerative ORC system. The model results showed good agreement with the experimental data for both fluids.

In all these models, the expansion process is divided into an isentropic process and an isochoric process. To the best of the authors' knowledge, none of the works reported in literature considered the expansion process as polytropic in the case of scroll expanders. Therefore, the present paper aims at enhancing the semi-empirical model of scroll expanders used so far for a better evaluation of the expander performance. More precisely, this modified model is applied to the experimental data of a non-regenerative ORC test bench making use of SANDEN TRS090F scroll expander using R134a as working fluid. In particular, the more detailed model here proposed is inspired from the benchmark model including also the geometrical specifications of the expander, built-in volume ratio (BVR), and swept volume (SV), as the fixed inputs to the model and not part of the model results. Indeed, apart from the use of a polytropic expansion process instead of an isentropic one, the novelties of the proposed model rely on a more detailed suction pressure drop and loss power models and on the optimization procedure which considers the

expander BVR and the SV as fixed inputs. Therefore, the model proposed in this study represents better the real expansion process by both removing the simplifying assumption of the isentropic expansion and enhancing the modeling procedure used in the literature which considers some expander geometrical parameters as outputs of the model. After its validation, the proposed model is assessed further in detail and it is used to represent the expander performance in different pressure ratios and shaft speeds numerically.

### 3.4.1 Experimental results

The experimental campaign was aimed at assessing the off-design performance of the scroll expander. The different working conditions of the system are recorded with a time interval of 1s for 10 minutes (600 data points) and then the average of the recorded data is considered. To determine whether the system is at the steady-state condition or not, the methodology used by Woodland et al. [34] and Ziviani et al. [35] is applied: the average of the first 30 data points are compared with the average of the last 30 data points that meaning two sample data with 9 minutes delay. If the average of the two groups shows a negligible deviation, the system is considered operating at the steady-state condition. For the sake of this analysis relative deviations < 1% for the pump discharge pressure, < 5% for the expander discharge temperature, and < 2.5% for the expander shaft speed are considered.

During the tests campaign, the system is run at different flow rates as far as the system boundaries are met. The top boundaries are related to the available thermal power at the evaporator to superheat the organic fluid or the electric generator's maximum rotational speed which is 1,500 rpm. The low boundaries are superheating degrees below 2 K and unstable performance of the system in low flow rates so low produced electric power that could not supply the minimum electric load. This approach allows reducing the total number of the tests compared

to the matrix-based tests while maintaining the proper off-design investigation of the system as well. Therefore, the scroll expander is tested in low shaft speeds compared to the available data in the literature for similar kinds of expanders that usually are in the range of 1,500-5,000 rpm for ORC applications [63]. Based on the approach above, 84 data points were recorded considering the expander operating range summarized in Table 3-1.

Table 3-1. Range of the expander experimental data

| Imposed | | | | | Obtained | | | | |
|---|---|---|---|---|---|---|---|---|---|
| $\dot{m}$ [g/s] | $T_{su}$ [°C] | SH [K] | $P_{ex}$ [bar] | N [rpm] | $\dot{W}_{sh}$ [W] | PR [-] | $T_{ex}$ [°C] | $\eta_{is}$ [%] | FF [-] |
| 47.0-76.5 | 46.5-75.4 | 2-24 | 5.3-7.8 | 7,52-1,416 | 179-416 | 1.6-2.3 | 23.5-58.3 | 30.5-38.8 | 1.1-1.6 |

The expander performances are described using the shaft power, the overall isentropic efficiency, and the volumetric performance that in the case of volumetric expanders is usually called the filling factor. The shaft power is directly calculated using the measured torque and shaft speed:

$$\dot{W}_{sh} = 2\pi\tau \cdot N/60 \tag{3-27}$$

where τ is the torque [N.m] and $N$ is the expander rotational speed [rpm].

In the case of small-scale volumetric expanders, friction and thermal losses are not negligible. Therefore, the conversion efficiency of the expander is expressed in terms of its overall isentropic efficiency which is considered as the ratio between the measured shaft power and the isentropic power using the following equation:

$$\eta_{s,exp} = \frac{\dot{W}_{sh}}{\dot{W}_s} \times 100 = \frac{\dot{W}_{sh}}{\dot{m}\left(h_{su,exp} - h_{dis,s,exp}\right)} \times 100 \tag{3-28}$$

where $\dot{W}_{sh}$ is the mechanical power of the shaft, $\dot{m}$ the working fluid mass flow rate and $h_{su,exp}$ and $h_{dis,exp}$ the enthalpy at the suction and discharge port.

The filling factor (*FF*) of a volumetric expander is defined as the ratio between the measured expander flow rate and the expander theoretical flow rate using Eq. (3-29), and it is directly associated with the expander internal leakages. The *FF* strongly depends on the shaft speed and it is weakly correlated to the expander suction pressure [35]. It is expected that the *FF* is above the unity for an expander since the gas must first fill the expansion chamber and then pressurize it to produce power. However, values below the unity (called *under-filling)* were reported in some studies in the literature [35,79]. However, if the gas density that fills the expander chamber is calculated using the measured temperature and pressure at the suction of the scroll revolute after suction pressure drop and heat losses, the calculated filling factor always remains above the unity.

$$FF = \frac{\dot{V}_{meas}}{\dot{V}_{th}} = 1 + \frac{\dot{V}_{leak}}{\dot{V}_{th}} = \frac{\dot{m}_{ref}/\rho_{su,exp}}{N \cdot SV_{comp}/(60BVR)} \tag{3-29}$$

where $\dot{V}_{meas}$ is the experimentally calculated volumetric flow rate at the expander suction, $\dot{V}_{th}$ is the theoretical volumetric flow rate at the expander suction, and $\dot{V}_{leak}$ is the leakage volumetric flow rate.

If $FF = 1$ and an expansion pressure ratio equal to the expander BVR is considered (ideal performance), the following conclusions can be drawn:

- The theoretical mass flow rate decreases as the suction temperature increases, and it increases in higher suction pressures. This is due to the lower suction density in higher temperatures and higher suction density in higher pressures.
- The ideal shaft power is almost independent of the suction temperature, especially in low suction pressures. The ideal shaft power increases

significantly as the suction pressure goes up. These trends depend on the strong influence of the pressure on the gas density, while it is weakly dependent on the suction temperature in the considered range of the calculations.

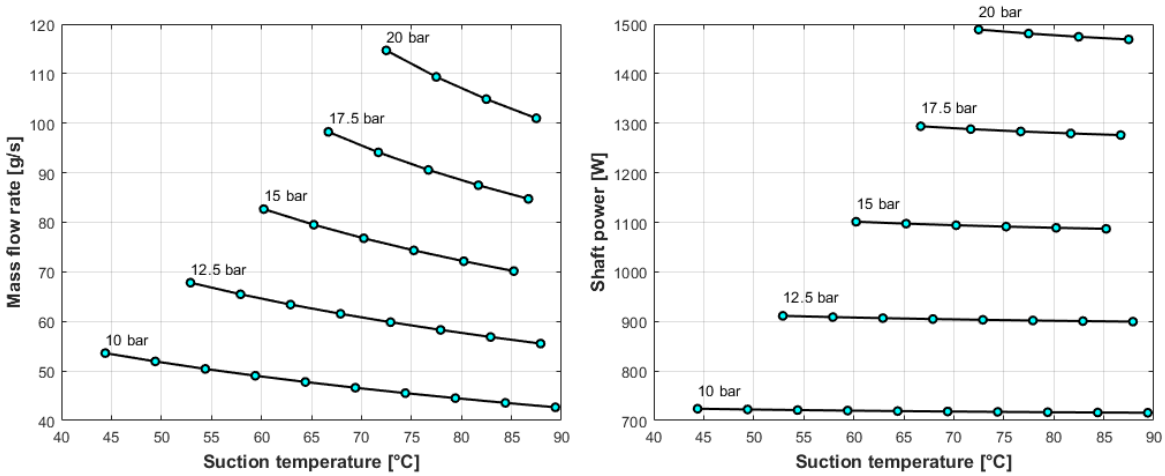


Figure 3-11. Theoretical mass flow rate (left) and ideal shaft power (right) in different suction temperatures and pressure and 1,500 rpm.

Figure 3-12 presents the expander experimental data cloud of the working conditions and performance of the scroll expander under investigation. The data are colored based on the cooling water temperature at the condenser inlet set on the chiller. Based on the obtained trends the following considerations can be drawn:

- For a given refrigerant flow rate, the expander pressure ratio increases with lowering the cold fluid temperature. This is due to the lower condenser pressures at lower cold fluid inlet temperatures.
- For a given cold fluid temperature, the expander pressure ratio increases with the refrigerant flow rate due to the higher pressures at the expander suction at higher flow rates.

- The overall isentropic efficiency is reduced in higher shaft speeds despite the lower leakage flow rate since the *FF* decreases in high shaft speeds indicating that the leakage flow rate is reduced. It means that the mechanical losses grow and become more effective on the calculated efficiency. This trend was also observed in the experiments conducted by Declaye et al. [80].

- The condenser inlet temperature, which dictates the expander discharge pressure, does not affect expander the filling factor and the overall isentropic efficiency. Instead, the produced shaft power increases on average at lower condenser inlet temperatures for the same suction pressure. Indeed, this corresponds to higher expander pressure ratios.

- The shaft power is increased almost linearly with the pressure ratio. The shaft power was increased with the pressure ratio with a decreasing rate in [80] forming a second-degree-like curve in high-pressure ratios. However, the range of the pressure ratio is limited in this work due to the limitation of the ORC test bench and this trend is not captured here.

- The shaft power increases with the expander suction pressure similar to the theoretical power presented in Figure 3-11. Indeed, higher expander suction pressures mean more gas to be expanded to generate power.

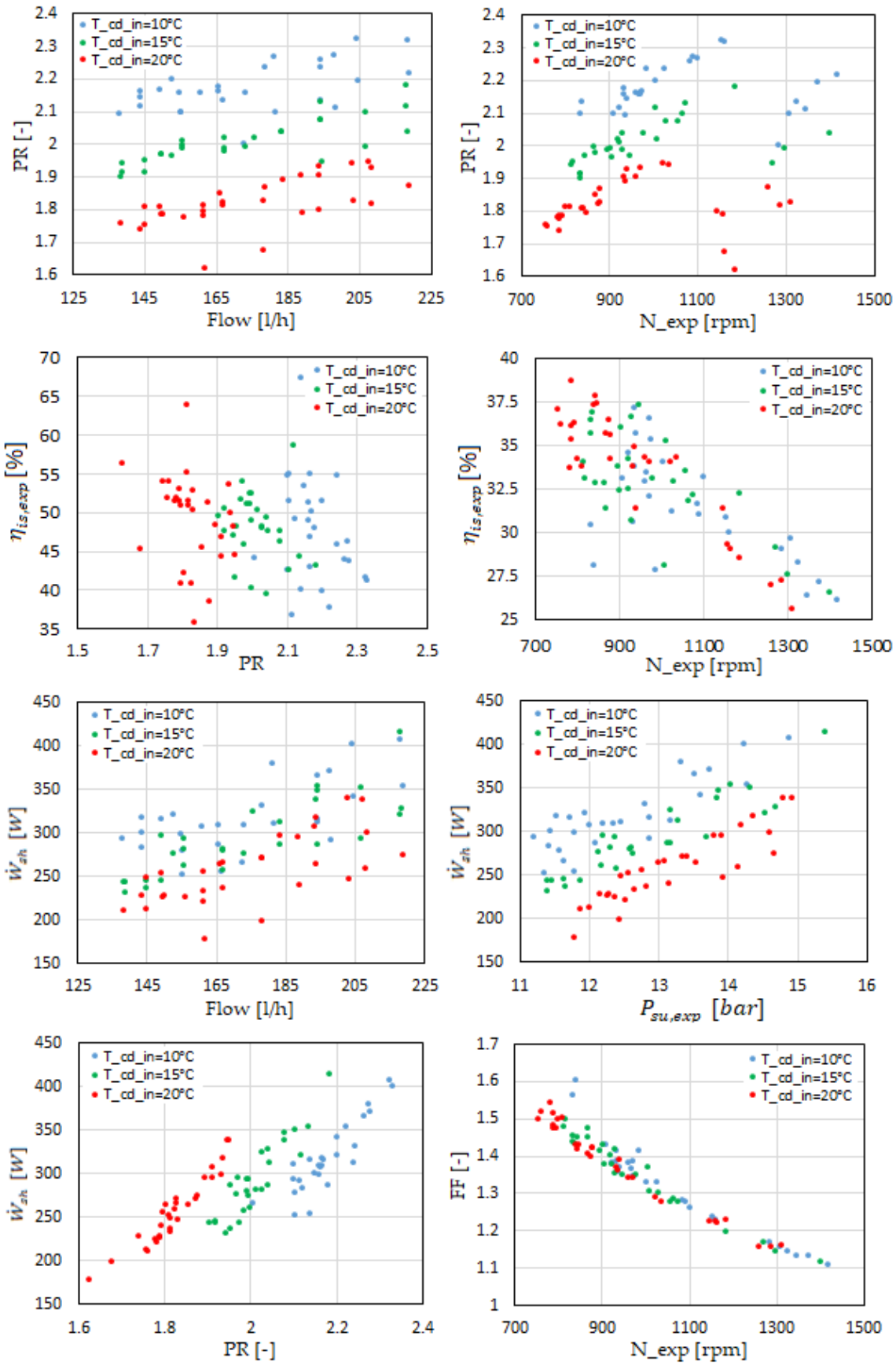


Figure 3-12. range of the expander working conditions and performance in the tests.

### 3.4.2 Numerical model

#### 3.4.2.1 Benchmark model (isentropic expansion)

The benchmark model [73] that is the most widely adopted model of scroll expander takes as inputs the expander suction pressure and temperature, the discharge pressure, the ambient temperature, the shaft speed, the BVR, and the swept volume and gives back as outputs the mass flow rate, the discharge temperature, the shaft power, and the overall isentropic efficiency. It is based on simplifying assumptions and several sub-models relevant to the physics of the flow during the expansion process to consider the related losses. These sub-models of the modified benchmark model [35], which considered the discharge pressure drop, are presented in the following and its schematic is presented in Figure 3-13.

- Suction pressure drop modeled considering an isentropic flow in a convergent nozzle (su to su,1);
- Isobaric heat transfer between the fluid and the expander shell at the suction (su,1 to su,2);
- Internal leakage modeled considering an isentropic flow in a convergent nozzle (su,2 to ex,2);
- Isentropic expansion to the expander BVR (su,2 to int);
- Isochoric expansion (int to ex,3);
- Isobaric heat transfer between the fluid and the expander shell at the discharge (ex,2 to ex,1);
- Discharge pressure drop modeled using isentropic flow in a convergent nozzle (ex,1 to ex);

The detailed formulations of the sub-models were discussed extensively in the literature [31,73,81]. This model requires eight empirical coefficients plus two geometrical parameters that only in the case of lack of information can be considered as tuning parameters as done by the two references quoted frequently in this work [35,73]. If the discharge pressure drop is not considered in the model as in the benchmark model, one less tuning coefficient is to be found obviously.

The coefficients are calculated by minimizing the objective function using optimization algorithms. The objective function used in this work is defined as in Eq. (3-30), which considers the sum of the residuals of the discharge temperature, the mass flow rate, and the shaft power. The objective function is minimized using the Genetic Algorithm in MATLAB™ [82]. This algorithm is especially recommended for finding the global minimum of non-linear functions when the function is very coarse with many local minimums. Furthermore, it is a derivative-free algorithm independent from any guess values so the global minimum of the objective function can be found bolstering the extrapolability of the model [83]. This code was used in similar modeling works as well [35,73,74,76].

$$f = \sum_{i=1}^{n} \left[ \frac{\left| T_{out,i,cal} - T_{out,i,meas} \right|}{T_{out,i,meas}} + \frac{\left| \dot{m}_{i,cal} - \dot{m}_{i,meas} \right|}{\dot{m}_{i,meas}} + \frac{\left| \dot{W}_{sh,i,cal} - \dot{W}_{sh,i,meas} \right|}{\dot{W}_{sh,i,meas}} \right] \tag{3-30}$$

where $n$ is the number of experimental data points, and subscripts *cal* and "*meas*" refer to the calculated and measured values respectively. However, it is suggested to avoid tuning of the geometrical parameters since an unrealistic value may be obtained unless a good and tight guess of the range of the parameters is known beforehand. In this work, the expander swept volume is obtained from the manufacturer specification sheet, and the expander BVR is obtained from a study with the same test bench and expander [20]. Hence, the geometrical parameters are fixed inputs here and the other empirical coefficients are to be found using the aforesaid procedure.

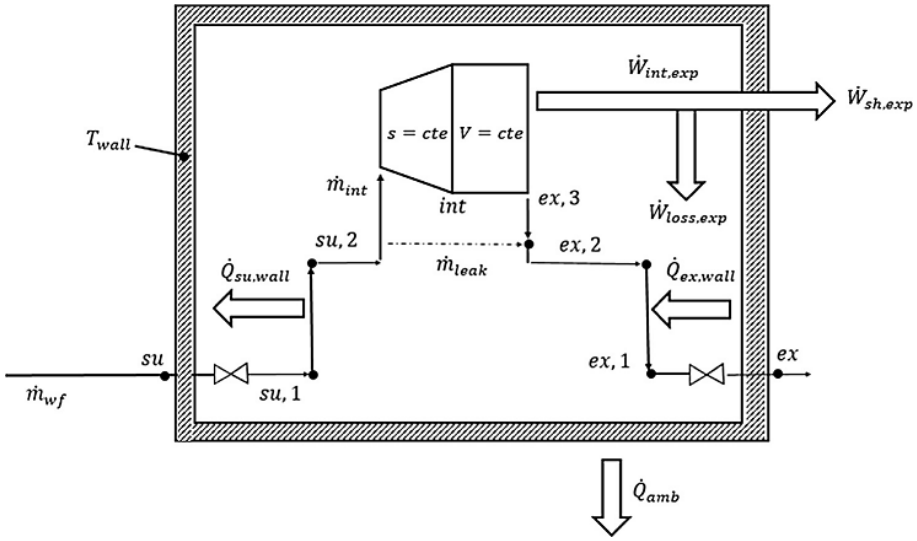


Figure 3-13. The benchmark model of scroll expanders adopted from [35].

#### 3.4.2.2 The proposed model (polytropic expansion)

Both the benchmark [73] and the modified benchmark [35] models are applied to the expander experimental data and the empirical coefficients are found. However, the results show some discrepancies mainly related to the differences between the experimental conditions and the modeling method proposed in the two references before. In this work:

- The expander is tested at lower shaft speeds compared to the references;
- The studied expander is lubricated, while it was oil-free in the benchmark models. However, the benchmark model was adopted to a lubricated expander in the literature [75];
- Above all, the two geometrical parameters, the BVR and the SV, are fixed inputs to the model while they were considered as the tuning coefficients in the benchmark models.

The benchmark model is modified considering a more realistic expansion model. A polytropic model is adopted instead of the isentropic model for the expansion process, and more detailed suction pressure drop calculations using mechanistic models are performed. It is suggested to avoid the tuning of the geometrical parameters with this procedure since an unrealistic value may be obtained unless a good and tight guess of the range of the parameters is known beforehand. Therefore, in this work, the expander swept volume is obtained from the manufacturer specification sheet and the expander BVR is obtained from a study with the same test bench and expander [20]. Hence, the geometrical parameters are fixed inputs here and the other empirical coefficients are found using the aforesaid procedure. The schematic representation of the modified model is shown in Figure 3-14. The proposed model is explained in the following only concerning the sub-models that differ from the benchmark model. Interested readers are invited to refer to the quoted papers for the details of the other sub-models.

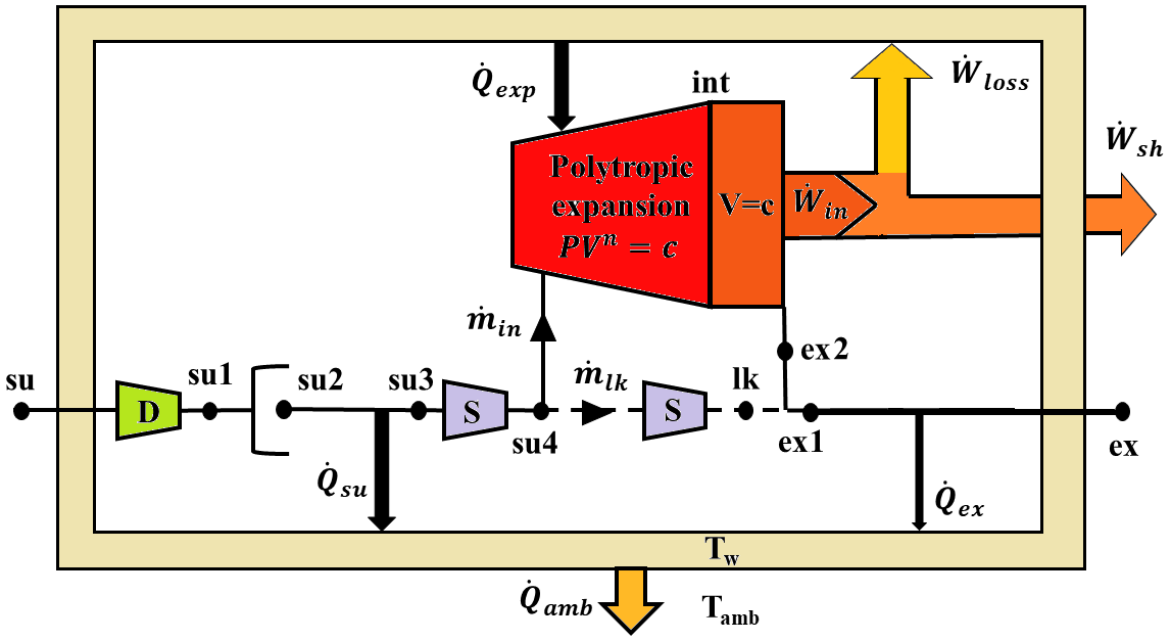


Figure 3-14. Schematic of the proposed expander semi-empirical model.

- Pressure drop in the expander suction connection (su to su1)

The pressure drop in the expander suction connection is modeled using a convergent nozzle assuming the changes in the gas density negligible:

$$V_{su} = \frac{\dot{m}_{tot}}{\rho_{su} \cdot A_{su}} \tag{3-31}$$

$$V_{su1} = \frac{\dot{m}_{tot}}{\rho_{su} \cdot A_{su1}} \tag{3-32}$$

$$h_{su1} = h_{su} + \frac{1}{2}\left({V_{su}}^2 - {V_{su1}}^2\right) \tag{3-33}$$

where $A_{su}$ and $A_{su1}$ are the cross-sectional areas of the suction port of the expander that is known from the datasheet, and $V$ is the gas velocity at these ports.

- Adiabatic sudden expansion (su1 to su2)

It is modeled using an evaluation of the gas kinetic energy loss when it passes through the suction port and enters the space between the suction port of the scroll revolute and the expander shell. One empirical coefficient, $K_{exp}$, must be found to tune this sub-model using the following equation.

$$P_{su,2} = P_{su,1} - \rho_{su,1} \cdot g \cdot K_{exp} \frac{{V_{su,1}}^2}{2g} \tag{3-34}$$

- Polytropic expansion (su4 to int)

In practice, the expansion process is polytropic. Therefore, the polytropic expansion model is considered to improve the accuracy of the model. In this case, a polytropic index needs to be identified. The polytropic index is considered as a function of the fluid isentropic index using an empirical coefficient ($a_{pol}$). During a polytropic process also heat transfer occurs and its direction depends on the polytropic index. If the polytropic index is lower than the isentropic index, heat is input to the fluid, while if it is higher than the isentropic index, the heat is taken from the fluid during

the expansion. The formulation of the polytropic work, expansion heat transfer, and internal point associated with the expander BVR are as the following:

$$n = a_{pol} \cdot K \tag{3-35}$$

$$P_{int} = P_{su,4}\left(\frac{V_{su,4}}{V_{int}}\right)^{n} = \frac{P_{su,4}}{BVR^{n}} \tag{3-36}$$

$$\dot{W}_{pol} = \frac{n}{n-1} P_{su,4} \frac{\dot{m}_{in}}{\rho_{su,4}} \left[1 - \left(\frac{P_{int}}{P_{su,4}}\right)^{\frac{n-1}{n}}\right] \tag{3-37}$$

$$\dot{Q}_{exp} = \dot{m}_{in}\left(h_{su,4} - h_{int}\right) - \dot{W}_{pol} \tag{3-38}$$

where $\dot{W}_{pol}$ is polytropic work power, $\dot{Q}_{exp}$ is the transferred thermal power during the expansion process, and $n$ and $K$ are the polytropic and isentropic indexes, respectively. The internal mass flow rate ($\dot{m}_{in}$) is that is calculated using the expander shaft speed, SV, and gas density at the suction of the scroll revolute as:

$$\dot{m}_{in} = \rho_{su4} \cdot SV_{exp} \cdot N/60 = \rho_{su4} \cdot SV_{comp} \cdot N/(60BVR) \tag{3-39}$$

The expansion heat transfer over the expander fictitious wall is then considered in the energy balance as presented in Eq. (3-40) to calculate the wall temperature, which in turn is required to calculate the suction and discharge heat transfer values.

$$\dot{W}_{loss} + \dot{Q}_{su} + \dot{Q}_{ex} + \dot{Q}_{exp} - \dot{Q}_{amb} = 0 \tag{3-40}$$

where $\dot{W}_{loss}$, $\dot{Q}_{su}$, $\dot{Q}_{ex}$, and $\dot{Q}_{amb}$ are the calculated loss power, suction heat transfer power, discharge heat transfer power, and heat loss from the expander wall to the ambient.

Regarding the calculation of the expander fictitious wall temperature, a modeling experience is worthy to be reported. Inspired by the similar models performed on the scroll compressor such as in [84,85], a simplifying assumption for the calculation of the wall temperature is tried out. In this model, the wall temperature is assumed

to be equal to the average temperature between the expander suction and its discharge. However, it was found that this assumption is not accurate for expanders that work at higher temperatures compared to compressors, and it leads to higher residuals in the optimization code or in negative ambient heat transfer in Eq. (3-40) that is unphysical.

- Mechanical loss power

The mechanical losses in the benchmark models were considered using a lumped model that includes all mechanical losses in a mechanical loss torque to calculate the loss power as the following:

$$\dot{W}_{loss} = \frac{2\pi}{60} N \cdot \tau_{loss} \tag{3-41}$$

where $T_{loss}$ is the tuning coefficient. It is found that a single value of this coefficient is not accurate enough to predict the expander experimental data accurately. It was also reported by Mendoza et al. [86] that the needed torque to move their scroll expander is related to the shaft speed using a linear correlation in the range of 245-490 rpm. Therefore, they used a correlated loss torque in the benchmark model to simulate their hermetic scroll expander in the range of their experimental data. In this work instead, the loss torque is found meaningfully correlated to the expander pressure ratio using a second-order polynomial correlation:

$$\tau_{loss} = C_1 (PR - 1)^{C_2} + C_3 \tag{3-42}$$

- Filling factor

The expander filling factor is a determining parameter for system-level simulations, in which the expander flow rate is the parameter used in iterative solvers. A sensitivity analysis is performed in this work to find the most effective physical parameters affecting the filling factor. As vividly visible in the experimental results reported in Figure 3-12, the first affecting parameter is the shaft speed. The second

physical parameter is the Stribeck number or the non-dimensional viscosity that is presented in Eq. (2-10). Hence, the expander filling factor is correlated to the shaft frequency and fluid non-dimensional viscosity calculated using the thermodynamic states of the fluid at the suction as in Eq. (3-43):

$$FF_{exp} = 50.66 + 6.206 \ln \bar{\mu} + 0.1998\omega + 0.01032\omega \cdot \ln \bar{\mu} + 0.1887(\ln \bar{\mu})^2 \quad (3\text{-}43)$$

### 3.4.3 Model validation and results

Table A4 reports a summary of the identified coefficients of the polytropic model and the obtained results after performing the optimization. It is worth noticing that the multiplier of the isentropic index is below unity showing a considerable deviation of the isentropic expansion process.

Figure 3-15 reports the calculated performance of the scroll expander using the proposed model and the coefficients presented in Table A4 with the experimental values. The results of the model are in good agreement with the experimental data for most points confirming the validity of the proposed model in the range of the experimental data. The measurement uncertainty of the experimental performance is calculated using two sources of uncertainty as detailed in Appendix (B).

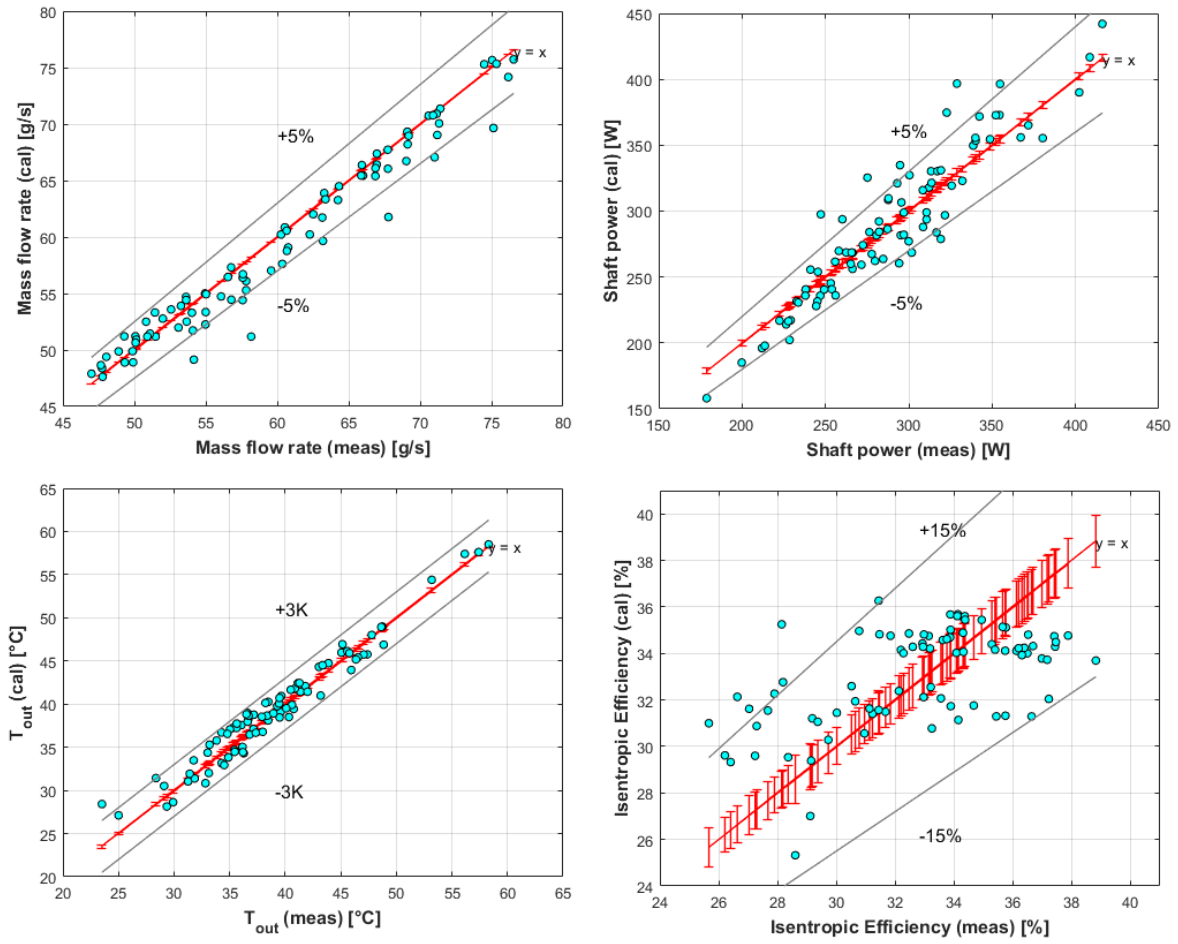


Figure 3-15. Calculated and measured expander performance.

Furthermore, the expander filling factor calculated using Eq. (3-43) is presented in Figure 3-16 showing a very good agreement between the model results and the experimentally calculated values.

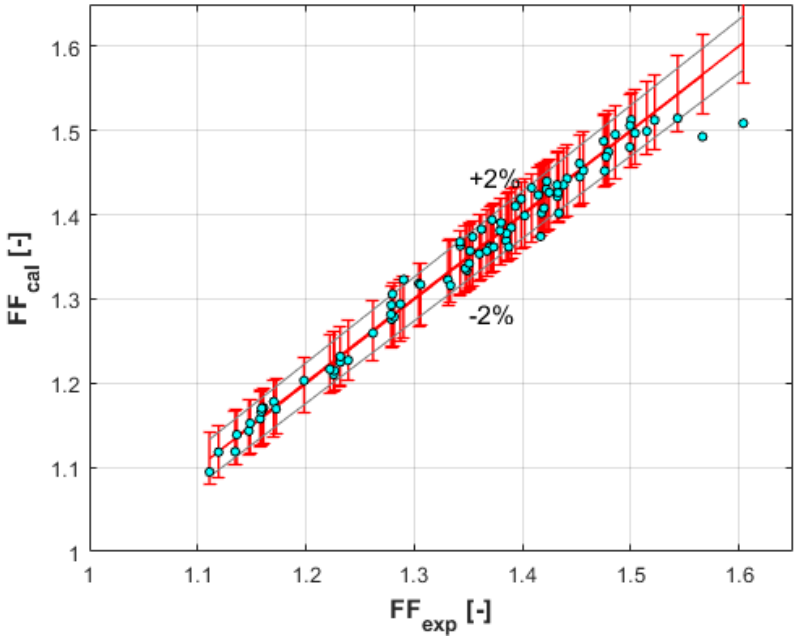


Figure 3-16. Calculated expander filling factor vs experimentally calculated one

If the discharge pressure is lower than the built-in pressure, which is the pressure associated with the expander BVR, the fluid is under-expanded. On the contrary, if the system pressure ratio is lower than the expander internal pressure ratio, over-expansion occurs. In both cases, the gas must change the pressure in the constant volume of the discharge chamber to comply with the imposed working conditions of the system. This inevitable process causes further losses to the flow and this effect can be appreciated in Figure 3-17 that reports the trend of the expander overall isentropic efficiency with pressure ratio for one of the experimental data sets. To this end, the expander suction pressure, temperature, and the shaft speed, which are the variable inputs of the proposed model, are taken from one arbitrary experimental point and the discharge pressure is changed to have different pressure ratios. The overall isentropic efficiency reduces when over/under-expansion occurs, which was observed in similar studies [20,35,73].

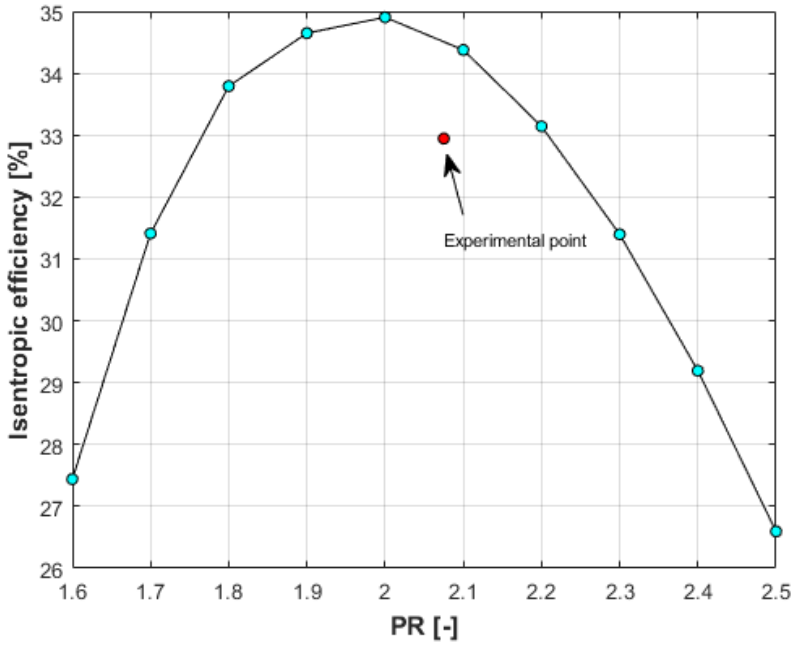


Figure 3-17. Calculated overall isentropic efficiency in different imposed pressure ratios.

The break-down of the different losses in the expander overall isentropic efficiency is presented in Figure 3-18. The largest share of the losses is due to the internal leakages, while the heat losses and the losses due to the deviation of the isentropic expansion allocate the minimum share of the losses. Therefore, the internal leakage flow is the key parameter that must be improved if a re-designing of the scroll expander is aimed.

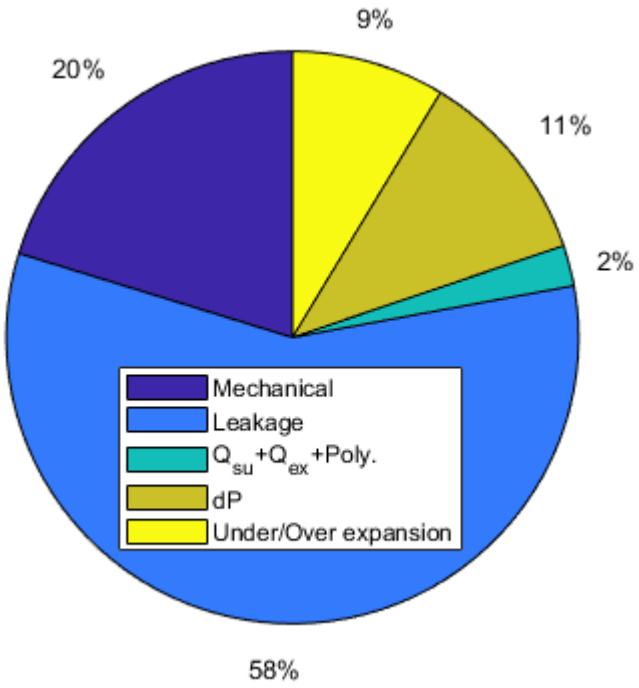


Figure 3-18. Break-down of the expander internal losses.

The performance of the scroll expander is mapped using the proposed model in this work avoiding significant extrapolation of the proposed semi-empirical model. The model is run in fixed suction pressure and temperature, but different shaft speeds and discharge pressures. The shaft power is increased with the shaft speed, but it is almost unchanged at higher speeds close to the electric generator's maximum speed. This trend is similar to the results showed in [86], in which the shaft power increased with the shaft speed up to a peak. In addition, the expander overall isentropic efficiency is reduced with the shaft speed as also in the experimental data shown in Figure 3-12 and reported in [80]. Both the shaft power and the overall isentropic efficiency show a maximum point with the expander pressure ratio. In the case of the overall isentropic efficiency, this trend was reported in several experimental studies [35,75,80], and for the shaft power, the reference that reached high pressure ratios to observe the peak of the shaft power with the pressure ratio in their experimental data is [80]. In addition, in the previous study using the same

expander and R245fa, a clear peak of the shaft power with the pressure ratio was observed [20].

This peak point is almost the same in different pressure ratios for the shaft power, but it moves to higher pressure ratios in higher shaft speeds for the overall isentropic efficiency as shown in Figure 3-19. Hence, the results suggest that the pressure ratio that corresponds to the maximum power is higher than the one associate with the maximum efficiency. Because in the WHR applications the heat source is usually free, the generated power may be preferred to the efficiency, unlike the traditional power systems. Therefore, the system should work in pressure ratios higher than the expander BVR to reach the maximum power, in this case 20% higher approximately, despite a marginal penalty of the overall isentropic efficiency. In other words, working in the under-expansion is preferred to the over-expansion conditions.

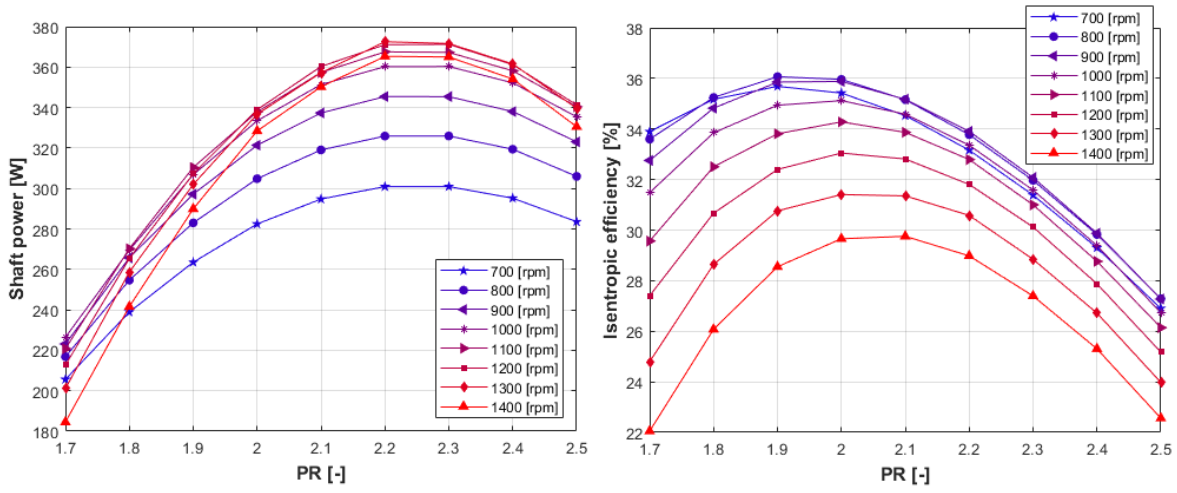


Figure 3-19. Performance mapping of the scroll expander using the proposed model

The expander filling factor is plotted in different shaft speeds and pressure ratios by changing the discharge pressure in Figure 3-20. The filling factor decreases to a

minimum point with the shaft speed for a given pressure ratio. In general, the internal leakages in a scroll expander are in two paths: the radial leakage through the gap between the bottom or top plate of the expander shell, and the flank leakages due to the clearance between the rotor and the stator [87]. Before elaborating on the model results, several points should be considered:

- Mendoza et al. [86] reported a maximum point for the volumetric efficiency with the shaft speed for their scroll expander tested with air, which the volumetric efficiency reduced afterward. This is the only reference that the turning point was observed clearly.

- The filing factor model was a polynomial correlation that should not be extrapolated.

- Some conditions that are shown numerically may not be achieved experimentally. For instance, in very low pressure ratios, the high shaft speed practically means the near-zero torque. In such conditions, the behavior of the expander may differ significantly from the tests that some torque is always applied to the expander shaft.

Considering the abovesaid points, the filling factor is reduced first since the friction between the stator and the rotor is increased so less flow can pass through the clearance gap. On the other hand, the rotor periodically blocks the suction port and reduces its area that causes some pressure drops. At high speeds, this blockage may grow up leading to higher suction pressure drops; hence, the flow follows the leakage paths more resulting in higher filling factors.

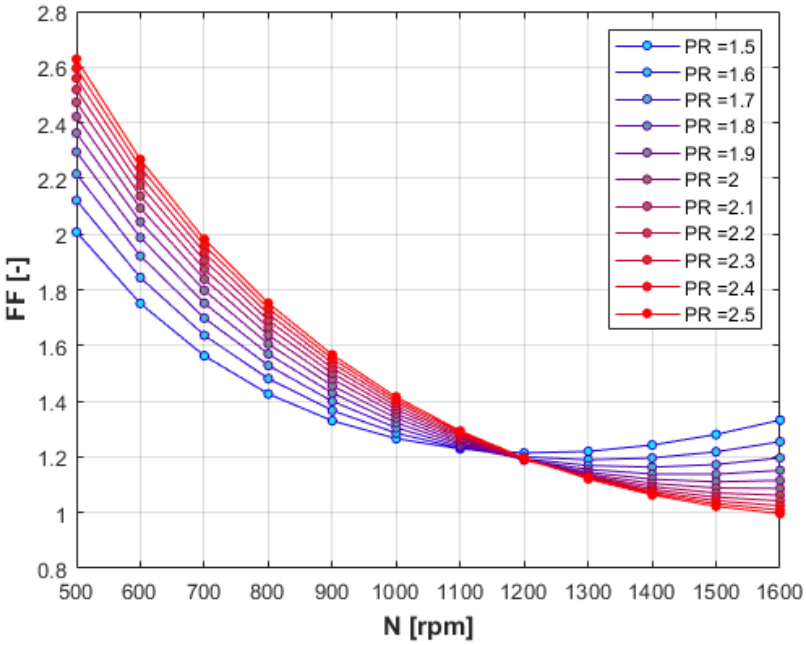


Figure 3-20. Mapping of the expander filling factor using the proposed correlation

To put it in a nutshell, the following points can be concluded from the model:

- The internal leakage flow rate penalizes most of the expander performance.
- The expander overall isentropic efficiency and the shaft power are assessed in different shaft speeds and pressure ratios concluding that the peak of the shaft power is at pressure ratios higher than the one that the maximum overall isentropic efficiency is achieved.
- The expander filling factor is found to be reduced with the shaft speed, but this reducing trend is valid up to a certain shaft speed.
- For low-grade WHR applications that the generated power is more important than marginal efficiency losses, the expander should work at pressure ratios almost 20% higher than its BVR.

- The shaft speed should be kept at about 20% lower than the electric generator nominal speed to have a high volumetric performance and avoiding further efficiency losses.

It should be emphasized that the model is semi-empirical meaning that its results are valid for the range of the working conditions not being extrapolated significantly, and for the specific expander geometry considered for the tests. Nevertheless, the proposed advanced model and the optimization procedure could be used in the future to predict the performance of other scroll expanders with good accuracy when the machine geometrical parameters, namely the BVR and the SV, are known.

## 3.5 Summary and conclusions

The modeling of the evaporator, condenser, refrigerant pump, and scroll expander is performed in this chapter using the recorded experimental data in the previous chapter. Different models for pressure drop and convective heat transfer coefficients of single-phase liquid, single-phase gas, two-phase boiling, and two-phase condensing flow regimes were tried to find the best combination resulting in the least difference between the model results and the experimental data. The refrigerant plunger pump is modeled using a set of empirical correlations. The scroll expander is modeled using a novel method that to the best of the author's knowledge, is the first model using a polytropic expansion process instead of the isentropic expansion assumption in the literature. Furthermore, the expander model takes the expander geometrical parameters, BVR and SV, as fixed inputs to the model unlike what was usually performed that these parameters were found from the model results. The results of the component models are used in the mass-sensitive modeling of the ORC system presented in the next chapter.

## 3.6 **Nomenclature**

| | |
|---|---|
| G | mass flux [kg.m$^{-2}$.s$^{-1}$] |
| $\dot{m}$ | mass flow rate [kg/s] |
| $\dot{V}$ | volumetric flow rate [m$^3$/s] |
| $\dot{W}$ | power (work) [W] |
| $\dot{Q}$ | power (heat) [W] |
| N | shaft speed [rpm] |
| T | temperature [°C] |
| P | pressure [Pa] |
| h | enthalpy [J/kg] |
| V ($v$) | velocity [m/s] |
| $C_p$ | specific heat [J.kg$^{-1}$.K$^{-1}$] |
| A | area [m$^2$] |
| g | gravitational acceleration [m/s$^2$] |
| K | isentropic index [-] |
| n | polytropic index [-] |

*Greek symbols*

| | |
|---|---|
| $\omega$ | shaft frequency [Hz] |
| $\eta$ | efficiency [%] |
| $\lambda$ | thermal conductivity [W.m$^{-1}$.K$^{-1}$] |
| $\tau$ | torque [N.m] |
| $\mu$ | dynamic viscosity [Pa s] |
| $\bar{\mu}$ | non-dimensional viscosity [-] |
| $\rho$ | density [kg/m$^3$] |

*Subscripts and superscripts*

| | |
|---|---|
| cal | calculated |
| meas | measured |
| exp | expander |
| comp | compressor |
| ev | evaporator |
| cd | condenser |
| L | liquid |
| V | vapor |
| tp | two phase |
| ref | refrigerant |
| vol | volumetric |
| sh | shaft |
| amb | ambient |
| su | suction |
| ex/dis | exit/discharge |
| th | theoretical |
| act | actual |
| leak/lk | leakage |
| ref | refrigerant |
| el | electrical |
| mech | mechanical |
| rev | reversible |
| is | isentropic |

*Acronyms*

| | | | |
|---|---|---|---|
| RMSE | Root Mean Square Error | rpm | rotation per minute |
| HTC | Heat Transfer Coefficient | SV | Swept Volume [$m^3$/rev] |
| Pr | Prandtl number [-] | SH | Superheating [K] |
| PR | Pressure Ratio [-] | ORC | Organic Rankine Cycle |
| FF | Filling Factor [-] | WHR | Waste Heat Recovery |
| BVR | Built-in Volume Ratio [-] | | |

# Chapter 4

# 4. Mass-sensitive modeling of the ORC system

*"One of the most insidious and nefarious properties of scientific models is their tendency to take over, and sometimes supplant, reality"*

Erwin Chargaff, Austro-Hungarian-born American biochemist

## 4.1 Introduction

As mentioned in Chapter 1, Introduction, one of the main goals of the thesis is to perform the assumption-free modeling of the experimentally studied ORC system. The main feature of such models is that it does not make any assumption regarding any system characteristics such as superheating degree in the evaporator or subcooling degree in the condenser. Instead, the model takes the components' specifications and geometries as inputs plus the same variables that an operator has for running the system. In general, these variables are the refrigerant pump speed, the hot fluid pump speed, the cold fluid pump speed, the hot fluid inlet temperature to the evaporator, the cold fluid inlet temperature to the condenser, the expander shaft speed that is adjusted using the electric or mechanical load, and the system initial mass charge. Other inputs are the specifications of the main system components, the working fluid, and the ambient temperature. A mass-sensitive model considers both the conservation of energy and the conservation of mass to simulate the system.

Mass-sensitive modeling of the ORC systems is a new topic and relatively few works were found in the literature as presented in Table 1-1. In addition to the novelty of this modeling approach, it is found in this work that the liquid receiver

model is needed and the simplified models of the liquid receiver in the literature, if it was considered in their system, is not adequate for the ORC system under the investigation. Therefore, the liquid receiver is studied with more detail using both the experimental data and the numerical methods. It is found that the liquid receiver was not flooded with the liquid when the condenser outlet is subcooled, and a liquid level was observed instead.

The mass charge models of the system components are presented in this chapter. Regarding the mass of the PHEs, a geometric parameter model named the void fraction (*VF*) is selected among numerous empirical models in the literature. It is found that the liquid level in the liquid receiver can substantially change the choice of the suitable *VF* model for the evaporator and the condenser.

The mass-sensitive model developed in this chapter uses the models of the system components presented in the previous chapter and their mass models conducted in this chapter. The mass-sensitive solver is used to predict the experimental data to evaluate its accuracy. Then, it is used to map the system's net electric performance by changing the pump speed and the expander speed when the other system boundaries are fixed.

## 4.2 **Mass charge modeling**

The mass-charge of an ORC system is one of the inputs when the tests or the utilization of the unit is intended. It affects directly the subcooling and the superheating degrees in the condenser and the evaporator, respectively. In addition, the amount of the refrigerant mass-charge is associated with the system's primary costs. It becomes more important especially in the case of the new refrigerants that are usually expensive, or mass production of ORC systems.

The total mass-charge of the ORC system is calculated using the sum of the mass of R134a associated with different components of the system. It should be noted that for having a confident mass distribution in the system, it must be measured for each component individually during the experiments. However, it was not considered in the design of the ORC test bench and only the level of the refrigerant in the liquid receiver can be read using the two pressure sensors implemented on the liquid receiver body. Therefore, the liquid level in the liquid receiver is the final node of the calculation of the total system mass.

Regarding the ORC system in this work, only the data points with the condenser water inlet temperature below 15 °C could be used to calculate the liquid level in the liquid receiver due to the limitation of the two pressure sensors implemented on the liquid receiver body that can measure up to 6 bar. Therefore, when the saturation pressure of the condenser was above this limit, the sensors could not read the pressure and the level of the refrigerant was unknown.

In this section, the mass-charge calculation of the ORC system is carried out. In the case of the mass charges of the PHEs, they are calculated using the previously obtained hydro-thermal models of the evaporator and condenser and different void fraction models, then the best model for the evaporator and the condenser is introduced. Hence, the void fraction models are presented in the following, then the modeling of the mass charge of each component is presented ending to the comparison between the real and the calculated mass charge of the studied ORC system.

### 4.2.1 Void fraction

Void fraction (*VF*) is one of the most important parameters associated with the two-phase flows in channels. The gas and liquid phases of a two-phase flow travel with

different speeds in a channel; hence, the volume occupied by each phase in a volume cell of the channel varies from the homogenous flow, in which both phases are considered at the same travel speed. It significantly affects the mixture properties such as density and viscosity in the cell. Therefore, if the spatial resolution method used for the hydro-thermal modeling of the channel was finite volume, or an accurate calculation of the working fluid mass of the two-phase zone is needed, *VF* must be calculated in each cell. *VF* is defined as the ratio of the area of the gas phase to the total cross-sectional area of the channel:

$$VF = \frac{A_g}{A_{tot}} = \frac{A_g}{A_l + A_g} \tag{4-1}$$

It can be defined similarly using the volume of gas over the total volume of the cell and if the geometry of the channel remains constant, the cross-sectional *VF* is coincident with the volumetric *VF*:

$$VF = \frac{\forall_g}{\forall_{tot}} = \frac{\forall_g}{\forall_l + \forall_g} \tag{4-2}$$

*VF* is a geometric parameter, unlike the vapor quality that is a transport parameter and is related to the morphology of the two-phase flow. Bubbly flow can be associated with the *VF*<0.2-0.3, the intermittent flow with 0.2-0.3<*VF*<0.7-0.8, and the mist flow can be characterized with *VF*>0.7-0.8 [88]. *VF* is vividly between zero and one. The schematic of these flow mechanisms is shown in Figure 4-1 using the cross-sectional *VF* representation.

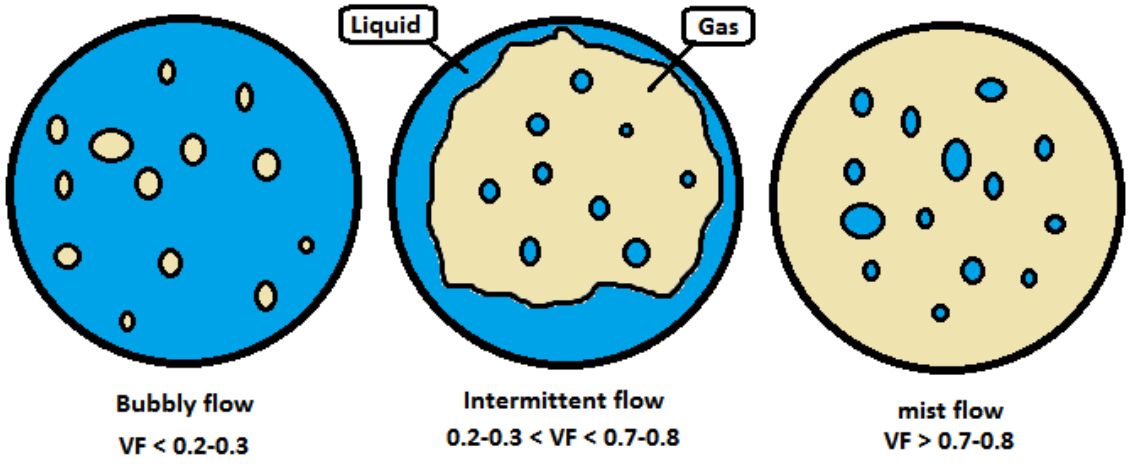


Figure 4-1. Schematic of characteristics of a two-phase flow using cross-sectional void fraction (*VF*)

*VF* is usually formulated using the gas-liquid speed ratio using the following equations:

$$\dot{m}_l = (1-x)\dot{m} = \rho_l \cdot v_l \cdot A_l = \rho_l \cdot v_l (1-VF)A \tag{4-3}$$

$$\dot{m}_g = x \cdot \dot{m} = \rho_g \cdot v_g \cdot A_g = \rho_g \cdot v_g \cdot VF \cdot A \tag{4-4}$$

where $x$ is the vapor quality and $v$ is the speed. Combining the last two equations yields to:

$$\frac{1-x}{x} = \frac{\rho_l}{\rho_g} \times \frac{v_l}{v_g} \times \frac{1-VF}{VF} \tag{4-5}$$

Defining the slip ratio (S) using Eq. (4-6), *VF* can be formulated as the function of S and properties of the fluid.

$$S = \frac{v_g}{v_l} \tag{4-6}$$

$$VF = \left(1 + S\frac{1-x}{x} \times \frac{\rho_g}{\rho_l}\right)^{-1} \tag{4-7}$$

The simplest *VF* model is derived considering the same speed of gas and liquid (S=1), which is called the homogenous *VF*:

$$VF_{hom} = \frac{x}{x + (1 - x)\frac{\rho_g}{\rho_l}} \tag{4-8}$$

The slip ratio is an unbounded flow number that can have positive or negative values; however, it is above the unity in most applications indicating that the phases are separated and flowing in the same direction and the gas phase is traveling faster than the liquid phase. It depends on the flow characteristics, the fluid properties, the channel geometry, and the channel incline.

The selection of the suitable *VF* model directly affects the refrigerant mass calculation of the evaporator and the condenser and consequently, the overall mass-sensitive modeling of the system. The suitable *VF* model for the evaporator and the condenser of the ORC unit is presented in the following.

### 4.2.2 Mass charge modeling of the system components

The refrigerant mass charge of each component of the system is presented hereunder. Accurate mass models of each component are crucial for the mass-sensitive modeling of the system, in which the conservation of mass is applied to the system to find out the thermodynamic states of different points of the system and its performance consequently.

#### 4.2.2.1 Evaporator and condenser

The mass in the PHEs is the sum of the mass of the single-phase gas and liquid zones plus the mass of the two-phase zone. To this end, the average density of the refrigerant in each zone must be known, then multiplying to the volume of the zone

in the channel the refrigerant mass is calculated. Regarding the single-phase zones, it is straightforward to use the average density calculated using the inlet and outlet densities of the zone. But for the two-phase zone, the void fraction must be known as discussed in the previous sub-section.

The mass charge solver of the PHEs is run after the hydro-thermal solver is completed. The two-phase zone is divided into several[1] volume cells using the equally spaced vectors of enthalpy, pressure, and saturated temperature that their boundaries are the two-phase boundaries obtained from the hydro-thermal solver. Therefore, *VF* is calculated using the average properties of the cell in the two-phase zone. In other words, the hydro-thermal solver of the PHEs uses the moving boundary method for spatial discretization, but the mass charge solver adopts the finite volume method for good accuracy. Finally, the mass of one channel of the PHE is calculated using the sum of the mass of the three zones. Therefore, the refrigerant mass of the single-phase zone is calculated using Eq. (4-9).

$$M_{SP} = \rho_{avg} \cdot A_c \left(\frac{A_{zone}}{w}\right) \tag{4-9}$$

where the subscript $SP$ refers to the single-phase (gas or liquid), $A_c$ is the cross-sectional area of the channel, $A_{zone}$ is the calculated area of the zone from the hydro-thermal solver, and $w$ is the width of the plate. For the two-phase zone:

$$M_{TP} = \sum_{i=1}^{n} \rho_{mix,i} \cdot A_c \left(\frac{A_{zone}}{w \cdot n}\right) \tag{4-10}$$

where the subscript *TP* refers to two-phase (boiling or condensation), *n* is the number of the cells, and $\rho_{mix,i}$ is calculated from Eq. (4-11) using the average properties of the cell.

[1] 20 cells showed adequate and more cell numbers did not affect the results.

$$\rho_{mix} = VF \cdot \rho_v + (1 - VF)\rho_l \tag{4-11}$$

Finally, the total refrigerant mass of the PHE is calculated using Eq. (4-12).

$$M_{tot} = \left(M_{SP,g} + M_{TP} + M_{SP,l}\right)n_{ch} \tag{4-12}$$

where $n_{ch}$ is the number of the channels of the refrigerant stream.

One of the aspects of the mass charge modeling that shows its importance and research value appears in the thermal modeling of HEs. Let us consider an exemplary evaporator[1] that its identical thermal performance can be the result of different sets of overall heat transfer coefficients (OHTCs) as shown in Figure 4-2. It is evident that very different sets of OHTCs give the identical overall thermal performance, but very different temperature profile and calculated mass charge accordingly. Therefore, a set of non-physical heat transfer coefficient correlations can result in an apparently correct overall simulation of a PHE. It may be misleading if one validates the thermal model of an HE using few experimental data points and finds good overall agreement, yet the model can extremely become wrong in off-design conditions since the convective heat transfer coefficient (CHTC) correlations do not correspond to the physical characteristics of the flow. Therefore, any efforts to get closer to the correct hydrothermal model and mass charge model of HEs increases the versatility, reliability, and robustness of the component model.

[1] It is considered as an PHE with the same characteristics of the evaporator of the studied ORC unit. The hot stream however is considered water and cold stream R134a. Inlet and outlet states of the streams and mass flow rate of R134a are arbitrary values. To calculate the mass of the two-phase zone, Rouhani II [91] void fraction model is used that is presented in the following pages. The two-phase zone is divided to 20 cells to spatially discretise it.

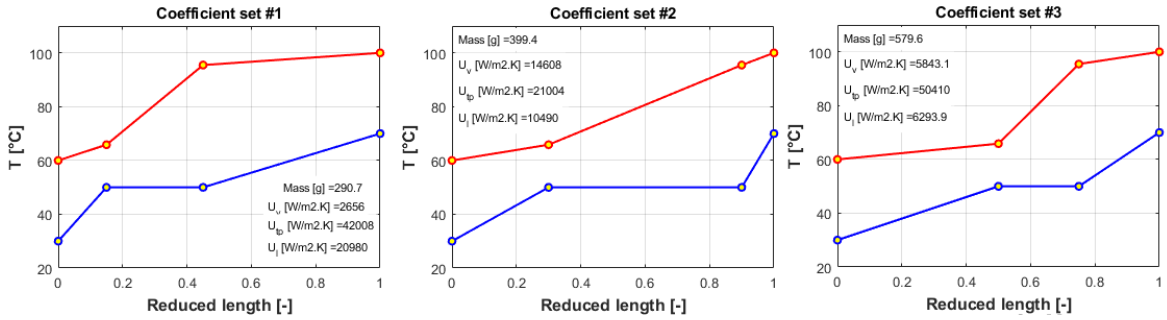


Figure 4-2. Identical thermal performance in an evaporator with different sets of OHTCs, temperature profiles, and refrigerant mass

#### 4.2.2.2 Pipes

The pipes include different states of R134a: liquid, high-pressure gas, and low-pressure gas. The length of the pipes is measured separately based on the state of the gas and the size of the pipes, and the refrigerant mass is calculated using Eq. (4-13).

$$M_{pipe,i} = \rho_i \left(\frac{\pi}{4} {d_i}^2\right) L_i \tag{4-13}$$

where $d$ and $L$ are the diameter and the pipe length respectively, and $\rho$ is the refrigerant density.

#### 4.2.2.3 Plunger pump

The pump is filled with liquid only. Its volume is calculated using the sum of the internal volume of the pump assumed equal to its swept-volume, and the inlet and outlet embedded pipe nipples. The refrigerant mass is calculated using Eq. (4-14).

$$M_p = \rho_{p,su} \left(\frac{\pi}{4} \left(L_{in} \cdot {d_{in}}^2 + L_{out} \cdot {d_{out}}^2\right) + SV_p\right) \tag{4-14}$$

where $SV$ is the swept volume.

#### 4.2.2.4 Scroll expander

The expander is charged with R134a in the gas phase. However, the density of the gas varies considerably during the expansion process. Therefore, the average density between the suction and the outlet of the scroll expander is considered. The expander volume is obtained from its datasheet (90 cc), and the refrigerant mass is calculated using the following equation.

$$M_{exp} = \left(\frac{\rho_{exp,su} + \rho_{exp,out}}{2}\right) \forall_{exp} \tag{4-15}$$

where $\forall_{exp}$ indicates the expander volume.

#### 4.2.2.5 Liquid receiver

The liquid receiver is a 3-liter container with the dimensions shown in Figure 4-3. The two pressure sensors are implemented on its body with a 200 mm distance from each other to read the liquid level using the hydraulic pressure of the column of the liquid. This configuration can measure the level only if it is between the pressure sensor levels resulting in the relative liquid level range between 28% and 72% approximately. As mentioned in Chapter 2 (Experimental investigations) regarding the limitations of the test bench, the two sensors can measure up to 6 bar; thus, the functionality of the level measurement system depends on the condenser saturation pressure. This results in the functionality of the liquid level measurement for R134a when the cold stream inlet temperature to the condenser is below 15 °C. In other words, the level measurement system is not suitable for R134a that is a high-pressure fluid in the condenser in common condensing temperature close to the ambient temperature. The relative liquid level (*RLL*) is calculated using Eq. (4-16).

$$RLL = \frac{\left(\frac{P_7 - P_6}{\rho \cdot g} + 0.125\right)}{0.45} \times 100 \quad (4\text{-}16)$$

Moreover, a liquid detector sensor is implemented on the liquid receiver body that sends a signal to the PLC board if the liquid level is below the sensor fork to shut down the refrigerant pump immediately.

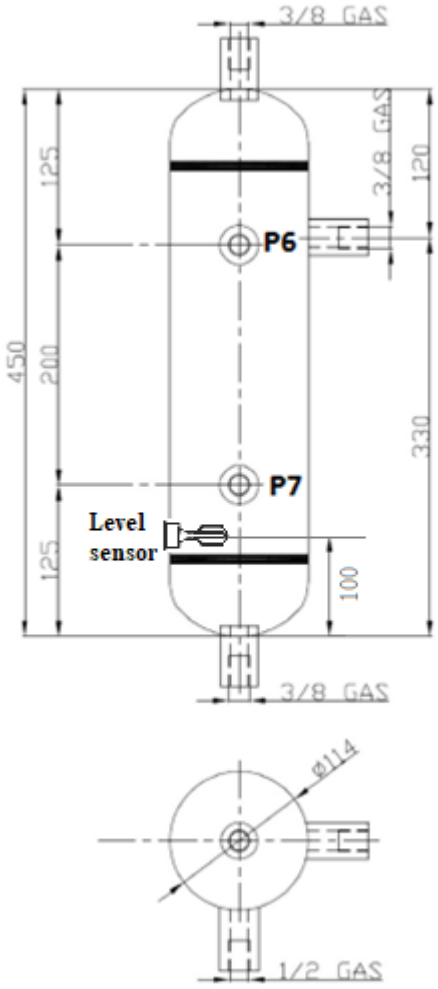


Figure 4-3. Dimension of the liquid receiver and location of the two pressure sensors (P6 & P7) the level safety sensor

The liquid receiver mass is calculated considering the saturated gas filled the rest of the space at the pressure equal to the condenser outlet state (at the vapor quality of 1 and the saturation pressure of $P_{cd,ex}$) as the following.

$$M_{LR} = \left(\frac{\pi}{4} {d_{LR}}^2\right)\left[\left(\rho_{p,su} \cdot H_{LR} \frac{RLL}{100}\right) + \left(\rho_{sat,g} \cdot H_{LR}\left(1 - \frac{RLL}{100}\right)\right)\right] \quad (4\text{-}17)$$

where $d_{LR}$ and $H_{LR}$ are the internal diameter and height of the liquid receiver.

In some studies [28–31] reported in Table 1-1, the liquid receiver was assumed filled with the liquid if the condenser outlet fluid is subcooled, and it was assumed emptied of liquid or with some level of the liquid when the condenser outlet is two-phase flow. These assumptions are controversial for several reasons:

- Non-condensable gases, if any exist, accumulate at the top of the liquid receiver resulting in some volume of the tank to be always empty.
- Expander lubricant oil, if any exist, has usually a lower density than the refrigerant[1]. Therefore, oil covers the top of the liquid surface in the tank that significantly reduces the evaporation/condensation mass transfer between the refrigerant liquid and gas in the tank. Hence, the refrigerant vapor may remain in the gas phase during the system operation.
- As the liquid level in the liquid receiver increases, the available refrigerant in the condenser reduces resulting in lower subcooling degrees. Therefore, the liquid level and the subcooling degree are interconnected, and assuming a fixed subcooling that forces the tank to be filled with the liquid is not precise.
- Assuming the liquid receiver empty if the condenser outlet is at the two-phase state as was adopted in some papers [28,29] in Table 1-1 meaning that

[1] In the ORC test bench studied in the thesis, the expander lubricant oil density is 25% lower than R134a density approximately.

the deposited liquid in the tank is vaporized due to the condenser performance. Hence, the liquid is expanded to the gas phase in a fixed volume that means a significant increment of the pressure, which increases the dew point of the fluid in the tank at the same time.

- If the liquid receiver works at a different temperature than the ambient one, any heat transfer between the tank body and the ambient can break the equilibrium mass transfer between the liquid and vapor phases in the tank.
- Unlike the papers presented in Table 1-1, SWEP company [89] that is the manufacturer of the BPHEs and HVAC systems has reported zero subcooling degree in the case of a through liquid receiver; instead, a surge receiver configuration is suggested as shown in Figure 4-4.
- The experimentally measured liquid level in the liquid receiver shows that the liquid receiver was not flooded with liquid.

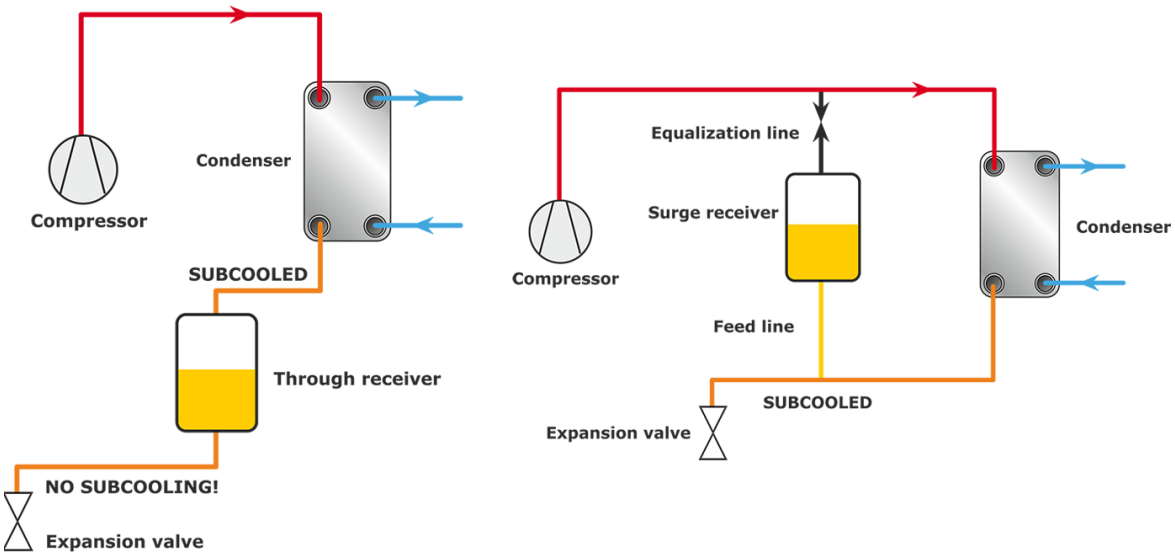


Figure 4-4. Through liquid receiver (left) and surge liquid receiver (right) configurations adapted from SWEP company website [89].

Therefore, much more time may be required to have a flooded liquid receiver in the steady-state condition compared to the time considered for a steady-state test. Furthermore, the impact of the transient behavior of the liquid receiver may not be significant on the thermodynamic states of the system, while it is very important on the refrigerant mass distribution in the ORC system. Therefore, the flooded assumption may not be true for all cases and must be taken with caution.

The measured liquid level using the two pressure sensors P6 and P7 gives the same indication regarding the liquid level in the liquid receiver; however, the measured liquid level cannot be taken as exact values due to pressure sensors accuracy. To better explain it, 1 cm of R134a liquid creates about 120 Pa pressure and associates with 83 g refrigerant mass in the liquid receiver. Considering the accuracy of the two sensors is 3,000 Pa, the measured refrigerant mass can be considerably different from the reality. Therefore, the experimental data are used as the indications only to find the suitable void fraction models for the evaporator and the condenser, which results in the least deviation between the calculated overall system refrigerant mass and the initial system mass charge. After the suitable void fraction models are known, the liquid level in the liquid receiver is calculated for each experimental point using the mass conservation in the system. This procedure is presented in the following.

### 4.2.3 Selection of the void fraction model

Hereunder, the suitable *VF* model for the evaporator and condenser of the ORC unit is determined considering the previous studies in the literature and indications from the experimental data of the liquid level in the liquid receiver. Both approaches lead to the same choice for the *VF* model for the evaporator and condenser.

Several *VF* models were presented in many studies using empirical correlations. Due to a large number of *VF* correlations, seven well-quoted ones plus the homogenous model are considered as the potential candidates in this work:

- Rouhani I is the modified version of the Rouhani and Axelsson [90] model that was originally obtained for water boiling. It was modified by Woldesemayat and Ghajar [91] to predict their experimental database. This correlation was found the best to predict experimentally calculated *VF* of two-phase flows of R134a in horizontal tubes in [92].

- Rouhani II is the modified version of Rouhani and Axelsson [90] model that was originally obtained for water boiling. It was modified by Woldesemayat and Ghajar [91] to predict their experimental database. This correlation was found the best to predict experimentally calculated *VF* of two-phase flows of R134a in vertical tubes in [92].

- Zivi [93] was used by Ziviani et al. [35] in the simulation of an ORC system.

- Premoli et al. [94] was suggested for the flows in vertical channels and was introduced as the best model to predict the total mass charge of an ORC system by Dickes [29]. Moreover, it was found the best model in [95], but no robust evidence was found in their work for this suggestion and it was based on the suggestion of two papers in the literature.

- Sun et al. [96] that was suggested for the water flow in tubes and was found an accurate model by Tang and Ghajar [97] to predict the experimental database adapted from the literature.

- Graham et al. [98] is among the few correlations that was suggested for refrigerant condensation (R134a and R410) in smooth horizontal tubes.

- Woldesemayat and Ghajar [91] suggested a universal correlation obtained using 2845 data points from the literature that could predict the database better than the other studied correlations.

The summary of the range of the experimental data used to validate or tune the empirical *VF* models in the literature is reported in Table 4-1. Moreover, *VF* correlations are reported in Appendix (E).

Table 4-1. Selected *VF* models with their range of the experimental data used for the model validation or tuning

| Model name/author | Fluid | $d_h$ [mm] | G [kg.m$^{-2}$.s$^{-1}$] | P [bar] | x [-] | Notes |
|---|---|---|---|---|---|---|
| Rouhani I [90,91] | Boiling Water | 4.7-25.4 | 665-1607 | 19-138 | 0-0.18 | Channels and tubes |
| Rouhani II [90,91] | Boiling Water | 4.7-25.4 | 665-1607 | 19-138 | 0-0.18 | Channels and tubes |
| Zivi [93] | Boiling Water | n.a. | 420-830 | 1-82 | 0-1 | Vertical rectangle channel |
| Premoli et al. [94] | n.a. | n.a. | n.a. | n.a. | n.a. | Vertical channels |
| Sun et al. [96] | Boiling water | n.a. | n.a. | 1.38-69 | n.a. | Vertical tubes |
| Graham et al. [98] | Condensing R134a & R410 | 7.04 | 75-450 | n.a. | 0.13-0.9 | Horizontal tubes |
| Woldesemayat and Ghajar [91] | n.a. | n.a. | n.a. | n.a. | n.a. | A universal correlation using. 2845 data points from the literature. System pressure and channel inclination are included in the model. |

To show the difference among the models, the predicted *VF* and density calculated from Eq. (4-11) are presented in Figure 4-5 using R134a and in a working condition similar to the evaporator of the ORC unit. It is evident that the homogenous model results in the least calculated mass of the two-phase zone in a channel.

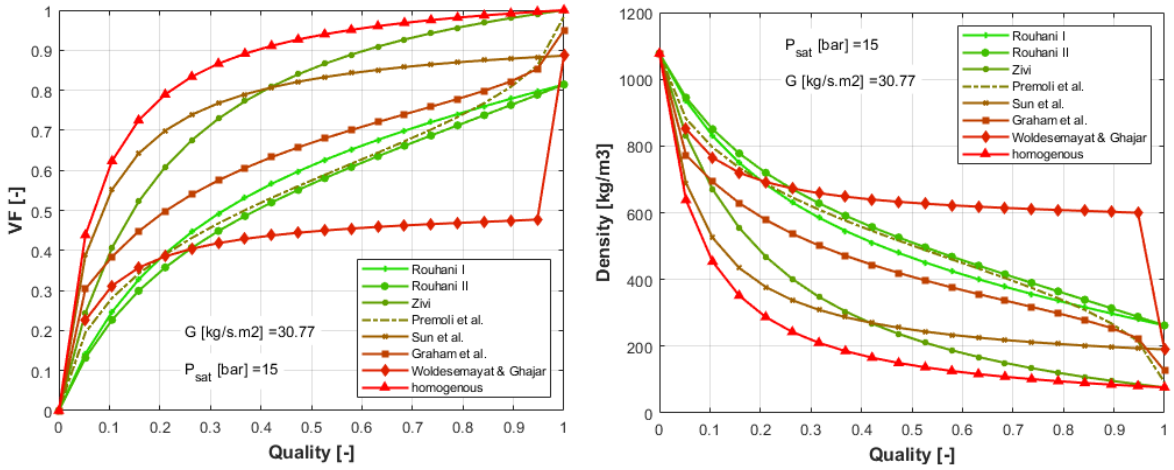


Figure 4-5. Void fraction (*VF*) and mixture density by vapor quality using *VF* models for R134a in an arbitrary working condition

To better have the indications regarding the suitability of the *VF* models for the evaporator and condenser, the range of the experimental data in which the model was tuned, the channel hydraulic diameter and inclination, and the working fluid should be considered. Hence, the range of the experimental data of the evaporator and the condenser are presented in Table 4-2.

Table 4-2. The working conditions of the PHEs of the ORC system

| PHE | Fluid | $d_h$ [mm] | G [kg.m$^{-2}$.s$^{-1}$] | $P_{in}$ [bar] | x [-] |
|---|---|---|---|---|---|
| Evaporator | R134a | 2 | 14.46-23.54 | 11.56-15.47 | 0-1 |

| | | | | | |
|---|---|---|---|---|---|
| Condenser | R134a | 2 | 12.05-19.62 | 5.32-7.82 | 0-1 |

The range of the mass flux in the channels of the PHEs is lower than the range of the experimental data of *VF* models in Table 4-1; therefore, a comparison based on the similarity of the working conditions may not be so helpful. However, the Rouhani II model was found an accurate model to predict experimentally measured *VF* of R134a in vertical tubes in [92]. The range of the working conditions of their study is reported in Table 4-3 showing that it was also valid in lower mass fluxes and higher vapor qualities compared to the original values reported in Table 4-1.

Table 4-3. The working conditions of the *VF* tests in [92]

| Tested geometry | Fluid | $d_h$ [mm] | G [kg.m$^{-2}$.s$^{-1}$] | P [bar] | x [-] |
|---|---|---|---|---|---|
| Horizontal Tubes | R134a | 7 | 40-150 | 8.39 | 0.1-0.9 |
| Vertical Tubes | R134a | 7 | 65-115 | 8.39 | 0.1-0.9 |

In addition, Rouhani models were found the best among 52 *VF* correlations to predict 1208 data points from the literature according to [97]. Therefore, the Rouhani II model seems the best choice for the evaporator and the condenser of the ORC system under investigation considering what was quoted in the literature. However, a supplementary approach is taken here to ensure the suitability of the choice. To this end, different *VF* models were tried to calculate the system mass considering the experimentally measured liquid levels as an acceptable approximation. The best *VF* model is the one that the difference between the calculated system mass and the real system mass is the minimum.

The mass charge of the ORC system is calculated using the sum of the mass of each component for each experimental data point with the calculated liquid level in the liquid receiver using the measured values by the two pressure sensors installed on the liquid receiver body. The measurements of the two pressure sensors indicate that the liquid receiver was not flooded with the liquid during the tests, which is contrary to the assumptions of the mass-sensitive models in the literature reported in Table 1-1 that considered the liquid receiver, if existed in the system, flooded with the liquid if the condenser outlet is subcooled, and emptied if the condenser outlet is two-phase.

In addition to the sensor measurements, the overall system mass calculation shows that the liquid receiver could not be flooded. As shown in Figure 4-6, even if the homogenous *VF* model is selected for the PHEs, which gives the minimum mass in the evaporator and condenser, the calculated system mass is significantly over-predicted if the liquid receiver is filled with liquid. This analysis confirms that the assumption of the flooded liquid receiver may not be true for all liquid receivers in all working conditions.

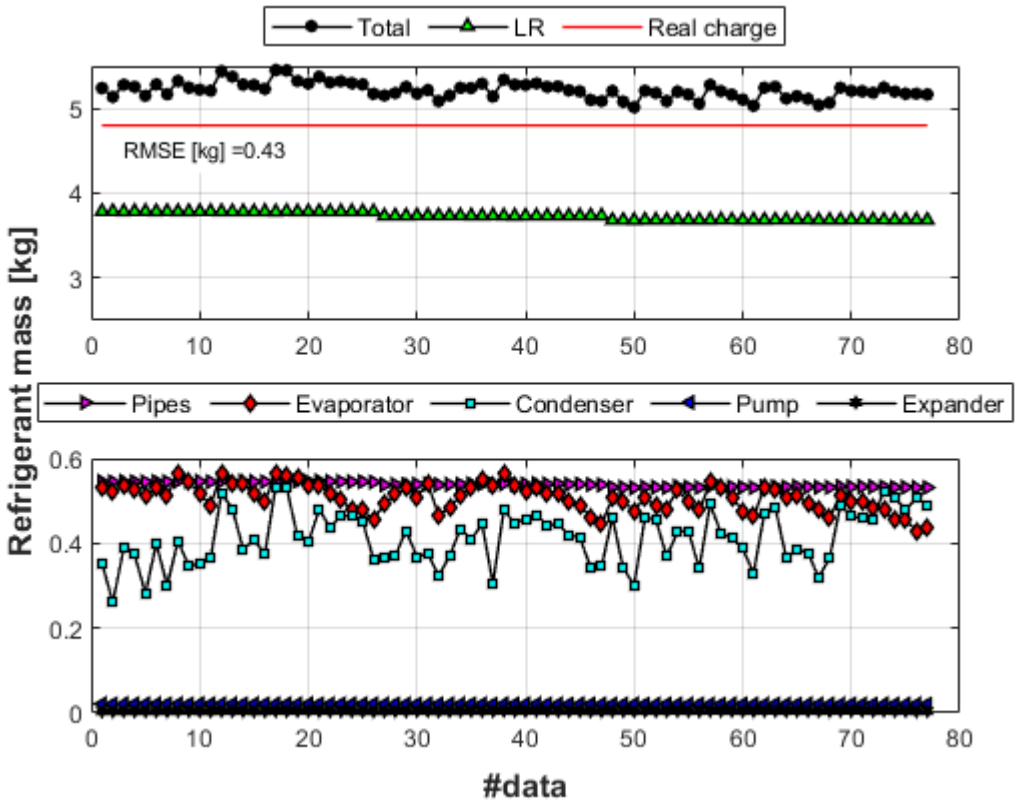


Figure 4-6. The calculated system mass assuming the flooded liquid receiver and using the homogenous *VF* model for the PHEs

To find the best *VF* model that results in the least deviation between the calculated and the real system mass charge, the system is solved using the seven *VF* models reported in Table 4-1 plus the homogenous model for the evaporator and the condenser (64 simulations), and the models with the least RMSE for the experimental data are selected as the best combination. The PHEs are solved using the hydro-thermal models described in chapter 3, Modeling of the ORC system components. Therefore, the accuracy of the mass model includes the accuracy of the thermo-hydraulic model of the PHEs since the length of each heat transfer zone depends on the CHTC of the zone. The best *VF* model is found the Rouhani II correlation for both evaporator and condenser confirming the choice based on the literature survey.

Results of the calculated mass of the ORC system and its components using the selected *VF* model, Rouhani II, and the measured liquid level in the liquid receiver are shown in Figure 4-7 confirming the good accuracy of the simulation despite all points are slightly underpredicted. In addition, the variation of the refrigerant mass is visible in the condenser unlike the evaporator, because the subcooling degree is changed in the condenser in different working conditions but the superheating degree is changed in the evaporator; hence, the liquid zone length is changed in the condenser that affects its mass, while gas zone length is varied in the evaporator that has a negligible refrigerant mass. Due to the limitations of the measuring range of the two pressure sensors, the system mass calculation could be performed for 23 points out of 84. Pure fluid properties are used for the calculation of the working fluid properties.

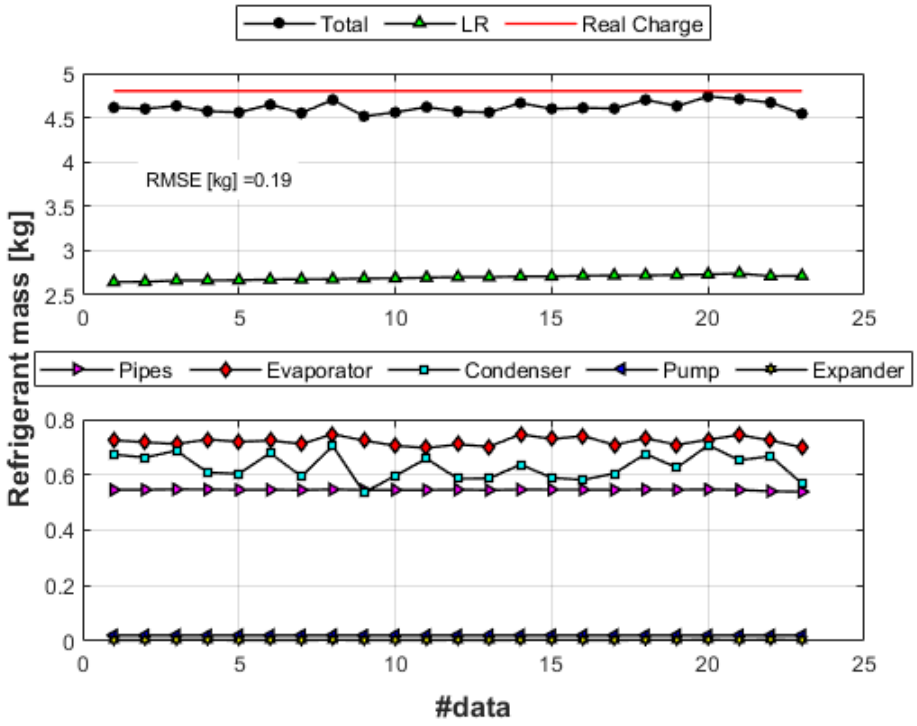


Figure 4-7. Calculated refrigerant mass of the ORC system and its components using Rouhani II *VF* model and measured liquid level in the liquid receiver for some experimental data points

The relative distribution of the mass charge in different components is illustrated in Figure 4-8 for one of the data points. The calculated mass of the PHEs includes the refrigerant mass of the inlet and outlet manifolds and pipe nipples. Furthermore, it is evident that the refrigerant mass in the expander and pump is negligible compared to the other components and can be neglected in the simulation. It was expected before the mass charge simulations since despite the pump includes liquid refrigerant, it has low internal volume. For the expander instead, the volume is relatively high, but it includes only the vapor phase with a low density.

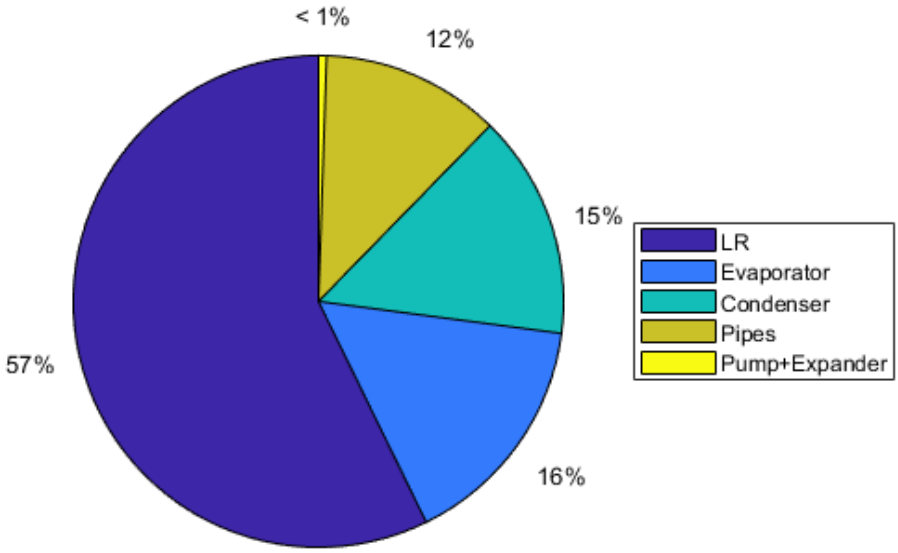


Figure 4-8. Relative refrigerant mass distribution in different components of the ORC system

The refrigerant mass distribution is calculated for all the experimental data points using the Rouhani II *VF* model for both the evaporator and the condenser are presented in Figure 4-9. In this figure, the initial system mass charge is the input, and the liquid receiver mass is the result. Considering the relatively limited range of the mass flow rate in the experimental data, the liquid receiver level was almost stable during the experiments and it never got flooded or emptied.

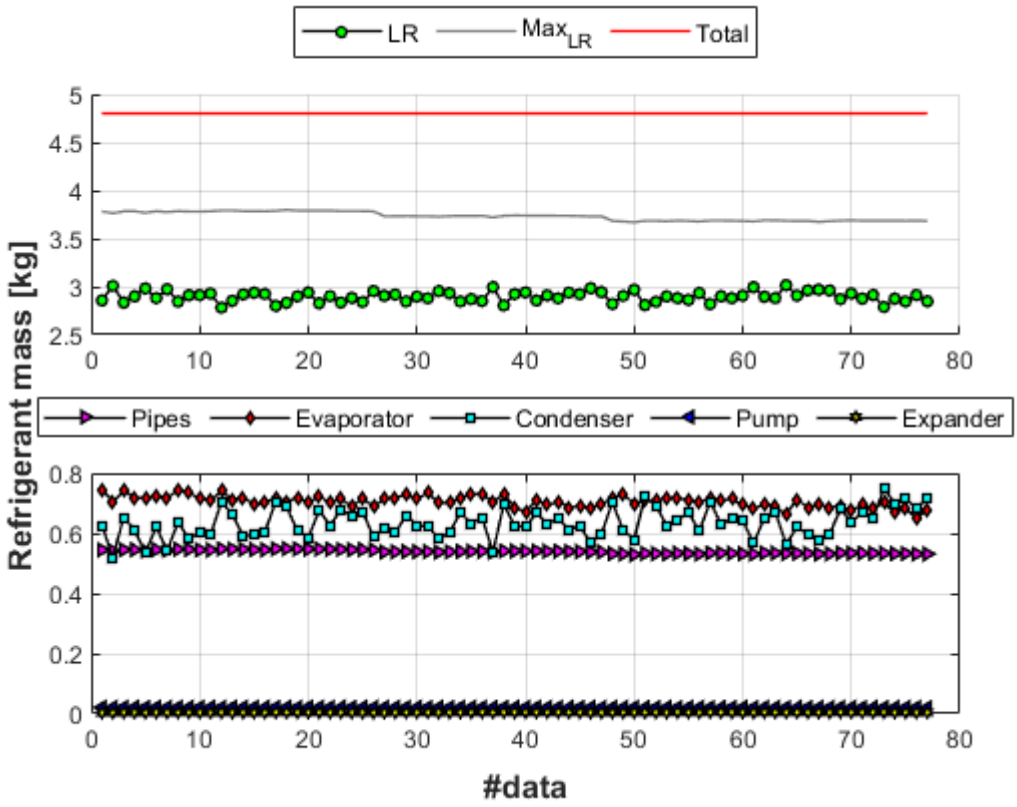


Figure 4-9. Simulated mass distribution in the ORC components using Rouhani II *VF* model for the experimental data

The calculated liquid receiver mass is higher than the measured values as presented in Figure 4-10 since the difference between the calculated system mass and the real initial mass charge observed in Figure 4-7 is accounted for in the liquid receiver mass that is obtained by subtracting the calculated mass of other components from the initial system mass. Nevertheless, the difference between the measured and the calculated refrigerant mass in the liquid receiver is not great and can be associated with the accuracy of the two pressure sensors installed on the liquid receiver body.

Furthermore, the calculated liquid level in the liquid receiver for all data points was found at about 77.64% with a 2.29% relative standard deviation. Hence, this level is considered for the liquid level of the liquid receiver as the fixed value and it is used in the mass-sensitive system modeling that is presented in the following.

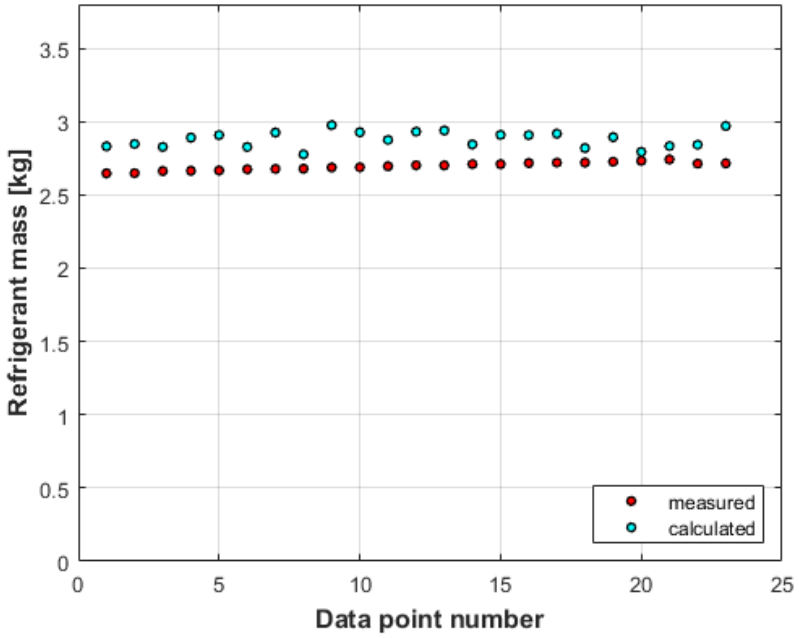


Figure 4-10. Measured and calculated refrigerant mass in the liquid receiver

### 4.2.4 The extrapolability of the liquid receiver mass model

The liquid receiver mass must be known in different working conditions and different system initial mass charges so the mass-sensitive solver can be extrapolated confidently. The average liquid level in the liquid receiver here is valid in the range of the experimental data and it may be different in the working conditions far from the range of the experimental data. Therefore, a model of the liquid receiver mass in different working conditions is needed to conduct mass-sensitive modeling. Having the liquid receiver mass model, the liquid level in the liquid receiver is part of the results of the solver along with the mass distribution in other components. In summary, the presented liquid receiver average mass cannot be extrapolated to working conditions far from the range of the experimental data in this work.

Regarding the liquid receiver mass in different system mass charges, it can be assumed that the average level can be estimated by considering the same ratio of

the system mass over the system mass in this study (4.8 kg) is valid for the liquid level in the liquid receiver too since the system components take some mass calculated using the models and the rest is stored in the liquid receiver. In other words, the other components take their share of refrigerant and the rest remains for the liquid receiver during the system operation. However, if the liquid receiver is flooded, the extra mass must go to the PHEs thus the components' mass models are not valid anymore since it is the flooded liquid receiver that dictates their mass now. In addition, if the liquid level is low in the liquid receiver, one cannot strongly guarantee that the system operates the same. Indeed, this issue was observed during the tests with a lower mass charge that despite the liquid detector sensor on the liquid receiver body, which is located at the level of about 22%, was not sending any signal confirming the presence of the liquid, the cavitation occurred in the pump. This can be due to the complex heat transfer between the subcooled liquid coming from the condenser and the saturated gas in the tank. In low liquid levels, the subcooling loss is big enough to prone the pump to cavitation. The subcooling loss is due to the heat transfer between the inlet subcooled liquid the saturated gas. Therefore, a minimum liquid level of 50% is recommended. Hence, the liquid receiver mass model can be extrapolated between 50% liquid level up to flooded liquid receiver meaning the initial system charge of 3-6.2 kg approximately. Therefore, the average relative liquid level in the liquid receiver in different initial mass charges can be estimated using Eq. (4-18). The proposed mass-sensitive solver can take the liquid receiver mass model in different initial mass charges to calculate the off-design system's performances.

$$RLL = \left(\frac{77.64}{4.8}\right) Mass_{ORC} \tag{4-18}$$

where 3 kg<$Mass_{ORC}$<6.2 kg.

## 4.3 **The system boundary and the refrigerant mass distribution**

The impact of four system boundaries on the refrigerant mass distribution is presented hereunder by fixing other parameters and changing the objective parameter. To this end, two points are chosen from the experimental data to isolate the objective parameter. However, the difference in the values of the system boundaries is marginal since keeping the other parameters constant in the experiments was difficult, especially the expander shaft speed that was adjusted using the electric load was not easy to handle during the experiments due to the phase rotation of the load. Nevertheless, small changes in the boundary values result in the changes in the mass distribution, which despite being small values, a meaningful trend is observed. The considered boundary conditions are the heat source temperature, the heat sink temperature, the refrigerant pump speed, and the expander shaft speed.

### 4.3.1 Heat source temperature

The superheating degree at the evaporator outlet and condenser inlet increases with the increment of the heat source temperature resulting larger area of the gas zone in both PHEs. Therefore, the refrigerant mass travels from the PHEs and fills the liquid receiver with the liquid refrigerant as shown in Figure 4-11.

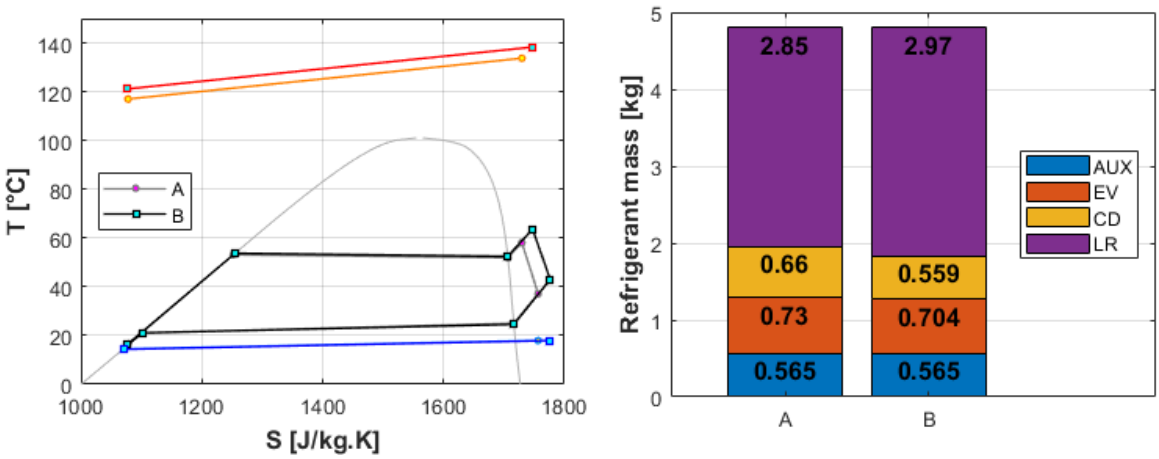


Figure 4-11. T_S diagram and mass distribution in different heat source temperatures; A: $T_{HF,in}$ = 134 °C, B: $T_{HF,in}$ = 138 °C (rows 41 & 44 in Table A5)

### 4.3.2 Heat sink temperature

By increasing the water inlet temperature to the condenser, the condenser pressure rises to maintain the temperature pinch in the condenser, which in its turn, leads to higher evaporator pressure. The inlet temperature of the evaporator increases; thus, the superheating degree in the evaporator and condenser increases. Therefore, the refrigerant mass accumulates in the liquid receiver as the gas zone area in the PHEs grows up. It is noteworthy that the subcooling degree remains almost the same value here due to the high capacity of the cold sink that the minimum temperature pinch is reached.

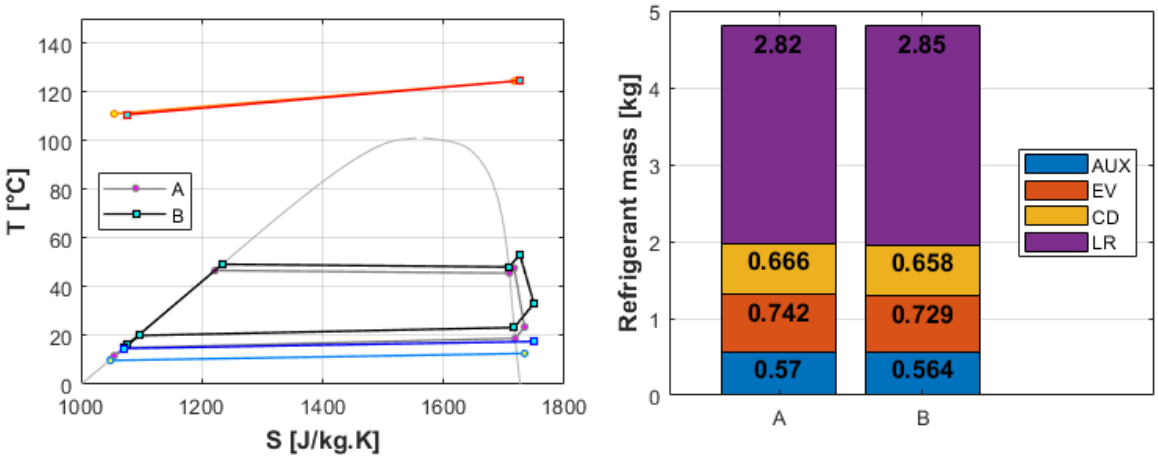


Figure 4-12. T_S diagram and mass distribution in different heat sink temperatures; A: $T_{CF,in}$ = 10 °C, B: $T_{CF,in}$ = 15 °C (rows 3 & 32 in Table A5)

### 4.3.3 Refrigerant pump speed

Similar to the previous discussions, the change in the superheating degree dictates the change of the mass distribution in the system and the liquid receiver mass. The higher pump speed at the fixed heat source and cold sink temperatures results in lower superheating in the evaporator outlet and condenser inlet. Hence, the evaporator and condenser mass increase in higher pump speeds, and the liquid receiver mass reduces.

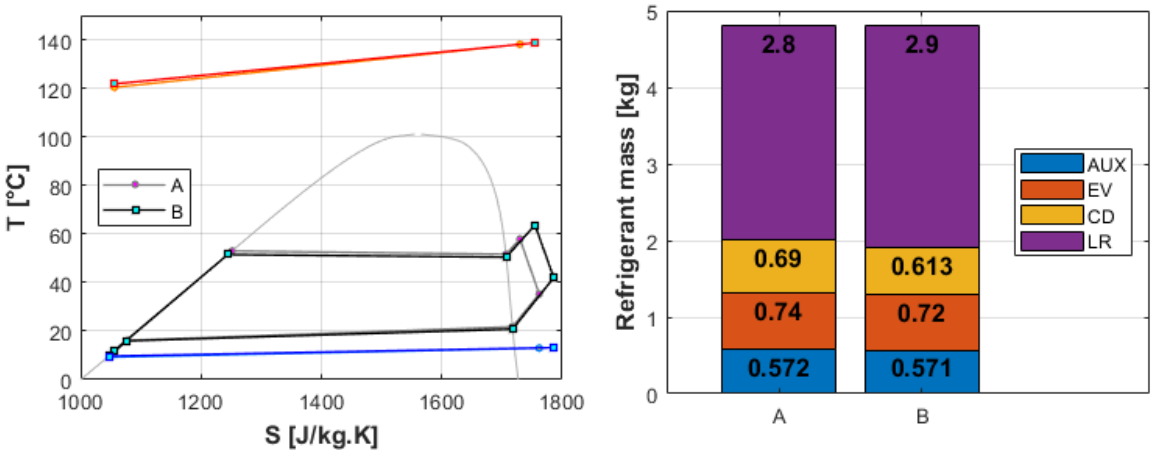


Figure 4-13. T_S diagram and mass distribution in different refrigerant pump speeds; A: $N_{p,ref}$ = 360 rpm, B: $N_{p,ref}$ = 330 rpm (rows 13 & 15 in Table A5)

### 4.3.4 Expander shaft speed

Expander shaft speed is changed by the electric load that adjusts the torque imposed from the electric generator to the expander shaft. When the expander shaft speed increases while the pump speed is constant, the expander suction density must be reduced to let the expander swallow the same pump mass flow rate in a higher volumetric flow rate at the expander suction. Therefore, the evaporator pressure lowers in higher expander shaft speeds corresponding to lower electric load (or mechanical torque). Lower evaporator pressure means a higher temperature difference in the evaporator resulting in a higher superheating degree. Like the previously presented impact of the superheating on the mass distribution, the higher the expander shaft speed the lower mass in the PHEs and the liquid receiver mass.

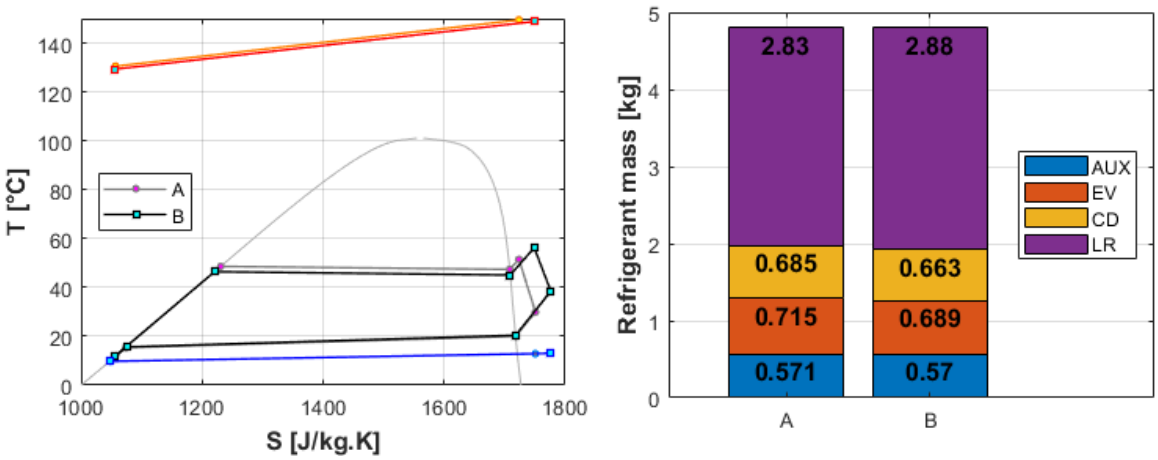


Figure 4-14. T_S diagram and mass distribution in different expander shaft speeds; A: $N_{exp}$ = 970 rpm, B: $N_{exp}$ = 1280 rpm (rows 24 & 25 in Table A5)

### 4.3.5 Evaporator and condenser mass-sensitivity analysis

To perform mass-sensitive modeling of the ORC system, it is necessary to understand the response of the mass of the PHEs to variations of their working conditions. Therefore, the impact of the evaporator superheating degree and pressure and condenser subcooling degree and pressure on the refrigerant mass is modeled using the developed hydro-thermal models and mass models of the PHEs.

The calculated condenser mass and subcooling degree, and the calculated evaporator mass and superheating degree are presented in Figure 4-15. The condenser mass increases with the subcooling degree and the evaporator mass reduces with the superheating degree. The first is due to the growth of the liquid zone in the condenser, and the latter is because of the enlarged gas zone in the evaporator.

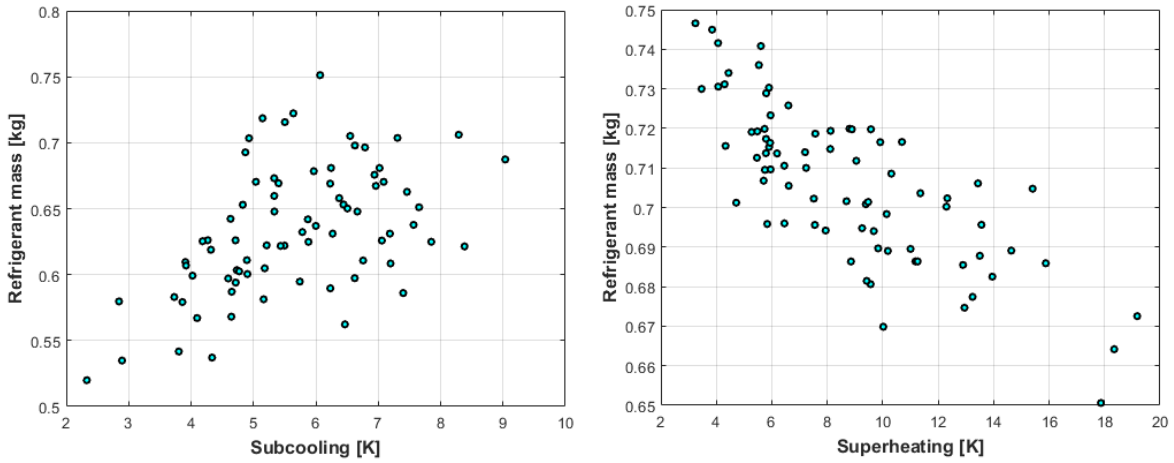


Figure 4-15. Condenser mass with subcooling degree (left), and evaporator mass with superheating degree (right)

The impact of the evaporator pressure on its superheating degree and mass and condenser pressure on its subcooling degree and mass is crucial to know before the mass-sensitive system modeling. Figure 4-16 shows that the subcooling degree increases with the condenser pressure, which is due to the higher average temperature difference between the hot and the cold streams resulting in a lower needed area for vapor and two-phase zones. Therefore, the remaining area of the condenser that is allocated to the liquid zone grows. Consequently, the condenser refrigerant mass increases. The trend of the superheating degree in the evaporator is opposite of the subcooling degree in the condenser, and it is reduced with the evaporator pressure. This is due to the lower average temperature difference between the hot and cold streams resulting in a bigger heat transfer area needed for the subcooled and two-phase zones. Hence, the remained area for the vapor zone is diminished and the superheating degree is reduced. Like in the condenser, the refrigerant mass in the evaporator is incremented with the evaporator pressure since the vapor zone is shrunk.

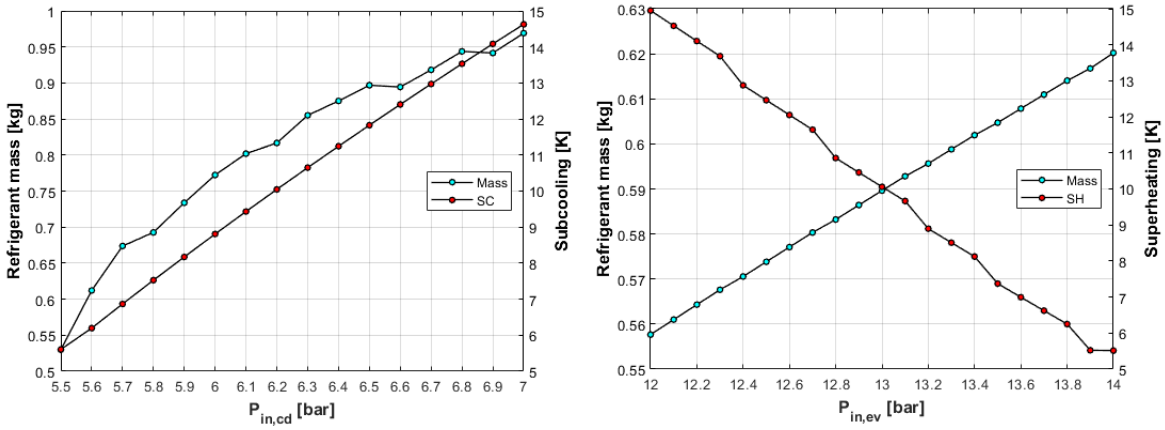


Figure 4-16. The impact of the pressure on the condenser mass and subcooling degree (left) and on the evaporator mass and superheating degree (right)

The mass model investigated in this work can be used to distinguish the impact of each component on the total mass charge of the system to minimize it during the design stage or to determine the amount of the needed refrigerant for a system.

Finally, it should be noted that despite the overall mass calculation of the system is accurate, the refrigerant mass of the PHEs depends on its hydro-thermal solution and it may not be the same as the reality since their refrigerant mass is not measured individually. Therefore, one may observe a slight deviation between the predicted mass of the evaporator and condenser if they are measured. However, in the case of the other components that work with single-phase working fluid, the mass calculations are expected to be correct since their models are straight-forward.

## 4.4 **Mass-sensitive modeling of the ORC system**

The ORC system investigated in the thesis simulated using the real boundaries of the system, which an operator has during the system run. Therefore, the system model is assumption-free. Furthermore, the system model uses the sub-models of its components presented in Chapter 3, Modeling of the ORC system components;

hence, the model is object-oriented. To have an assumption-free system model, conservation of mass is needed to be applied to the components in addition to the conservation of energy. Thus, the mass models of the components presented in this chapter are needed to be applied to the system modeling as well. The schematic of the mass-sensitive model of the system with needed inputs and expected outputs is presented in Figure 4-17.

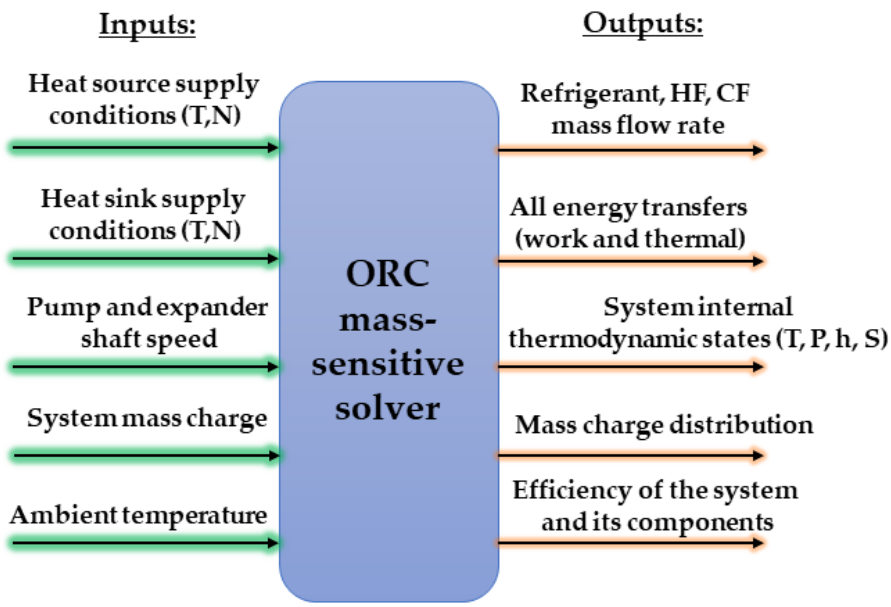


Figure 4-17. Schematic of inputs and outputs of the ORC mass-sensitive model

As presented in Chapter 1 in sub-chapter Mass-sensitive system modeling, relatively few works were considered the mass-sensitive modeling of the ORC systems in the literature as reported in Table 1-1. Moreover, these models assumed a simple model for the liquid receiver if it was considered in the system. While it was showed in this chapter that the liquid receiver may not be flooded with the liquid refrigerant in all systems and all working conditions when the condenser outlet is subcooled, and both the experimentally measured liquid level in the liquid receiver and the model results confirmed this statement. Therefore, the mass-

sensitive modeling of the ORC system is performed considering the average liquid level of 77.64% in the liquid receiver found from the modeling results in this chapter. It is noteworthy that this average liquid level is valid for the range of the experimental data; hence, the liquid receiver mass model must be known if it is going to be used in the mass-sensitive system modeling in very off-design conditions.

### 4.4.1 Model algorithm

The mass-sensitive model of the ORC system consists of four guess values that are determined by the minimization of four residuals in four iterative nested loops. The model is assumption-free and the inputs to the model are the real system boundaries plus the components specifications. The structure of the solver is designed based on the inputs and outputs of the models of the components. The guess values are the pump suction pressure, pump discharge pressure, expander discharge pressure, and pump suction temperature.

The pump discharge pressure is found in the internal iterative loop by minimizing the residual of the mass flow rate that is calculated using the mass flow rate of the pump and the mass flow rate of the scroll expander for the given shaft speed and discharge pressure. The pump discharge pressure determines the expander suction pressure, which in its turn, determines the expander suction density. In other words, the high-pressure side of the system is found so the mass flow rate produced by the pump can be devoured by the expander for the given shaft speed and discharge pressure. The guessed expander discharge pressure is corrected in the next loop by minimizing the difference between the condenser discharge pressure and the pump suction pressure, which is one of the guess values itself. In the next loop, the guess value of the pump suction temperature is updated so it becomes close enough to the calculated condenser outlet temperature. In the outer loop, the

pump suction pressure is adjusted so the calculated system mass becomes equal to the initial system mass charge. Indeed, the pump suction pressure indicates the subcooling degree in the condenser, which directly affects the condenser mass charge and consequently the overall system mass. The solution is converged when the four residuals are below 0.01. The flowchart of the mass-sensitive solver of the ORC system is presented in Figure 4-18.

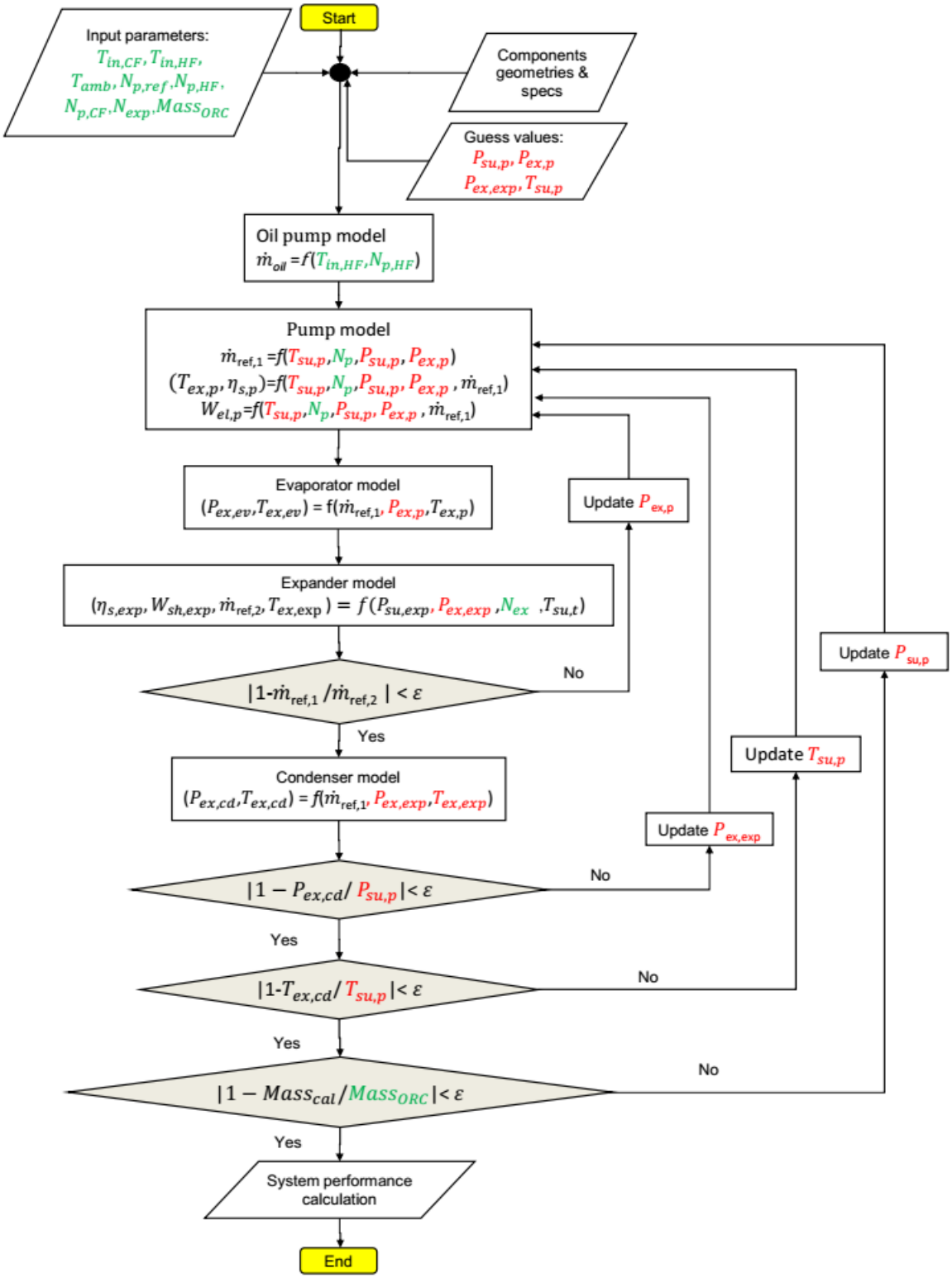


Figure 4-18. Flow chart of the mass-sensitive solver of the ORC system

### 4.4.2 Model validation

To validate the mass-sensitive solver, it is used to predict the experimental data when the model inputs are adopted from the experimental data. One hint for the guess values is to have high enough expander discharge pressure to avoid temperature cross in the condenser. The average computation time of the developed solver is about 200 s in MATLAB© 2020a using one core CPU Intel®-2.5 GHz base speed. However, the computation time may be very different for different points depending on how close the guess values are to the final solution.

Figure 4-19 shows the calculated temperature and pressure of some points of the system compared with the measured values. The simulation results are in good agreement with the experimental data. Therefore, the model is accurate enough to predict the thermodynamic states of the system at different points.

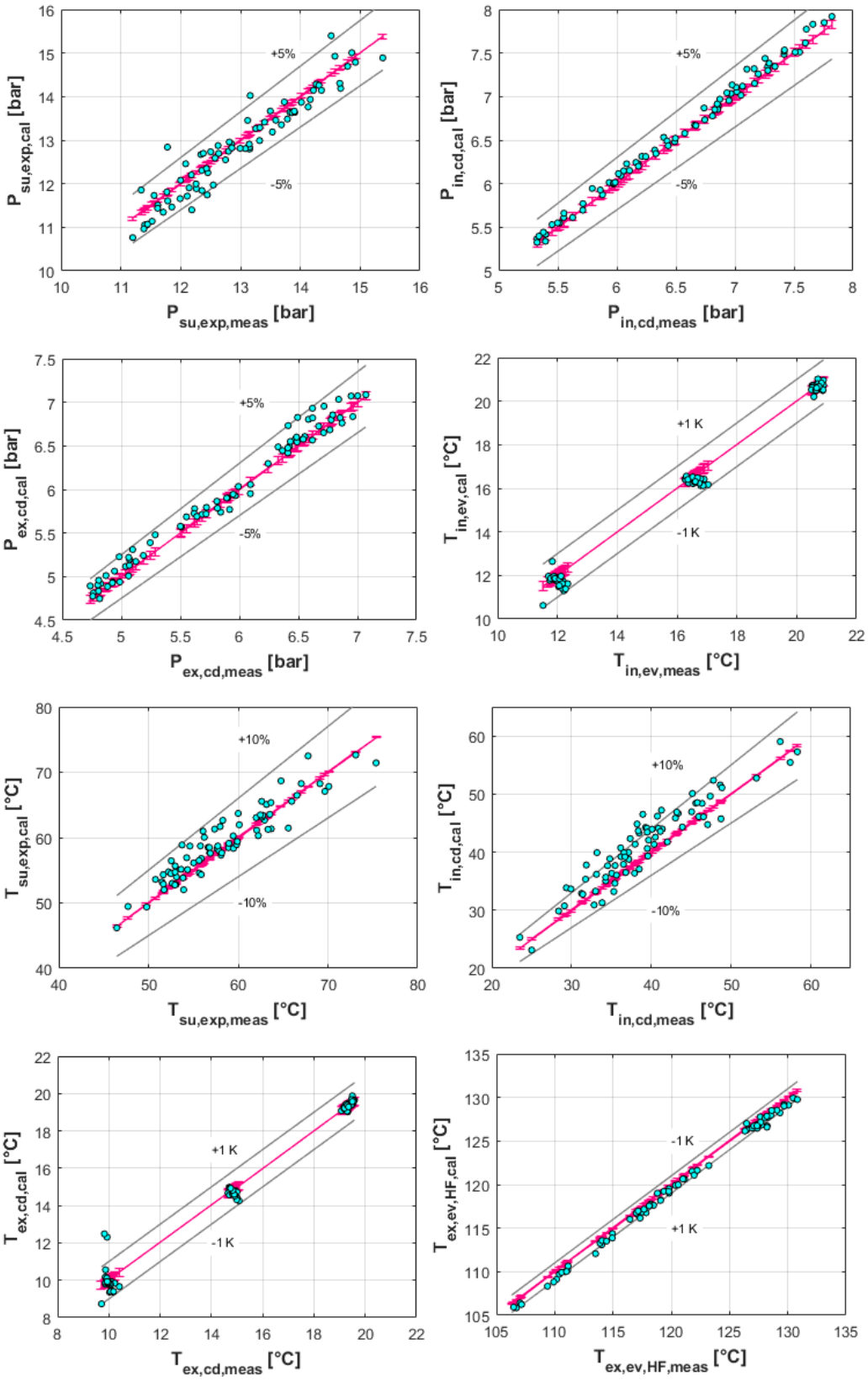


Figure 4-19. Measured and calculated temperature and pressure of different points of the system using the mass-sensitive model

Due to the error propagation of the models of the components, it is expected to have higher errors in the system-level simulation compared to the results of each component model. Scroll expander performance is particularly important to the overall accuracy of the system model. Figure 4-20 presents the expander performance in terms of the shaft and electric power, isentropic efficiency, and filling factor. Compared to the results of the expander shaft power shown in Figure 3-15, the accuracy is expectedly lost since the error due to the expander model is summed with the error of the suction and discharge pressure. Nevertheless, the expander performance is predicted with acceptable accuracy.

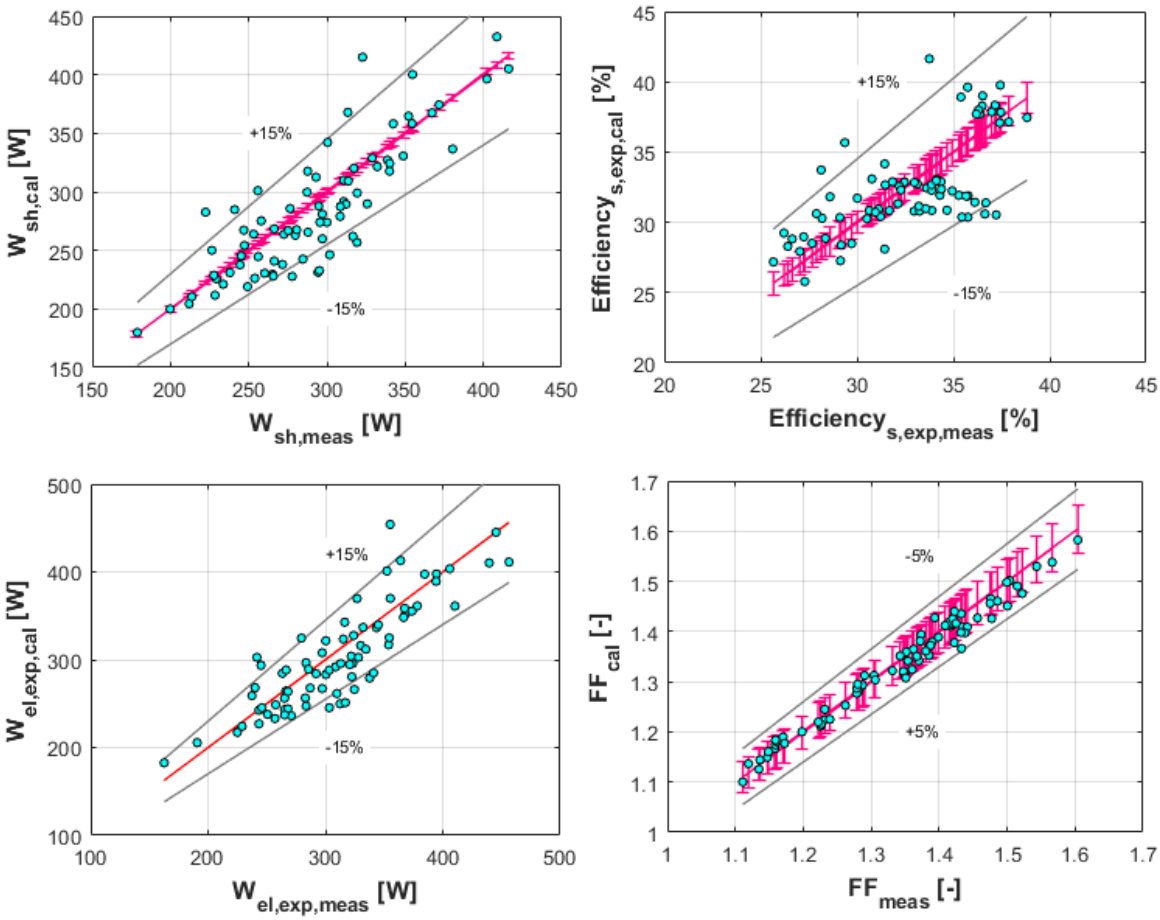


Figure 4-20. Measured and calculated expander performance using the mass-sensitive model

The pump electric power consumption and its mass flow rate are shown in Figure 4-21 representing a good agreement between the pump performance obtained from the mass-sensitive solver and its measured performance.

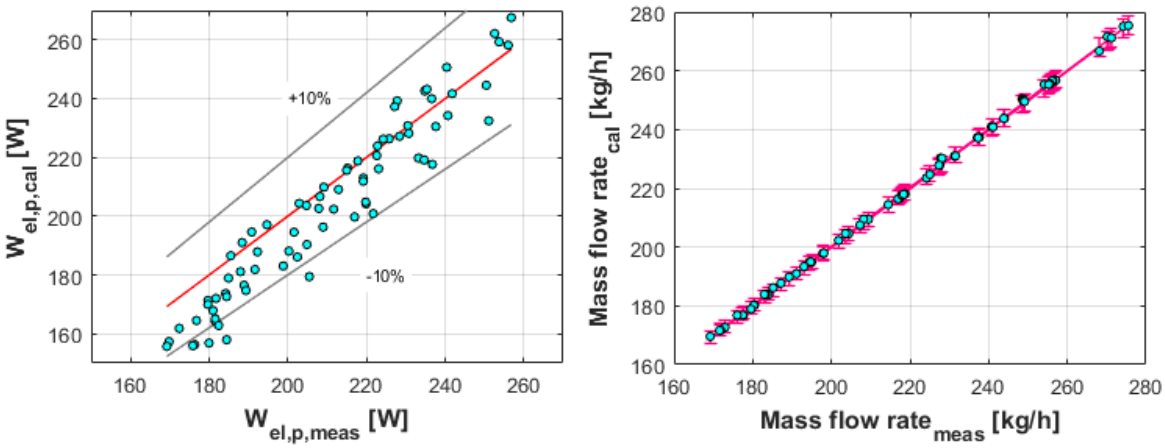


Figure 4-21. Measured and calculated pump performance using the mass-sensitive model

The highest error of the model is observed in the net electric efficiency[1] as shown in Figure 4-22, in which the error of the thermodynamic parameters and the performance of the components are accumulated. Despite most points are in good accuracy, some are predicted with relatively high errors. However, due to generally low values of the net electric efficiency, the absolute error is low like 0.5%, but the relative error is high.

In addition to the accumulative error of the sub-models, some of this error is due to the use of the average liquid level in the liquid receiver. Despite the relative standard deviation of the liquid level was 2.29% that is accounted as a low value,

[1] It is calculated using the thermal power of the hot fluid stream in the evaporator.

the difference of the liquid receiver mass must be compensated by condenser mass by changing the subcooling degree. Therefore, the pump suction pressure would be under/over-predicted when the liquid level in the liquid receiver is higher/lower than the average value to minimize the residual of the system's overall mass.

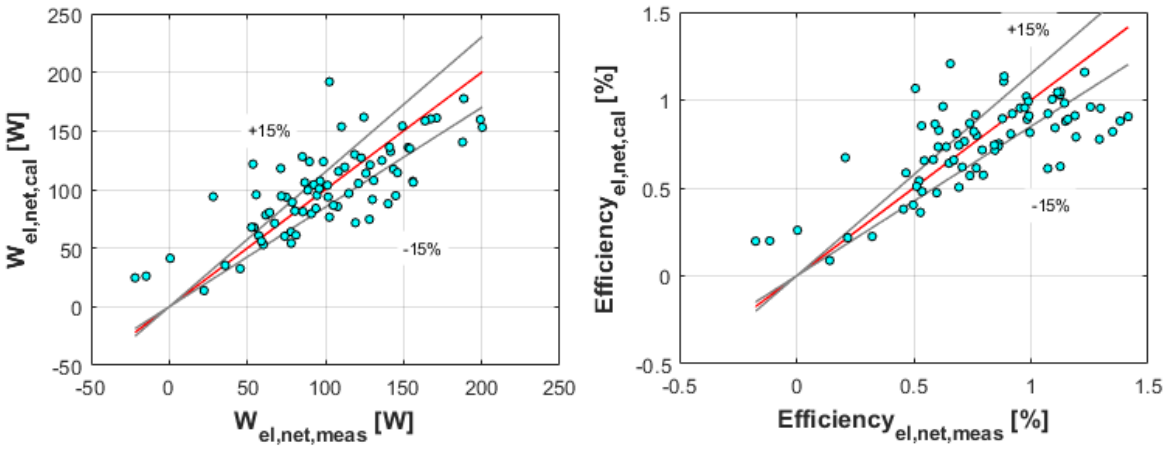


Figure 4-22. Measured and calculated net electric power and efficiency using the mass-sensitive model

### 4.4.3 Model results

After its validation, the mass-sensitive model is used to map the system performance in a matrix of two system boundaries to present the optimum point for the system. To avoid extrapolation of the sub-models, the range of the system boundaries is kept as the range of the experimental data. Indeed, the ORC system was tested in a range of the system boundaries that was possible due to the different system limitations presented in Chapter 2, Experimental investigations. For instance, the heat source power was not enough to superheat the refrigerant at pump speeds above 400 rpm in the experiments. Hence, the studied system with the given components specifications cannot operate reliably in the steady-state mode in extrapolated working conditions.

The mass-sensitive model is run changing the pump speed and expander shaft speed keeping the other system boundaries fixed. The net electric system performance map is presented in Figure 4-23. The optimum operating point of the studied system is at an expander speed of 900 rpm and pump speed of 400 rpm approximately, in which both the net electric power and net electric efficiency are at their maximum.

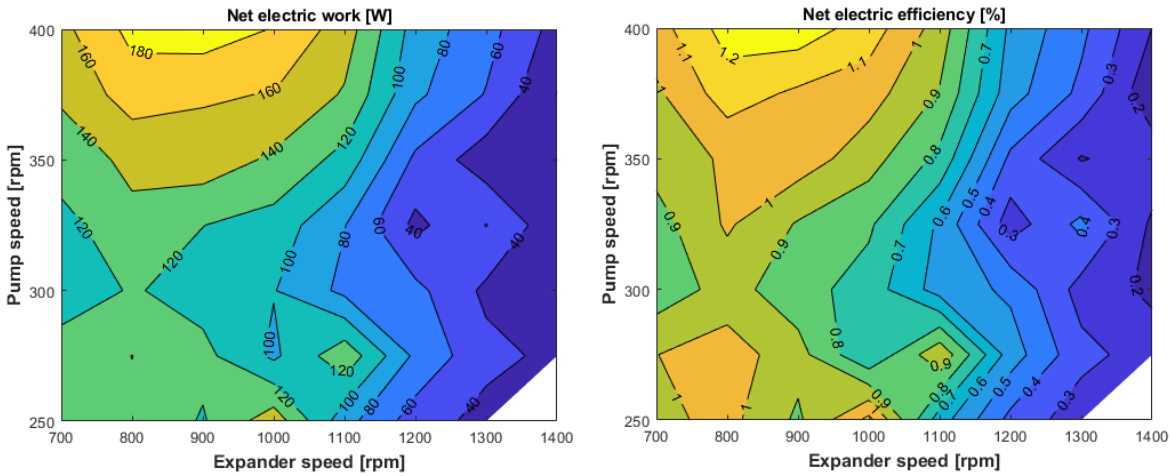


Figure 4-23. Net electric work map (left) and net electric efficiency map (right) of the ORC system with the pump speed and the expander speed ($T_{HF,in}$ = 150°C, $N_{P,HF}$ = 1400 rpm, $T_{CF,in}$ = 15°C, $T_{amb}$ = 15°C)

## 4.5 **Summary and conclusions**

This chapter aimed to present an assumption-free, object-oriented model of the ORC system under the investigation. The assumption-free system model means that the solver requires the same inputs that an operator has during the system operation, and the system performances are to be predicted. To be assumption-free, the conservation of the refrigerant mass must be considered in addition to the conservation of energy, hence the mass-sensitive model is proposed. The proposed algorithm of the mass-sensitive model consists of four residuals that must be

minimized in four iterative loops by adjusting four system parameters that were guess values initially. The mass-sensitive model is robust, and it is consistent with the characteristics of the sub-models. The liquid receiver is found to be partially filled with liquid refrigerant in the experiments that shows that the simplifying liquid receiver models used in the literature so far may not be valid for all systems in all working conditions and the liquid receiver has a more complex nature.

The sub-models of the main system components developed in the previous chapter were used in the mass-sensitive solver using MATLAB© functions making the model object-oriented. The errors created in each sub-model naturally accumulates in the system solver resulting in a higher error of the system-level modeling compared to the models of each component.

The mass-sensitive model is finally used to map the net electric performance when the pump speed and the expander speed are changed. Therefore, the mass-sensitive model can be used to predict the thermodynamic states at different locations of the system, the components' performances, the refrigerant mass distribution that is particularly important for the liquid level in the liquid receiver, and the overall system performances. The results of the model have shown that the system is potentially able to operate in higher net efficiency producing more electric power if more thermal power is provided in the heat source.

## 4.6 **Nomenclature**

| | | | |
|---|---|---|---|
| A | area [$m^2$] | x | vapor quality [-] |
| ∀ | volume [$m^3$] | M | mass [kg] |
| $\dot{m}$ | mass flow rate [kg/s] | *w* | width [m] |
| ρ | density [$kg/m^3$] | d | diameter [m] |
| *ν* | velocity [m/s] | L | length [m] |

| | | | |
|---|---|---|---|
| g | gravitational acceleration [m/s$^2$] | exp | expander/experimental |
| H | Height [m] | sat | saturated |
| $d_h$ | hydraulic diameter [m] | HF | Hot Fluid |
| G | mass flux [kg.m$^{-2}$.s$^{-1}$] | CF | Cold Fluid |
| P | pressure [Pa] | ref | refrigerant |
| T | Temperature [K] | ev | evaporator |
| N | rotational speed [rpm] | cd | condenser |
| h | enthalpy [J/kg] | el | electric |
| S | entropy [J/K] | s | isentropic |
| $\eta$ | efficiency [%] | cal | calculated |
| W | Power (work) [W] | sh | shaft |

*Subscripts and superscripts*

| | |
|---|---|
| g | gas |
| l | liquid |
| tot | total |
| hom | homogenous |
| c | cross section |
| TP | Two Phase |
| SP | Single Phase |
| su | suction |
| ex | exit |
| p | pump |

*Acronyms*

| | |
|---|---|
| ORC | Organic Rankine Cycle |
| PHE | Plate Heat Exchanger |
| VF | Void Fraction [-] |
| SV | Swept Volume [m$^3$/rev] |
| RLL | Relative Liquid Level [%] |
| RMSE | Root Mean Square Error |
| CHTC | Convective Heat Transfer Coefficient [W.m$^{-2}$.K$^{-1}$] |
| FF | Filling Factor [-] |

**Chapter 5**

# 5. The impact of the expander oil

*"Essentially, all models are wrong,*
*but some are useful"*

George Box, British statistician

## 5.1 Introduction

Several issues penalize the ORC performance especially at small scales and many studies have aimed to tackle the technical issues to improve the system efficiency. Besides the intrinsic low efficiency of such systems due to the relatively lower Carnot efficiency compared to the traditional Rankine cycles, several system components such as the expander machine and the pump, are not mature and efficient resulting in further efficiency losses. At micro and small scales, another issue that has an impact on the performance degradation of these systems is the expander lubricant oil. In such systems, volumetric expanders are usually preferred compared to dynamic turbines, and most of them are obtained converting volumetric compressors [62]. These machines are usually lubricated to have a better volumetric efficiency by decreasing the internal leakages, better mechanical efficiency by reducing the frictional losses and a longer lifetime consequently. However, a separate oil loop is often absent because it is usually a costly option for such systems while their low cost is a determining factor in their marketing. Therefore, the lubricant oil can mix with the refrigerant and migrate through the system components penalizing their performance.

In the literature, the impact of the lubricant oil on the performance of the components was studied in heating, ventilation, and air conditioning (HVAC) systems to some extent. In general, it is advantageous that the lubricant oil has high miscibility with the refrigerant to return to the compressor as the refrigerant circulates in the system [99]. For example, Popovic et al. [100] reported that both the capacity and the COP of the studied refrigeration system working with R134a was higher using a more miscible lubricant. However, the presence of oil is normally disadvantageous for the overall system performance, whatever its miscibility, apart from lubricating the valve seats and rotary machines [101]. In a heat pump system, the performance of the evaporator and condenser is degraded due to the oil entrainment and it is notably reported that the evaporator pressure drop is approximately doubled in such systems also [102]. Navarro et al. [103] tested five commercial reciprocating compressors using R407C as the working fluid and Polyolester (POE) oil as the lubricant. Their results showed that the measured oil circulation rate (OCR) was not sensitive to the system working conditions, but a different average value was observed for each compressor. In addition to the OCR, it is important to know the place where the oil can be trapped to facilitate the return of the oil to the compressor using relevant installation measures or the oil traps [104].

Despite the impact of oil entrainment has been investigated in HVAC systems, its influence on ORC systems has been often neglected. This becomes more important in micro scales since the volumetric expanders are more suitable, which are lubricated in a considerable share compared to turbines that are usually oil-free. It is evident in Figure 5-1 that shows the different lubrication strategies based on the expander technology in the literature up to 2017.

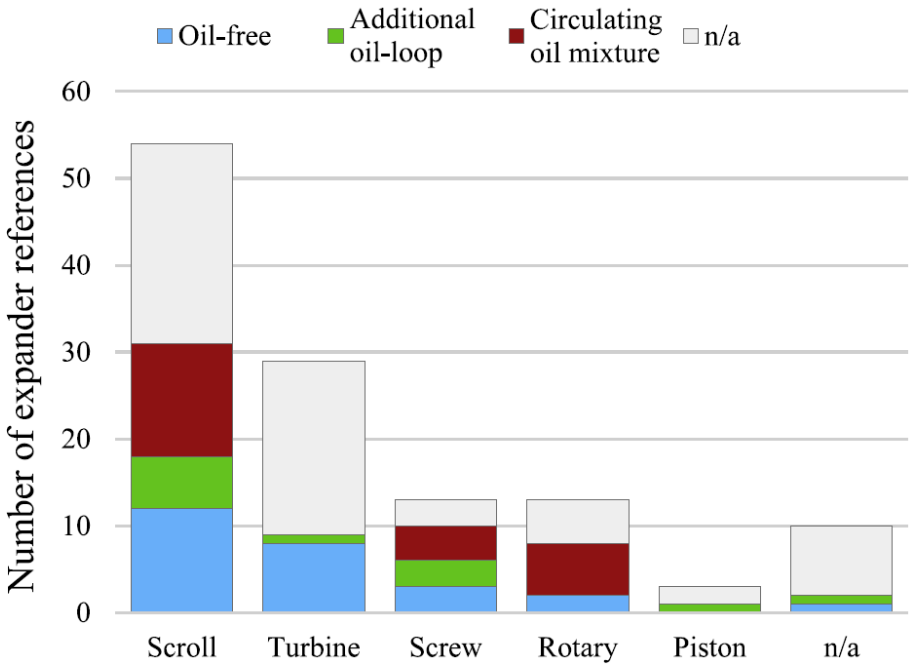


Figure 5-1. Expander lubrication strategies (adopted from [105])

Despite its importance in micro-to-small scale ORC systems, the oil entrainment has been addressed only in a few studies. Desideri et al. [106] tested a regenerative ORC system equipped with a single screw expander modified from a standard compressor with a nominal shaft power of 11 kW. They tested the system with two organic fluids of SES36 and R245fa in different working conditions. The screw expander was lubricated during the test maintaining the oil concentration of 3.23%. The oil presence was considered in the calculation of the thermal power of the components considering the oil mass fraction and specific heat neglecting the refrigerant miscibility in the model. Using this simplifying assumption, they reported the thermal balance in the evaporator, the condenser, and the regenerator. They concluded that the evaporator had thermal losses since the thermal load of the hot stream was higher than the one of the refrigerant stream and the deviation was higher than the measurement uncertainties. In the case of the condenser and regenerator, the deviation was in the range of the measurement uncertainties thus a negligible heat loss was considered. They did not perform any reconciliation

method to fit the thermal load of the hot and cold streams in the evaporator considering the lubricant-refrigerant mixture.

Feng et al. [107] conducted an experimental study on the impact of the expander oil on the performance evaluation of different components of a non-regenerative, 3 kW ORC system working with R123 and a scroll expander. They used the simple model considering the mass fraction of the oil and refrigerant to calculate the enthalpy of the mixture. Like the reference work quoted above, the refrigerant miscibility was not considered, but a weighting coefficient was used in the model to reconcile the thermal load calculation of the refrigerant stream to minimize the difference between hot and cold stream thermal load unbalances. The tests were performed in five oil concentrations ranging from 1.25% to 9% in three superheating degrees of 5, 10, and 15 K. They showed that the pump behavior was enhanced considering oil, but the expander shaft work and electric power were penalized as the oil concentration increased. The heat transfer coefficients in the evaporator and condenser were reduced due to the oil entrainment as well. The system thermal efficiency was not sensitive to oil concentration except in low superheating degrees, in which the system thermal efficiency was reduced with the oil concentration.

Like the reference above, Yang et al. [108] used a weighting coefficient to calculate the thermal load of the refrigerant stream in the evaporator, and they used the same weighting coefficient as Feng et al. [107]. Their system was a non-regenerative, 2 kW ORC unit using scroll expander and plunger pump tested with R245fa and with the oil concentration of 0.12-10%. Their results showed that the expander isentropic and volumetric efficiencies were increased especially when the oil concentration was increased from 0.12% to 1%, but they were not changed much in higher oil concentrations. Therefore, their conclusions are in contrast with what was deduced by Feng et al. [107] about the impact of oil concentration on the expander's performances.

Two recent studies were found considering the mixture properties using the refrigerant miscibility models in an ORC system. In his doctoral thesis published in 2019, Dickes [29] studied a regenerative, 2 kW ORC system tested using R245fa and a scroll expander. The experimental data were adjusted to respect some physical constraints such as positive temperature pinch in the evaporator, condenser, and regenerator plate heat exchangers (PHEs), the positive pressure drop in the PHEs and the expander, positive pressure drop in the pipe between the pump discharge and the evaporator inlet, and the expander discharge and the condenser inlet using double sensor measurements, and thermal power balance between the hot and cold streams in the PHEs. The measured values were adjusted in the range of the sensors for each data set if needed, to reconcile them with the physical constraints. The second step was performed by adding the expander oil to the calculations of the working fluid properties considering the refrigerant solubility and mixture properties calculations. The reconciliation was performed on the PHEs only to ensure the reliability of the experimental data if oil was considered, yet the impact of the oil on the expander performance or modeling of the components was not assessed. The first approach of the data reconciliation he used seems controversial since the accuracy of sensors can be reported as the measurement uncertainties instead of adjusting the data. Instead, the latter approach is used in this paper to calculate the OCR and the reconciled performance of the components of the ORC system.

In 2021, Dawo et al. [109] tested a micro-scale ORC unit consisted of a 1 kW scroll expander and diaphragm pump with R1224yd(Z), R1233zd(E), R1336mzz(Z), and R245fa. They aimed to study the drop-in fluids for R245fa and to investigate their interaction with lubricants. They observed the thermal imbalance in their evaporator, especially in low superheating degrees. Therefore, they used the simple oil model neglecting the refrigerant miscibility model, the mixture model considering the same refrigerant miscibility model used by Dickes [29], and they

proposed a new miscibility model as well. Their model needed to be tuned using a separate experimental procedure for each working fluid, then the tuned model could be applied to calculate the thermal load of the cold stream of the evaporator considering the lubricant-refrigerant mixture properties. Despite simplicity of their model and good accuracy to reconcile the evaporator data, their model cannot be tuned from the reconciliation of the experimental data directly and needs their experimental procedure to tune the model for the specific working fluid. These three mixture models are described with more details in the subsection 5.3.2.

The final aim of this chapter is to provide a theoretical approach to assess the impact of the expander oil on the performance of a micro-scale ORC system and its main components. Hence, the main novelties rely on:

- A theoretical approach to calculate both the OCR and evaporator thermal losses in a micro-scale ORC system.
- The impact of the lubricant oil on the performance degradation of the PHEs of the ORC unit using lubricant-refrigerant properties considering the refrigerant miscibility models.
- The impact of the lubricant oil on the mechanical and volumetric efficiencies of the scroll expander.

In this chapter, a theoretical method is adopted to resolve the unphysical observation in the experimental data by considering the impact of the expander lubricant oil on the working fluid transport properties. This approach can be adopted in similar systems to reconcile the raw experimental data with the calculated OCR to have a more realistic estimation of the system performance considering the oil entrainment. In this work, the thermal balance between the hot and cold streams of the PHEs is considered as the raw experimental data that did not respect the physical conditions. Hence, the lubricant-mixture properties are considered to modify the raw experimental data until the physical conditions are

met. However, different systems working in various conditions would require a different or additional set of physical criteria to modify the experimental data. Yet, the same approach can be adopted to minimize the unphysical values using the expander lubricant oil entrainment analysis. The experimental procedure and the experimental data presented in the chapter Experimental investigations are used here to study the impact of the lubricant oil on the performance of the scroll expander, evaporator, and condenser of the ORC system.

## 5.2 **Experimental raw data analysis**

In this section, the raw data of the PHEs thermal load obtained experimentally are presented again and discussed further. It is noteworthy that initially the diathermic oil flow rate is estimated based on the model presented on page 33, then the raw data are analyzed to ensure that the measured data are physically consistent and meaningful.

The thermal balance of the evaporator and the condenser of the ORC unit are illustrated in Figure 5-2. The uncertainty of the measurements of the thermal loads is calculated using two sources of uncertainty as presented in Appendix (B). The measurement uncertainties of the cold and hot streams of the condenser do not cover each other showing that the deviation is not due to the measurement inaccuracies, but other reasons are at work. In general, the possible causes of the deviation in the thermal load are:

- Heat loss of the PHEs to the ambient.
- Miscalculation of the thermodynamic properties of R134a in the gas phase due to the presence of the lubricant oil.

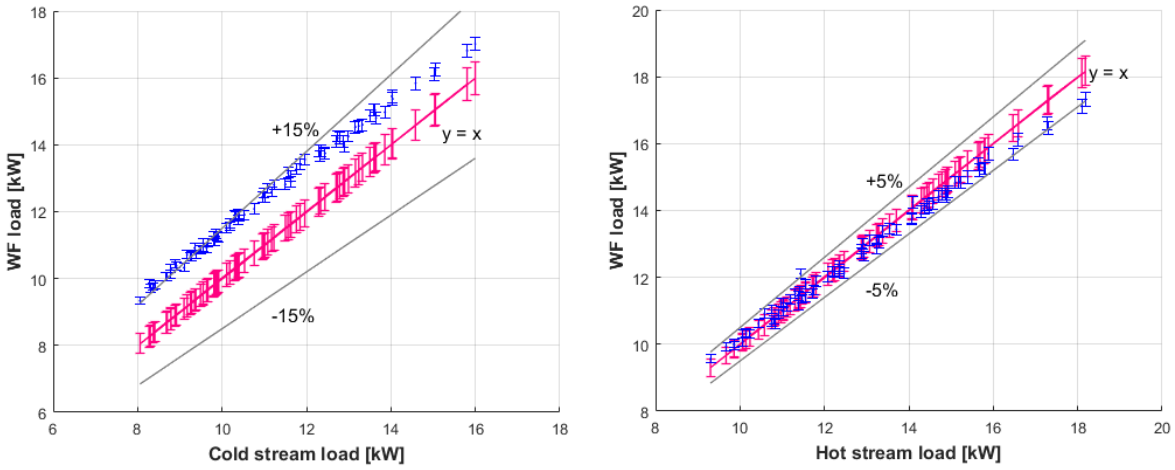


Figure 5-2. The thermal balance between the hot and cold streams of the condenser (left) and evaporator (right)

Ideally, in any heat exchanger (HE) the thermal load of the two streams must be equal. However, the thermal load of the hot stream is always higher than the one of the cold stream in practice due to the unavoidable thermal losses to the ambient. The deviation between the hot and the cold stream thermal loads is higher in case of poor insulation or higher working temperatures. Therefore, for the ORC unit under investigation, it is expected that the evaporator shows considerably higher thermal deviation compared to the condenser since the diathermic oil inlet temperature is between 120-150°C, while the condenser inlet temperature is in the range of 10-20°C very close to the ambient temperature. Nevertheless, concerning the raw data obtained experimentally, an opposite occurs as clearly evident in Figure 5-2. Indeed, here the thermal load deviation in the evaporator is lower than the deviation at the condenser.

In an ORC system, the higher the ratio of the expander lubricant oil mass to the refrigerant mass the higher the influence on the performance. However, the impact of the oil entrainment may not be tangible at some working conditions even at micro-to-small scales. For example, when the vapor speed in the pipes and the HEs is low, the oil can accumulate and affect the heat transfer, or the pressure drop. At

high vapor speeds, oil blows with the high-speed gas and is dragged away from the HE walls. In the ORC unit under investigation, the lubricant oil caused instability in the evaporator, where the cold stream (refrigerant) enters from the bottom and the hot stream (diathermic oil) enters from the top that is the recommended piping for vertical HEs, especially at low flow rates. When the inlets of the hot and the cold streams were reversed, this issue was resolved. Therefore, it is suggested to consider such implications for the PHEs when the oil entrainment is expected.

Therefore, depending on the system size, the initial refrigerant charge, and the vapor speed in the components, the impact of the lubricant oil can be negligible or significant, exactly defined or stochastic. In general, the lubricant effect can be observed when the following conditions occur:

- low refrigerant initial mass charge,
- gas or two-phase flows,
- low vapor speed in pipes or HEs,
- upward gas or two-phase flow.

In this chapter, a theoretical method is adopted to assess the impact of the oil entrainment on the thermal balance of the PHEs in an ORC system using the correct calculation of thermodynamic properties of the working fluid. To this end, the raw experimental data previously shown is modified based on a two-step data reconciliation approach in the following. At the first step, the lubricant-R134a mixture properties are considered in the PHEs performance calculations; then, the contribution of the heat losses in the evaporator is included in the second step.

Regarding the first step, the oil circulation rate (OCR) needs to be assessed before the calculation of the lubricant-R134a mixture properties. The straightforward method to find the exact OCR during system operations to physically take a sample from a location where the mixture is in the liquid phase. The sample tank must be

weighed before and after the sampling procedure to obtain the weight of the mixture. Then, the refrigerant evaporates and only the oil remains in the tank by exposing the sample to the ambient pressure. Using the obtained oil mass and the lubricant-refrigerant mixture mass, the OCR can be calculated. Another way consists of isolating one component or a certain length of the pipes using sudden valve closure during the system operation. The so-called *hold-up* liquid can be weighted like the procedure described above for the sampling method to find the exact OCR.

Apart from the experimental methods, the OCR cannot be obtained directly using the common measurements of the properties of the working fluid. Nevertheless, it may be captured indirectly using a data reconciliation approach that drives the experimental results to a physically consistent data set. In the following, the calculation of the OCR is performed based on the data reconciliation of the energy balance in the PHEs of the ORC test bench.

## 5.3 Description of the models

### 5.3.1 lubricant-refrigerant mixture

The lubricant oil is usually presented in ORC systems when a lubricated expander machine is adopted. Despite the lubricant can be separated from the mixture and redirected to the expander machine using an oil separation circuit, it is usually a costly option for such systems that their low cost is a determining factor in their marketing.

The key point to study the impact of the lubricant oil on an ORC system is finding the mixture properties in different system working conditions. The miscibility of the lubricant and the refrigerant was studied in the literature for the refrigeration systems, but it has been mostly neglected by the ORC community. If the lubricant

oil-refrigerant properties are modeled, their influence on the performance of the components of the system can be deduced.

The refrigerant is mixed with the expander lubricant oil with a specific fraction depending on the miscibility of the lubricant and the refrigerant. Hence, the lubricant-refrigerant mixture circulates in the ORC system. When the refrigerant is in two-phase, the lubricant remains in the liquid phase due to its considerably high boiling point. Therefore, the lubricant is enriched in the liquid mixture gradually as the vapor quality of the refrigerant increases resulting in a two-phase, two-component mixture as illustrated schematically in Figure 5-3. The components (lubricant and refrigerant) and the phases (liquid and gas) are appeared randomly showing the complex nature of a lubricant-refrigerant mixture.

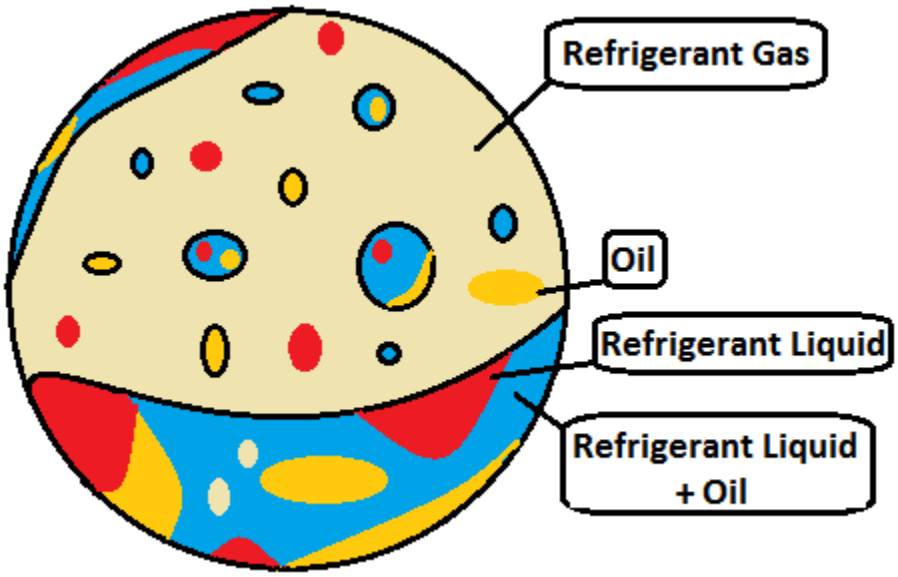


Figure 5-3. Schematic of the two-phase, two-component lubricant oil-refrigerant mixture in a channel cross-section

Since the amount of the lubricant is usually much lower than the refrigerant in the system, the stochastic nature of the mixture is often neglected. Therefore, it is

assumed that if any lubricant is presented, it is mixed with the liquid refrigerant. Hence, no pure lubricant is presented separated from the pure liquid refrigerant. In other words, the mixture state is the refrigerant gas-phase plus the liquid refrigerant and lubricant mixture, represented by the ivory and the blue phases in Figure 5-3.

This simplifying assumption is physically consistent due to the low mass fraction of the oil compared to the refrigerant resulting in a higher chance of being dissolved with the refrigerant. Hence, the main impact of the expander lubricant is the misinterpretation of the real state of the fluid as shown by Dickes [29]. The mixture mass flow rate is calculated as the following:

$$\dot{m}_t = \dot{m}_{ref,L} + \dot{m}_{ref,V} + \dot{m}_{oil} \tag{5-1}$$

The refrigerant miscibility indicates the ratio of the liquid refrigerant mass flow rate over the lubricant-refrigerant mixture mass flow rate as the following:

$$w_{ref} = \frac{\dot{m}_{ref,L}}{\dot{m}_{ref,L} + \dot{m}_{oil}} \tag{5-2}$$

The second effective parameter is the oil circulation rate (OCR) that is the oil mass flow rate over the total mass flow rate in the channel cross-section:

$$K_{oil} = \frac{\dot{m}_{oil}}{\dot{m}_{ref,L} + \dot{m}_{ref,V} + \dot{m}_{oil}} \tag{5-3}$$

reminding the definition of the vapor quality:

$$x = \frac{\dot{m}_{ref,V}}{\dot{m}_{ref,L} + \dot{m}_{ref,V}} \tag{5-4}$$

The three parameters in Eqs. (5-2), (5-3), and (5-4) are dependent on each other, so one can be calculated using the other two such as in the following:

$$x = \frac{1 - w_{ref} - K_{oil}}{1 - w_{ref} - K_{oil} + w_{ref} \cdot K_{oil}} \tag{5-5}$$

$$w_{ref} = \frac{1}{1 + (\frac{K_{oil}}{1 - K_{oil}})(\frac{1}{1 - x})} \quad (5\text{-}6)$$

The impact of lubricant on the mixture properties can be calculated using the previous equations. The properties of the R134a and PAG-SP10, the lubricant oil used in the experiment, are calculated using properties of the pure refrigerant from CoolProp [110] and lubricant properties calculated from the equations presented in Appendix (A).

- Mixture enthalpy

Enthalpy of any mixture can be calculated using the sum of the mass-weighted enthalpy of the components and the enthalpy change of the mixing process that is released or absorbed during the process due to the interaction among the substances or compounds forming the mixture:

$$h_{mix} = \Delta h_{mix} + \sum x_i \cdot h_i \quad (5\text{-}7)$$

In the case of the lubricant-refrigerant mixture in ORCs, the enthalpy of mixing ($\Delta h_{mix}$) is negligible meaning that the mixing is ideal, and the mole fraction of the pure substances is the same as the mixture. Hence, the mixture enthalpy can be simplified as in Eq. (5-8.

$$h_{mix} = \sum x_i \cdot h_i \quad (5\text{-}8)$$

Considering the two-phase, two-component state of the mixture, the definitions of the refrigerant miscibility, and that of the OCR, the lubricant-refrigerant mixture enthalpy can be calculated:

$$\dot{m}_t \cdot h_{mix} = \dot{m}_{ref,L} \cdot h_{ref,L} + \dot{m}_{ref,V} \cdot h_{ref,V} + \dot{m}_{oil} \cdot h_{oil} \quad (5\text{-}9)$$

$$h_{mix} = \frac{w_{ref} \cdot K_{oil}(1 - K_{oil})}{1 - w_{ref} - K_{oil} + w_{ref} \cdot K_{oil}} . h_{ref,L} + \frac{(1 - w_{ref} - K_{oil})(1 - K_{oil})}{1 - w_{ref} - K_{oil} + w_{ref} \cdot K_{oil}} h_{ref,V} + K_{oil} \cdot h_{oil} \quad (5\text{-}10)$$

Therefore, the mixture enthalpy can be calculated if the thermodynamic state of the mixture (temperature and pressure), $w_{ref}$ and $K_{oil}$ are known. Moreover, the enthalpy and the OCR of the liquid single-phase mixture can be simplified using the following equations:

$$h_{mix} = \frac{\dot{m}_{ref,L} \cdot h_{ref,L} + \dot{m}_{oil} \cdot h_{oil}}{\dot{m}_t} = w_{ref} \cdot h_{ref,L} + (1 - w_{ref}) h_{oil} \quad (5\text{-}11)$$

$$K_{oil} = 1 - w_{ref} \quad (5\text{-}12)$$

Hence, the properties of the liquid mixture are similar to the pure refrigerant due to the relatively low fraction of the lubricant compared to the refrigerant in the ORC systems; thus, it is assumed identical to the pure refrigerant liquid properties in this study.

On the contrary, as the vapor quality increases the impact of the oil entrainment on the fluid enthalpy is substantial and the calculated mixture enthalpy is lower than the pure refrigerant enthalpy as shown in Figure 5-4.

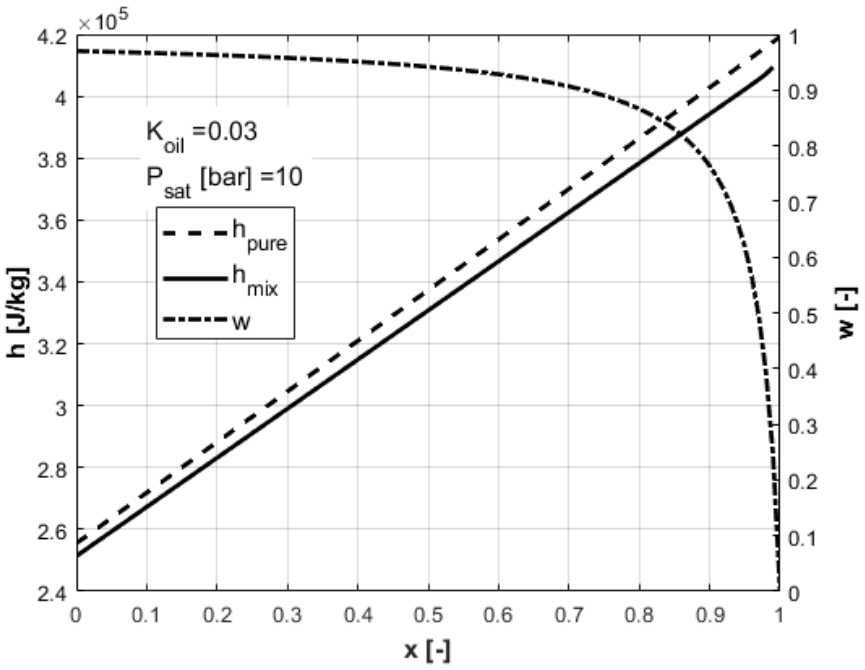


Figure 5-4. The calculated mixture enthalpy and pure R134a enthalpy by the vapor quality for a given saturation pressure and OCR

- Mixture density

The mixture density is an important parameter in the calculation of the refrigerant mass of the PHEs of the system and the calculations of the flow speed in the PHEs channels or the pipes. It can be calculated using a correction factor to the ideal mixture density:

$$\rho_{mix} = \frac{1}{K_\rho}\rho_{ideal} = \frac{1}{K_\rho}\left(\frac{\rho_{oil}}{1 + w_{ref}\left(\frac{\rho_{oil}}{\rho_{ref,L}} - 1\right)}\right) \tag{5-13}$$

The correction factor $K_\rho$ depends on the liquid temperature and composition. To calculate $K_\rho$ for the mixture of R134a and PAG oil, the experimental data presented in [111] are used. To this end, the genetic optimization algorithm is used to minimize an objective function that represents the difference between the calculated mixture density from Eq. (5-13) and the experimental data in the reference work in

the range of their data ($0.069 < w_{ref} < 0.832$ and $272\ K < T < 361\ K$). The results of the optimization led to $K_\rho = 0.9634$ for R134a-PAG mixture. The calculated density using the tuned model is presented versus the experimental values in Figure 5-5 showing a good agreement.

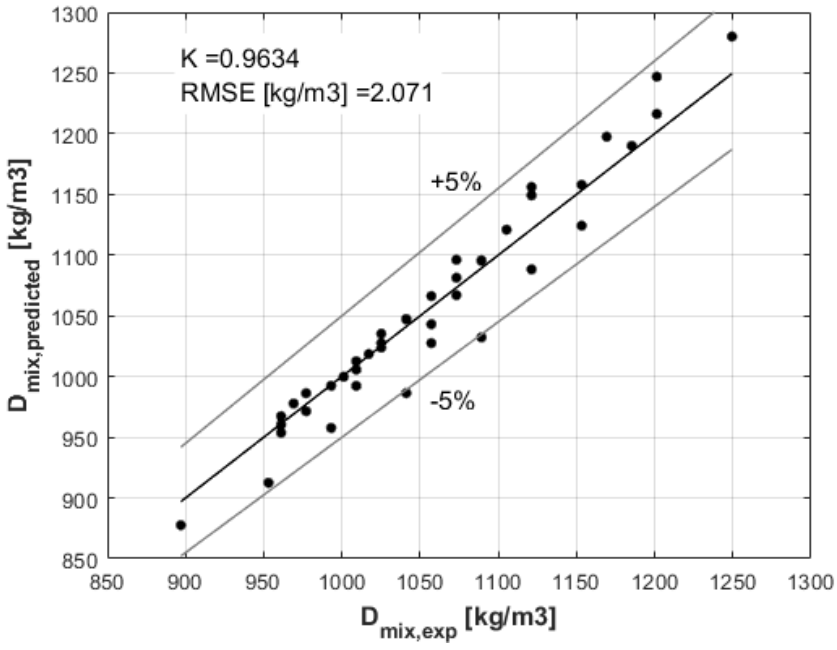


Figure 5-5. The calculated density of R134a-PAG oil mixture vs experimental data adapted from [112]

The mixture density calculated using Eq. (5-13) is presented in Figure 5-6 different refrigerant miscibility percent ($w_{ref}$ %) with temperature. It is evident that the difference between the mixture and the pure fluids densities is more sensitive to the temperature when the refrigerant miscibility is lower, and the mixture density is insensitive to the refrigerant miscibility at the temperature of about 80 °C.

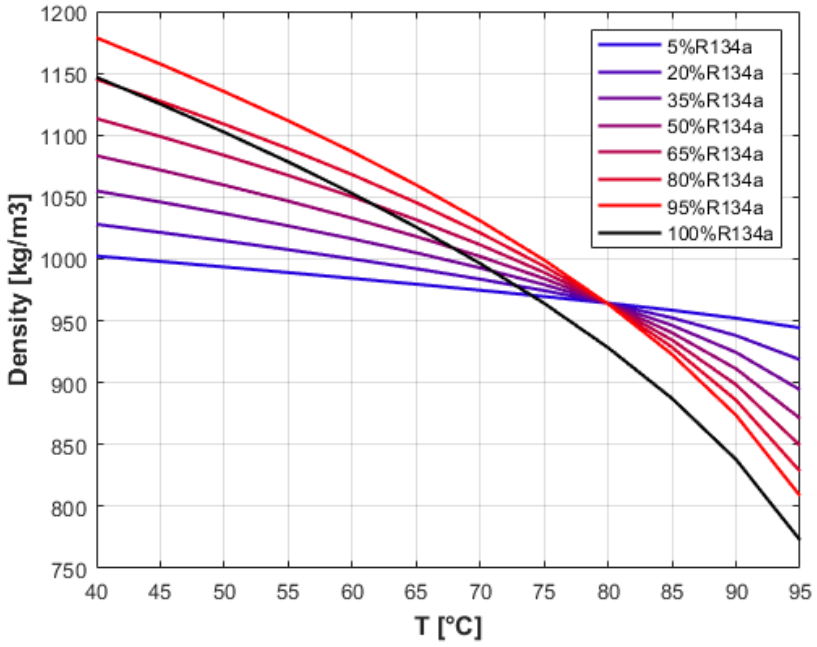


Figure 5-6. R134a-PAG mixture density with temperature for different refrigerant miscibility percent ($w_{ref}$%)

The other properties of the lubricant-refrigerant mixture such as the mixture kinematic viscosity, the specific heat, the thermal conductivity, and the surface tension are provided in Appendix (A).

### 5.3.2 Lubricant-refrigerant models

As mentioned in section 5.1, the lubricant-refrigerant mixture was modeled in three ways in the literature. These models are presented hereunder.

#### 5.3.2.1 Based on the weighting coefficient model

This basic model neglects the refrigerant miscibility and modifies the calculations of the thermal load based on a weighting coefficient as presented by Feng et al. [107] and Yang et al. [108] as the following:

$$\dot{Q}_{rec} = \dot{m}_{ref}\left(h_{out,ref} - h_{in,ref}\right)\delta + \dot{m}_{oil} \cdot C_{p,oil}(T_{out} - T_{in}) \quad (5\text{-}14)$$

where subscripts in and out refer to inlet and outlet of the refrigerant in a heat exchanger that its thermal load balance needs to be reconciled, and $\delta$ is the weighting coefficient to be obtained to fit the thermal load of the hot and cold streams. It was found 97.8% in [107,108].

#### 5.3.2.2 Based on Grebner and Crawford's model

This empirical model considers refrigerant miscibility defined in Eq. (5-2) that depends on the temperature and pressure of the mixture and saturated temperature of the pure refrigerant. The refrigerant miscibility is calculated implicitly using empirical correlations presented by Grebner and Crawford [111] that requires seven empirical coefficients, which are reported in Table 5-1. This model was used to reconcile the experimental data in [29,109].

$$\theta = (1 - w_{ref})(A + BP) \quad (5\text{-}15)$$

$$\theta = \frac{T - T_{sat}(P)}{T_{sat}(P)} \quad (5\text{-}16)$$

$$A = x_1 + \frac{x_2}{{w_{ref}}^{0.5}} \quad (5\text{-}17)$$

$$B = x_3 + \frac{x_4}{{w_{ref}}^{0.5}} + \frac{x_5}{w_{ref}} + \frac{x_6}{{w_{ref}}^{1.5}} + \frac{x_7}{{w_{ref}}^{2}} \quad (5\text{-}18)$$

Table 5-1. Empirical coefficients of the miscibility model for R134a-PAG lubricant mixture adapted from [111]

| $x_1$ [-] | $x_2$ [-] | $x_3$ [$Pa^{-1}$] | $x_4$ [$Pa^{-1}$] | $x_5$ [$Pa^{-1}$] | $x_6$ [$Pa^{-1}$] | $x_7$ [$Pa^{-1}$] |
|---|---|---|---|---|---|---|
| $-7.1524667 \times 10^{-2}$ | $5.9851602 \times 10^{-2}$ | $2.4849483 \times 10^{-7}$ | $-4.3146787 \times 10^{-7}$ | $2.4660432 \times 10^{-7}$ | $-5.4479260 \times 10^{-8}$ | $4.3488114 \times 10^{-9}$ |

#### 5.3.2.3 Based on Raoult's law

This model considers refrigerant miscibility and presented in a recent paper in 2021 [109]. To tune this model, a separate test is needed. The lubricant-refrigerant mixture was injected into a tank, which its temperature and pressure were measured. Therefore, the OCR was known for each test. The refrigerant miscibility was calculated by calculating the vapor mass in the tank using Eq. (5-19) to calculate the refrigerant vapor quality in the tank.

$$m_{ref,V} = \frac{\forall_{tot} - m_{oil} \cdot v_{oil} - m_{ref} \cdot v_{ref,L}}{v_{ref,V} - v_{ref,L}} \tag{5-19}$$

Hence, the refrigerant miscibility can be calculated using Eq. (5-6). The calculated refrigerant miscibility in the tank was used to calculate the fitting parameter "c" in Eq. (5-20) for each working fluid, which is the extended version of Raoult's law.

$$P = x_{ref} \cdot P_{ref,sat} \cdot e^{\theta.c} \tag{5-20}$$

where $x_{ref}$ is the mole fraction of liquid refrigerant, $\theta$ is the dimensionless superheating degree defined as Eq. (5-16), and "c" is the fitting parameter. $x_{ref}$ can be calculated using the known refrigerant miscibility in the tank.

$$x_{ref} = \frac{\frac{w_{ref}}{M_{ref}}}{\frac{w_{ref}}{M_{ref}} + \frac{1 - w_{ref}}{M_{oil}}} \tag{5-21}$$

Therefore, the fitting parameter "c" can be found for a fluid to fit the calculated pressure from Eq. (5-20) with the measured pressure of the tank in different temperatures. This is also a disadvantage of this model since it cannot be tuned directly from the experimental data of an HE and needs a separated experimental procedure. The fitting coefficient is provided for R245fa, R1224yd(Z), R1233zd(E), and R1336mzz(Z) in the range of the temperature of 20-140°C in [109]. The

advantage of this model compared to the Grebner and Crawford model is that it needs one empirical coefficient only to tune the model.

### 5.3.3 Properties of R134a-PAG oil mixture

In this work, Grebner and Crawford model is used to calculate the refrigerant miscibility for R134a-PAG oil mixture since the coefficients of the model were available in [112]. The OCR ($K_{oil}$) is the only unknown variable needed to calculate the mixture enthalpy using Eq. (5-10). The presence of the lubricant leads to misinterpretation of the real state of the fluid. While in theory, the pure refrigerant is considered with no liquid phase even if it is slightly superheated, the mixture includes the same amount of oil mass traveling in the system with some refrigerant in the liquid phase that is remained dissolved in the oil. Therefore, the difference between the mixture temperature and saturation temperature of the pure refrigerant is considered as the *apparent superheating*.

It is evident from Figure 5-7 that the mixture temperature increases despite the vapor quality is between 0.9 and 1. Moreover, the refrigerant miscibility ($w_{ref}$) reduces as the quality increases showing that the oil is enriched in the mixture and more refrigerant is separated from the mixture and turned to the gas phase. For instance, at an approximate vapor quality of 0.97, the apparent superheating is about 1.3 K at $w_{ref}$=0.5 showing that half of the liquid mixture is oil and the other half is the refrigerant liquid. It can be concluded that the state of the fluid would be interpreted wrongly especially in low superheating degrees (below 5 K).

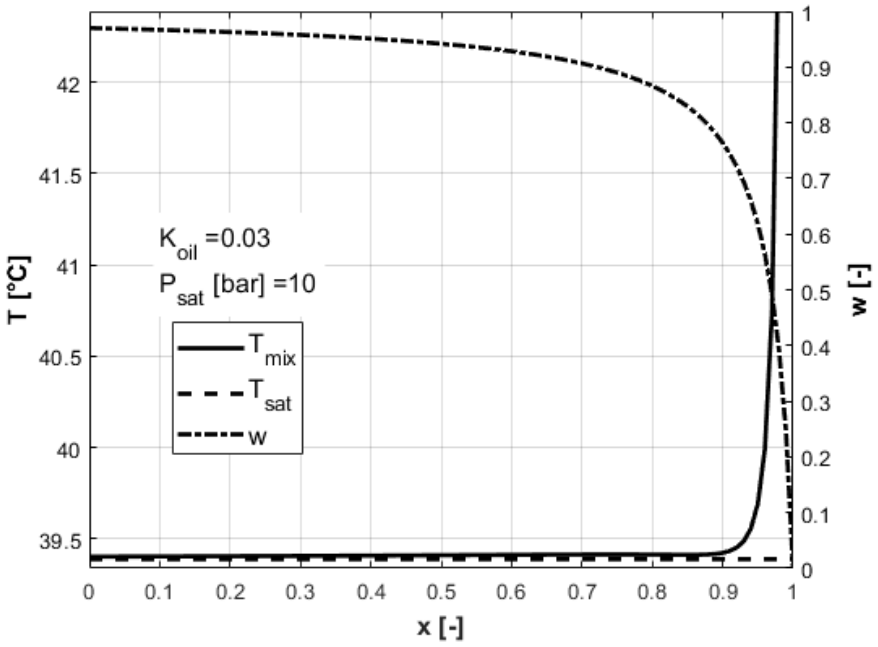


Figure 5-7. Apparent superheating and refrigerant solubility by the vapor quality for R134a-PAG oil mixture

It is evident from Figure 5-8 that in higher OCRs ($K_{oil}$), the mixture temperature increment starts at lower vapor qualities resulting in higher errors in the calculation of the properties of the mixture if the pure refrigerant is considered.

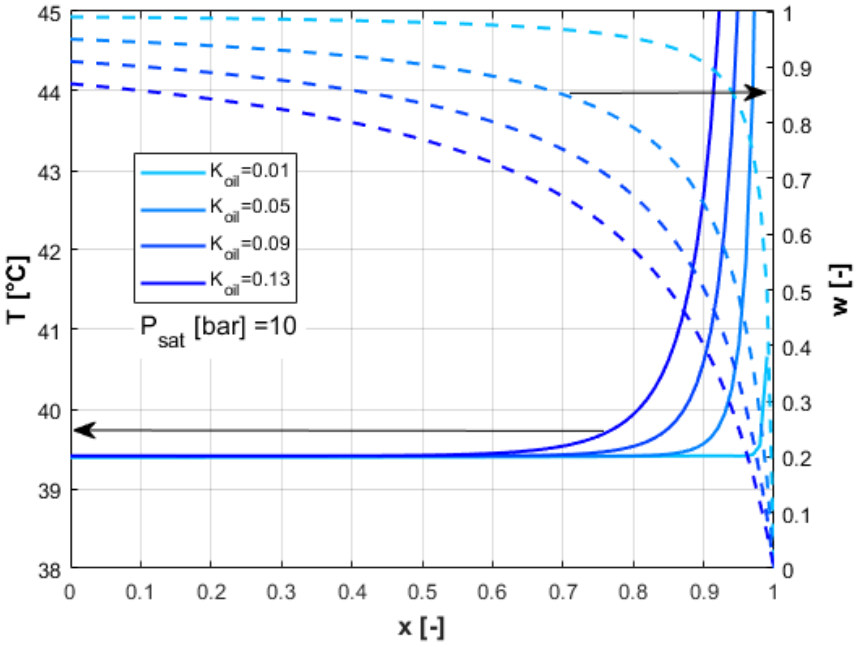


Figure 5-8. Impact of OCR on the apparent superheating and oil solubility by vapor quality for R134a-PAG oil mixture

In addition, the use of the pure refrigerant properties results in the wrong interpretation of the fluid state or its properties in low superheating degrees in relatively low OCRs as mentioned before, and it happens in all the conditions in high OCRs as illustrated in Figure 5-9. Moreover, the increment of the mixture temperature when the refrigerant is in the two-phase state affects the saturation properties of the fluid simultaneously. It results in variations of the temperature and pressure in both high-pressure and low-pressure sides of the ORC system and triggers instability issues in low superheating degrees or high OCRs.

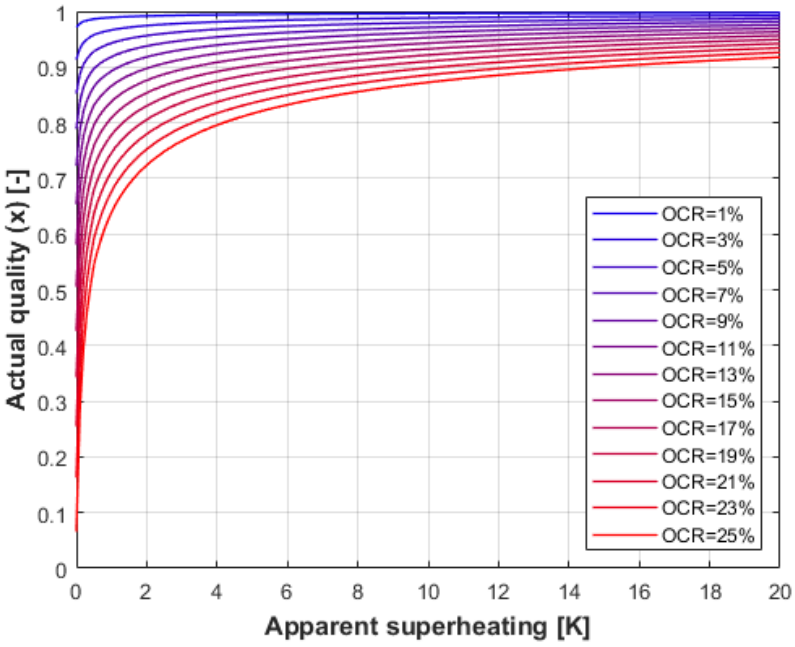


Figure 5-9. Actual quality by apparent superheating in different OCRs for R134a-PAG oil mixture

Isothermal lines in the p-h diagram for the lubricant oil-R134a mixture are shown in Figure 5-10. The mixture curves (solid lines) are very close to each other. Moreover, they show an opposite trend in comparison to that of the pure refrigerant (dashed lines), for which the enthalpy decreases as the pressure increases. Furthermore, a turning point is formed in the mixture curve after which the enthalpy reduces significantly with a relatively low increment of pressure. These trends are explained in two steps in the following:

- Increasing mixture enthalpy with pressure:

The mixture consists of the vapor refrigerant, the liquid refrigerant, and the lubricant oil. Looking at the p-h diagram of R134a, the enthalpy of the liquid increases slightly with the pressure at a fixed temperature, and the enthalpy of the gas increases as the pressure decreases. As can be seen in Figure 5-11, the refrigerant miscibility increases with the pressure meaning that some vapor is turned into

liquid. Therefore, the gas pressure is reduced resulting in an increment in its enthalpy. The mixture enthalpy that is the weighted sum of the liquid phases and the gas phase is increased by the pressure consequently. This trend is valid up to the point that the gas condensation is relatively low and the real vapor quality shown in Figure 5-11 does not change significantly and the refrigerant miscibility increases marginally.

- The turning point and the reducing mixture enthalpy via pressure:

At the turning point, the real vapor quality is reduced sharply in Figure 5-11 showing the refrigerant vapor is changing the phase to the refrigerant liquid considerably. Hence, the latent heat of the phase change is taken from the mixture enthalpy and its effect becomes superior to the increasing liquid and gas enthalpies explained previously resulting in the decrease of the mixture enthalpy as the trend of the pure fluid. Therefore, a turning point is formed that indicates the approximate location of the saturated condition of the mixture. In addition, the refrigerant miscibility begins to increase drastically in Figure 5-11 at this point confirming the increased rate of the vapor condensation.

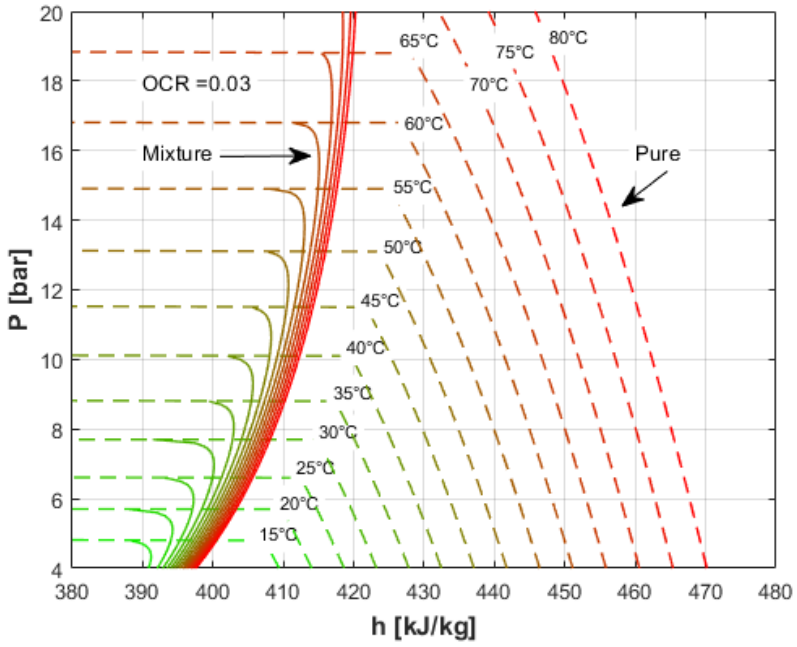


Figure 5-10. Isothermal plots on the p-h diagram for pure R134a (dashed lines) and R134a-lubricant mixtures for OCR = 0.03 (solid lines)

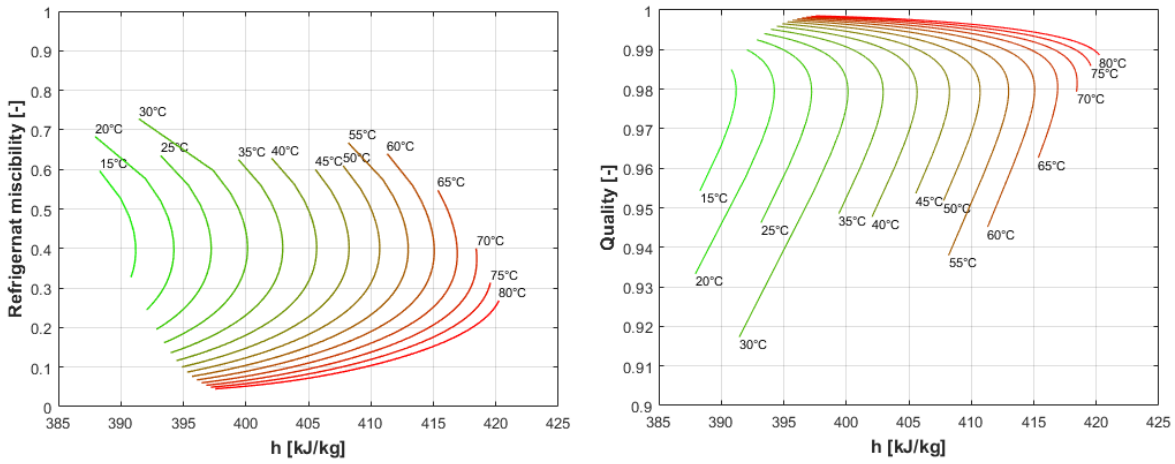


Figure 5-11. The refrigerant miscibility (left), and the vapor quality (right) versus the mixture enthalpy for OCR = 0.03

## 5.4 Results and discussion

The impact of the lubricant on the performance of the system is presented in this section. Using the above-presented models, the OCR is assessed based on the experimental raw data. Then the mixture properties are used to obtain the physically consistent experimental data. Finally, the impact of the lubricant-refrigerant mixture on the performance of the expander in terms of its mechanical and volumetric efficiencies is also assessed.

### 5.4.1 OCR calculation

In general, the presence of the lubricant oil is expected to reduce the capacity of a PHE when the phase change occurs inside. In a small-scale ORC system, at the outlet of the evaporator or the inlet of the condenser the working fluid is in its vapor phase and consequently, any change of the thermodynamics properties of the mixture reflects on the variation of the HE capacity.

Therefore, if the condenser is considered, the deviation between the thermal load of the hot and cold streams shown in Figure 5-2 decreases. The OCR can be obtained by minimizing the thermal load deviation of the hot and cold streams of the condenser, and the same OCR is applied to the evaporator assuming OCR remains the same in all components of the system in the steady-state conditions. Therefore, the OCR ($K_{oil}$) and the refrigerant miscibility ($w_{ref}$) are to be found. The latter can be calculated from Eqs. (5-15 to (5-18) using the experimental data, and the OCR remains an unknown parameter. The OCR is obtained by minimizing the following objective function for each experimental data point using the genetic algorithm:

$$f = \left( \frac{Q_{cd,ref,rec} - Q_{cd,water}}{Q_{cd,water}} \right)^2 \tag{5-22}$$

where $Q_{cd,ref,rec}$ is the thermal load of the refrigerant stream calculated using the mixture enthalpy, and $Q_{cd,water}$ is the thermal load of the water stream in the condenser. The minimum OCR is equal to zero meaning no lubricant is traveling in the system and the lubricant is trapped in the scroll expander; the maximum value of the OCR is equal to the uniform distribution of the lubricant mass in the total refrigerant mass as presented in Eq. (5-23).

$$0 < K_{oil} < \frac{m_{oil}}{m_{ref} + m_{oil}} \tag{5-23}$$

The maximum OCR for the studied ORC test bench is about 0.035 calculated using the measured initial mass charge of the system and the nominal lubricant oil charge of the scroll expander adapted from its datasheet. The obtained OCR is plotted for the experimental data points. The calculated OCR can be correlated to the shaft frequency as shown in Figure 5-12 using the following correlation with $R^2$ = 0.81 valid for the range of the experimental data:

$$OCR = 296.1e^{-0.0748\omega} - 437.5e^{-0.08017\omega} \tag{5-24}$$

The OCR shows a meaningful dependency on the expander shaft speed indicating that the expander lubricant oil blends more with the refrigerant at lower shaft speeds since the internal leakage flow increases as the shaft speed decreases. In contrast with the expanders, it was observed experimentally in [99] that the OCR increased almost linearly with the rotary volumetric compressor frequency. Hence, the internal leakages increase in low shaft speeds in compressors that means the reduction of their volumetric efficiency.

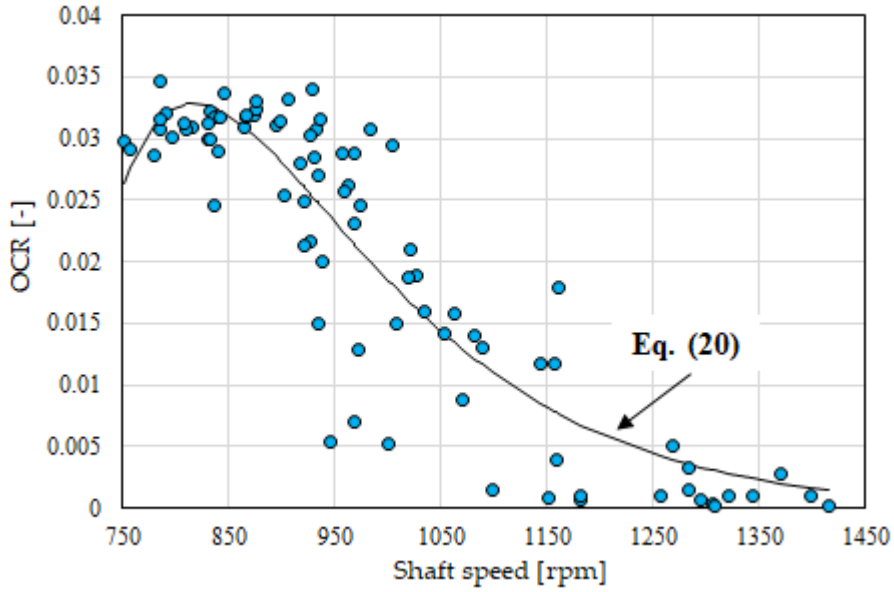


Figure 5-12. Calculated OCR with expander shaft speed for the experimental data

To better appreciate the trend of the internal leakages with the shaft speed, the expander volumetric efficiency, usually called the filling factor is considered. The filling factor is defined as the ratio between the measured expander flow rate and the expander theoretical flow rate as in Eq. (5-25) and it is expected to have the values above unity.

$$FF_{exp} = \frac{\dot{V}_{meas}}{\dot{V}_{th}} = 1 + \frac{\dot{V}_{leak}}{\dot{V}_{th}} = \frac{\dot{m}_{ref}/\rho_{su,exp}}{N_{exp} \cdot SV_{comp}/(60BVR)} \quad (5\text{-}25)$$

When $FF_{exp} < 1$, the flow rate is lower than the ideal one since the expansion chambers are not filled during the machine rotation; when $FF_{exp} = 1$ the leakages in the interstices between the rotor and the stator are zero and the whole fluid expands in the chambers; finally, if $FF_{exp} > 1$, a part of the flow rate reaches the discharge port through the interstices and does not contribute to the power generation.

Figure 5-13 reports the trend of the filling factor with the expander shaft speed. The filling factor decreases almost linearly with the expander shaft speed indicating that the internal leakages reduce at higher shaft speeds. Therefore, both the filling factor

and the OCR reduce as the internal leakages decrease; hence, the expander lubricant oil is remained in the expander and is less mixed with the refrigerant.

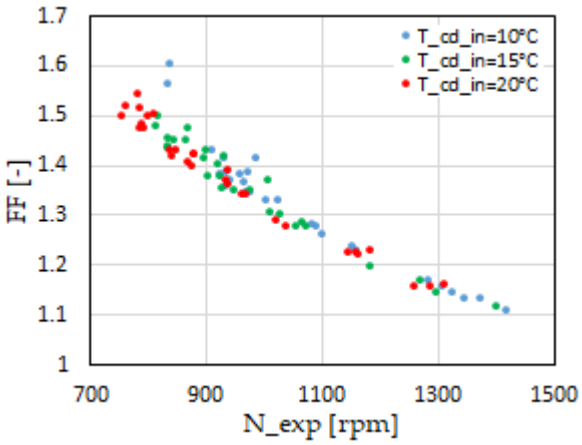


Figure 5-13. Expander filling factor with expander shaft speed using the experimental data (colored by the condenser inlet temperature set on the chiller)

### 5.4.2 Reconciled data analysis

Once the OCR has been assessed, the thermal performance of the evaporator and the condenser of the ORC unit under investigation is calculated using the mixture properties as reported in Figure 5-14. The deviation of the thermal load of the streams in the condenser is minimized for all data points using the reconciled data, but the discrepancy is grown in the evaporator as expected.

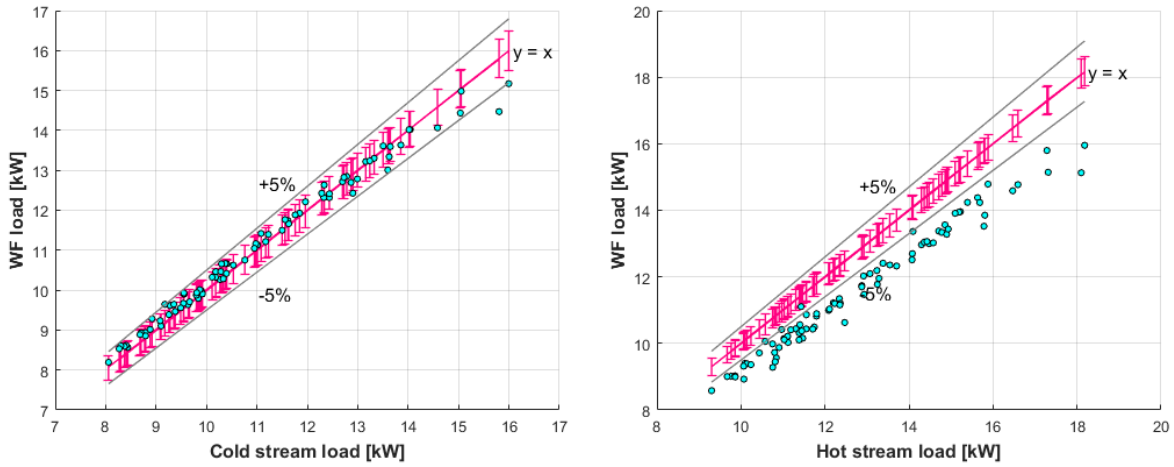


Figure 5-14. Condenser (left) and evaporator (right) thermal balance using oil-refrigerant mixture properties

The thermal load deviation of the streams in the evaporator that appears after the data reconciliation is due to the evaporator thermal losses from the insulation box and the pipes between the temperature sensors and evaporator inlet and outlet ports. Such losses are estimated considering the difference between the evaporator and the pipe wall temperatures and the ambient temperature for each data point according to Eq. (5-26):

$$Q_{waste,ev,i} = (U \cdot A)_i (T_{wall,i} - T_{amb,i}) \tag{5-26}$$

The wall temperature ($T_{wall,i}$) is assumed equal to the average temperature of the evaporator hot and cold streams:

$$T_{wall,i} = \frac{1}{4}\left(T_{oil,in} + T_{oil,out} + T_{ref,in} + T_{ref,out}\right)_i \tag{5-27}$$

The "*U.A*" is assumed to be a function of the difference between wall temperature and ambient temperature using a power-law expression:

$$UA_i = a\left[1 + \left(T_{wall,i} - T_{amb,i}\right)^b\right] \tag{5-28}$$

The coefficients "$a$" and "$b$" are found using the minimization of the objective function according to Eq. (5-29):

$$f = \sum_{i=1}^{n} \left( a \left[ 1 + \left( T_{wall,i} - T_{amb,i} \right)^{b} \right] \left( T_{wall,i} - T_{amb,i} \right) - \left( Q_{oil.i} - Q_{ref,i} \right) \right)^{2} \quad (5\text{-}29)$$

Based on this procedure, "$a$" and "$b$" are found 2 and 0.5, respectively. Therefore, the evaporator waste heat is calculated for all the experimental data points. Figure 5-15 shows the modified evaporator thermal balance considering both the lubricant-R134a mixture properties and the waste heat above discussed. As evident, by including the thermal losses into the model the deviation between the two streams decreases significantly.

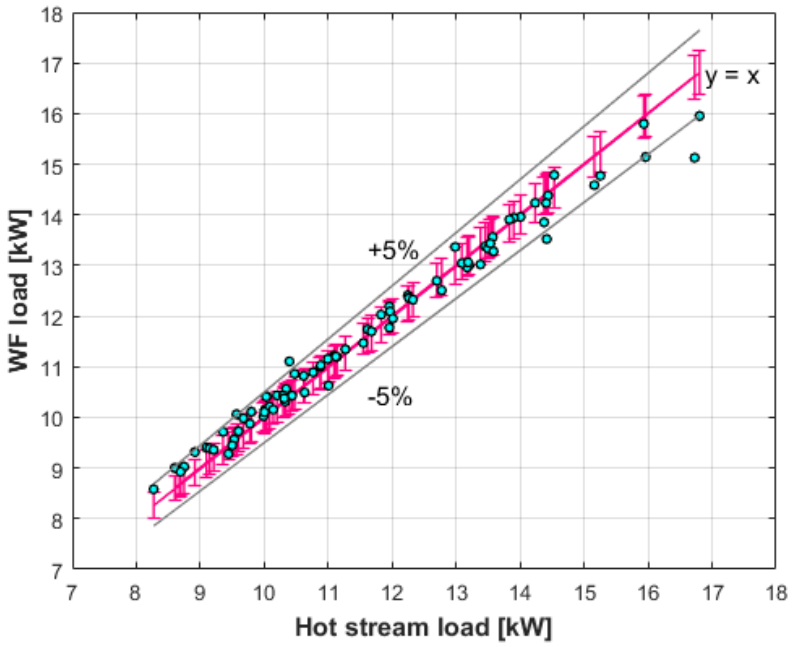


Figure 5-15. Evaporator thermal balance using mixture properties and considering the simulated waste heat

Figure 5-16 shows the calculated "$U.A$" of the diathermic oil stream waste heat with the temperature difference between the evaporator wall and the ambient.

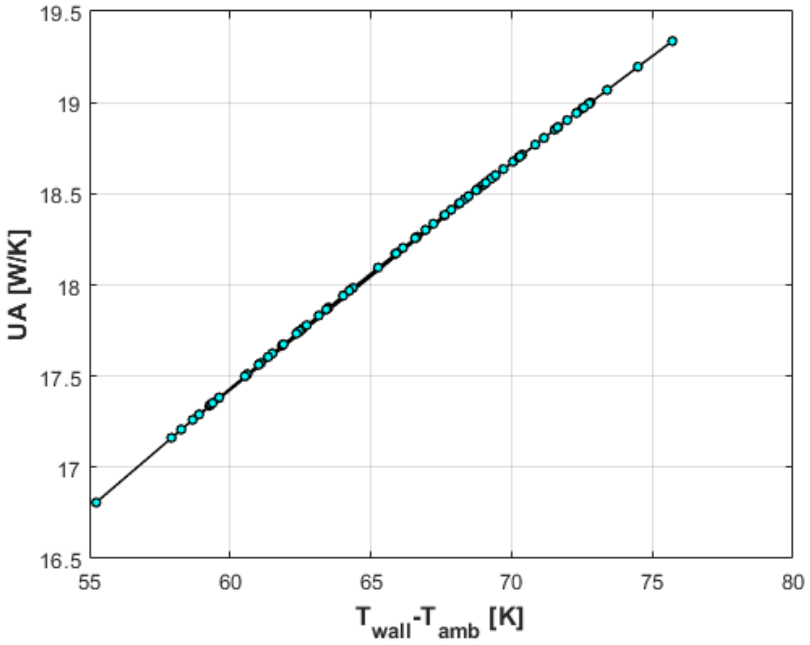


Figure 5-16. The calculated U.A of the evaporator thermal loss by the temperature difference between the evaporator wall and ambient

### 5.4.3 Impact of the lubricant on the PHEs

The capacity loss of a heat exchanger due to the oil entrainment is here defined as in Eq. (26):

$$Capacity\ loss = \frac{\dot{Q}_{pure} - \dot{Q}_{rec}}{\dot{Q}_{pure}} \times 100 \tag{5-30}$$

The capacity loss at the evaporator means that the system efficiency is penalized for a given produced shaft power. The relative thermal capacity losses of the evaporator and the condenser are presented in Figure 5-17. As can be noticed, the oil entrainment affects the PHEs performance more severely in lower refrigerant mass flow rates thus showing its impact, especially at lower thermal power. For this reason, oil entrainment is more important when the system is operating in low power production mode.

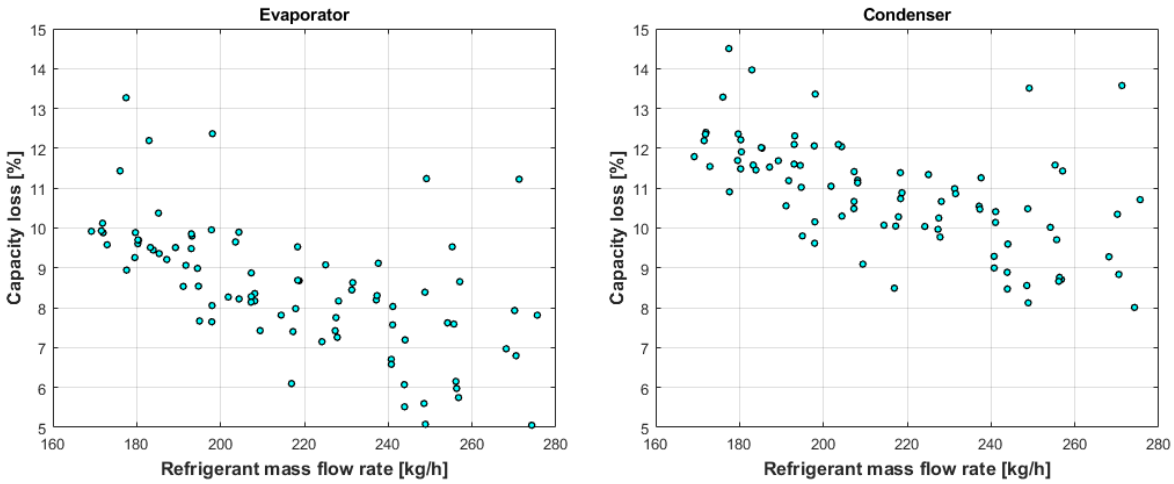


Figure 5-17. Evaporator and condenser capacity loss due to the lubricant oil entrainment in different refrigerant mass flow rates

Moreover, the lubricant affects condenser performance more than the evaporator one. This is consistent with the convection modes: in the evaporator bubbling mixes the lubricant oil, reducing the thermal resistance due to the oil film on the heat exchange surface; in the condenser instead, the oil forms a film on the heat exchange surface. This point is further investigated in the following. The impact of the lubricant on the performance of an evaporator for a given OCR, working pressure, and inlet subcooling degree, is presented in Figure 5-18 for different outlet superheating degrees. In particular, the difference between the specific power using pure R134a and that using lubricant-R134a mixture model increases with superheating degree. In other words, the lubricant impacts the evaporator performance more severely in higher superheating degrees, in which the flow is dried out and the oil covers a larger surface area due to the absence of the bubbles.

These numerical results are verified experimentally in Figure 5-18 by calculating the evaporator capacity loss with superheating degrees, using an average value for each group. Despite the OCR is not fixed in the experiments, the average capacity loss increases indicating that the difference between the evaporator thermal power using the pure R134a and the mixture is increased as well.

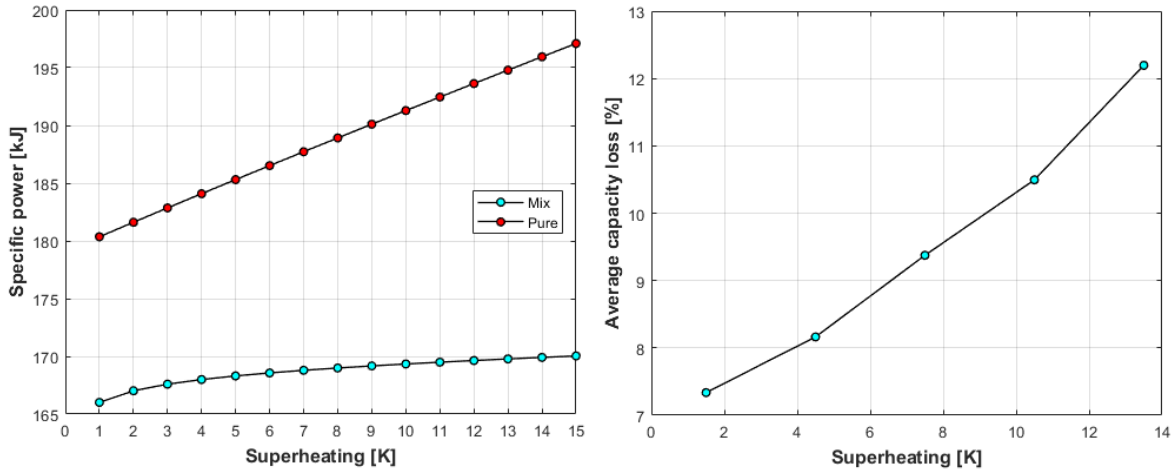


Figure 5-18. The specific power in an evaporator for pure and mixture models in different superheating degrees (left) for OCR = 0.031, and the average of the evaporator capacity loss using the experimental data (right) for the average OCR = 0.031

The presence of the lubricant also affects the calculations of the system mass charge due to the changes in the calculated mass density. The mass charge of a system is particularly important since not only it has economic and environmental impacts, but it also affects the superheating and subcooling degrees in the evaporator and the condenser and consequently, the system's overall performance [113]. In the literature, the mass-sensitive modeling of ORC systems was performed in several studies considering the system initial mass charge as the system boundary and the mass distribution in the system as the result [28,31].

To show the impact of the lubricant oil on such mass-sensitive modeling, the evaporator mass is calculated in the following for a given inlet and outlet working conditions using pure and mixture properties. To this end, the evaporator length is divided into several cells assuming that the heat flux is uniform in the liquid, two-phase, and vapor zones and neglecting the pressure drops. The enthalpy of each node is calculated using the previous node enthalpy and the heat flux. Then, the average cell density is calculated using the cell enthalpy and pressure, and the cell mass is calculated using Eq. (5-31).

$$dm = \rho_{avg} \cdot A_c \cdot dx \cdot n_{ch} \tag{5-31}$$

where $n_{ch}$ is the number of the channels of the evaporator that is considered equal to half the number of the evaporator plates. In the calculation of the cell density in the two-phase zone, the void fraction (*VF*) is used that considers the different speeds between the gas phase and the liquid phase in a channel. The definition of the *VF* and different *VF* models were presented in the chapter Modeling of the ORC system components. For the analysis, Zivi's correlation [93] presented in Appendix (E) is used.

In the case of the lubricant-refrigerant mixture, the liquid density in the subcooled zone or the two-phase zone calculations are performed using the presented equations. The results showed in Figure 5-19 reveal the significant impact of the evaporator mass calculation if the oil is considered, which is about 6.5% higher. A similar effect presents for the condenser and the pipes; hence, the overall system mass charge and its distribution are affected considerably by the oil entrainment and it must be considered if OCR is measured or calculated.

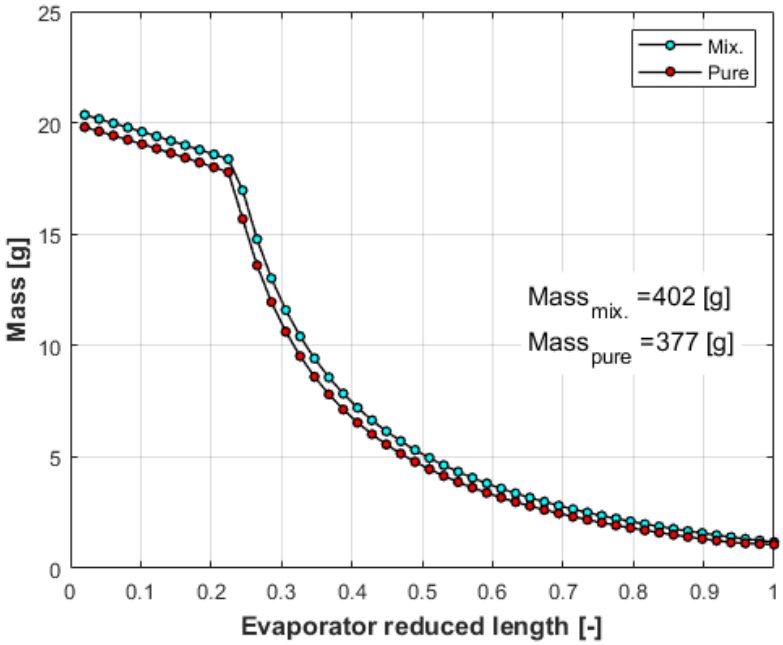


Figure 5-19. Evaporator mass calculation using pure and mixture properties for a given inlet subcooling and outlet superheating degrees and OCR = 0.03

### 5.4.4 Impact of the lubricant on the expander

The impact of the oil entrainment on the performance of the expander is also assessed. Roughly, at the suction and the discharge of the scroll expander the lubricant mass flow rate is the same. In general, the expander suction and discharge thermodynamic states are determined using the measured temperature and pressure. In the case of the expander, both the suction and discharge are in the gas phase and the impact of the oil is considered at the same time. Therefore, the oil entrainment has an impact on the expander mechanical efficiency calculated according to Eq. (5-32):

$$\eta_{mech,exp} = \frac{\dot{W}_{sh}}{\dot{W}_{th}} \times 100 = \frac{2\pi/60N \cdot \tau}{\dot{m}(h_{su} - h_{dis})} \times 100 \quad (5\text{-}32)$$

Figure 5-20 reports the impact of the lubricant oil on the expander mechanical efficiency, which is significantly reduced if the reconciled data using lubricant-

refrigerant mixture thermodynamic properties are considered. Indeed, for the same shaft power, the calculated thermal power of the expander is increased, and consequently, the mechanical efficiency decreases.

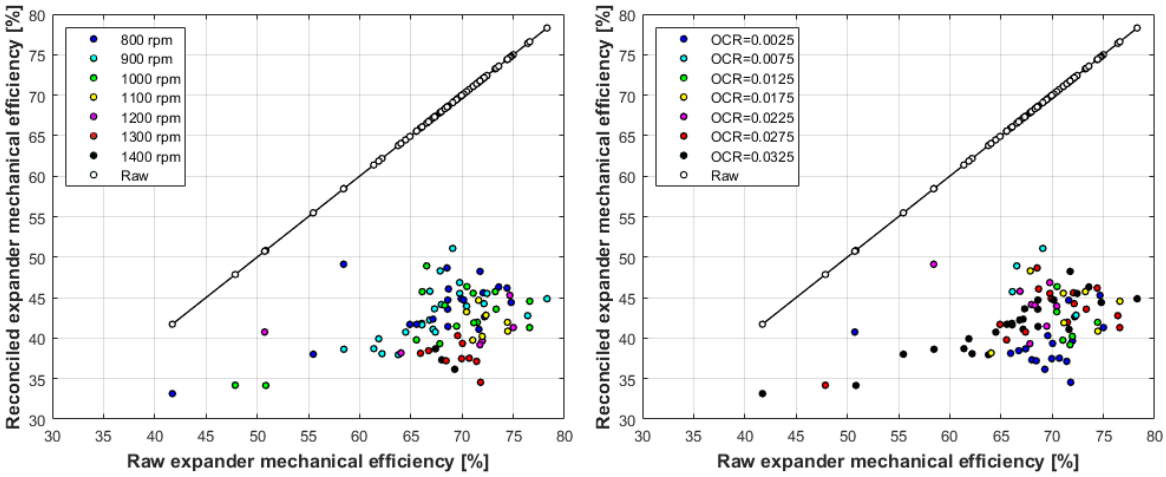


Figure 5-20. Expander mechanical efficiency for raw experimental data vs reconciled experimental data colored by shaft speed (left) and OCR (right)

The density of the lubricant-refrigerant mixture at the suction of the expander also affects the expander filling factor presented in Eq. (3-21). To this end, the two-component, two-phase mixture density is calculated using the lubricant-liquid refrigerant density according to Eq. (5-13), and the calculated real vapor quality using Eq. (5-5). Hence, the density of the mixture at the expander suction is calculated as:

$$\rho_{su,exp} = \rho_{mix,l} + x_{mix}\left(\rho_{pure,g} - \rho_{mix,l}\right) \tag{5-33}$$

The results of the expander filling factor using the raw experimental data and the reconciled data are presented in Figure 5-21. As can be noticed, if the lubricant-refrigerant mixture properties are considered in the calculations, the calculated filling factor is lower, especially at lower shaft speeds. The lower is the filling factor

the better the volumetric performance; hence, unlike the mechanical efficiency, the volumetric performance of the expander is improved if oil entrainment is considered.

As previously discussed, the internal leakages are lower at higher shaft speeds and the OCR is lower as well. The lower filling factor with the lubricant-refrigerant mixture indicates that the expander internal leakage is limited keeping the filling factor below 1.3 approximately, unlike its evaluation using the raw data that results in more than 60% of the intake gas as the internal leakage. Therefore, in case of unexpectedly high filling factors such as the data reported in a previous study [20], which despite making use of the same kind of expander of the present investigation reported a filling factor in the range 2-10 with R245fa as the working fluid, it may be related to the oil entrainment in the ORC system.

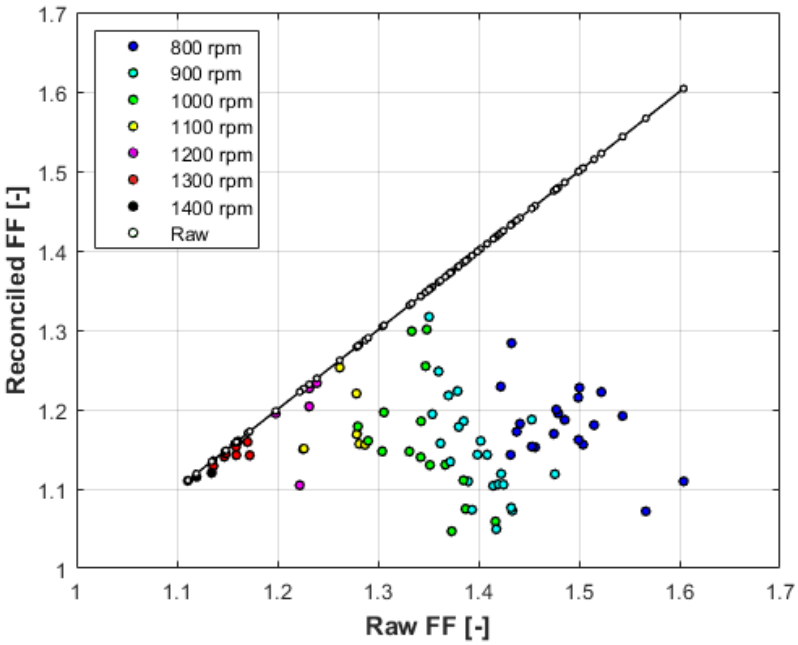


Figure 5-21. Reconciled expander filling factor vs raw expander filing factor colored by shaft speed

## 5.5 Summary and conclusions

The impact of the expander lubricant oil on the performance of the heat exchangers and the scroll expander of a micro-scale ORC unit is investigated in this chapter. The oil circulation rate (OCR) is calculated using a theoretical and numerical method for each experimental data set instead of direct measurements. Then, the properties of the lubricant-refrigerant mixture are considered to investigate the impact of the presented of the lubricant in different system working conditions. Results showed that the impact of lubricant oil is not negligible in micro-scale ORC systems unlike what is usually assumed in the literature.

Both the OCR and the expander filling factor are strongly associated with the expander shaft speed. At higher shaft speeds, the expander volumetric efficiency is improved indicating lower internal leakages, and the calculated OCR is reduced accordingly. This finding is in contrast with the HVAC system studies, in which the OCR and the volumetric efficiency are penalized at higher shaft speeds of the volumetric compressor. On the contrary at lower pressure ratios, in which the expander works at lower shaft speeds, high leakages occur. Therefore, in micro-to-small-scale ORC systems, low-cost oil separator systems are recommended to avoid further degradation of the system performance, or oil-free expander devices are to be preferred to avoid any penalization of their mechanical and volumetric performances.

## 5.6 **Nomenclature**

| | |
|---|---|
| $\dot{m}$ | mass flow rate [kg/s] |
| $\dot{W}$ | Power (work) [W] |
| $\dot{Q}$ | Power (heat) [W] |
| $x$ | vapor quality [-] |
| $x_i$ | mole fraction [-] |
| $x_{ref}$ | refrigerant liquid mole fraction [-] |
| S | slip ratio [-] |
| N | shaft speed [rpm] |
| T | temperature [K] |
| h | enthalpy [J/kg] |
| $C_p$ | specific heat [ J $kg^{-1}$ $K^{-1}$] |
| w | refrigerant miscibility [-] |
| $A_c$ | cross-sectional area [$m^2$] |
| A | Area [$m^2$] |
| D | diameter [m] |
| f | friction factor [-] |
| v | velocity [m/s] |
| $n_{ch}$ | Number of Channels |
| M | molar mass [kg/kmol] |

*Greek symbols*

| | |
|---|---|
| θ | non-dimensional superheating [-] |
| $\omega$ | shaft speed [Hz] |
| $\delta$ | weighting coefficient [-] |

*Subscripts and superscripts*

| | |
|---|---|
| sat | saturated |
| cal | calculated |
| exp | expander |
| rec | reconciled |
| su | suction |
| dis | discharge |
| meas | measured |
| sh | shaft |
| avg | average |
| V | vapor phase |
| L | liquid phase |
| mix | mixture |
| leak | leakage |
| ev | evaporator |
| t | total |
| th | theoretical |
| ref | refrigerant |
| cd | condenser |
| comp | compressor |
| amb | ambient |

*Acronyms*

| | |
|---|---|
| VF | Void Fraction [-] |
| FF | Filling Factor [-] |

| | |
|---|---|
| WF | Working Fluid |
| PR | Pressure Ratio [-] |
| BVR | Built-in Volume Ratio [-] |
| rpm | rotations per minute |
| SV | Swept Volume [l/rev] |
| HVAC | Heating, Ventilation, Air Conditioning |
| WHR | Waste Heat Recovery |
| ORC | Organic Rankine Cycle |
| lpm | liters per minute |
| CHTC | Convective Heat Transfer Coefficient |
| OCR ($K_{oil}$) | Oil Circulation Rate [-] |
| (P)HE | (Plate) Heat Exchanger |
| Re | Reynolds number [-] |
| Pr | Prandtl number [-] |

## Chapter 6

# 6. Regenerative Flow Turbine (RFT)

*"Everything is theoretically impossible, until it is done"*

Robert A. Heinlein, American sci-fi author

## 6.1 Introduction

In small-scale ORC systems, the expansion machine represents the key component as far as the performance, reliability, and capital cost are concerned. Expanders can be categorized into dynamic expanders and volumetric expanders [61]. However, dynamic expanders or turbomachines are subjected to some technical constraints in small-scale ORCs such as high rotational speeds of the impeller to achieve the nominal blade Mach number of the turbine and the high isentropic efficiencies [18]. Moreover, turbomachines are usually more expensive than volumetric expanders [15] limiting their applications at sizes higher than 50 kW.

As regards volumetric machines, they are characterized by lower flow rates and shaft speeds and higher pressure ratios compared to dynamic turbines. So far, most of the volumetric expanders used in the power generation are formerly compressors for air conditioning and refrigeration applications converted to be used as expanders. Pantano and Capata [114] conducted a numerical expander selection study for a bus engine WHR system. Among the candidates, they considered inward-flow radial turbine, vane, screw, and scroll expanders. Several criteria such as efficiency, reliability, costs, lubrication, and compactness were considered in the selection. Their results showed that the considered vane expander was at the bottom

of the list, while the others were rated very closely with a slightly better score for screw expander. Imran et al. [63], instead, conducted a comprehensive literature review on piston, vane, screw, and scroll expanders for low-grade WHR finding that the scroll and screw expanders are the most suitable machines. Despite the overall score of screw expanders was stated slightly higher compared to scroll expanders, the cost score of the scroll expanders was significantly lower. Also, Dumont et al. [64] confirmed that scroll expanders represent a good choice for ORC systems in the power range 1-10 kW. In their work, authors compared four types of volumetric machines, namely piston, screw, roots, and scroll expanders finding that the latter was able to achieve the highest isentropic efficiency. Nevertheless, according to Galloni et al. [115], the cost of the scroll expander is three times higher than the total cost of the evaporator and the condenser heat exchangers and almost ten times higher than that of the vane pump thus highlighting the influence of the expander on the overall investment cost of an ORC unit.

In literature, many researchers have focused on scroll expanders for small-scale ORCs. For example, Lemort et al. [75] investigated a hermetic scroll expander with a built-in volume ratio (BVR) of 3 using R245fa as working fluid for ORC applications. Their results showed that the electric output power was 298-2032 W and isentropic efficiency was 34-71% with a pressure ratio (PR) between 2 and 5.8. In addition, they found that the produced power increased almost linearly with PR, while the isentropic efficiency reached the peak at a PR slightly higher than the expander BVR and dropped sharply for PRs lower than the BVR. Gao et al. [116], instead, studied experimentally two scroll expanders with different displacements using R245fa in the same operating conditions. Results showed that the bigger expander outperformed in terms of isentropic efficiency for PR in the range of 3-5.2. In particular, the isentropic efficiency was 41-72% for the expander with $86 \times 10^{-3}$ l/rev SV, and it was 15-62% for the one with $66 \times 10^{-3}$ l/rev SV. Moreover, they found that the small expander in an open circuit test bench using air showed an isentropic

efficiency in the range of 62-70% and a power of 70-310 W which was almost double the shaft power with R245fa.

Table 6-1 reports the main performance parameters of expanders used in small-scale ORC systems. Performance data of these expanders have been taken from [63], unless otherwise specified, neglecting some peculiar cases where the working conditions or performances were far out from the range of the other values. Furthermore, shaft speeds do not define the limits of the possible values but describe the range of the applicability studied in the literature. In addition to these, also Tesla turbine has been considered as an interesting expansion device in small-scale ORC systems in some recent studies [117,118]. It is noteworthy to say that the performance data of Tesla turbines reported in Table 6-1 come from an ongoing experience in small-scale power systems, while the others are more mature technologies and have exhibited higher isentropic efficiencies.

Table 6-1. The range of the main performance parameters of the selected expanders in ORC systems [63]

| Parameter | Piston | Screw | Scroll | Tesla [117,118] |
|---|---|---|---|---|
| Maximum shaft speed [rpm] | 3,100 | 6,000 | 5,000 | 8,000 |
| Maximum BVR [-] | 15 [119] | 6 | 4.57 | n.a. |
| Maximum Pressure Ratio (PR) [-] | 4.5 | 10.2 | 10.6 | n.a. |
| Power [kW] | 0.004-1.64 | 1.1-800 | 0.0002-12 | 0.05-30 |
| Efficiency [%] | 10-76 | 20-88 | 20-86 | 20-60 |

Based on the data reported in the literature, volumetric type expanders have reduced performances at low pressure ratios and mass flow rates. On the contrary, Tesla turbines become inefficient at high flow rates and pressure ratios, which makes them suitable for micro-scale power systems up to 5 kW.

Hence, the analysis of the available literature on small-scale ORC systems has highlighted the need for reliable and low-cost expanders for WHR applications able to operate also in low flow rates. According to a recent literature review by Zhao et al. [120] and the best of the author's knowledge, none of the papers available in the open literature has addressed the potential of regenerative flow turbines (RFTs) for small-scale ORC applications.

### 6.1.1 The regenerative flow turbine

Whether a regenerative flow turbomachine drives the fluid (pumps or compressors) or derives power from the fluid (turbines), the operating principle of the machine is the same: part of the flow follows a peripheral path through the channel, while the rest enters the impeller pockets and returns to the channel continuously. This secondary flow (regenerative flow) exchanges momentum between the impeller and the mainstream (in the peripheral direction) resulting in a helical trajectory in the peripheral direction and generating a pulse pressure variation inside the flow [121].

Although a regenerative flow turbomachine is known as a dynamic machine similar to a centrifugal turbomachine [122], the pressure changes in the peripheral direction rather than in the radial direction [123]. In literature, semi-empirical models were mainly developed to investigate the performance of regenerative flow pumps (RFPs) [124–127], blowers (RFBs) [128], and compressors (RFCs) [129]. At low flow rates, the circulatory velocity, which represents the swirl of the flow and its normal

vector is in the peripheral direction, increases resulting in more swirls of the flow [122]. This means that an RFP provides a high head when it works at low flow rates, with a straight head-capacity curve [128]. On the other hand, RFCs and RFPs are less efficient at low flow rates as reported in many studies [121,130,131].

As positive displacement machines, regenerative flow turbomachines have shown so far low efficiencies, typically between 35% and 50% [132], which have restricted their adoption in power systems. However, such machines inherit some interesting characteristics without the issues of wear and lubrication [131]. Similar to positive displacement machines, they can handle two-phase flows to some extent [122], which makes them suitable to operate with hot or volatile liquids as a pump [125], or with a few degrees of superheating in small-scale power plants as a turbine. In addition, self-priming, low net-positive-suction-head (NPSH), compact design, high-temperature capability, noiseless operation, high reliability, and low manufacturing costs are other merits of these machines [122,131].

Therefore, despite the limited isentropic efficiency, the rising interest in small-scale ORC systems for WHR applications in the last decade is giving chances also to regenerative flow turbines (RFTs). Moreover, such machines have low construction costs compared to radial flow turbomachines and even volumetric expanders making them a low-cost and viable alternative expander to the previously discussed machines in micro-scale WHR applications.

So far, only a few researchers have focused on RFTs using experimental and numerical studies to improve their efficiencies. For instance, Balducci and Bartolini [133] conducted a test campaign using an RFT with compressed air. In a similar study, Bartolini and Salvi [134] studied the same RFT experimentally to assess its performance in gas pipelines as an alternative to conventional expansion valves.

However, to the best of the author's knowledge, there is no CFD or one-dimensional analysis of RFTs in the literature that provides useful insights into their operation

at different working conditions. Compared to the experiments, the computational analysis is advantageous due to its high repeatability, lower costs, and reduced time. In the case of RFTs, it is especially useful to observe the complex swirling flow [124]. In these cases, CFD results reveal the most important advantage of understanding the internal physics of the fluid dynamics of the flow that can be hardly assessed with experimental tests [135]. However, due to the complexity of the geometry of RFTs in some cases, considerable simplifications may be needed to obtain good mesh quality and refinement, and stable solutions [122]. In any case, CFD studies on performance optimization should be employed with caution and it is recommended to calibrate results with experimental data [135].

Therefore, the performance of the RFT with the same geometry studied by Balducci and Bartolini [133] has been investigated using CFD analysis in ANSYS Fluent [136]. The results of the test campaign are used for the validation of the model, and then the validated model is used to predict its performance at higher temperature ranges. The main goal of this work was indeed to develop a robust CFD model of RFT that can support the future design optimization of this machine for small-scale ORC and cryogenic applications.

Moreover, no studies in the literature have examined the performances of RFTs using organic fluids. Therefore, the performance of an RFT with R245fa as the working fluid and operating in a non-regenerative ORC system is numerically investigated in this study. Three-dimensional CFD simulations are conducted to evaluate expander performance with varying operating conditions. Then, these results are included in the numerical model to examine its potential in ORCs. Finally, the performance of the proposed expander is also compared with that of two different scroll expanders available in the literature. Hence, the main novelties of this chapter are: i) modeling of an RFT with air and R245fa using CFD analysis ii) numerical evaluation of the RFT for micro-scale ORC systems considering a real

test bench as the reference; iii) comparison between the proposed RFT and scroll expanders.

## 6.2 CFD simulations of an RFT prototype

In the following, the CFD model has been described then the results of the model validation are presented using the experimental results presented in the literature. The validated CFD model then is used to assess the performance of the RFT prototype with air and ideal gas model using non-dimensional analysis. The model then is used to simulate the RFT prototype with R245fa, a popular refrigerant in ORC systems in the literature using a real gas density model. In the following, results of the CFD model are adopted in a system-level study to investigate its performance in the ORC system studied in this work. Finally, the CFD results are used to compare the RFT prototype with two scroll expanders with different BVRs using R245fa showing the pros and cons of the RFTs compared to one of the most common expander machines in low-grade ORC systems.

### 6.2.1 Numerical model

The geometry of the RFT under investigation is the same as the one in the experimental works by Bartolini et al. [133,134] with minor modifications to facilitate the subsequent mesh generation. The main parts of the RFT modeled in this work include the impeller, the casing, the stripper, and the inlet and outlet ports. The impeller consists of a disk with blades on both sides to better balance the impeller. The casing covers the impeller on both sides and creates the channel from the inlet to the outlet. The machine used in the experimental tests has a double effect impeller that is symmetrical with respect to the plane perpendicular to the rotational axis (Figure 6-1. a-b). Therefore, only one side of the impeller has been

considered in the present CFD analysis (Figure 6-1. c-d) to save some computational efforts without impacting the quality of the results. Hence, Figure 6-1. c and d show half of the turbine geometry and the impeller with respect to the symmetry plane. As shown in Figure 6-1. c, the stripper separates the inlet from the outlet of the machine to avoid leakage flow between them while a small gap separates the impeller blades from the stripper body to avoid fracture of the stripper [133]. However, this causes some leakages from the inlet of the machine toward the outlet and, as a consequence, a minimum gap is recommended in RF turbo-machines [131]. In practice, this gap depends on construction tolerances and resistance of the stripper material against deformation during the operation of the turbine due to imposed pressure by the flow.

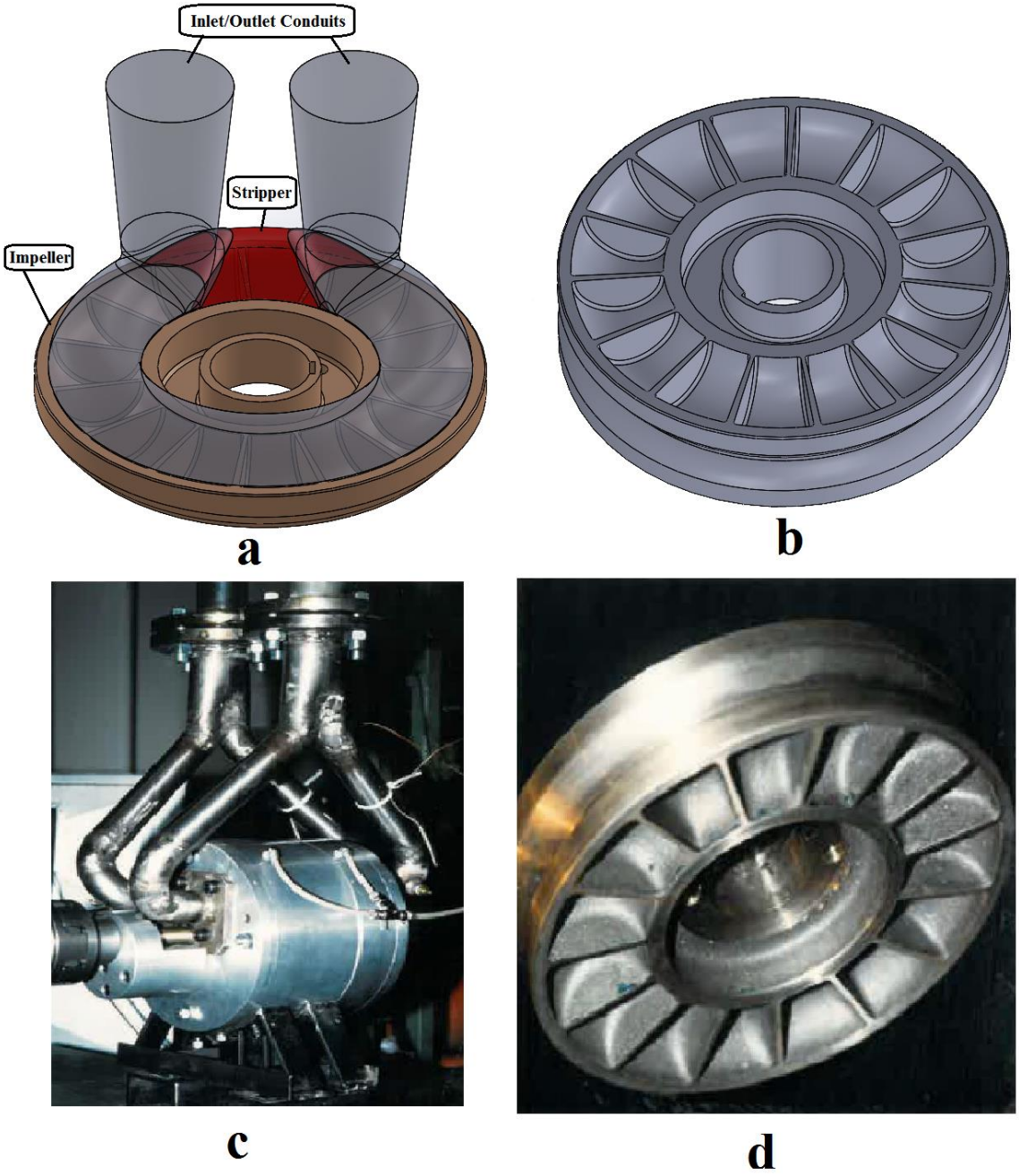


Figure 6-1. The RFT and the impeller: experimental apparatus (a and b) [133] and 3D model (c and d)

The mesh domain is illustrated in Figure 6-2 with the zoom-in of the constructed mesh in the clearance gap between the stripper body and the impeller tips to capture the high-speed leakage flow accurately (18 nodes/mm). The asymmetric plane crosses the middle of the impeller, whose normal vector is the axis of the impeller.

Wall boundary mesh is used at the impeller walls because of the strong impact of the fluid-wall interaction on the machine behavior. More precisely, inflation consisting of a first layer height equal to 0.05 mm, a growth rate of 1.1, and 10 layers minimum have been set-up.

Moreover, the dimensions of the RFT shown in Figure 6-2 are reported in Table 6-2. The channel (hatched area) and the impeller in this study are halved circles with equal radius, separated by a 0.5 mm gap. This gap exists also between the stripper and the blade tips causing leakage losses, as described before.

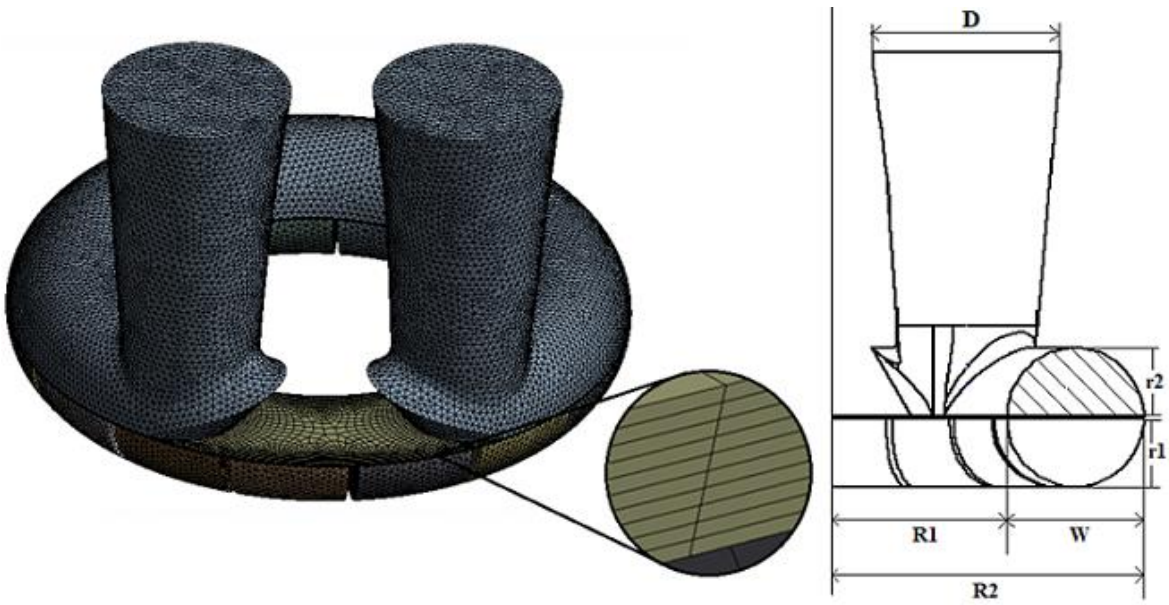


Figure 6-2. Mesh domain of the RFT (left) and half-section view with dimensions nomenclature (right)

Table 6-2. Normalized dimensions of the RFT ($W$ = 27.6 mm)

| *D/W* | *R1/W* | *R2/W* | *r2/W* | *r1/W* | $\pi(R1+R2)/(n.W)$ |
|---|---|---|---|---|---|
| 1.388 | 1.292 | 2.292 | 0.5 | 0.5 | 0.75 |

The independence of the numerical results from the mesh quality is assessed by comparing the CFD results using different mesh densities. In particular, the number of elements has been varied from 0.6 to 2.8 million showing that the mesh independence is met for an element count higher than 0.9 million. Figure 6-3 shows the variation of the outlet temperature with mesh density highlighting this outcome. Therefore, a mesh domain including 314,426 nodes and 946,227 elements has been considered for the simulations.

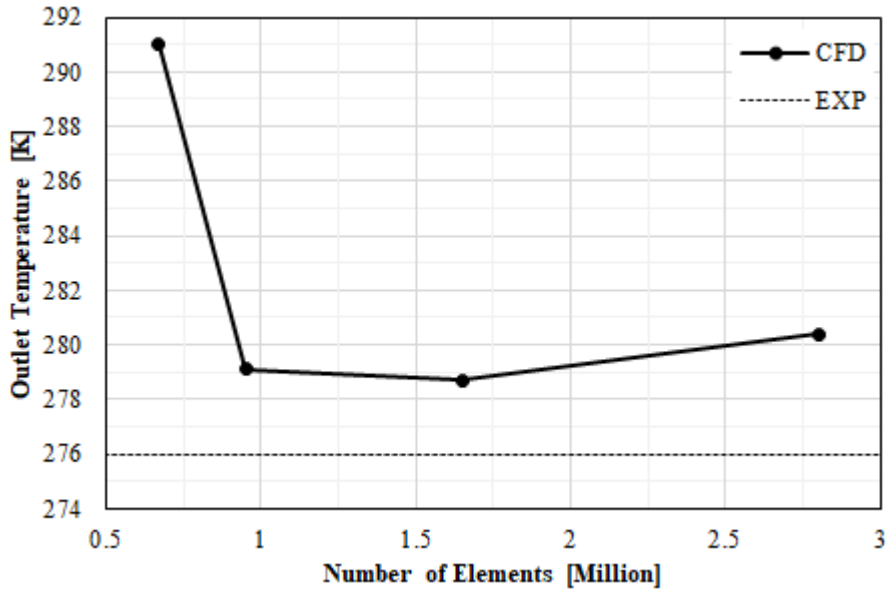


Figure 6-3. Variation of the outlet temperature by the mesh number

Because of the complexity of the flow, the numerical model of the RFT must accurately predict also the strong wall-fluid interactions, the pressure gradients, and the velocity field of the high-swirling flow in a curvy domain. The Reynolds Stress Model (RSM) is an anisotropy turbulent model recommended for this type of flow regime and geometry [137]. This model also makes use of near-wall algorithms to predict the wall-fluid interactions and the pressure gradients caused by the blades. Therefore, the Reynolds Stress benchmark model (BSL) is used for this

purpose using k-ω SST (Shear-Stress Transport) as the initial solution. These models are ω-based solvers insensitive to free stream initial conditions and are also able to switch automatically between near-wall models where the fine mesh is adopted and wall functions when the mesh is coarser, which makes the model independent from the mesh quality adjacent to the walls [138]. To benefit from the features of the ω-based solver in near-wall flow modeling, inflation is used for meshing the impeller walls as described previously. $Y^+$ (non-dimensional wall distance) depends on the distance of the first node from the wall, fluid density and viscosity, and the wall shear stress[1]; therefore, it varies in different walls and working conditions of the RFT. For instance, for an impeller rotational speed of 6,000 rpm, the average $Y^+$ values on the impeller walls are about 17 and 53 for the mass flow rates of 0.1 kg/s and 0.3 kg/s respectively, which confirms the use of log-law wall models [139]. The pressure-velocity coupling is solved using the PISO scheme, and PRESTO! is chosen for the pressure discretization scheme as suggested for 3-D domains with highly swirling flows [138].

The numerical model is based on the following assumptions to simplify the modeling of the RFT. The considered working fluid is air as the experimental works [133,134]. The ideal gas model is adopted for the density since compressibility effects are non-negligible. The variations of the fluid viscosity with temperature in the narrow gaps are considered using the Sutherland three-coefficient model.

The rotation of the impeller is considered using a steady-state model, the Moving Reference Frame (MRF) also known as the Frozen Rotor approach. This approach is considerably less costly in comparison with transient models and adopted in many CFD analyses of RF turbo-machines [121,123,140–142]. Inlet and outlet (backflow)

[1] $y^+ = \frac{y\sqrt{\rho.\tau_w}}{\mu}$

boundary conditions that have been used for both the validation of the numerical model and the performance study of the RFT are reported in Table 6-3.

Table 6-3. Boundary conditions of the CFD model

| Inlet BCs | | | | Outlet BCs | | | | N (rpm) |
|---|---|---|---|---|---|---|---|---|
| Mass flow rate (kg/s) | | Temperature (K) | | Pressure (bar) | | Temperature (K) | | |
| V[1] | PS[2] | V | PS | V | PS | V | PS | 1,500, 3,000, 6,000 |
| 0.075-0.21 | 0.1-0.3 | 295 | 393 | 2.42-4.2 | 3 | 272.8-287.5 | 363 | |

Axial and radial leakages are neglected, while the leakages between the impeller tips and the stripper wall are considered. Indeed, axial and radial leakages can be significantly minimized using existing sealing solutions already adopted in traditional gas turbines whilst those between the impeller tips and the stripper wall are typical of RF machines. Furthermore, heat losses through the walls are assumed negligible considering the rapid expansion of the gas throughout the turbine and the limited temperature difference between the turbine walls and ambient because of the relatively low operating temperature.

The same model is used then to simulate the RFT prototype with R245fa, a popular refrigerant that was adopted widely in ORC studies in the literature. This fluid is adopted so the RFT can be compared with two scroll expanders with different BVRs

[1] Validation

[2] Performance Study

tested with R245fa afterward. Therefore, the Peng-Robinson real gas model is used for calculations of R245fa density instead of the ideal gas model.

### 6.2.2 Validation of the CFD model

The obtained results from the CFD analysis are compared with the experimental data provided in [133]. In particular, the discharge temperature and the static-to-static isentropic efficiency are considered as the reference parameters. As regards their experimental tests, the authors set up a test rig with an air compressor, two storage tanks, the RFT under analysis, and the measuring instruments. The inlet pressure was fixed to 8 bar in all the experiments, while the inlet temperature was not declared. Because the air was not heated up in their experiments (it was just compressed and stored in the tanks), room temperature (as reported in Table 6-3) is considered as inlet temperature for the CFD simulations. The mass flow rate, instead, was measured using pressure difference at the inlet and outlet of an orifice.

Regarding the temperature, the CFD model overpredicts the outlet temperature in most of the cases. Consistently, the CFD model underestimates the isentropic efficiency compared to the values obtained during the tests as shown in Figure 6-4. This can be since the inlet temperature is estimated to the ambient temperature while the exact experimental values were not declared. However, the numerical results are generally in good agreement with the experimental data in different mass flow rates and shaft speeds.

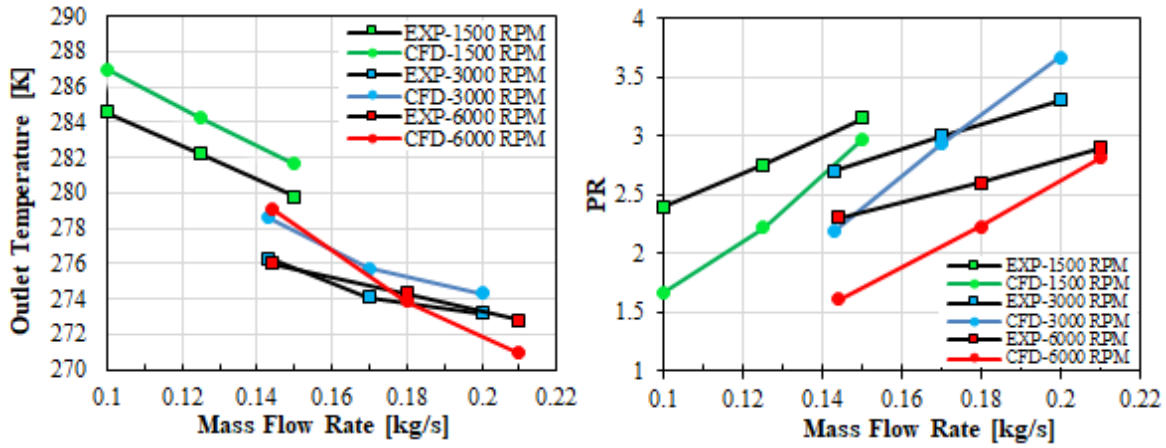


Figure 6-4. Comparison of outlet temperature (top) and isentropic efficiency (bottom) between CFD results and the experimental data [133,134]

Although the inlet temperature in the simulations may differ slightly from those of the tests, because the inlet temperature was set to room temperature in the CFD analysis, it is unlikely to expect that the adiabatic assumption of the model has a significant influence on the obtained results. Because the average wall temperature of an RFT employed in small-scale low-temperature ORC systems is substantially lower than those in conventional steam or gas turbine power plants, it can be stated that the adiabatic assumption does not significantly affect the accuracy of the CFD results. In any case, since the accuracy of the model was in an acceptable range, the CFD model was then used to predict the performance of the RFT at higher inlet temperatures like those achieved in typical small-scale ORC plants.

### 6.2.3 Flow characteristics

In general, RF turbo-machines can exploit a multi-stage expansion in a single impeller. In previous researches, it was found that the number of blades affects the performance of RFPs significantly [124]. Moreover, some flow characteristics such as the mass flow rate and the flow compressibility influence the number of

circulations of the flow (stages) [121]. Figure 6-5 shows the iso-pressure surfaces to represent the number of effective stages in the studied RFT with air.

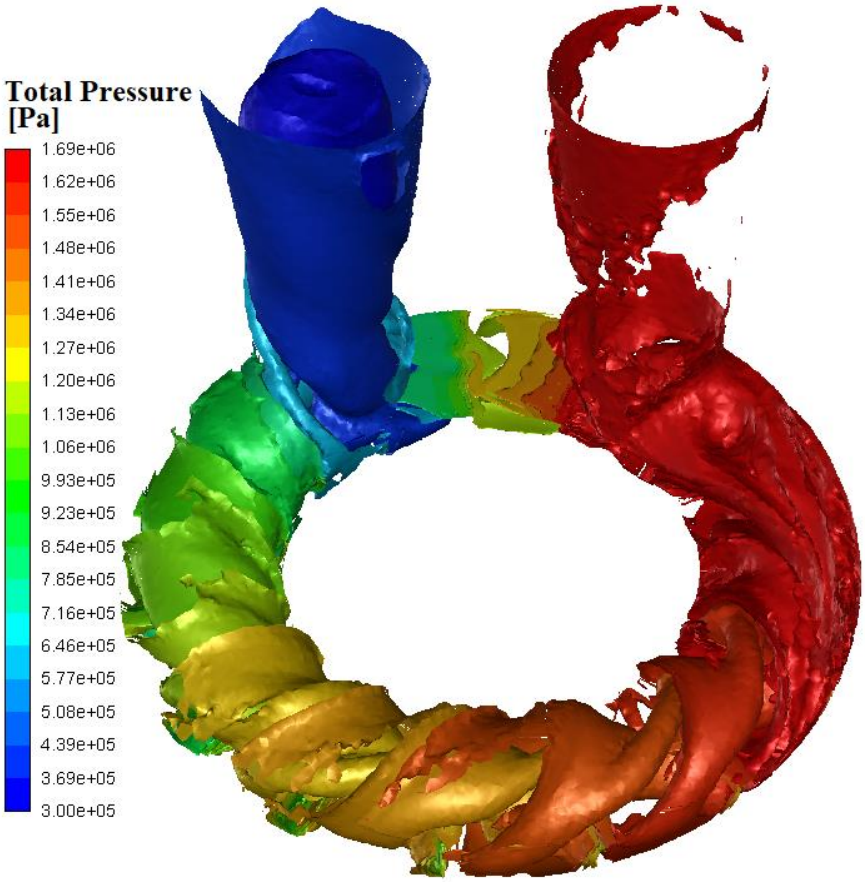


Figure 6-5. Iso-pressure surfaces using air at 3,000 rpm and 0.3 kg/s

It is evident from Figure 6-5 that the flow requires a sufficiently long path before being guided accordingly to the blade design. Indeed, the gas takes a while before starting the swirling pattern. This effect is even more clear in Figure 6-6. b, where the average total pressure along the channel is reported with respect to the points in the middle of the channel depicted in Figure 6-6. a. Three different regions are detectable: the first one is the acceleration region where the total pressure does not change considerably and the circulatory velocity increases until the flow becomes fully developed. Then, the linear region is distinguished by a constant pressure

gradient along the peripheral direction, and finally, the outlet region where a greater pressure drop occurs.

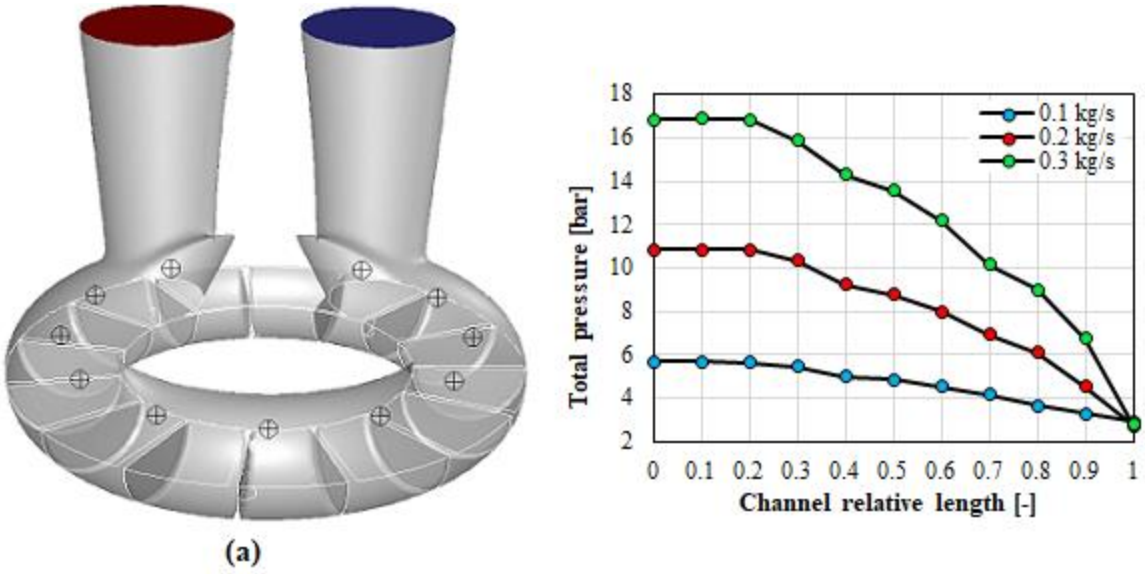


Figure 6-6. a) position of sample points along the channel, b) Variations of total pressure along the channel using air at 3,000 rpm and different mass flow rates

### 6.2.4 RFT performance using air and R245fa

In this section, a comparison of the performance of the machine using air and ideal gas model with that using R245fa and real gas model is carried out to highlight the impact of the working fluid. To this end, the RFT performance is described using the common non-dimensional numbers of the turbomachines: the static pressure ratio, the total-to-static isentropic efficiency, and the stage loading. The first two are defined in Eqs. (6-1) and (6-2) as the following.

$$PR = \frac{P_1}{P_2} \tag{6-1}$$

$$\eta_{t,s} = \frac{\dot{W}_{act}}{\dot{W}_s} = \frac{\dot{m}(h_{01} - h_{02,act})}{\dot{m}(h_{01} - h_{2,s})} \tag{6-2}$$

where subscripts "1" and "2" indicate the inlet and outlet of the RFT respectively, "0" indicates total enthalpy, and "act" and "s" refer to actual and isentropic conditions respectively. The values of temperature and pressure are obtained using the area-weighted average of the CFD results, and then other properties of the fluid are calculated using CoolProp fluid database in MATLAB® software.

In non-hydraulic turbomachines, the stage loading is the key design parameter similarly to the head coefficient of hydraulic turbomachines; it is usually expressed in terms of the non-dimensional parameter $\psi$ [143]:

$$\psi = \frac{\Delta h_0}{U^2} \tag{6-3}$$

Therefore, the stage loading indicates the amount of the specific work produced in each stage of the turbine for a given impeller speed. The higher the stage loading, the higher the work density of the expansion for the given shaft speed and dimensions of the RFT.

The streamlines of the total temperature are represented in Figure 6-7 showing the flow characteristics of the RFT. The flow is a combination of the mainstream, along the peripheral direction in the channel, and the regenerative stream, due to the swirling flow that transfers the momentum between the mainstream and the impeller. In Figure 6-7, the leakage flow that passes through the small gap between the impeller blades and the stripper wall is also shown. Furthermore, the outlet plane, in which the outlet properties of the fluid are evaluated is presented. It is selected far enough from the outlet boundary to avoid any interference of the outlet boundary conditions (backflow) on the calculated performances of the machine. On the contrary, in the calculation of the PR, the pressure at the outlet boundary is adopted as in real systems, in which the outlet pressure is imposed by the saturation temperature at the condenser.

In addition, Figure 6-7 shows the velocity vectors in a typical section. The maximum flow velocities are achieved in a zone near the center of the plane, shifted slightly toward the external radius of the impeller. Moreover, the swirling flow whose normal vector is perpendicular to that plane is visible.

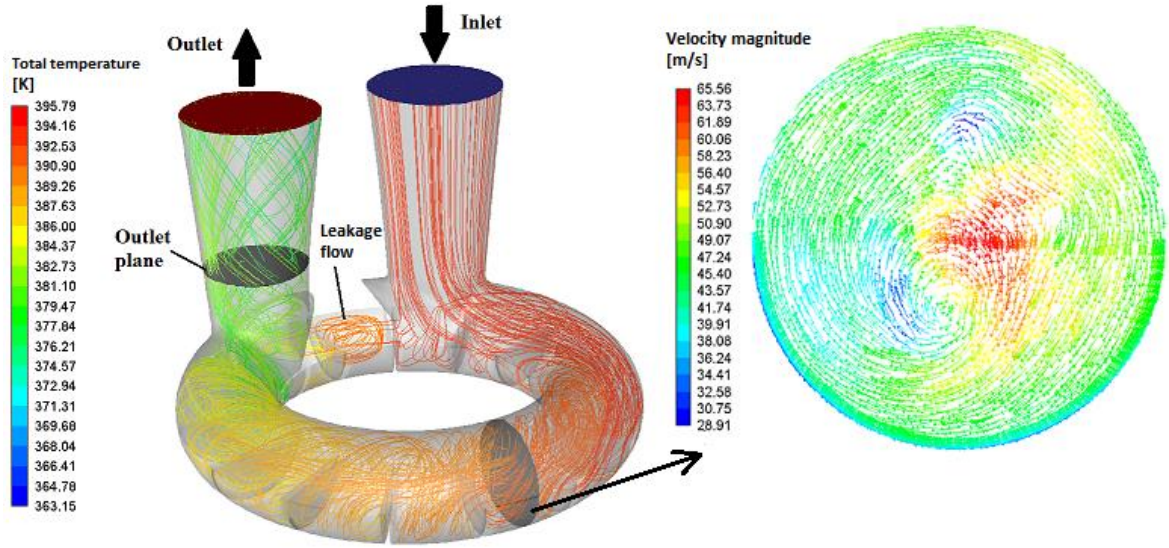


Figure 6-7. Streamlines colored by the total temperature (left) and velocity vectors colored by velocity magnitude in a typical section (right) (R245fa, 3,000 rpm, $\dot{m}$ = 0.5 kg/s, $T_{su}$ = 120 °C)

The flow streamlines for both air and R245fa are shown in Figure 6-8 at the same working conditions. The R245fa flow develops less the swirl than the air since the molecular weight of R245fa is almost 4.6 times higher than that of the air. As a result, the enthalpy change between the inlet and outlet of the turbine is lower in the case of R245fa.

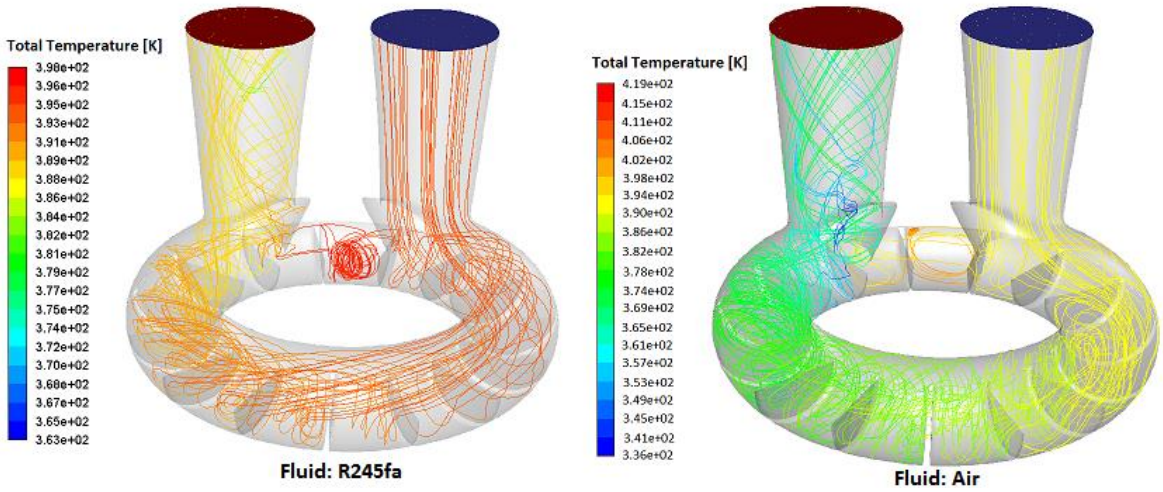


Figure 6-8. Streamlines colored by the total temperature for R245fa (left) and air (right) (6,000 rpm & $\dot{m}$ = 0.3 kg/s & $T_{su}$ = 120 °C)

At the same time, the lower swirl and moment exchange between the impeller and the mainstream in the channel entails lower losses and higher isentropic efficiencies of the RFT when operating with R245fa compared with air. On the contrary, the stage loading is lower as depicted in Figure 6-9. Indeed, more swirls result in higher stage loading but lower isentropic efficiency due to the higher losses during the expansion. In addition, the difference in the stage loading between the two fluids grows at lower rotational speeds due to the increase of the difference between the number of the swirls of the two fluids.

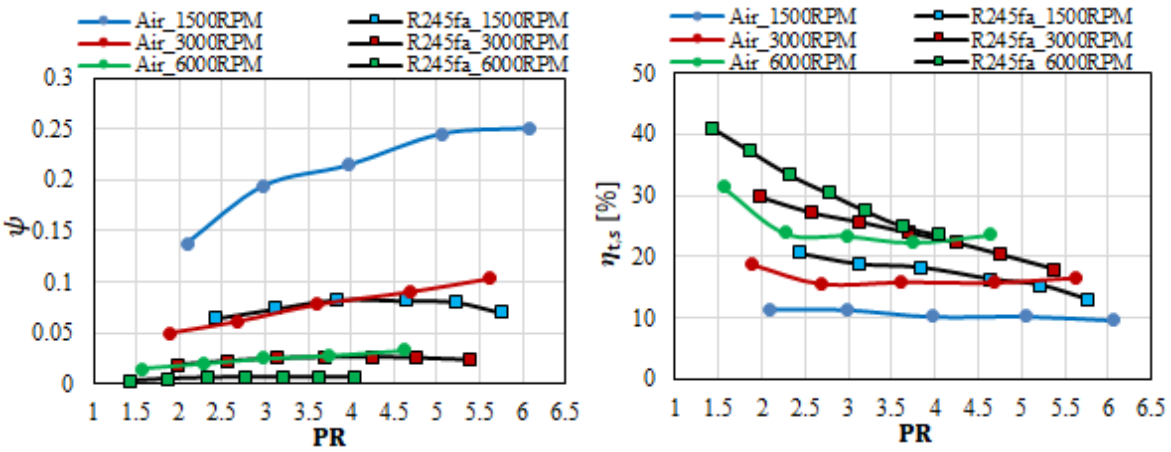


Figure 6-9. Stage loading (left) and total-to-static isentropic efficiency (right) vs PR using air and R245fa

As regards the losses in an RFT, in general, they can be categorized into (i) losses at the inlet/outlet conduits due to the sudden contraction/expansion; (ii) losses due to different fluid velocity vectors angles and the blade angles; (iii) frictional losses; and (iv) leakage losses [122]. To better highlight the impact of the leakage losses, an analysis of the entropy loss coefficient is carried out to compare the effect of different zones of the RFT on the isentropic efficiency loss. An entropy loss coefficient is a non-dimensional number representing the loss in the isentropic efficiency and it is introduced for turbines as the following [144]:

$$\zeta = \frac{T_2 \cdot \Delta s}{h_{02} - h_2} \tag{6-4}$$

where the index "2" indicates the outlet of the zone, and "$\Delta s$" is the entropy change in the zone calculated using the ideal gas correlation for air and real fluid properties for R245fa.

In particular, to better understand the impact of the leakage losses, the entropy loss coefficient is calculated in three different zones: from the inlet boundary of the RFT to the inlet of the channel, from the inlet of the channel to the outlet of the channel, and between the inlet and the outlet of the leakage gap zone. For the sake of

comparison, the relative entropy loss coefficient is used, which is the $\zeta$ calculated in each zone divided by the total $\zeta$ calculated from the inlet boundary of the RFT to the outlet plane shown in Figure 6-7. Figure 6-10 shows the impact of each zone on the isentropic efficiency loss using the relative entropy loss coefficient. The isentropic efficiency loss in the leakage gap has a significant contribution, even comparable with the total losses that occur along the channel during the expansion of the gas. Therefore, minimizing the gap is strongly suggested to improve RFT performance.

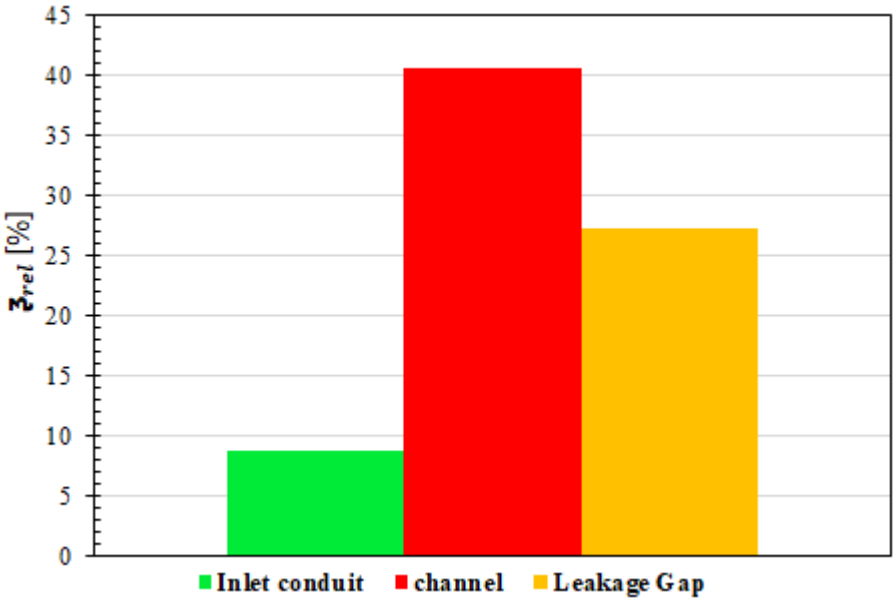


Figure 6-10. Relative entropy loss coefficient in three zones at (air, 3,000 rpm, $\dot{m}$ = 0.3 kg/s, $T_{su}$ = 120 °C)

In the following, the performances of the geometrical scaled-down RFT with R245fa are presented. The scale-down factor of 0.5 is taken and it is a necessary approach to suit the range of the RFT mass flow rate to be adopted in the ORC system simulation and to be compared with the two scroll expanders that their models are

adopted from the literature. Hence, the CFD boundary conditions of the scaled-down RFT prototype are reported in Table 6-4.

Table 6-4. Boundary conditions of the CFD model for the scaled-down RFT with R245fa

| Inlet boundary condition | | Outlet boundary condition | Rotational speed [rpm] |
|---|---|---|---|
| Mass flow (kg/s) | Temperature (°C) | Pressure (bar) | |
| 0.05-0.25 | 100-160 | 3 | 1,500, 3,000, 6,000 |

The performances of the RFT to be evaluated in the ORC system are expressed in terms of the static pressure ratio, the output power, and the total-to-static isentropic efficiency: As clearly visible in Figure 6-11, the PR increases linearly with the mass flow rate. In contrast with traditional turbines, the PR is higher at lower rotational speeds. This trend was also observed by [133] during their experiments, and in the numerical results with air [145]. The reason is related to the rotation of the impeller blades that creates a void effect in the channel. As a result, at higher rotational speeds more gas flows through the channel for a given pressure ratio as in volumetric machines, or lower swirls occur at higher speeds for a given mass flow rate, thus reducing the PR.

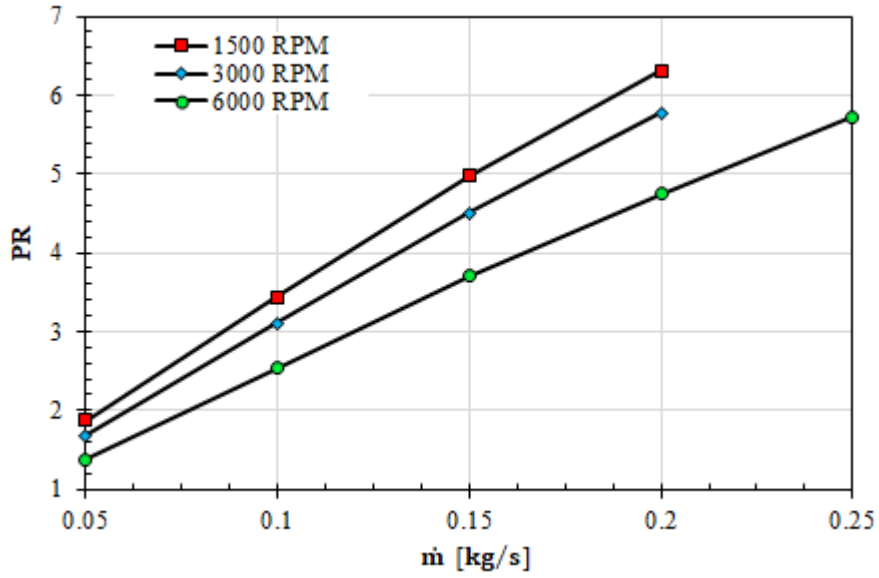


Figure 6-11. Static pressure ratio by the mass flow rate for different shaft speeds ($T_{su}$ = 120 °C)

The low isentropic efficiency of RFTs is undoubtedly the main barrier to their use in power systems. Figure 6-12 represents the isentropic efficiency with varying mass flow rates for different rotational speeds of the impeller. The isentropic efficiency is higher at low mass flow rates and so low PRs. This peculiarity is interesting for ORC applications as will be discussed further. Moreover, the RFT shows higher isentropic efficiencies at higher shaft speeds. Nevertheless, higher rotational speeds are not here investigated using CFD simulations since the impact of the increasing frictional losses with the shaft speed is not included in the model and consequently, the obtained results would be biased.

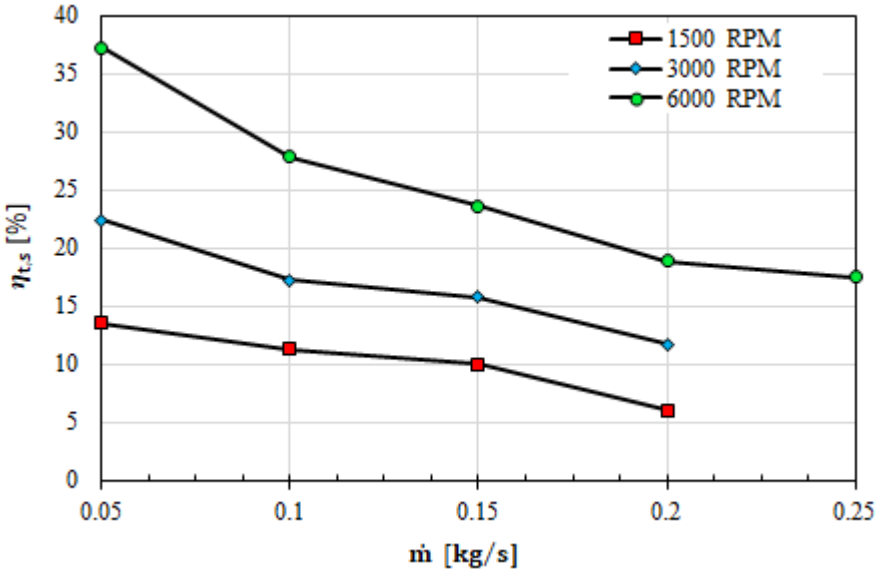


Figure 6-12. Isentropic efficiency by the mass flow rate for different shaft speeds ($T_{su}$ = 120 °C)

The output power of the machine is depicted in Figure 6-13. In general, the power increases almost linearly with the mass flow rate up to a certain value. At this point, the maximum number of swirls is formed and any additional mass flow rate blows through the channel without exchanging momentum with the impeller, while it intensifies the secondary flows resulting in even power loss at 1,500 rpm. The secondary flows do not contribute to power production but increasing the isentropic efficiency loss and entropy generation. In other words, the flow becomes highly distorted and random. For this reason, the isentropic efficiency drops more steeply at shaft speeds of 1,500 & 3,000 rpm in the highest mass flow rate, but it is not visible at 6,000 rpm, in which the critical mass flow rate is not captured.

The effect of the secondary flows can be better understood using the trend of the stage loading plotted in Figure 6-13 on the right. The stage loading increases with the mass flow rate until the maximum number of the main swirls is reached. Then, any increase in the mass flow rate results in the stage loading reduction, and negligible or negative change of the produced power. This critical mass flow rate

could be caught at the low and medium rotational speeds as shown in Figure 6-13. Therefore, the mass flow rate should not exceed specific values for each rotational speed. Furthermore, the difference between the output power at different shaft speeds is lower at low mass flow rates.

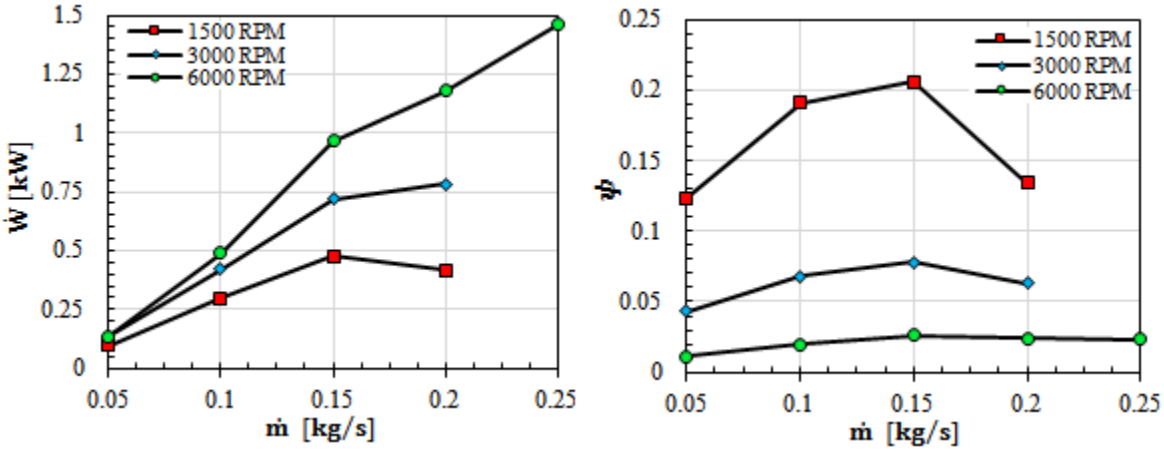


Figure 6-13. Output Power (left) and stage loading (right) by mass flow rate in different shaft speeds ($T_{su}$ = 120 °C)

Secondary flows are the additional swirling flows to the main swirling flow that contribute significantly to the entropy generation and consequently the isentropic efficiency loss during the gas expansion. The swirling flows are observed in three main directions, the main swirling flow with the normal vector in the peripheral direction as shown in Figure 6-7, some with the normal vector in the radial direction as in Figure 6-14, and the others with the normal vector in the axial direction as illustrated in Figure 6-15. The latter two appear as the flow is developed in the channel and forms the main swirl, and they amplify as the flow gets closer to the outlet. It is evident from Figure 6-14 that the entropy generation in the flow is associated with these secondary flows. The secondary flows are the result of the severe pressure gradient of the compressible flow on the sides of the impeller. It reveals a feature of the momentum transfer in the turbine that as the main swirling

flow enters the impeller pocket, it collides with the blade, and due to the coarse design of the impeller body and impeller tips, distortion and secondary flows are created. Such analyses are useful in the future design of RFTs to devise suitable implications to reduce the secondary flows during the expansion.

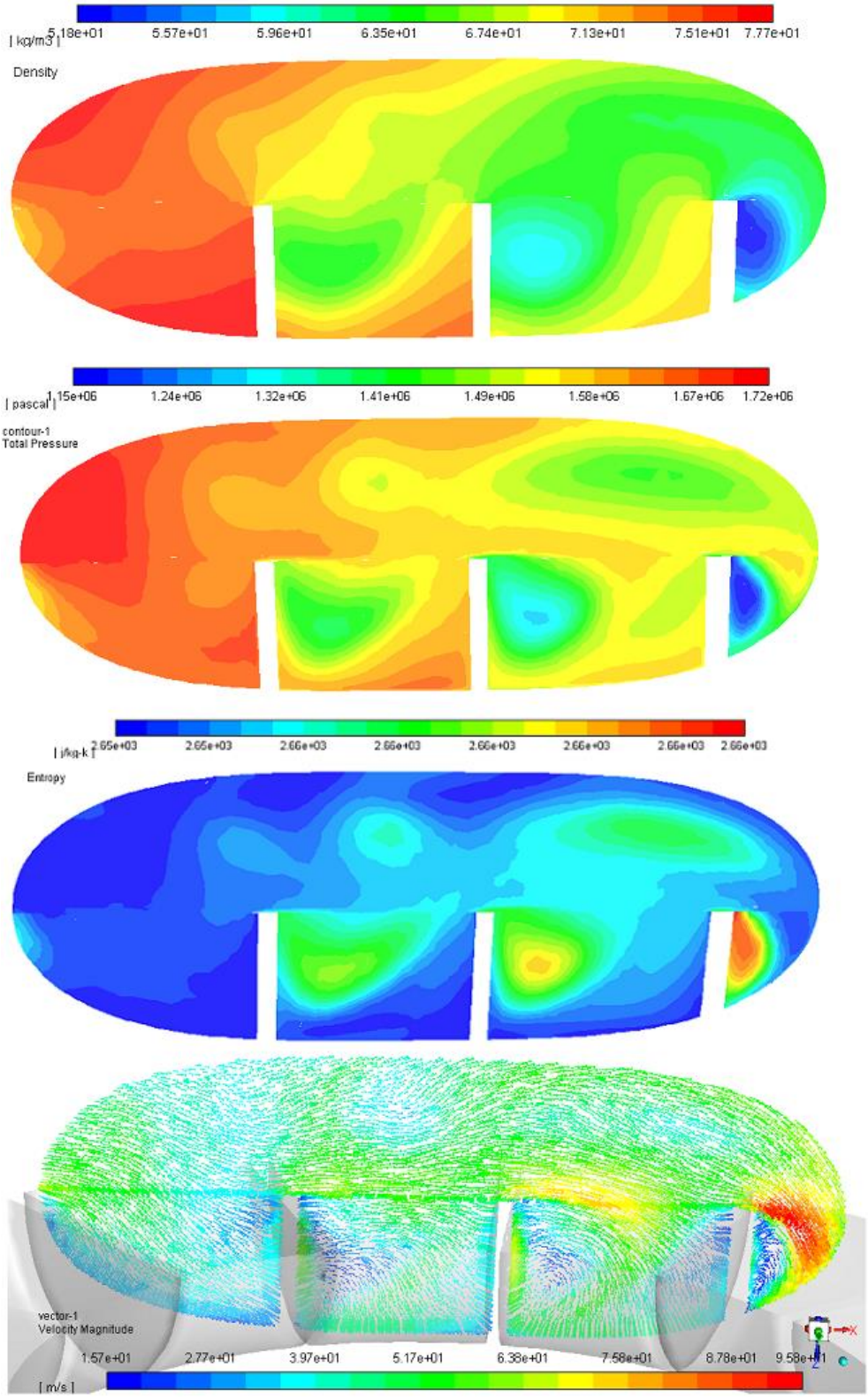


Figure 6-14. The density, total pressure, and entropy contours and velocity vectors in a plane including some impellers and the channel (R245fa, 6,000 rpm, $\dot{m}$ = 0.2 kg/s, $T_{su}$ = 120 °C)

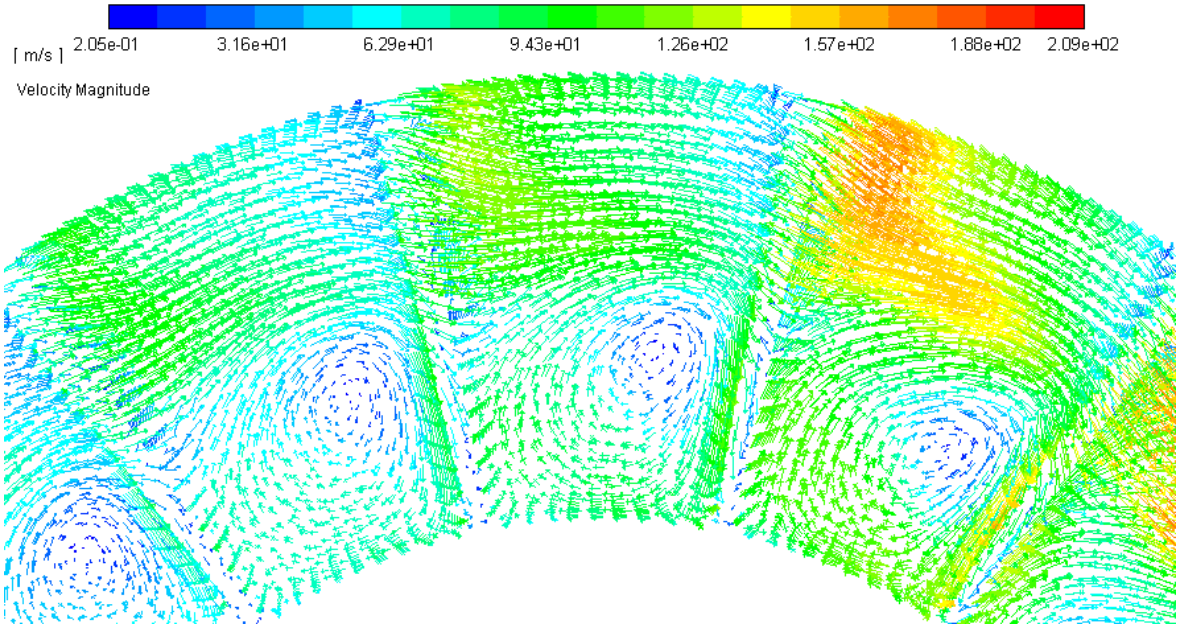


Figure 6-15. Velocity vectors at the impeller-channel intersection (R245fa, 1,500 rpm, $\dot{m}$ = 0.2 kg/s, $T_{su}$ = 120 °C)

To better present the complex 3-D flow and especially the secondary flows around the impeller blades with the radial normal vector, the velocity vectors are shown in planes with different impeller radius in Figure 6-16. The flow accelerates in the peripheral direction because of the expansion.

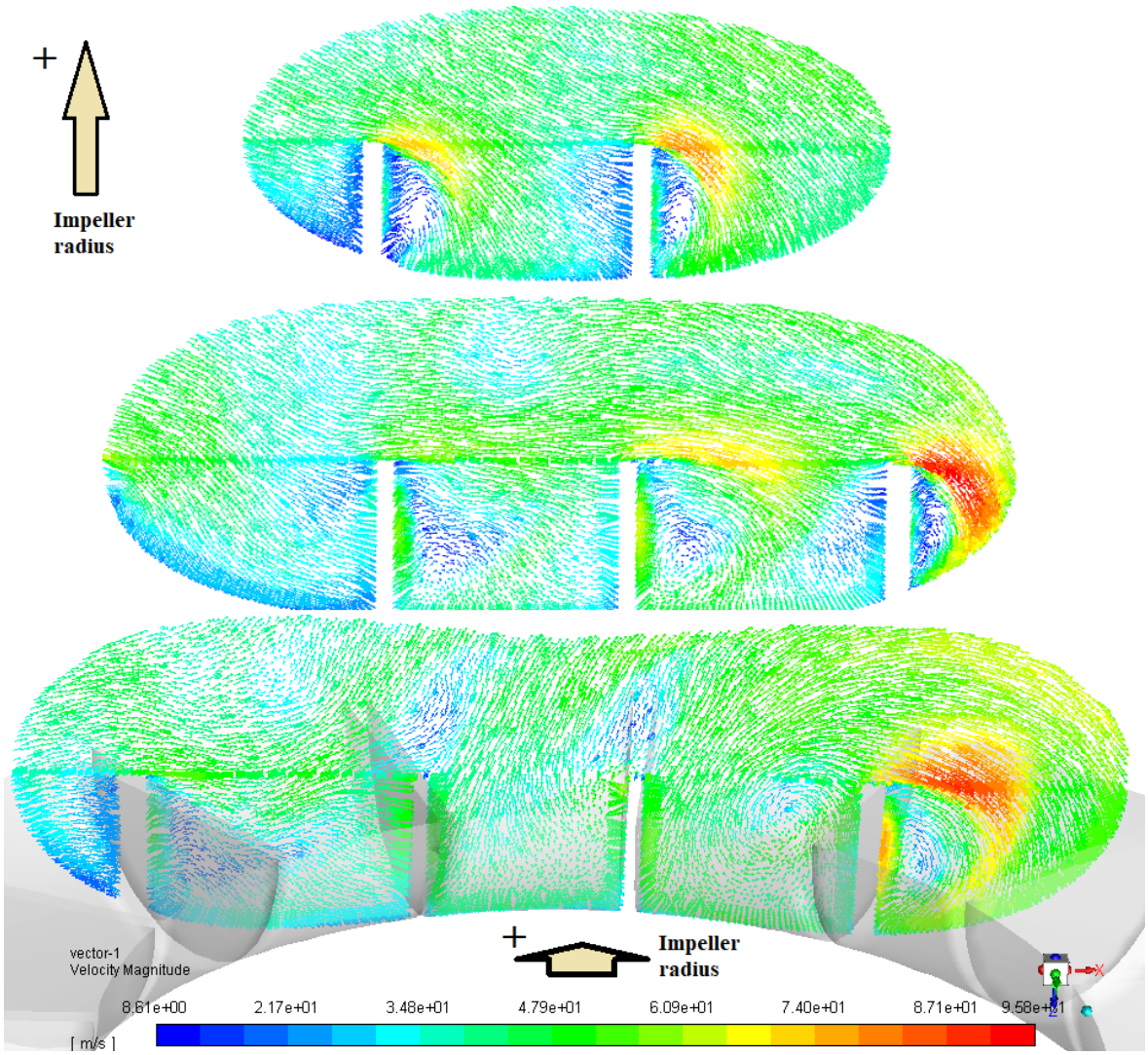


Figure 6-16. Velocity vectors at the planes at different impeller radii (R245fa, 6,000 rpm, $\dot{m}$ = 0.2 kg/s, $T_{su}$ = 120 °C)

To better understand the effect of the swirling flow on the presented RFT performance, the vorticity magnitude is used. The definition presented in the ANSYS Fluent users guide describes well its relevance to the flow swirl intensity: "it is magnitude of the vorticity vector. Vorticity is a measure of the rotation of a fluid element as it moves in the flow field, and it is defined as the curl of the velocity vector" [138].

Vorticity magnitude is presented in different shaft speeds and mass flow rates in and in different locations in the RFT during the expansion in Figure 6-17. It is evident that the vorticity magnitude is lower in the higher shaft speeds meaning a lower swirling of the flow confirming the higher isentropic efficiency in Figure 6-12 and the lower stage loading in Figure 6-13 in higher shaft speeds. Moreover, the slope of the vorticity magnitude curve is reduced as the mass flow rate increases referring to the critical mass flow rate discussed a few paragraphs before.

While the relation between the isentropic efficiency and the main swirling flow is more straightforward, and it is also evident that it does not follow the stage loading trend, the output power is related to the stage loading and the mass flow rate simultaneously. In the case of the highest shaft speed, the stage loading is almost constant, and the power increases linearly in high mass flow rates. At 3,000 rpm, the stage loading drops slightly, and the power is incremented marginally. Finally, the sharp drop of the stage loading pulls down the power at 1,500 rpm. Therefore, a trade-off can be taken to obtain high power and efficiency by ascending trend of the stage loading via the mass flow rate, even if very smooth, and keeping the vorticity magnitude low. However, feasible design implications to maintain such characteristics must be examined and assessed, which is out of the scope of this work.

In addition, the vorticity magnitude increases from the inlet to the channel end, then it gets damped as it gets closed to the turbine outlet boundary. Its trend shows that the swirling flow is intensified in the second half of the channel curvature after the flow is developed in the first half. In addition, the same trend is observed for the secondary flows in Figure 6-14 and Figure 6-15.

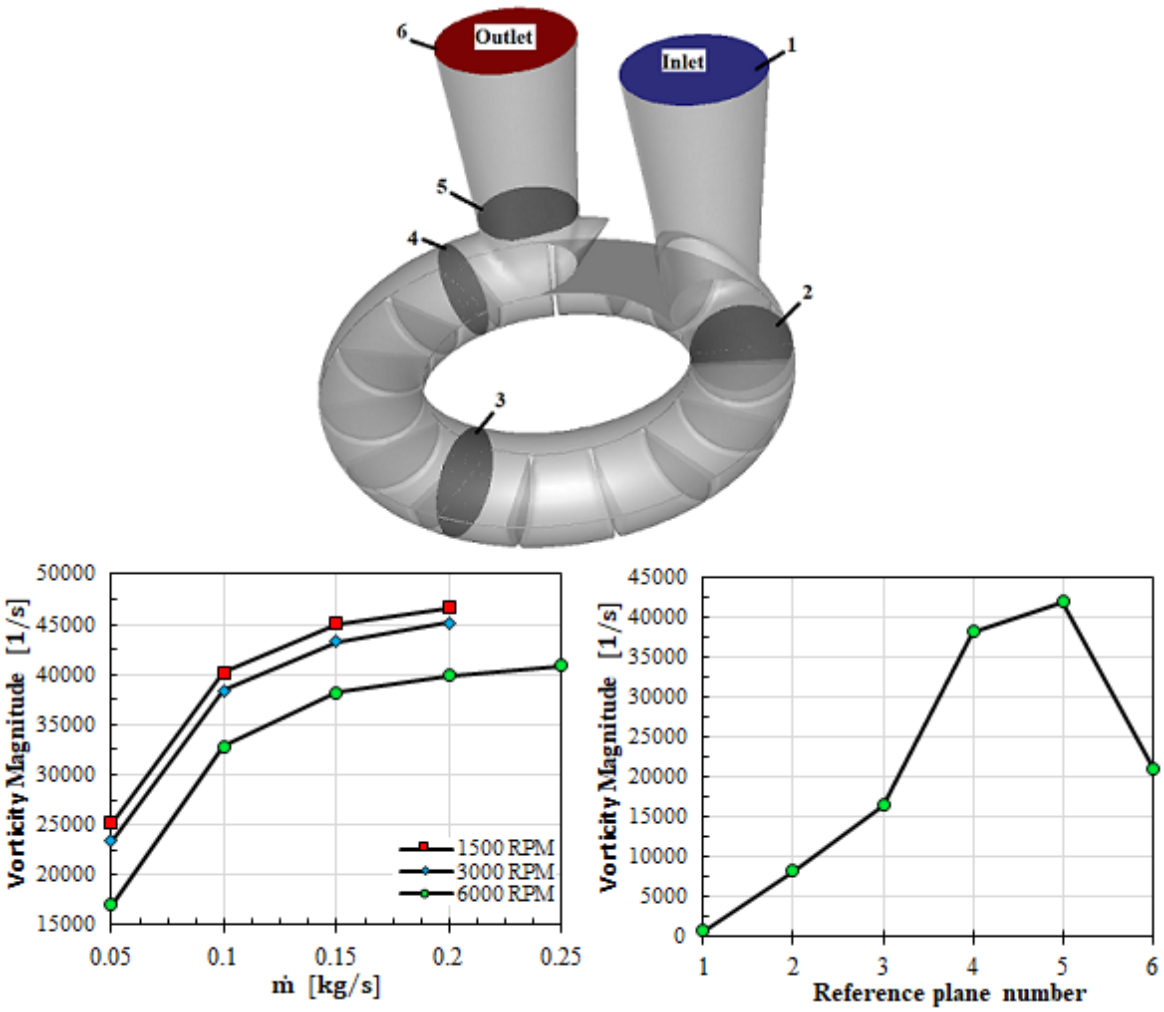


Figure 6-17. The vorticity magnitude by the mass flow rate for different shaft speeds at plane 4 (down left) and the vorticity magnitude in different locations of the RFT numbered and shown in the top figure (down right) (6,000 rpm & $\dot{m}$ = 0.15 kg/s)

Hence, the RFT shows the best performance at the maximum shaft speed considered in this work. Therefore, the rest of the simulations are performed at the shaft speed of 6,000 rpm.

The impact of the suction temperature on the performance of the RFT is assessed as shown in Figure 6-18. As can be seen, the increase of the suction temperature marginally improves the performance at low mass flow rates, while improvements grow significantly at higher mass flow rates. In terms of isentropic efficiency, the

performance of this expander is penalized with the mass flow rate; therefore, in the case of low-temperature WHR applications low mass flow rates are preferable.

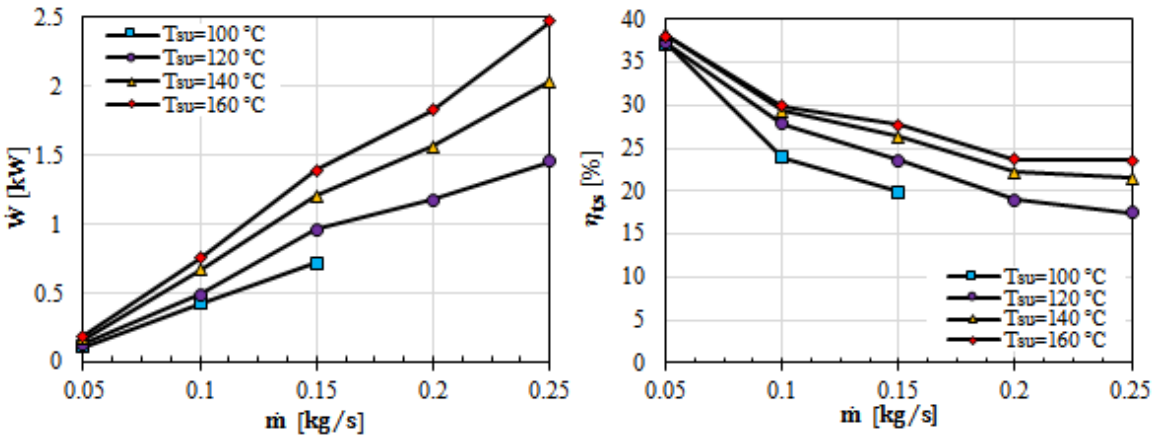


Figure 6-18. Output Power (left) and efficiency (right) by mass flow rate in different $T_{su}$ (6,000 rpm)

### 6.2.5 The RFT in the ORC system

The presented results of the scaled-down RFT performance in the previous section are used in this section for the ORC system simulation. To this end, the total-to-total isentropic efficiency is used since the temperature and pressure sensors of the ORC unit measure total values and the RFT model must be consistent with the calculations of the system's thermodynamic states. The previously developed semi-empirical models of the ORC components are used here to simulate the system with the RFT assuming that the RFT performance with R134a would be the same as its performance using R245fa that is presented in the previous section. In fact, this assumption is acceptable only to have an overall estimation of the ORC system with the RFT. However, this assumption makes sense for the study knowing that the molecular weight of the two refrigerants is not very different.

The ORC system model aims to find the system working conditions, in which the preset values of superheating and subcooling degrees are met for a given refrigerant pump speed. The cooling water mass flow rate is considered constant and equal to the chiller water mass flow rate as in the real test bench, and its inlet temperature to the condenser is considered equal to the assumed ambient temperature of 15 °C.

The flow chart of the ORC system using the simulated RFT is shown in Figure 6-19. The component-oriented model of the system is consisted of two main iterative loops to find the diathermic oil pump speed and temperature to maintain the preset superheating degree, and to adjust the pump discharge pressure to reach the preset subcooling degree. The maximum and minimum oil pump speeds are taken from the pump datasheet and the minimum of the experimental database, respectively. In addition, the evaporator and condenser sub-models include internal iterative loops to find the outlet temperature and pressure of the hot and cold streams using the tuned geometry-independent, semi-empirical models presented in the chapter Modeling of the ORC system components.

Therefore, the model finds the system solution without taking any benchmark assumption to reach a specific turbine and pump suction thermodynamic states specified by the operator.

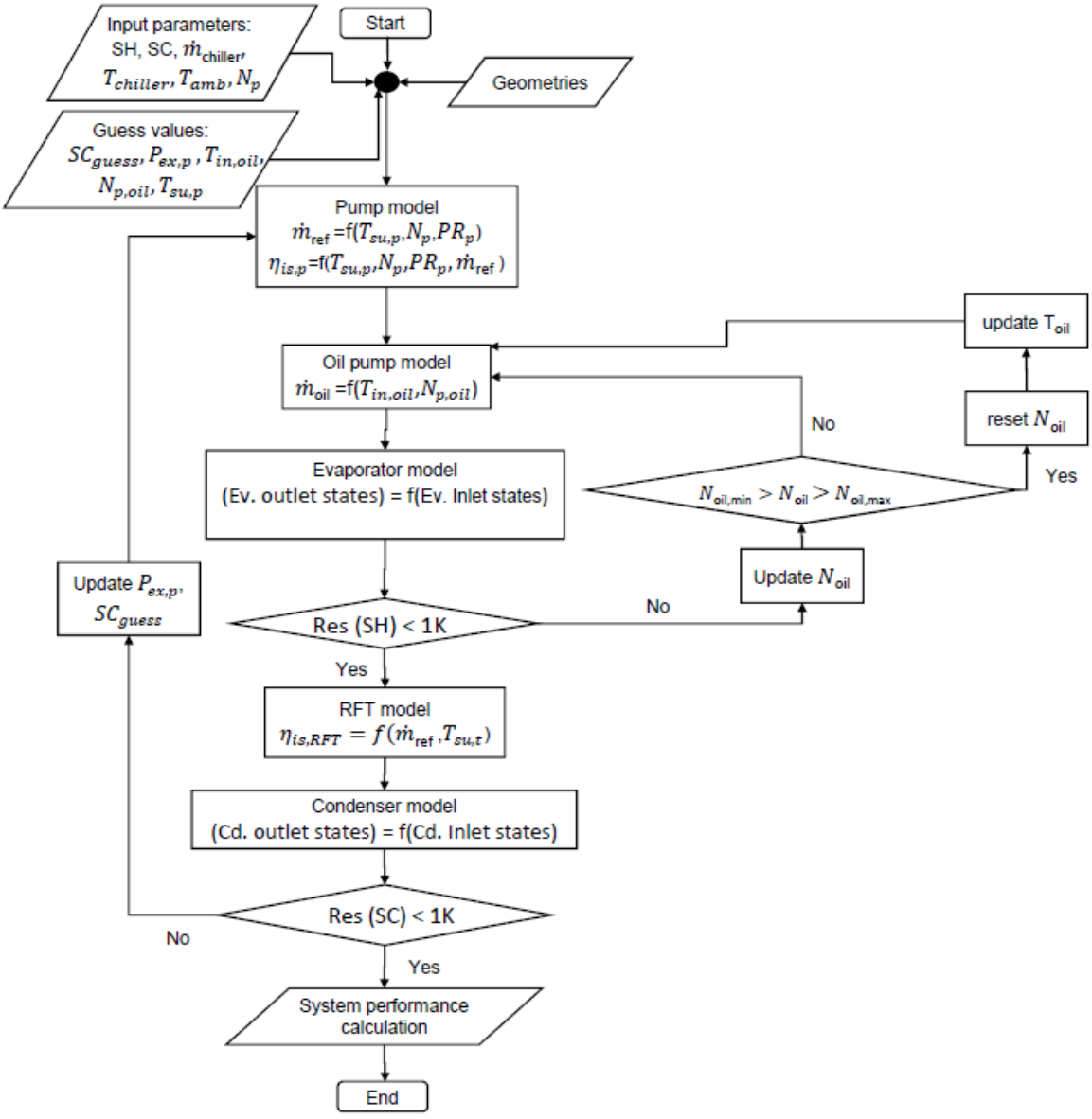


Figure 6-19. Flow chart of the ORC system solver using the experimentally tuned geometry-independent, moving boundary models of the PHEs

The system net efficiency is calculated as the ratio of the net of the RFT and pump mechanical specific works over the evaporator specific thermal load ($Q_{ev}$) as the following:

$$\eta_{net} = \frac{W_{net}}{Q_{ev}} = \frac{W_{exp} - W_p}{Q_{ev}} \tag{6-5}$$

To better appreciate the performance of the ORC unit, the system reversible efficiency ratio is used:

$$\eta_{rel} = \frac{\eta_{net}}{\eta_{rev}} \tag{6-6}$$

This expression reports the efficiency losses compared to the reversible cycle efficiency. The calculation of the reversible efficiency is performed considering a variable temperature heat source and assuming its exploitation down to the ambient temperature according to [15] as presented in Eqs. (6-7) and (6-8). The lower limit can be usually considered the ambient temperature except in some cases like waste heat recovery from the combustion exhaust gases, where the lower bound is higher to avoid the condensation of the corrosive substances.

$$\eta_{rev} = 1 - \frac{T_{amb}}{\bar{T}_H} \tag{6-7}$$

$$\bar{T}_H = \frac{T_{H,1} - T_{amb}}{\ln\left(T_{H,1}/T_{amb}\right)} \tag{6-8}$$

where $\bar{T}_H$ indicates the mean temperature of the variable temperature heat source exploited down to the ambient temperature, and $T_{H,1}$ is the inlet temperature of the hot working fluid in the evaporator.

The ORC system performances are presented in Figure 6-20 in a range of the low expansion pressure ratios (1.4-2). The system gross efficiency increases with the mass flow rate while the system net efficiency is changed marginally due to the increased refrigerant pump power consumption. The increasing pump power consumption leads to a smooth growth in the net power production, while the turbine produced power shows a steeper trend compared to the net power production.

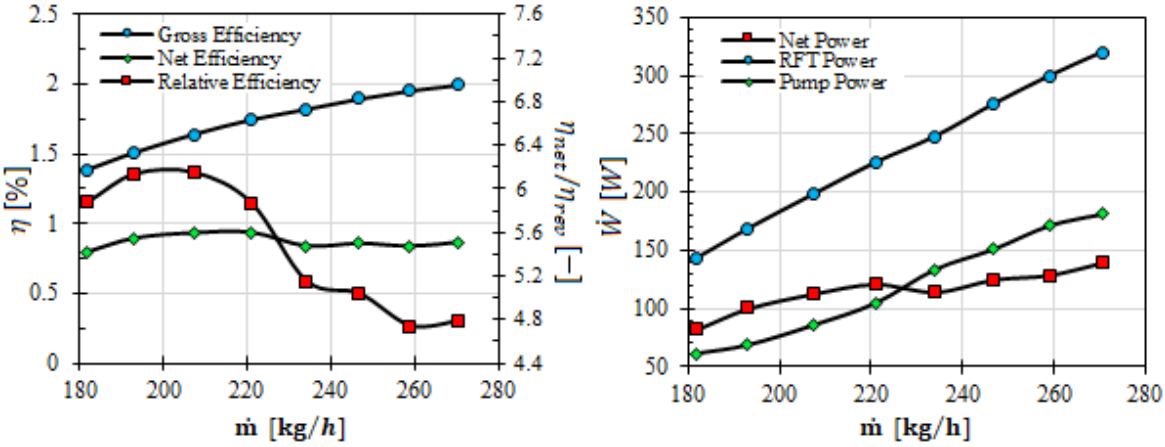


Figure 6-20. The system gross, net, and reversible efficiency ratio (left), and the system net, RFT and pump produced and consumed powers (right) by the mass flow rate of R134a

The reversible efficiency ratio instead shows a peak in Figure 6-20 as the net efficiency increases slightly in low mass flow rates, but it drops as the net efficiency does not alter considerably yet the reversible efficiency increases constantly as the oil inlet temperature goes up as shown in Figure 6-21.

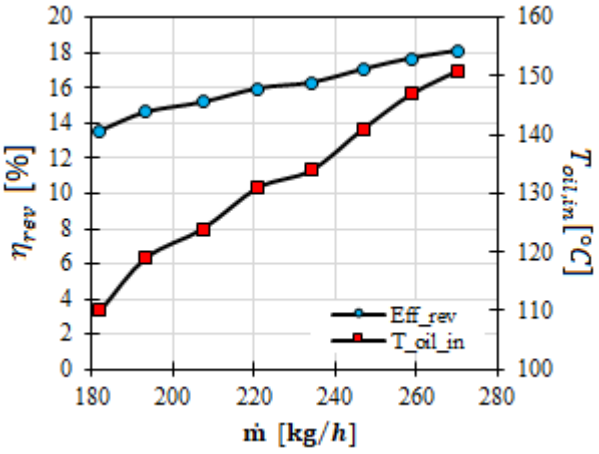


Figure 6-21. The reversible efficiency and oil inlet temperature to the evaporator by the mass flow rate of R134a

Therefore, the ORC system is expected to work with a net efficiency of below 1% using the RFT prototype and R134a in almost the same range of the mass flow rate that the scroll expander is tested. Let's compare the system mechanical efficiency using the experimental data of the scroll expander with R134a with the simulated system efficiency with the RFT. The mechanical efficiency is calculated using the expander measured shaft power and fluid enthalpy change in the pump as the pump shaft work was not measured.

$$\eta_{mech,net} = \frac{\dot{W}_{net}}{\dot{Q}_{ev}} = \frac{\dot{W}_{sh} - \dot{W}_{mech,p}}{\dot{Q}_{ev}} = \frac{\dot{W}_{sh} - \dot{m}_{ref}\left(h_{ex,p} - h_{su,p}\right)}{\dot{m}_{ref}\left(h_{ex,ev} - h_{su,ev}\right)} \tag{6-9}$$

The experimental results of the net mechanical efficiency are represented in Figure 6-22. Compared to the net efficiency using the RFT, it can be deduced that the system performance with the low BVR scroll expander is superior in some points while is inferior in others. This will be discussed further in the following section, where the isentropic efficiency of the RFT prototype is compared with the experimentally calculated efficiency of this scroll expander with R245fa adopted from the literature.

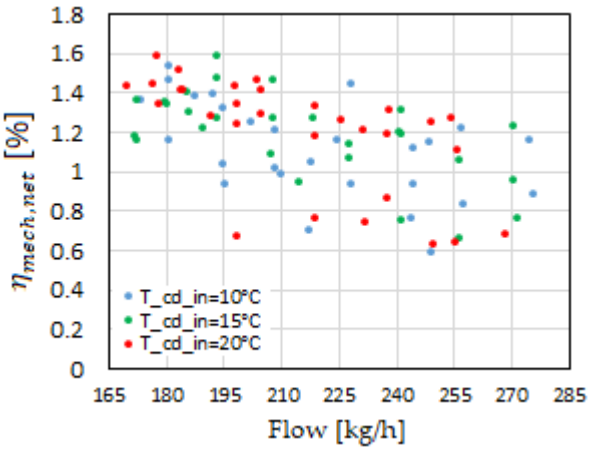


Figure 6-22. Net system mechanical efficiency using the experimental data of the scroll expander with R134a

In addition, another simulation of the same ORC system with the RFT prototype and using R245fa is performed to assess the performance of the ORC test bench with R245fa and using the RFT prototype, and also to present the system net efficiency when a more efficient pump is used to highlight better the impact of the refrigerant pumps in low-temperature power systems.

The modeling is performed assuming geometrical details[1] for the PHEs to use geometry-dependent models and a finite volume discretization scheme when the experimentally tuned models are absent. Pressure drops in the PHEs are neglected, oil and refrigerant pump mass flow rates are modeled using their theoretical mass flow rates, and the nominal isentropic efficiency of 85% is adopted for the refrigerant that is declared by the manufacturer.

In addition to the different component models, the system modeling approach is different as well. In fact, the kind of assumptions, limitations, inputs, and outputs of the component models model determines the most suitable modeling approach of the system consequently. For example, the pressure drops in the PHEs are neglected in this model, thus the expander pressure ratio is the same as the pump pressure ratio. This indicates the main difference in the system-level modeling that the condenser pressure is the input to this model and the cooling water mass flow rate is assumed as one of the adjustable variables to reach the preset subcooling degree in the condenser similar to the evaporator that the set superheating degree is maintained by adjusting the oil mass flow rate and the oil inlet temperature to the evaporator. The model is explained in detail in the following.

The following parameters have been considered as inputs to the model: (i) the mass flow rate of R245fa; (ii) the condensing pressure of R245fa; (iii) the superheating and

[1] The chevron angle and the corrugation pitch are the only unknown geometrical parameters that are assumed 45 degree and 3.5 mm respectively for the simulation purposes.

subcooling degree at the evaporator and the condenser respectively; and (iv) the hot source (oil) and cold sink (water) inlet temperatures as reported in Table 6-5.

Table 6-5. Inputs to the ORC unit model

| | | | |
|---|---|---|---|
| Oil inlet temperature | 100-120 °C | Organic fluid mass flow rate | 0.05-0.12 kg/s |
| Water inlet temperature | 20 °C | Condenser pressure | 3 bar |
| Superheating in the evaporator | 5 K | Ambient temperature | 15 °C |
| Subcooling at the pump inlet | 5 K | Organic fluid | R245fa |

For the scope of our analysis, the water inlet temperature has been assumed 5 K higher than the ambient temperature which corresponds to the common working condition of ORC systems using ambient temperature as the cooling medium. Thermo-physical properties of R245fa and water are obtained using CoolProp fluid database in MATLAB®, while oil properties are calculated using the table of properties provided by the supplier.

The model works according to an iterative procedure that calculates the mass flow rate of the hot source and the cold sink for the given mass flow rate of the refrigerant to reach the specified superheating and subcooling degrees. Specifically, 5 K superheating and subcooling at the evaporator and condenser are assumed.

Therefore, the main outputs of the iterative solver are: (i) the oil and the water mass flow rates needed to achieve the specified superheating and subcooling degree; (ii) the rotational speed of the pumps of the hot and cold heat transfer fluid and the working fluid; and (iii) the thermodynamic states of the fluids in different points to assess the performance of the ORC unit and its components. The scheme of the second model of the ORC unit is illustrated in Figure 6-23.

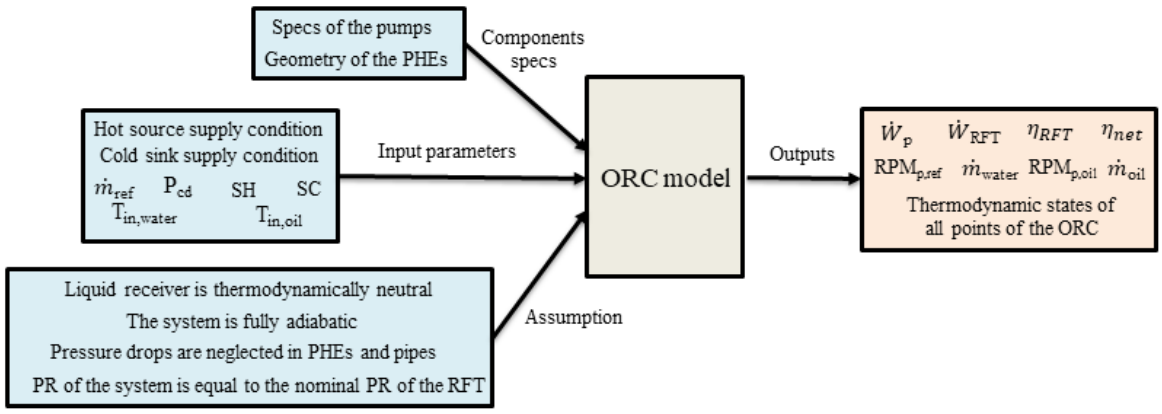


Figure 6-23. ORC model block diagram using geometry-dependent, finite volume models of the PHEs

The energy balance in the evaporator and condenser is solved using the finite volume method following an iterative procedure. The heat exchanger is divided into several nodes along their length, while a uniform distribution of the flow along the width of the plates is considered and pressure drops are neglected. Hence, the relevant state-of-the-art correlation is called in each cell of the cold and hot streams to estimate the convective heat transfer coefficient (CHTC) using the local properties of the fluids in both streams. These correlations are semi-empirical models obtained from the experimental studies of various organic fluids in PHEs with different geometries for boiling [146], single-phase [147], and condensation [148] CHTCs. For the single-vapor phase CHTC of R245fa, the correlation suggested in [54] is used. For the cooling water in the condenser, the correlation presented by Khan et al. [149] is adopted. All the considered correlations are reported in Appendix (C). The flow chart of the iterative solver of the ORC unit and that of the PHEs are presented in Figure 6-24.

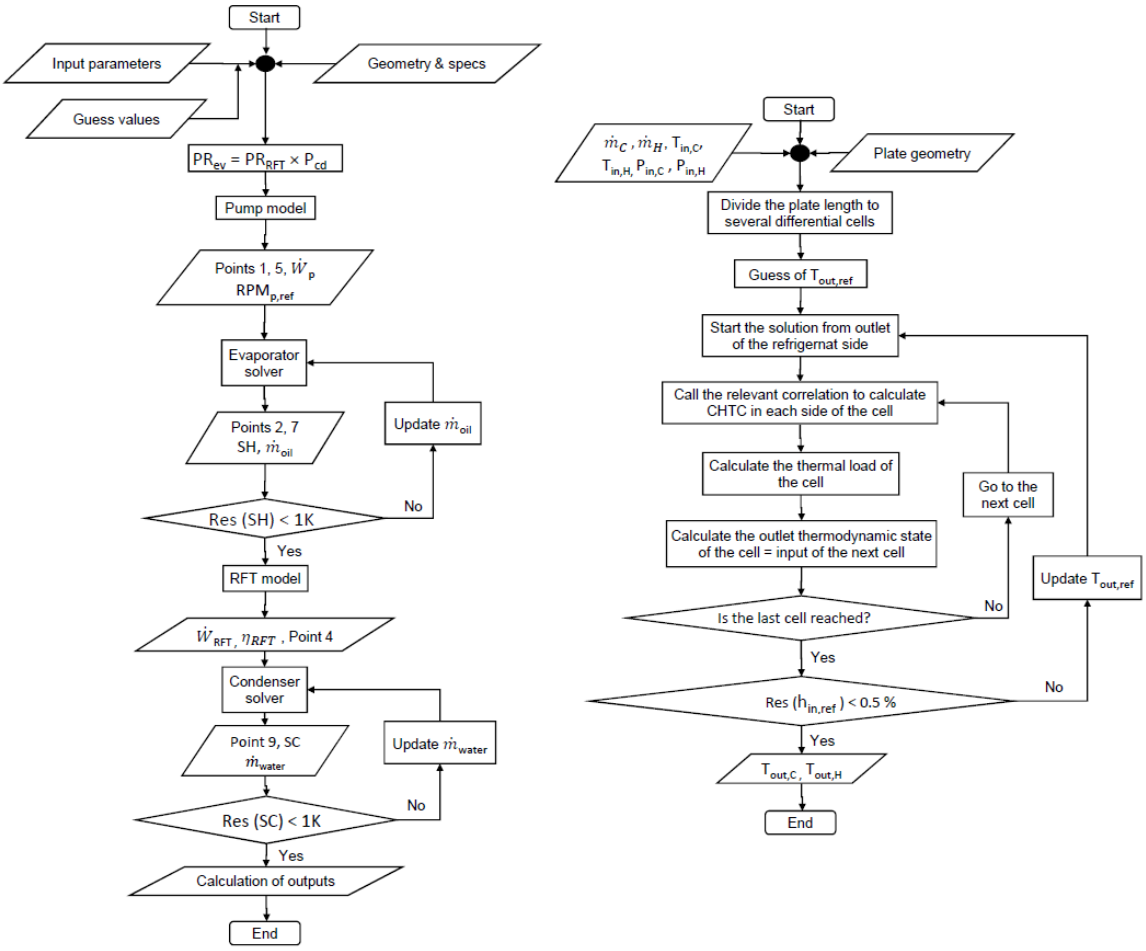


Figure 6-24. Flow chart of the ORC unit solver (left) and of the PHEs solver (right)

The net produced power by the ORC unit increases with the mass flow rate despite the growth rate of the net efficiency decreases because of the negative trend of the RFT isentropic efficiency as evident on the right of Figure 6-25. The net efficiency of the ORC unit is in the range of 1-2.3%; these low values are also due to the low temperature of the heat source that intrinsically lowers the efficiency of the power system. However, compared to the real system model using the semi-empirical pump model, the net efficiency is readily higher confirming the significant impact of the refrigerant pump on the net performance of the low-temperature power systems. Therefore, if an efficient pump is selected for a low-grade ORC system, the system performance is strongly correlated with the expander performance, especially the net produced power.

As regards the reversible efficiency ratio, it increases continuously with the mass flow rate up to a certain value and after that, it fluctuates within a small range. These up-and-down trends are related to the increment of the heat source inlet temperature leading to an increment of the reversible efficiency. The code starts with the fixed oil inlet temperature in the evaporator, then the oil mass flow rate is found using an iterative solver to reach 5 K refrigerant superheating within the specified tolerance. When the oil mass flow rate reaches the maximum of the oil pump, the oil inlet temperature increases one step, and the aforesaid procedure is repeated to find the oil flow rate again.

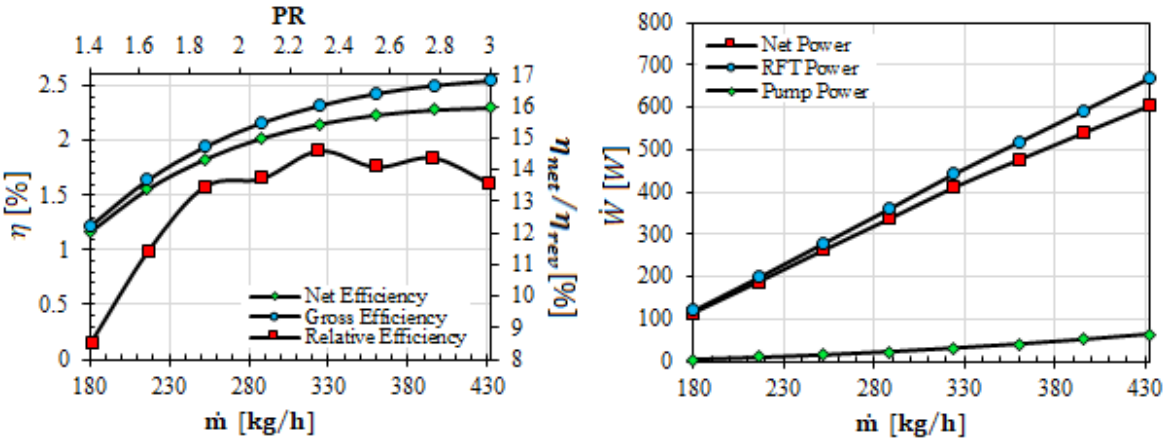


Figure 6-25. The system gross, net, and reversible efficiency ratio (left), and the system net, RFT and pump produced and consumed powers (right) by the mass flow rate of R134a

Finally, it is noteworthy that the gross efficiency of both system simulations, one using R134a and another using R245fa as the working fluid, is like each other in the range of the studied mass flow rates.

### 6.2.6 Comparison between the RFT prototype and the scroll expanders

To evaluate the potential of the RFT under investigation for ORC applications, its isentropic efficiency is compared to those of two scroll expanders reported in the literature. Indeed, scroll machines are common expanders for micro-scale ORC systems, and their performance extensively assessed using R245fa as working fluid. More precisely, the first machine that is considered is a 5 kW scroll expander with a BVR equal to 3.5, whose semi-empirical model was developed by Ziviani et al. [35]. This is the improved version of the model introduced by Lemort et al. [73] obtained using a series of experimental tests. Hence, the benchmark model used in this work includes the following losses: (i) suction and discharge pressure drops; (ii) suction and discharge heat transfer between the working fluid and the expander shell; (iii) heat loss from the expander shell to the ambient; and (iv) leakage flow inside the expander. This model is elaborated in Chapter 3, Modeling of the ORC system components.

The second scroll expander has a BVR of 1.9 and was tested by Campana et al. [20] using R245fa in low flow rates and low PRs and it is the same expander tested and modeled in this work. This expander is the same that was used in the experimental study of the ORC system in the thesis. The convenience of considering both these scroll expanders comes from the merits of the RFT in low PRs and the fact that the efficiency of the scroll expanders falls sharply in PRs lower than their BVR due to the over-expansion losses [80].

The thermodynamic state of the working fluid at the suction is defined using the PR calculated for the RFT at each mass flow rate considering the discharge pressure fixed at 2.5 bar and 5 K superheating degree at the suction pressure. Figure 6-26 shows the comparison between the RFT prototype and the scroll expander having a BVR of 3.5. As can be noticed, the isentropic efficiency of the RFT is higher at lower

PRs (and low mass flow rates accordingly), where the scroll expander becomes inefficient.

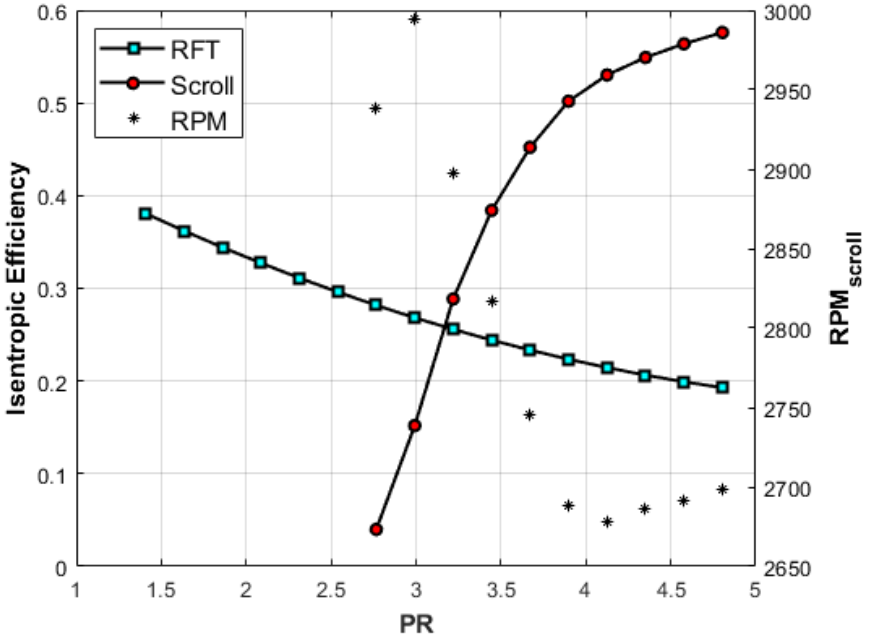


Figure 6-26. Comparison between the isentropic efficiency of the RFT and the scroll expander (BVR=3.5) in different PRs and the same suction thermodynamic state of R245fa. The shaft speed of the scroll expander is reported too.

Regarding the second scroll expander, it has a BVR of 1.9 and was tested with R245fa in low mass flow rates and PRs in a similar ORC unit [20]. During the test campaign, the suction pressure of the expander was fixed while the outlet pressure was varied to obtain different PRs and the shaft speed ranged between 150 and 1,500 rpm. Figure 6-27 shows the comparison of the isentropic efficiency of the scroll expander (BVR = 1.9) with that of the RFT at low PRs. By comparing Figure 6-26 and Figure 6-27, the lower-BVR scroll expander operates with higher isentropic efficiency at low PRs compared to the higher BVR one because of the fewer losses due to over-expansion. As a result, the operating conditions in which the RFT has

higher isentropic efficiencies shrink. Nevertheless, in very low PRs, the RFT is still advantageous since the isentropic efficiency of the scroll expander falls steeply. On the contrary, despite being lower in a wide range of operating conditions, the isentropic efficiency of the RFT changes less with the pressure ratio. Therefore, the examined RFT proves to be suitable for low-temperature WHR applications also when considerable fluctuations of the heat source are expected. This is the case, for example, of a vehicle engine whose operation can significantly change during the running of the vehicle. Instead, volumetric machines like scroll expanders have some limits and their reliability may deteriorate in case of high fluctuations of the heat input.

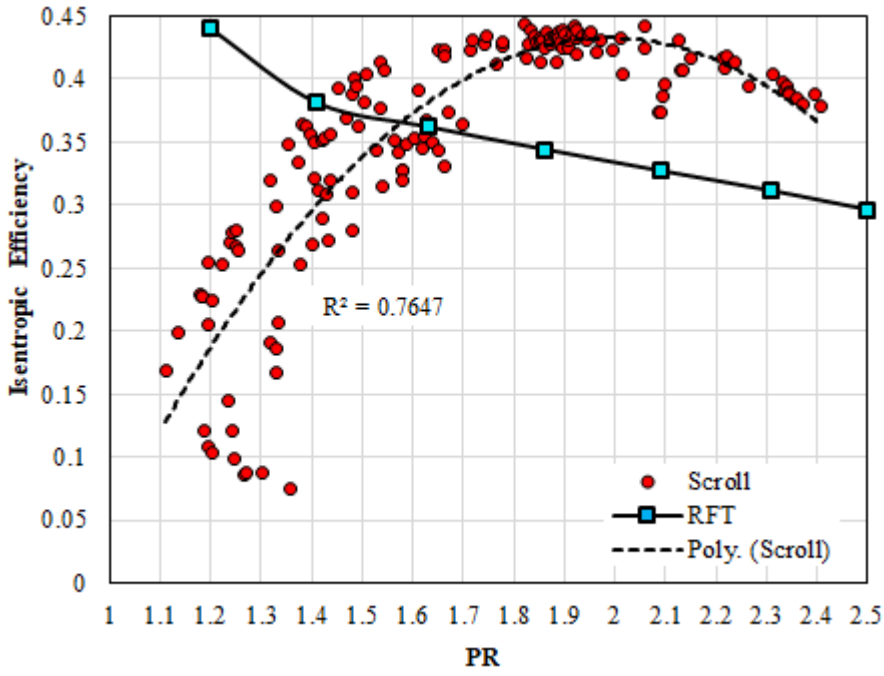


Figure 6-27. Comparison between the isentropic efficiency of the RFT and the scroll expander (BVR=1.9) in different PRs and the same suction thermodynamic state of R245fa

Therefore, the comparison has shown that the considered RFT has some advantages compared to scroll expanders which could make them competitive with existing machines adopted in small-scale ORCs at present.

## 6.3 Summary and conclusions

In this chapter, the performance of an RFT operating with R245fa has been numerically studied and its potential in ORC systems for WHR applications analyzed. Then, the performance of the proposed expander has been compared with those of two scroll expanders having different BVRs (1.9 and 3.5) with varying PRs and mass flow rates. The first-time investigation of this expander for WHR applications has provided useful insights into its merits and criticalities. The main results of the analysis carried out are summarized as follows:

- the isentropic efficiency of the RFT achieves a peak of about 44% at the maximum rotational speed and the minimum mass flow rate considered in the simulations (6,000 rpm & 0.04 kg/s).
- the output power increases with the mass flow rate almost linearly up to a certain limit depending on the rotational speed of the turbine.
- the PR of the RFT decreases with the shaft speed, thus confirming the peculiarity of this type of turbine, which combines some characteristics of dynamic turbines and some others of volumetric expanders.
- the maximum power output and the net efficiency of a non-regenerative ORC unit using the RFT under investigation are about 600 W and 2.3% for a working fluid mass flow rate in the range 0.05-0.12 kg/s.
- compared to two scroll expanders reported in the literature, the proposed RFT has shown higher isentropic efficiencies at low PRs and flow rates.

Moreover, the isentropic efficiency of the RFT changes less with PR thus making it suitable for WHR applications characterized by high fluctuations of the heat source.

Compared to scroll expanders, the merits of the RFT are not limited to the better performance at low PRs and flow rates but also its low manufacturing cost needs to be considered in such comparison. Furthermore, such results are obtained considering a first design RFT. A further re-engineering of the turbine aimed at reducing the main losses, especially reducing the leakage flow through the clearance gap between the stripper body and the blade tips can improve the performance of the machine by increasing its isentropic efficiency also at higher PRs and flow rates.

## 6.4 **Nomenclature**

| | |
|---|---|
| Bd | Bond number [-] |
| Bo | boiling number [-] |
| $d_h$ | hydraulic diameter [m] |
| g | gravitational acceleration [m/s$^2$] |
| h | specific enthalpy [J/kg] |
| $h_{lg}$ | phase change latent heat [J/kg] |
| L | length [m] |
| $\dot{m}$ | mass flow rate [kg/s] |
| N | shaft rotation speed [rpm] |
| Nu | Nusselt number [-] |
| Pr | Prandtl number [-] |
| Re | Reynolds number [-] |
| T | temperature [°C] |
| U | impeller velocity [m/s] |
| $\dot{W}$ | power [kW] |
| We | Weber number [-] |
| $x$ | vapour quality [-] |
| $G$ | mass flux [kg/m$^2$.s] |
| n | number of blades |

*Greek Symbols*

| | |
|---|---|
| $\beta$ | chevron angle [degree] |
| $\gamma$ | corrugation aspect ratio [-] |
| $\Delta$ | differential operator [-] |
| $\eta$ | isentropic efficiency [-] |
| $\mu$ | dynamic viscosity [Pa.s] |
| $\rho$ | density [kg/m$^3$] |
| $\phi$ | surface enlargement factor [-] |
| $\psi$ | stage loading [-] |

*Subscripts and superscripts*

| | |
|---|---|
| 0 | total |
| 1 | inlet |
| 2 | outlet |
| amb | ambient |
| act | actual |
| C | cold |
| cal | calculated |
| cd | condenser |
| eq | equivalent |
| ev | evaporator |
| H | hot |
| l | liquid phase |
| lo | liquid only |
| m | mean |
| P | pump |
| ref | refrigerant |
| rev | reversible |
| S | isentropic |
| su | suction |

t,s total-to-static

V vapor phase

W wall

*Acronyms*

BVR Built-in Volume Ratio [-]

CHTC Convective Heat Transfer Coefficient

lpm liters per minute

PR Pressure Ratio [-]

ORC Organic Rankine Cycle

RFC Regenerative Flow Compressor

RFP Regenerative Flow Pump

RFT Regenerative Flow Turbine

RPM Revolutions Per Minute

SC subcooling

SH superheating

SV Swept Volume [l/rev]

WHR Waste Heat Recovery

# Chapter 7

# 7. An application of micro-ORC systems for WHR & CHP

*"A sapient without deeds is like a bee without honey"*

Saadi Shirazi, Persian poet & writer

## 7.1 Introduction

The mass-sensitive, component-oriented modeling of a micro-scale ORC system studied in this work is presented in the previous chapters. In addition, the regenerative flow turbine (RFT) is a novel turbine suitable for low-grade ORC systems is investigated. In this chapter, a micro-scale ORC system (mORC) coupled with an integrated electricity production system is investigated. The aim is to study the performance of the mORC system as the bottoming cycle for waste heat recovery (WHR) of the top cycle, which is a Steam Injected micro Gas Turbine (SImGT) fed by the produced biogas from a fluidized-bed gasifier. The integrated system is based on the renewable energy source (biomass) for stand-alone combined heat and power (CHP) production. The integrated system is modeled in detail to achieve realistic system performance. The description of the component-oriented modeling of the integrated system and its performance are described in the following.

### 7.1.1 Gasifier + SImGT + mORC

Nowadays, biomass is the dominant renewable energy source among EU-28 with about two-thirds of the final energy production from solid, gaseous, and liquid

biomass sources [150], and it is estimated that bioenergy would contribute to about 30% of the global primary energy supply in 2050 [151]. Several studies have stated that the use of biomass can potentially meet the world's current energy consumptions if the sustainability issues of this renewable energy source can be efficiently resolved [152,153].

Indeed, biomass is abundant and available in many places from agro-industrial residues to municipal wastes, it is inherently inexpensive, and it may be renewable. In recent years, the development of advanced thermo-chemical processes has fostered the traditional uses of biomass energy from agro-industrial residues into distributed power generation systems. However, suitable small-scale energy systems have to be developed and optimized to efficiently convert the low-density energy of biomass fuels into heat and electricity production [154].

The simplest way to convert the potential energy of biomass for electricity production is its direct burning in a steam or gas power plant. However, the inefficient combustion process of such a fuel entails significant environmental pollution and leaves behind a huge amount of slag and ash residuals in the combustor chamber. Gasification is another option to exploit biomass for power production as extensively investigated in the last decades by many researchers [155]. Depending on the oxidant used in the process, i.e. air, oxygen, $CO_2$, or steam, the composition of the produced synthesis gas (syngas) and its Lower Heating Value (LHV) vary considerably. The use of air is the most common approach, but this results in diluted syngas with nitrogen, which consequently has a low-LHV [156]. In general, oxygen can increase the efficiency of the gasification process and the LHV of the produced syngas, but it is a costly choice. $CO_2$ can be used as the oxidant agent [157], especially when it is available on-site from the by-products of other processes. Another attractive option to avoid diluted syngas is steam gasification using an indirectly heated gasifier. Thanks to the use of steam, the conversion rate of the carbon content in the gasification process increases thus

resulting in a less tar-contaminated product [153]. However, thermal energy is needed to produce steam and a more complex start-up plan is required.

One option to exploit the produced syngas is using it in external or internal combustion engines (ECEs or ICEs). In case of poor conditioning, tar and alkali compounds are expected to be present in the syngas, and consequently, externally fired combustors are preferred. In this case, the syngas can be ignited at the same pressure as the gasifier (usually atmospheric pressure), and the fuel booster is not required. As a result, there is no necessity to cool down the syngas. Hence, the syngas can be directly injected into the combustion chamber at high temperatures resulting in a more efficient gasification process [158]. However, a high-temperature heat exchanger is required to transfer the heat from the combustion chamber to the working fluid of the power cycle [158], which represents a significant item of cost in small-scale plants. If the syngas passes through adequate conditioning stages, it can be exploited directly in ICEs, or it can be injected into the combustor of Gas Turbines (GTs). In these cases, the syngas must be pressurized to a pressure slightly higher than the pressure in the engine or the combustion chamber, thus a fuel booster must be considered in the system.

At plant scales lower than 300 kWel, despite lower electrical efficiencies compared to ICEs, micro GTs (mGTs) have revealed several advantages compared to ICEs such as reduced emissions, lower noise, and vibration, reduced maintenance, higher reliability, and flexibility in fuel selection [159]. Furthermore, thanks to technological advancements in mGTs, not only the gap in performance with ICEs is being narrowed, but also some merits of the mGTs have arisen. Several design solutions such as Humid Air Turbines (HAT), Evaporative Gas Turbines (EvGT), and Steam-Injected Gas Turbines (SIGT) have been employed to simultaneously enhance the performance of mGTs, and to reduce the emissions, especially NOx [160]. In SIGT cycles, steam is injected downstream the compressor to increase the mass flow rate in the turbine thus increasing the net produced power. Moreover,

the injected steam locally cools down the flame in the combustion chamber resulting in less $NO_x$ and CO emissions.

In addition, steam injection adds flexibility to the power cycle in case of direct use of the rejected heat for CHP purposes, and it has been adopted widely in medium-scale cogeneration systems (few MWel) [161]. In particular, the rejected heat from the system can be used to produce the steam when the electric demand is high, or it can be exploited directly in the heat exchanger of the CHP in case the thermal demand is at the peak. Thus, the steam injection can increase the operating hours of cogeneration units with a positive impact on their economic competitiveness [162].

In steam gasifier reactors, coupling the gasifier with an mGT system facilitates the thermal integration of the gasifier unit since the steam can be produced by exploiting the thermal energy of the flue gas from both the combustor of the gasifier and the combustion chamber of the mGT unit. However, humidified cycles have been studied only partially in mGTs, in which radial turbo-machines are usually adopted. In such systems, the compact design limits the modifications to the existing configuration and also the amount of steam that can be injected [161]. Hence, studies have focused on the impacts of humid turbines on the performance of power cycles and the economic aspects of this design solution. For example, De Paepe et al. [162] conducted a simulation of a humid Steam Injected micro Gas Turbine (SImGT) unit in Aspen Plus® and compared the simulation with experimental results. They adopted Turbec T100 unit and modified it to inject steam downstream the compressor. Their simulation showed that the electrical efficiency increased 2.2% at fixed output work when 5% of the mass flow rate of air is replaced by steam. In addition, their simulation results were optimistic compared to the experimental results. A hybrid power system consisted of a SImGT (Turbec T100) and a Solid Oxide Fuel Cell (SOFC) was tested by Ferrari et al. [163]. They studied the effect of varying the mass flow rate of the injected steam (up to 30 g/s) downstream of the compressor on several operational characteristics of the mGT.

Their results showed that at a fixed power output, the shaft rotational speed and the fuel mass flow rate decreased as the mass flow rate of the injected steam increased. In other words, the extra work produced by steam injection and thus less required fuel to produce fixed power output was superior to the increase of the fuel required to produce the steam. Stathopoulos and Paschereit [164] conducted a techno-economic analysis of an mGT (Turbec T100) for cogeneration in dry and wet modes using Aspen Plus®. The flue gas from the turbine was exploited in a heat exchanger to produce warm water in the dry mode, while a Heat Recovery Steam Generator (HRSG) was considered additionally to the heat exchanger of CHP to produce steam (up to 35 g/s) in the wet mode. They showed that the fuel mass flow rate decreases in the wet mode at a fixed produced power. Moreover, the efficiency of the mGT increased 2.7% in the wet operation at maximum mass flow rate of the injected steam, while the thermal power of CHP decreased dramatically. Their results confirmed longer annual operation time and higher electricity production of SImGT compared to the dry operation, and it can be an attractive investment for CHP market. A SImGT (Turbec T100) unit integrated with a gasifier has been investigated by Renzi et al. [161]. They compared the system fuelled with the produced syngas with that using natural gas. They also developed a 1-D model of the combustion chamber to study the effect of the steam injection on the emissions. Keeping the outlet temperature of the turbine fixed at the design point, their results showed that the fuel mass flow rate increased with higher mass flow rates of the injected steam. In addition, by increasing the mass flow rate of steam (up to 56 g/s), both the net output power and the electrical efficiency of the integrated system increased.

To the best of the author's knowledge, no work can be found in the literature addressing the interactive coupling of a gasifier, a SImGT, and a bottom Organic Rankine Cycle (ORC) unit and considering a realistic process design. ORC systems, indeed, are considered as one of the most common and competitive technologies to

convert thermal energy from low-grade heat sources into electricity [20] thus potentially recovering the thermal power output of the top mGT. In recent years, many researchers have focused on ORCs, and some studies have been performed on coupling ORC systems to mGTs. For example, Invernizzi et al [165] conducted a thermodynamic simulation study of ORC systems powered by the exhaust of mGT units using several fluids. They concluded that by adopting an ORC unit, it is possible to increase the net electric power by 1/3 approximately, which results in the rise of the net efficiency of a 100 kW turbine from its nominal value of 30% to about 40%. Techno-economic analysis of ORCs coupled with biomass-fuelled Externally Fired GT (EFGT) was performed by Camporeale et al [166]. Their thermodynamic study on a 1.3 MW EFGT showed that both the output electric power and net electric efficiency of the system increased by about 50% while the output thermal power reduced by approximately 74%. They also concluded that the EFGT+ORC system is more profitable than the simple EFGT unless when the thermal energy demand or heat selling price is high.

Therefore, in this study, a small-scale CHP system consisting of a dual-fluidized-bed gasifier, an mGT system, and an Organic Rankine Cycle (ORC) as the bottom cycle has been simulated in Aspen Plus®. Steam is considered as the oxidant in the gasifier unit thus perfectly matching with the SImGT system. The subsystems have been modeled considering the practical requirements and characteristics of the main components, which results in a more realistic calculation of the net performance of the integrated system. In particular, the energy performances of the system have been evaluated with varying operating conditions by considering the mass and energy balances of each component while the related $CO_2$, CO, and $NO_X$ emissions are roughly estimated. Therefore, the main novelties of this study rely on: (i) the proposed configuration which takes into account the main practical issues related to the integration of the different subsystems; (ii) the improved gasifier model in Aspen Plus® that performs the energy balance of the reactor using a

combustor model and an auxiliary fuel; and (iii) the modeling of proper gas conditioning units for a given biomass feedstock to meet the practical requirements of a syngas-fuelled mGT.

## 7.2 **Modeling of an integrated system**

The integrated system is designed with the final aim of obtaining a reliable and efficient biomass-fuelled distributed power system. In particular, the following main sub-systems have been included in the model: (i) a 600 kWth biomass input gasifier and the related gas conditioning units; (ii) a SImGT unit based on the Turbec T-100 mGT with nominal electric power and thermal output of 100 kWel and 155 kWth respectively; (iii) a regenerative ORC unit with a nominal rated power of 10 kWel/100 kWth.

More precisely, several hot gas conditioning units have been considered in the design of the integrated system to purify the produced syngas to the allowable level required by mGTs as reported in [156]. The hot gas conditioning units are a dolomite reactor, ceramic filter candles, a kaolin bed for alkali removal, an HCL adsorber reactor, and an $H_2S$ adsorber reactor modeled in separate blocks downstream the gasifier reactor. The advantage of using the hot gas conditioning units is to limit the thermal dissipation to the ambient, which can improve the gasification efficiency by 3-4% [167]. Therefore, the high enthalpy of the syngas can be recovered in a heat exchanger for process purposes, which in this study corresponds to the steam generation. Finally, the partially conditioned syngas is cooled down before entering the fuel booster to avoid its inefficient performance, and its water content is separated resulting in dry and purified syngas. The purified syngas is then ignited in the combustion chamber of the mGT, and the flue gas expands in the turbine to produce electricity. Eventually, the flue gas of the mGT unit is mixed with the flue gas of the gasifier combustor. The flue gas of the system

is exploited in the evaporator of the ORC system to produce additional electric power. Figure 7-1 shows the schematic configuration of the proposed integrated system together with the design temperatures and pressures that are input into the model.

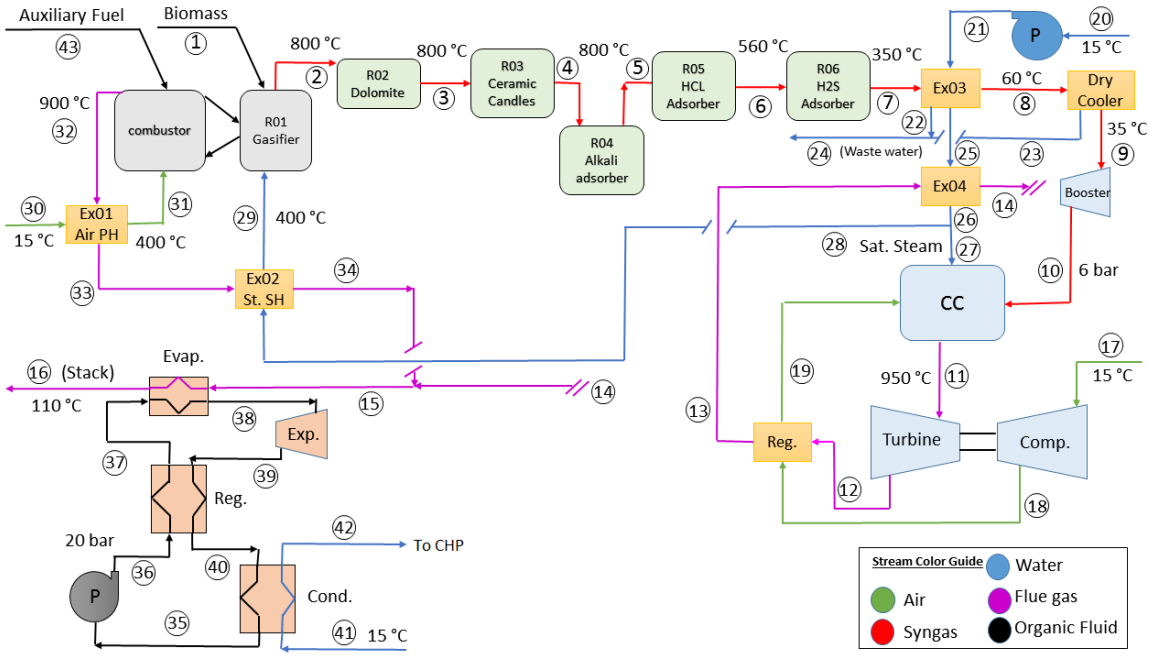


Figure 7-1. Schematic of the integrated system

Regarding the Heat Recovery Steam Generator (HRSG) unit, steam is produced in the first stage by cooling down the purified syngas to 60 °C (Ex03) then the water is heated up in another heat exchanger (Ex04) using hot flue gas out of the combustion chamber to reach a steam condition with 10°C of superheating. A fraction of the produced steam is sent to the combustion chamber of the mGT unit and the rest is superheated using the flue gas of the combustor of the gasifier in a heat exchanger (Ex02) to reach the design temperature of 400 °C. Hence, the total mass flow rate of the input water corresponds to the sum of the process steam mass flow rate calculated based on the steam-to-biomass ratio (S/B) and the mass flow rate of the

steam that is injected into the combustion chamber. Therefore, depending on the working conditions of the gasifier and the SImGT unit, the mass flow rate of the water is varied leading to fluctuations of temperatures of the flue gas streams. In turn, these fluctuations affect the thermal and electrical power production of the mGT and the bottoming ORC unit.

### 7.2.1 Gasifier and gas conditioning units

In a real gasification unit, the gasifier itself, the dolomite reactor, the ceramic filter candle, and the kaoline bed are embedded in one reactor. However, in the simulation model developed in Aspen Plus®, they have been considered as separated blocks as shown in Figure 7-1. In addition, the thermal integration of the whole system is considered in the simulation, which is important in the gasification process especially when steam must be generated.

- Fluidized-bed gasifier

The gasifier under investigation is a dual-fluidized-bed reactor that realizes the partial oxidation of the biomass at atmospheric pressure and high temperatures (about 800 °C). Steam is used as the oxidant agent and the biomass is hazelnut shell whose properties are reported in Table 7-1 along with the main input parameters of the gasifier model. The same proximate and ultimate analysis reported in Table 7-1 are used in the model. In addition, the gasification reactions used in the model are summarized in Table 7-2.

Table 7-1. Gasifier input parameters, and physical and chemical properties of hazelnut shell [168,169]

| Input parameters | values | | | Unit of measurement | |
|---|---|---|---|---|---|
| Steam to Biomass ratio (S/B) | 0.25-1 | | | kg of steam/kg of biomass | |
| $T_{gasifier}$ | 800 | | | °C | |
| $P_{gasifier}$ | 1 | | | Bar | |
| Proximate analysis, dry basis (% wt) | | | | | |
| Volatile matter (%) | | Fixed carbon (%) | | Ash (%) | |
| 78.66 | | 20.08 | | 1.26 | |
| Ultimate analysis, dry basis (% wt) | | | | | |
| Carbon (% wt) | Oxygen (% wt) | Hydrogen (% wt) | Nitrogen (% wt) | Chlorine (% wt) | Sulfur (% wt) |
| 46.76 | 45.83 | 5.76 | 0.22 | 0.76 | 0.67 |
| LHV (MJ/kg), raw | 17.228 | | LHV (MJ/kg), dry | 18.727 | |
| Bulk density (kg/m$^3$) | 319.14 | | Moisture (%) | 7.9 | |

Table 7-2. Gasification and combustion reactions [170]

| Reaction | Reaction name | Heat of reaction | Reaction number |
|---|---|---|---|
| Heterogeneous reaction | | | |
| $C + 0.5\ O_2 \rightarrow CO$ | Char partial combustion | (-111 MJ/kmol) | (7-1) |
| $C + H_2O \leftrightarrow CO + H_2$ | Water-gas reaction | (+172 MJ/kmol) | (7-2) |
| Homogeneous reactions | | | |
| $H_2 + 0.5\ O_2 \rightarrow H_2O$ | $H_2$ partial combustion | (-283 MJ/kmol) | (7-3) |
| $CO + H_2O \leftrightarrow CO_2 + H_2$ | Water-gas shift | (-41 MJ/kmol) | (7-4) |
| $CH_4 + H_2O \rightarrow CO + 3H_2$ | Steam-methane reforming | (+206 MJ/kmol) | (7-5) |

The adopted model of the gasification process is the improved model described in [170] by adding a combustor model to consider the realistic energy balance of the gasifier reactor and considering the production of alkali compounds during the gasification process.

The gasifier reactor externally surrounds the combustion chamber, which in turn heats it indirectly. Heat is exchanged by the circulation of the bed material between the combustion chamber and the gasifier chamber, and the heat transfer through

the combustor walls. Hence, a fraction of the thermal energy needed for the pyrolysis of the input raw biomass is provided by the combustor. More precisely, 20% of the total carbon content of the raw biomass equivalent to almost 10% of the input biomass mass flow rate (see Table 7-1) is considered as the unreacted char that is transferred to the combustor. The remaining part of the thermal load must be provided using an auxiliary fuel (charcoal in this study). The high-temperature flue gas produced in the combustor is then used in two heat exchangers to heat the inlet air of the combustor of the gasifier to the design temperature (Ex01) and to superheat the inlet steam to its design temperature (Ex02) as shown in Figure 7-1.

- Gas conditioning units

As mentioned in the previous section, gas conditioning is performed to meet the operational requirements of the mGTs. The main contaminants that are considered detrimental for an mGT are: particles, tar, $H_2S$, HCL, and Alkali compounds (NaOH and KOH) [156]. In this study, toluene and benzene are considered as tar since they allocate most of the volume fraction of the tar produced in the gasification process and they are more likely to condensate and deposit in the equipment [171]. The models used in this work to simulate the production of tar, $H_2S$, and HCl are presented in [172]. To simulate the production of Alkali compounds, an RStoic reactor is added considering the following stoichiometric reactions [173]:

$$Na_2O + H_2O \rightarrow 2NaOH \quad (7\text{-}6)$$

$$K_2O + H_2O \rightarrow 2KOH \quad (7\text{-}7)$$

Several parameters influence the concentration of the contaminants in the syngas. The more important ones are the biomass type, the gasifier type, the gasification agent, and the gasification process temperature. In this study, all these parameters are considered in the design of the integrated system to achieve a *passive purification* in the design. Such design considerations are described in the following.

The high-temperature operation of the gasifier increases the tar cracking significantly. According to [174] if the temperature of the gasifier reactor increases from 700 °C to 850 °C the tar forming reduces by 74%. In addition, the tar cracking process in both the dolomite and the ceramic candles becomes very inefficient at low temperatures [175]. Therefore, the temperature of the gasifier and the three embedded conditioning reactors is considered uniform and the same in the simulations (equal to 800 °C). Fluidized-bed gasifiers have shown a more flexible performance compared to fixed-bed ones with the main advantage of high power density meaning higher biomass flow rate per installed reactor area [154]. Generally speaking, steam gasification is one of the most efficient techniques to achieve the highest stoichiometric yield of hydrogen [176,177]. The S/B ratio has a significant effect on the concentration of the tar contaminants and the composition of the produced syngas. For instance, studies [178,179] showed that in a dual-fluidized-bed gasifier the maximum content of $H_2$ and the least tar concentration in the syngas was produced for an S/B = 1.4. Hazelnut shell is a sustainable biomass feedstock since it is not in competition with food production and it allows the use of agricultural waste. Furthermore, hazelnut shells have several advantages compared to other kinds of waste biomass: uniform size, high LHV and less produced contaminants during the syngas production. In particular, the content of sulfur, chlorine, and ash in hazelnut shells are relatively low compared to many other biomass stocks [180]. From this perspective, it is suitable for gasification and allows to produce a good quality syngas [168,181].

Despite considering all the above-said *passive purification* measures in the design of the system, the use of *active purification* units is still inevitable to meet the purity requirements of mGTs. According to the model, the first reactor considered downstream the gasifier is the dolomite reactor. Dolomite is mixed with the bed material in the gasifier mainly to enhance the high-temperature tar cracking process inside the gasifier [182]. The conversion rates considered in the model for tar

(benzene, $C_6H_6$, and toluene, $C_7H_8$) and inorganic impurities in the dolomite reactor are shown in Table 7-3.

Table 7-3. Conversion rate (X) of relevant contaminants in the dolomite reactor [183–188]

| | |
|---|---|
| $X_{C6H6}$ (%) | 80 |
| $X_{C7H8}$ (%) | 50 |
| $X_{H2S}$ (%) | 85 |
| $X_{HCl}$ (%) | 85 |
| $X_{NH3}$ (%) | 95 |

After the dolomite reactor, innovative ceramic filter candles filled with Ni-catalyst pellets are adopted. They are located in the freeboard of the gasifier to remove particulate matter and tar and to increase the methane conversion reaction [175]. The conversion rates used in the model are taken from the experimental results of a bench-scale study, in which a fluidized-bed gasifier equipped with ceramic candles partially filled with commercial Ni-catalyst pellets was investigated [175]. The conversion rates are average values of tests performed at the gasifier temperature of almost 820 °C and with an S/B = 0.5. The conversion rates are reported in Table 7-4 assuming the temperature of the ceramic candles equal to that of the gasifier.

Table 7-4. Conversion rate (X) of reactive substances in the ceramic candle at S/B=0.5 [175]

| | |
|---|---|
| $X_{CH4}$ (%) | 90 |
| $X_{C6H6}$ (%) | 95 |
| $X_{C7H8}$ (%) | 88 |

Further details on the models of these two gas conditioning reactors (dolomite reactor and ceramic filter candles) developed in Aspen Plus® can be found in [172]. The third active purification unit is the kaolin bed aims at removing alkali compounds. Kaolin can be mixed with the bed material or can be placed in the freeboard of the gasifier; hence, its operating temperature is considered the same as the gasifier reactor. According to [189] a bed of kaolin is considered to remove the alkali from the gas with a conversion rate of 71% for both the NaOH and KOH at the operating temperature of 800 °C.

The next two purification reactors are the hot gas conditioning units that are adopted to reduce HCL and $H_2S$ concentrations, and they are located outside the gasifier reactor in the real case. Even though the operating temperature of these two reactors is lower than the gasifier temperature, they can be considered hot gas conditioning units. According to Dou et al [185], $NaHCO_3$ is one of the best alkali-based sorbents able to remove HCl to concentrations lower than 1 ppm in the temperature range of 526-650 °C. Hence, in this study $NaHCO_3$ is considered to reduce HCl according to the following reaction:

$$NaHCO_3(s) + HCl(g) \rightarrow NaCl(s) + H_2O(g) + CO_2(g) \quad (7\text{-}8)$$

Eventually, the last gas conditioning reactor is the $H_2S$ adsorber which makes use of ZnO catalysts at design temperatures of 350 °C to reduce the $H_2S$ concentration to less than 1 ppm [190]. The reaction considered in the model is the following:

$$ZnO + H_2S \rightarrow ZnS + H_2O \quad (7\text{-}9)$$

After being purified to some extent, the syngas is cooled down before the fuel booster to avoid inefficient compression. Hence, the syngas is cooled down from 350 °C to 60 °C in the first heat exchanger of the HRSG unit (Ex03) thus heating the water supply. Then, it is cooled down to 35 °C in a dry cooler and its moisture content separated from the syngas before entering the fuel booster (S9 in Figure 7-1). Considering the atmospheric condensation temperature of benzene and toluene at

80.15 °C and 110.6 °C respectively [191], and the fact that alkali compounds become solid at 350 °C and 1 bar [192], all tar and alkali compounds are removed as the water condensates in Ex03 and the dry cooler and they are accumulated in wastewater stream (S24 in Figure 7-1).

### 7.2.2 mGT and HRSG unit

To include the realistic performance of the mGT unit, the Turbec_T100 is considered and the following main components are included in the model: (i) a centrifugal compressor; (ii) a single-shaft radial turbine; (iii) a regenerator; and (iv) a combustion chamber. Table 7-5 reports the nominal performance of the mGT unit fuelled by natural gas (NG) [193,194].

Table 7-5. Nominal performance of Turbec_T100 fuelled by NG*

| | | | |
|---|---|---|---|
| Net Electric Power | 100 kW ± 3 kW | Turbine inlet temperature (S11) | 950 °C |
| Thermal Power | 155 kW ± 5 kW | Turbine outlet temperature (S12) | 650 °C |
| Fuel consumption (NG, LHV = 49 MJ/kg) | 24.5 kg/h | Exhaust gas temperature (S13) | 270 °C |
| Electrical Efficiency | 30% ±1 % | Compressor outlet temperature (S18) | 214 °C |
| Nominal mass flow rate | 0.8 kg/s | Shaft rotational speed | 70,000 rpm |
| Turbine efficiency | 0.826 | Pressure in the combustion chamber | 4.5 bar |
| Compressor efficiency | 0.768 | $NO_x$ and CO emissions | <15 ppmv at 15% $O_2$ |

*Data based on ISO standard conditions of ambient pressure and temperature and relative humidity of 101.3 kPa and 15 °C and 60% respectively, neglecting pressure drops at the inlet and exhaust.

To include the off-design behavior of the mGT in the simulation, the performance curves of the compressor and the turbine have been taken from the mathematical models developed by Wang and Cai [159], as carried out also in other studies [195,196]. More precisely, Figure 7-2 shows the characteristic curves in terms of reduced pressure ratio and reduced efficiency of both the compressor and the

turbine versus the reduced mass flow rate for different reduced rotational speeds. The definition of these non-dimensional numbers is presented in the following with the same order that they are quoted:

$$\dot{\pi} = \pi/\pi_0 \tag{7-10}$$

$$\dot{\eta} = \eta/\eta_0 \tag{7-11}$$

$$\dot{G} = (G\sqrt{T_{in}/P_{in}})/(G_0\sqrt{T_{in,0}/P_{in,0}}) \tag{7-12}$$

$$\dot{N} = (N/\sqrt{T_{in}})/(N_0/\sqrt{T_{in,0}}) \tag{7-13}$$

where 0 indicates the nominal design values presented in Table 7-5. The mechanical efficiency of the turbine is fixed to 95% for all the operating conditions.

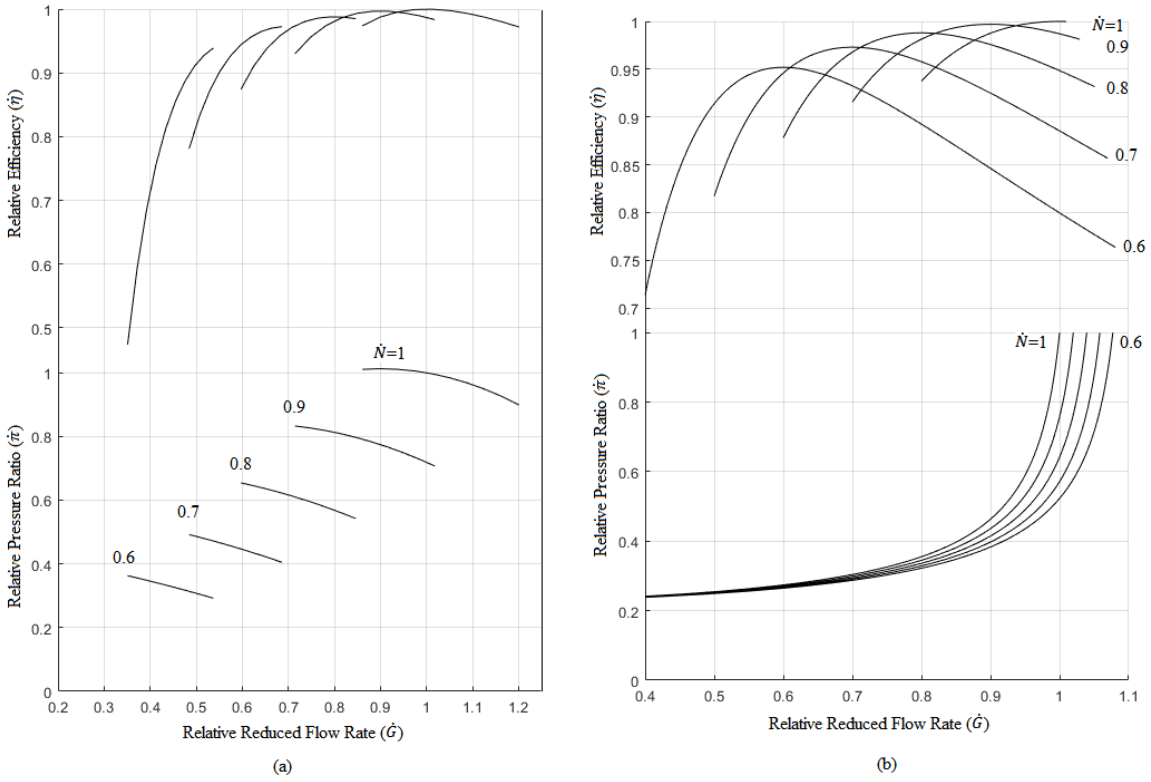


Figure 7-2. Characteristic curves of a) compressor, b) turbine

In a SImGT, the total inlet mass flow rate to the turbine is equal to the sum of the compressed air, the injected steam, and the fuel mass flow rates. As it is evident from Figure 7-2, at nominal operating conditions the turbine works close to the choked flow; as a consequence, the inlet mass flow rate of the compressor is reduced to avoid a choked flow in the turbine. On the other hand, the mass flow rate of air in the compressor must be monitored to prevent compressor surge.

In the present model for a given mass flow rate of the injected steam, the mass flow rate of the fuel (syngas) is calculated by keeping fixed the inlet temperature of the turbine at 950 °C. In addition, to predict the effect of the injected steam on the overall emissions of the mGT, the most relevant reactions in the combustion chamber have been included in the model. However, such emissions do not depend only on the relative mass flow rate of the steam and the syngas, but also on many other parameters such as the LHV of the syngas, the geometry of the combustion chamber, the turbulence effects, the interaction between the steam and the fuel-air mixture and the local position of the steam injectors with respect to the flame [161]. Therefore, zero-dimensional models are not able to properly predict the impact of steam injection on emissions of an mGT. As a consequence, the results of the 1-D model of the syngas-fueled combustion chamber of the same mGT unit obtained by Renzi et al. [161] are considered in this study thus taking into account a specific geometry of the combustion chamber and the location of the steam injectors. Eventually, isentropic and mechanical efficiencies of the fuel compressor are assumed equal to 85% and 95% respectively, whilst power consumption of the water pump is neglected.

### 7.2.3 Organic Rankine Cycle (ORC)

In an ORC unit, the working fluid is selected depending on its operating temperatures and environmental requirements (such as zero ODP, low GWP, and

low flammability). According to Clemente et al. [197], who investigated the performance of an ORC system coupled with a 100 kWel mGT with different working fluids, Isopentane, Isobutane and R245fa revealed to be the most suitable fluids. Moreover, Vera et al. [158] proved that Isopentane allows achieving the maximum thermal efficiency and electricity production in case an ORC unit is used as the bottoming power cycle of a syngas-fueled gas turbine. However, this fluid is highly flammable, and the performance of the ORC system does not reduce so much when R245fa is adopted. Therefore, in this study, R245fa has been considered as the working fluid considering its widespread adoption in low-temperature, small-scale ORC systems [20].

As regards the proposed ORC unit, it works according to a regenerative cycle at pressures lower than 20 bars. In particular, the mass flow rate of the working fluid is adjusted according to the mass flow rate and the inlet and outlet temperatures of the hot stream (the flue gas from the mGT unit) at the evaporator. The minimum outlet temperature of the flue gas (S16 in Figure 7-1) is fixed to 110 °C to prevent any condensation of the water and corrosive substances at the exhaust. Hence, any change in the mass flow rate of the water in the HRSG unit results in a variation of the mass flow rate and the performance of the bottom ORC unit.

Table 7-6 represents the main design parameters of the ORC unit. To protect the pump from two-phase flow, a sub-cooling of 5 °C is considered at the condenser. Moreover, a temperature difference between the cooling water inlet and the saturation temperature of R245fa at the condenser is considered equal to 30 °C, which results in a pressurized condenser that is advantageous for its operation.

Table 7-6. Design parameters of the ORC system

| | | | |
|---|---|---|---|
| Organic Fluid | R245fa | Expander isentropic efficiency | 60% |
| Regeneration efficiency | 67% | Pumps (for organic fluid and water) isentropic efficiency | 70% |
| Super-heating at the turbine inlet | 10°C | Expanders and pumps mechanical efficiency | 90% |
| Sub-cooling at the pump inlet | 5°C | Maximum pressure | 20 bar |

## 7.3 **Results and Discussion**

In this section, the results of the steady-state simulations of the system are presented with varying input parameters. Different mass flow rates of the injected steam are considered and their influence on the output work and efficiency of both the mGT and the bottoming ORC unit is assessed. In the case of the mGT fed by syngas, the inputs are the S/B ratio and the mass flow rate of the injected steam, while the latter is the only required input when NG is considered as the fuel. The maximum mass flow rate of the injected steam is determined in a way that the ratio between the steam and the air mass flow rates remains below 3% to prevent combustion issues. This would increase the rated power of the system up to 3-5% [160]. It should be noted that the combustion issues become more severe when fuel with low LHV is used in the combustion chamber. Therefore, considering the nominal air mass flow rate of the Turbec_T100, a maximum mass flow rate of the steam equal to 25 g/s is considered in the simulations. Furthermore, the performance of the integrated system is assessed also for different S/B ratios ranging from 0.25 to 1.

The thermal integration of the gasifier unit with its combustor is considered to properly assess the additional mass flow rate of the charcoal needed in the gasification process. This auxiliary fuel is included in the calculations of the net efficiency of the system with the final aim to obtain a more realistic evaluation of the performance of the whole system.

To validate the gasifier model, the performances of the gasifier reactor obtained in Aspen plus® are initially compared with those obtained by the 1-D model developed by Pallozzi et al [198] in MATLAB©. The latter includes the kinetic reactions along the axis of the dual fluidized-bed reactor using hazelnut shells as biomass feedstock and it has been validated with experimental data [195,199,200]. Figure 7-3 shows the variations of the syngas composition along the axis of the gasifier for an S/B ratio of 0.25, a gasification temperature of 800 °C, and atmospheric pressure.

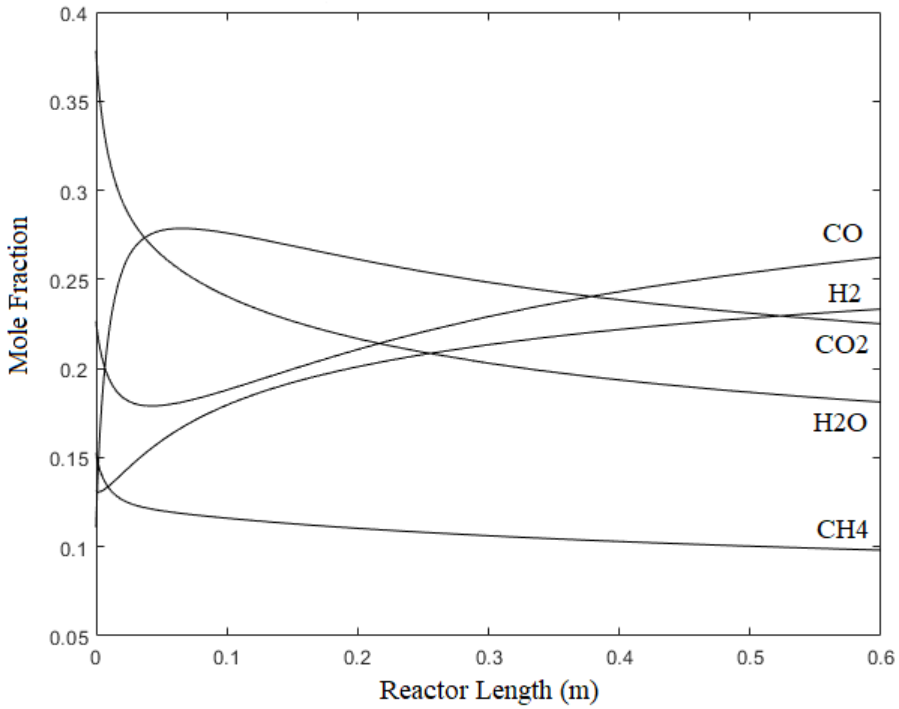


Figure 7-3. Variations of the composition of the syngas along the axis of the gasifier reactor for S/B=0.25 (1-D model)

Figure 7-4 shows the comparison of the syngas composition obtained from the 1-D model and the Aspen Plus® model (for S/B ratios of 0.25 and 1). As can be seen, the syngas composition of both models is comparable although higher $H_2$ and lower $CO_2$ productions are obtained by the Aspen Plus® model. The discrepancy in the

results goes back to the inherent difference in the models. The 1-D model depends on some specific parameters of the reactor such as its geometry (i.e. the length and the diameter), the local flow regime, and the velocity of the particles. The gasifier model in Aspen Plus®, instead, is performed using an RGibbs reactor that simulates the reactions to minimize the free Gibbs energy of the reactants. In other words, it considers the maximum rate of reaction when the reactants reach their minimum Gibbs energy. Therefore, the thermodynamic model in Aspen considers the maximum rate of the reactions as in an infinite-length reactor, while the 1-D model is referred to the geometry and the flow regime of a specific reactor. Hence, the conversion of reactants to produce $H_2$ is lower in the 1-D model compared to the thermodynamic model in Aspen Plus®.

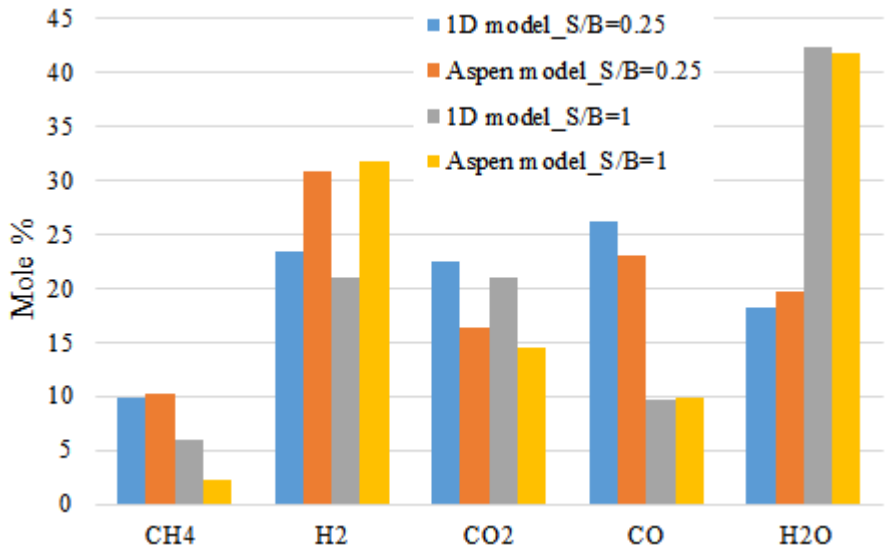


Figure 7-4. Composition of the produced raw Syngas using the 1-D model and Aspen model

Another difference between the two models is the different impact of the S/B ratio on the mole fraction of $H_2$ as can be noticed in Figure 7-4. This is due to the different S/B ratios at which $H_2$ concentration reaches the peak. Hence, S/B=1 indicates

different excess steam values for the gasification process in the models. In other words, the $H_2$ concentration depends on how far S/B=1 is from the S/B ratio which maximizes the $H_2$ concentration. This explains the increase of $H_2$ concentration by increasing the S/B ratio from 0.25 to 1 in the Aspen model, while it is decreased in the 1-D model. Therefore, a sensitivity analysis on the composition of the raw syngas has been carried out using the two models as shown in Figure 7-5, keeping the gasification temperature and pressure constant at 800 °C and 1 bar and varying the S/B ratio.

From a thermodynamic point of view, it is evident that the concentrations of $H_2$ and $CO_2$ increase with the increase of S/B ratio (because of the endothermic reactions of the water-gas shift (Eq. (7-4)) and the steam-methane reforming (Eq. (7-5)) until a certain amount. Then, when more steam than the one converted by the reactions is added, the concentrations of all the products decrease. More precisely, the concentrations of CO and $CH_4$ decrease monotonously with the S/B ratio, while the concentration of the water (reactant) increases (Eqs. (7-4) & (7-5)). Similar trends were reported in the literature using modeling tools [201,202].

Kinetics of the reactions tells us increasing the water concentration lowers the gas speed in the reactor increasing the residence time of the components. Excess steam favors the dissociation of $H_2O$ reacting with the solid carbon (biomass) moving the water-gas reaction to the right (Eq. (7-2)). In turn, it favors the water-gas shift (Eq. (7-4)) with the formation of $CO_2$ at the expense of char, $CH_4$, CO, and also tar as illustrated by numerous experimental data [203–205]. Therefore, the kinetic advantage leads to a higher rate of $CO_2$ production from water-gas shift (Eq. (7-4)), and it shifts the $CO_2$ peak to the right in the 1-D model as well that is visible in Figure 7-5 by comparing $CO_2$ concentration in the 1-D and Aspen Plus® models.

Finally, we can state that steam is beneficial for the gasification process but only up to the value that it can be converted. To this end, the results presented in Figure 7-5

show that it is beneficial to enhance the gasification process, but up to a certain value before the gas mixture is diluted with steam and its LHV falls further. However, if the steam conversion is enhanced (e.g. increasing the gasifier temperature) the optimum S/B ratio increases considerably.

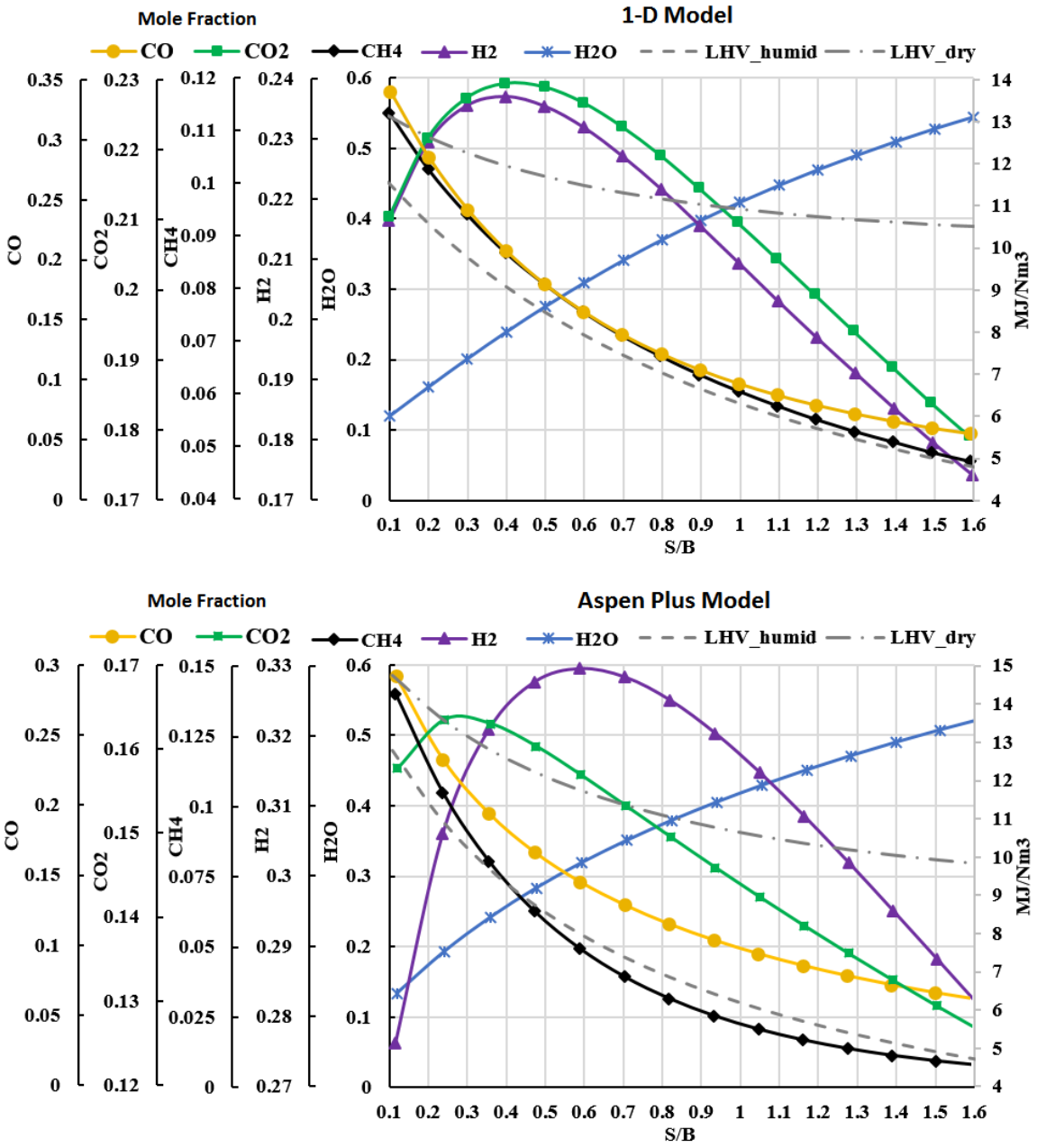


Figure 7-5. Composition of the syngas at different S/B ratios

The S/B ratio affects not only the performance of the gasifier reactor but also those of the integrated system. Therefore, a sensitivity analysis is carried out to find out the near-optimum S/B ratio for the integrated system simulated in this study.

Figure 7-6 shows the trend of the net work and the efficiency of the integrated system and the produced thermal load in the condenser of the ORC unit (CHP) with varying S/B ratio for 15 g/s mass flow rate of injected steam. As can be seen, both the net work and the efficiency reduce slightly with S/B, while the available thermal power for CHP decreases significantly. Indeed, at higher values of the S/B ratio, the reduction of the system's overall performance is caused by the higher thermal energy consumption for steam production. As a result, the available energy in the flue gas stream (S15 in Figure 7-1) is decreased resulting in lower power production by the ORC unit. On the contrary, the produced power by the mGT remains almost unchanged, while the net power of the integrated system decreases. Also, the input mass flow rate of the biomass remains nearly the same since the input mass flow rate of the flue gas to the turbine (S11 in Figure 7-1) is almost constant and consequently, the input energy to the system does not change considerably. Hence, the overall efficiency of the integrated system decreases with higher S/B ratios, and higher mass flow rates of the process steam are detrimental to the performance of the integrated system. Consequently, the latter needs to be set to the minimum required by the gasification process.

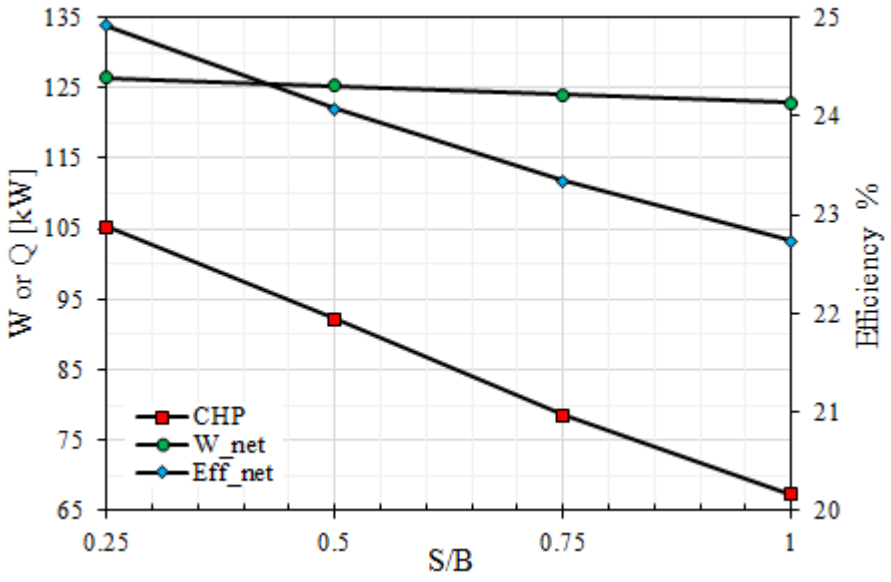


Figure 7-6. Performance of the integrated system fed by syngas at different S/B with a constant mass flow rate of the injected steam at 15 g/s

On the other hand, it is well-known from the literature that higher S/B ratios decrease the tar contaminants in the produced syngas [171]; indeed, it is the main advantage of higher S/B values. In fact, tar is one of the most critical issues of a gasification system since it can clog the equipment thus causing its periodic shutdown. Therefore, a good trade-off between the performance of the integrated system and the tar contamination needs to be made to obtain the near-optimum value of the S/B ratio. Considering the opposite effect of the S/B ratio on the overall performance of the integrated system, the gasification process, and the tar production, the performance of the integrated system is presented for the S/B ratio of 0.5 in the simulations.

After the gasification process, the obtained raw syngas passes through several conditioning units to meet the requirements of the mGT. The composition of the syngas passing through the conditioning units shown in Figure 7-1 is reported in Table 7-7. By comparing the last two columns, it is evident that the final syngas to be injected into the combustion chamber is tar and alkali-free gas containing only

some contaminants with concentrations below the allowable limits required by mGTs.

Table 7-7. Composition of the syngas out of each conditioning reactor of the integrated system shown in Figure 7-1

| **Component** | **R01 (S2): Gasifier (raw syngas)** | **R02 (S3): Dolomite** | **R03 (S4): Ceramic candles** | **R04 (S5): alkali removal** | **R05 (S6): HCL adsorber** | **R06 (S7): H2S adsorber (purified syngas)** | **(S9): Dry Cooler (Dried syngas)** | **Allowable concentration** [190,206,207] |
|---|---|---|---|---|---|---|---|---|
| $H_2$ (%mole fraction) | 32.420 | 32.600 | 45.300 | 45.300 | 45.300 | 45.300 | 56.100 | n.a. |
| CO (%mole fraction) | 16.180 | 16.104 | 20.400 | 20.400 | 20.400 | 20.400 | 25.300 | n.a. |
| $CO_2$ (%mole fraction) | 15.710 | 15.700 | 14.000 | 14.000 | 14.000 | 14.000 | 17.600 | n.a. |
| $H_2O$ (%mole fraction) | 28.520 | 28.600 | 19.300 | 19.300 | 19.300 | 19.300 | 0 | n.a. |
| $CH_4$ (%mole fraction) | 6.230 | 5.900 | 5.200 | 5.200 | 5.200 | 5.200 | 0.600 | n.a. |
| $NH_3$ (ppm) | 864.345 | 105.400 | 94.000 | 94.000 | 94.000 | 94.000 | 117.000 | n.a. |
| $H_2S$ (ppm) | 939.123 | 188.132 | 167.000 | 167.000 | 167.000 | 0.400 | 0.500 | <1.000 |
| HCl (ppm) | 987.145 | 198.453 | 176.000 | 176.000 | 0.500 | 0.500 | 0.500 | <0.500 |
| NaOH (ppm) | 87.700 | 87.702 | 87.700 | 22.000 | 22.000 | 22.000 | 0 | <0.050 |
| KOH (ppm) | 172.670 | 172.000 | 172.000 | 44.000 | 44.000 | 44.000 | 0 | <0.050 |
| $C_7H_8$ (g/Nm$^3$) | 11.500 | 2.300 | 0.200 | 0.200 | 0.200 | 0.200 | 0 | <0.005 |
| $C_6H_6$ (g/Nm$^3$) | 13.500 | 6.600 | 0.300 | 0.300 | 0.300 | 0.300 | 0 | <0.005 |

Table 7-7 shows the trend of the mass flow rate of the air in the main compressor and that of the fuel (biomass) with the mass flow rate of the injected steam into the combustion chamber. In the investigated range of the mass flow rate of the injected steam reported in Figure 7-7, the reduction of the air mass flow rate in the compressor does not cause its surge and consequently, the rotational speed of the compressor (and also of the turbine) can be kept at nominal values (about 70,000 rpm). On the contrary, the mass flow rate of the fuel increases with that of the air to maintain the inlet temperature of the turbine at the design value. Figure 7-7 also shows that the mass flow rate of the turbine is almost constant thus proving that the turbine works close to the choked conditions similar to its nominal design operation.

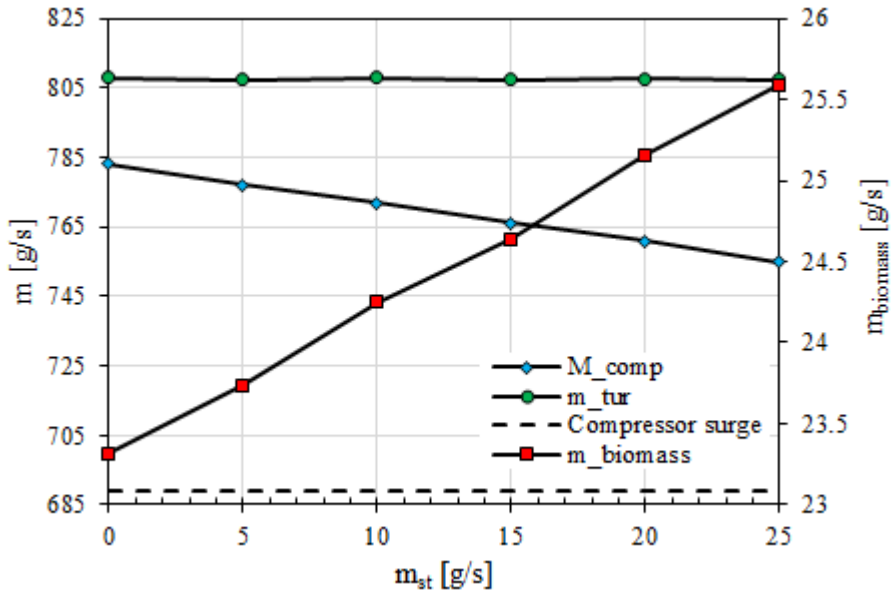


Figure 7-7. The mass flow rate of compressor, turbine, and the syngas via the mass flow rate of the injected steam at S/B = 0.5

The performances of the integrated system and its sub-units in terms of the net output power of the mGT ($W_{mGT}$), of the ORC unit ($W_{ORC}$), of the mGT+ORC ($W_{net}$),

the thermal power output from the ORC unit (CHP), and the overall efficiency of the whole system with varying the mass flow rate of the injected steam are reported in Figure 7-8. It is evident that steam injection increases the net power of the mGT because of the higher mass flow rate in the turbine and the lower mass flow rate in the compressor compared to the nominal operation of the mGT. However, the net efficiency of the system is penalized because of the increase in the mass flow rate of the fuel resulting in more work required by the fuel booster. In addition, the mass flow rate of the auxiliary fuel increases to heat the additional mass flow rate of the steam to the design temperature of the gasifier. Therefore, the total energy input to the integrated system increases since the input biomass mass flow rate, the fuel booster work, and the mass flow rate of the auxiliary fuel to the combustor of the gasifier reactor increase. Therefore, the ratio of the net produced power and the input energy to the integrated system, which defines the overall efficiency of the system, decreases slightly unlike what was concluded in a study on a similar system where the fuel booster and the auxiliary fuel requirements were neglected [161]. Furthermore, the available CHP power is decreased revealing the fact that steam generation reduces the available energy at the bottoming ORC unit. In summary, steam injection increases the net power production with minor degradation of the net efficiency and a significant drop of the CHP thermal output.

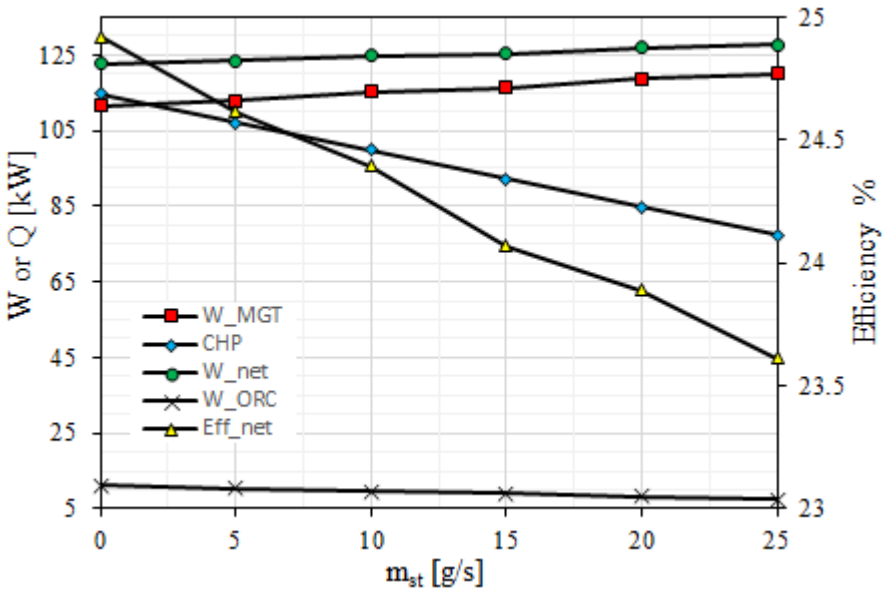


Figure 7-8. Performance of the integrated system fed by syngas at different mass flow rates of the injected steam at S/B = 0.5

To better appreciate the performance of the integrated system, it has been simulated also using NG as fuel thus highlighting the effect of the fuel type on its performance. By comparing Figure 7-7 and Figure 7-9, it can be stated that the trends of the mass flow rates are similar in both cases. Furthermore, even though the mass flow rate of air decreases more with biomass fuel than with NG, the compressor does not meet the surge line in either case and the rotational speed of the shaft remains at the nominal values of about 70,000 rpm for all the operating conditions.

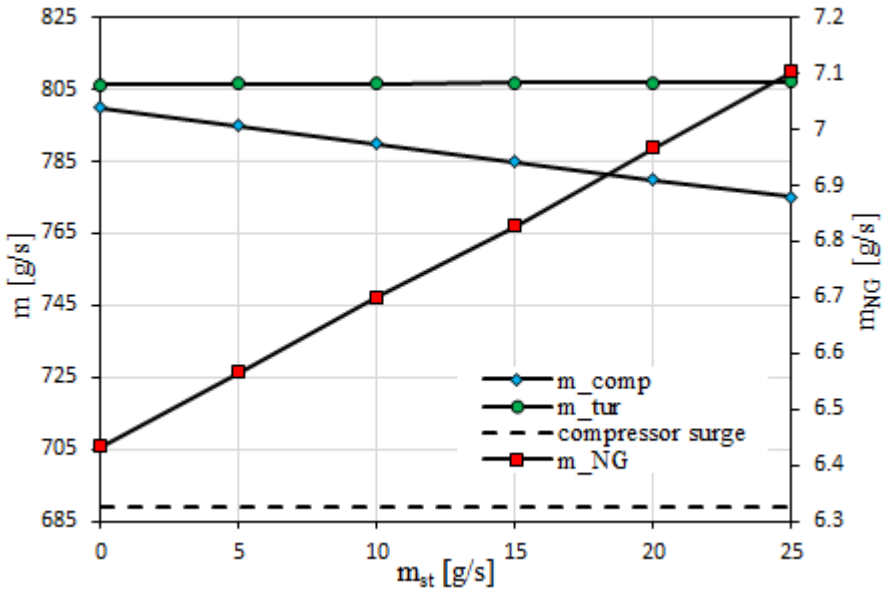


Figure 7-9. The mass flow rate of compressor, turbine, and NG via the mass flow rate of the injected steam

Figure 7-10 shows the performance of the system fuelled by NG. It can be noticed that the performances of the biomass-fuelled SImGT are reduced compared to the SImGT fed by NG (especially the overall electrical efficiency). However, the role of the bottoming ORC unit becomes more important when syngas is used as fuel because of the increase of both the net work of the ORC unit and the thermal power of the CHP.

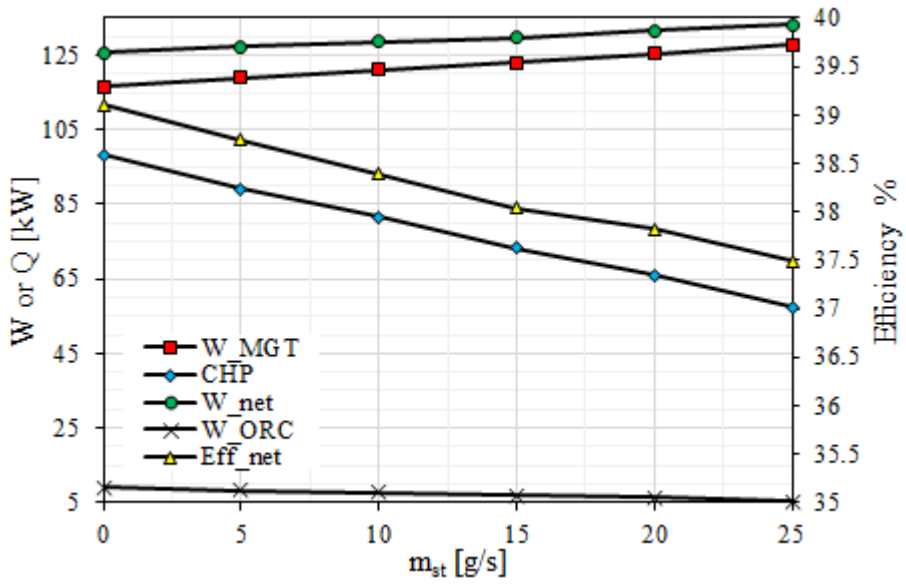


Figure 7-10. Performance of the integrated system fed by NG at different mass flow rates of the injected steam

Finally, Table 7-8 reports a summary of the comparison of the performances of the proposed system with those of similar works available in the literature. By comparing the performances of the proposed configuration with those of similar systems reported in the literature, it can be observed that despite the absence of a bottoming ORC unit, the system investigated by Renzi et al [161] reaches an overall electrical efficiency higher than those reported in other works. However, in their study, the authors used the exhausts from the turbine to produce steam for the mGT only. In this work, instead, also the auxiliary fuel consumption that is required by the gasifier and the fuel booster energy consumption are included in the calculation of the overall system efficiency. Furthermore, Renzi et al [161] considered a more than double (56 g/s) mass flow rate of the injected steam, and they did not clearly report the type of the gasifier and the LHV of the biomass used in their calculations. As regards the adoption of the bottoming ORC unit, its positive impact is more appreciable in other works compared to the here proposed integrated system. This

is mainly due to the small size of the top mGT system considered in this study compared to the other integrated systems.

Table 7-8. Comparison of the performance of the system in this study with relevant systems in the literature

| Performance parameters | Gasifier + SImGT + ORC (present work) | Gasifier + EFGT + ORC [158] | Gasifier + ICE + cascade ORC [208] | Gasifier + EFGT + ORC [166] | Gasifier + SImGT [161] |
|---|---|---|---|---|---|
| Gasifier type | Fluidized bed | downdraft | downdraft | Biomass furnace (direct combustion) | n.a. |
| Biomass type | Hazelnut shell | Olive tree pruning | Spruce chips | n.a. | Forestry residual |
| LHV of biomass [MJ/kg], dry | 18.727 | 16-18 | n.a. | n.a | n.a. |
| Biomass consumption [kg/h] | 92 | 217 | 250.1 | 3600 | n.a. |
| Top cycle net power [kW] | 120.12 | 150.2 | 298.3 | 1383 | _ |
| ORC net power [kW] | 7.5 | 57.1 | 40[a], 31[b] | 700 | _ |
| Net power [kW] | 127.6 | 207.3 | 369 | 2083 | 129.4 |
| Exhaust temperature [°C] | 110 | 290 | 527.6[a] | 400 | _ |
| ORC working fluid | R245fa | Isopentane | R123[a], R245fa[b] | Toluene | _ |
| ORC efficiency [%] | 8.7 | 20.4 | 14.6[a], 5.8[b] | 19 | _ |
| Overall efficiency [%] | 23.6 | 20.7 | 28.3 | 23 | 28.5 |
| Overall efficiency without ORC [%] | 22.2 | 15.3 | 22.9 | 15.3 | _ |

[a] upper cycle of the cascade

[b] lower cycle of the cascade

As described previously, the black-box models used in this study are not able to fully predict the effect of the steam injection on the emissions of the combustion.

Hence, emissions have been estimated using the results of the 1_D simulation of the combustor chamber developed by Renzi et al [161]. Their model was performed for the specific geometry of a combustion chamber with three distinguished zones: the pilot zone, the main zone, and the dilution zone. Using this model, they concluded that the best configuration of the steam injectors to reduce the final temperature without affecting the combustion can be obtained by injecting 20% of the steam in the pilot reactor and the remaining part in the last reactor. They reported the concentration of $NO_x$ and CO emissions in several mass flow rates of the injected steam (0-56 g/s). Assuming their combustion chamber is used in the integrated system simulated in this study and using the interpolation of their results, it is estimated that by injecting 25 g/s of steam the $NO_x$ and CO emissions will be reduced by 54.5% and 93.6% respectively when the SImGT is fuelled by syngas, which represents another advantage of the SImGT besides the increase of the net work of the system.

Although its merits, the SImGT causes a series of technical problems. Indeed, mGTs are usually compact systems, and modifications on their configuration are not always feasible. In addition, since the turbine is working close to the choked condition, the air mass flow rate in the compressor needs to be decreased when steam is injected. Consequently, the compressor performance gets closer to the surge point and unstable conditions. Therefore, the maximum mass flow rate of the injected steam should be limited not only to avoid combustion issues in the combustion chamber but also to avoid unstable performances of the compressor.

## 7.4 **Summary and conclusions**

A micro-CHP system consisting of a fluidized-bed gasifier, a 100 kWel mGT, and an ORC unit, as the bottom cycle, is investigated considering a realistic process configuration to meet practical issues of the integrated system, especially the gas

conditioning needed to purify the produced syngas to reach the limits of mGTs. The integrated system operates with higher net electric power than its nominal operation thanks to the bottoming ORC unit and the steam injection in the combustion chamber. However, results have shown that the overall electric efficiency is penalized slightly by adopting the wet cycle. In particular, the syngas-fuelled integrated system reaches a maximum net power production of 127.6 kWel with 23.6% overall electrical efficiency using 25 g/s steam injected into the combustion chamber. Moreover, results confirm the reduction of the performances of the integrated system especially the overall electrical efficiency when the mGT is fuelled with syngas instead of NG. Nevertheless, the produced thermal power in the condenser of the ORC unit is increased showing the ability of the integrated system to meet higher users' thermal demands in small-scale CHP applications.

The SImGT configuration entails also environmental benefits in terms of reduced $NO_x$ and CO emissions. However, the adoption of steam injected combustion in micro-scales has also some limitations and it should be adopted with caution because of the risk of compressor surge. In addition, further implications should be considered when a low LHV fuel such as syngas is injected into the combustion chamber since the steam injection can negatively affect the combustion process.

Nevertheless, the performed thermodynamic analysis proved that the integration of different energy conversion systems could result in significant energy and environmental benefits thus potentially contributing to more sustainable development and diffusion of distributed power production technologies.

## Chapter 8

# 8. Conclusions and perspectives

*"Science never solves a problem without creating ten more"*

George Bernard Shaw, Irish playwright and critic

The thesis has followed the general strategic target:

*Investigating the micro-scale organic Rankine cycle (ORC) systems to facilitate their deployment in low-grade waste heat recovery (WHR) applications for electricity production.*

To reach this strategic target, several goals have been considered. The main goal of the thesis is to develop an object-oriented, assumption-free model of an experimentally studied micro-scale ORC system using mass-sensitive modeling. This method is a new approach applied to ORC systems since it uses only the components' specifications and the real system boundaries as inputs without making any assumptions regarding the system working conditions. To this end, the model accounts for the two fundamental conservation laws of thermodynamics namely the conservation of energy and the conservation of mass. Therefore, the model can predict the thermodynamic states in different locations of the system, the performance of the components, the system's overall performance, and the refrigerant mass distribution in off-design conditions.

In addition to the intrinsic technical issues penalizing the performance of micro-scale ORC systems, the negative impact of the expander lubricant oil has been

studied. The impact of the lubricant oil has been investigated using a theoretical approach by the reconciliation of the experimental data and using the lubricant-refrigerant miscibility models. It has been found that the lubricant oil reduces the heat exchangers' capacity and penalizes the system performance to an appreciable extent. Therefore, it cannot be neglected in micro-scales unlike what is commonly done in the literature so far.

The other goal that has been followed in the thesis to fulfill the strategic target is to introduce an alternative expansion device for micro-scale ORC units in low-temperature WHR systems. Hence, the regenerative flow turbine is studied numerically for ORC systems for the first time.

Finally, comprehensive system-level modeling of an ORC system as the bottoming cycle of a steam-injected-micro gas turbine system fed with the syngas produced in a dual-fluidized-bed gasifier is performed. The goal of this study was to study the potential of the ORC systems in a WHR application integrated with a renewable energy system using a through simulation considering full-scale conservation of mass and energy.

The specific conclusions drawn for the different topics are presented in each chapter, and further conclusions are made here considering the overall results and the overview of the thesis.

## 8.1 **Conclusions**

A micro-scale ORC system has been tested in a wide range of the working conditions to evaluate the system performance in off-design. The results of the tests have shown performances and some limitations of the system and its components that are elaborated in Chapter 2, Experimental investigations. In Chapter 3, Modeling of the ORC system components, the semi-empirical models of the system

components are presented using the experimental data. These models plus the mass models presented in the next chapter are used in Chapter 4, Mass-sensitive modeling of the ORC system with a detailed study of the liquid receiver. Because the impact of the expander lubricant oil on the performance of the heat exchangers, the scroll expander, and the overall system is found significantly important; yet, it has been mostly neglected in the literature. This phenomenon has been studied theoretically using the data reconciliation method in Chapter 5, The impact of the expander oil. These four chapters are based on the experimental campaign on the micro-scale ORC system to tackle the main goal of the thesis. The following conclusions are drawn from this analysis:

- Enough subcooling degrees must be considered during the system design. A relatively low cooling capacity can result in zero subcooling degrees, and a relatively high cooling capacity can cause a low subcooling degree at the condenser outlet. Hence, an adjustable cooling capacity, or a sub-cooler heat exchanger are recommended. Initial mass charge is increased to have more subcooling in the experiments.
- The pump performance is found a critical parameter on the net system performance in the experiments. It was also reported in the literature that the pump selection is critical for an ORC system especially in micro-scales unlike traditional Rankine cycles.
- The scroll expander has been modeled using an improved empirical model adapted from the literature. Unlike the models in the literature, the two geometrical parameters of the expander namely the swept volume (SV) and the built-in volume ratio (BVR) were taken as fixed inputs to the model instead of being part of the results as a simplifying modeling approach. Results have shown that the polytropic expansion model plus the improved suction pressure drop models result in a more accurate model compared to the isentropic expansion model, which is the most common model in the

literature. Furthermore, the lumped loss torque model has been found as a function of the expander pressure ratio.

- The peak of the shaft power has been found at higher pressure ratios compared to the maximum point of the overall isentropic efficiency. This is particularly important for low-grade WHR applications, in which the produced power is more important than the efficiency. The results showed that the tested expander should operate at pressure ratios 20% higher than its BVR approximately. In addition, the shaft speed should be kept about 20% lower than the electric generator nominal speed to have a high volumetric performance and avoiding further efficiency losses.
- Regarding the mass models of the system components, it has been found that the liquid receiver is not flooded with the liquid despite the condenser outlet is subcooled unlike the models in the literature. Moreover, the selection of the void fraction model is important since it directly affects the overall system mass in a mass-sensitive solver. The best void fraction model for the evaporator and the condenser, Rouhani II [91], has been found among eight modes in the literature that results in the least deviation between the calculated system mass and the real system mass charge.
- The results of the mass-sensitive solver are used to map the system electric performance in terms of net electric power and net electric efficiency. For the specific ORC test bench studied in the thesis, the optimum operating point was found at the pump speed of about the maximum of the range of the experimental data (400 rpm), and the expander shaft speed of about 60% of the electric generator nominal speed (900 rpm). In fact, the power input is not enough to increase the pump speed and simultaneously assure a superheated gas at the expander suction. Thus, higher shaft speeds are achieved at the pump speed of 400 rpm, but only at lower shaft torque resulting in lower produced power and efficiency.

- The presence of the expander lubricant oil has been found destructive on the overall system performances; hence, oil-free expanders or oil separator loops are recommended especially in micro scales that usually are not common in commercial systems. The presence of the oil causes capacity loss in the evaporator and condenser of the system. Regarding the scroll expander performances, the mechanical efficiency (defined as Eq. (5-32)) is penalized while the filling factor is reduced in low shaft speeds if the impact of the lubricant is considered, which a means better volumetric performance.
- The oil circulation rate (OCR) and the expander filling factor have been found strongly associated with the expander shaft speed. The lower OCR and the lower filling factor are observed in higher shaft speeds indicating that the lubricant has remained in the expander and the internal leakages have reduced.

In Chapter 6, Regenerative Flow Turbine (RFT), a novel turbine has been studied numerically that is found a good alternative expander for very low pressure ratios, in which a popular volumetric machine like scroll expander cannot work efficiently. The following conclusions are drawn regarding the RFT in the ORC systems:

- The RFT is a kind of dynamic turbine that has some features of volumetric expanders as well. For example, its power and pressure ratio change almost linearly with the shaft speed as volumetric expanders, yet the principle of the flow is based on the swirling flow that exchanges momentum between the main stream and the impeller.
- The RFT is compared with two scroll expanders with BVR of 1.9 and 3.5. Its performances have been found superior to these two expanders in low pressure ratios. Moreover, its isentropic efficiency changes less with the pressure ratio; thus, its performance is more reliable for low-grade WHR applications. An interesting application for such turbines is car WHR systems, in which the reliability of the expander in low pressure ratios is very

important. The cost and compactness are other competitive features of the RFT compared to the common volumetric expanders.

Finally, the use of ORC systems as the bottom cycle of an integrated renewable energy CHP system has been investigated in Chapter 7, An application of micro-ORC systems for WHR & CHP. The following conclusions are drawn:

- The impact of the bottom cycle on the overall system efficiency is subsided as the nominal capacity of the top cycle reduces. It means that the WHR becomes less effective as the size of the top cycles reduces.
- Regarding the specific integrated system studied, the steam injection into the micro gas turbine to increase the output power is more effective than the bottom ORC cycle. However, the wet cycle technology slightly reduces the system efficiency that can be compensated using the bottom ORC unit.
- The bottom ORC adds flexibility to the integrated system in the case of CHP. To this end, the system can adapt its operational mode depending on the users' demand to produce extra electricity using the ORC system or more steam injection to the combustion chamber, or to deliver more thermal power to the CHP heat exchanger.

## 8.2 **Perspectives**

Despite several conclusions drawn from the thesis, several questions have arisen that some are presented hereunder as perspectives for future research works.

- The liquid receiver has been found partially filled despite the condenser outlet is subcooled unlike the simplified models in the literature. The liquid level has been found almost stable in the tests that is adequate for the mass-sensitive system modeling. Nonetheless, a more detailed model of the liquid receiver is necessary to simulate the subcooling loss and the liquid level in

various working conditions for different tank geometries. Moreover, the impact of other parameters such as the presence of the expander lubricant oil on the liquid level in the liquid receiver should is unknown.

- The oil circulation rate has been calculated using a theoretical approach through a data reconciliation method applied to the condenser of the ORC unit. This theoretical approach should be adopted in further experimental studies to investigate its credibility and versality.
- Despite the impact of the expander lubricant oil is found non-negligible, it is not considered in the hydrothermal modeling of the PHEs. This is because the impact of the expander lubricant on the boiling, condensation, and gas-phase HTC correlations are missed in the literature. Indeed, it is expected that the HTC in two-phase or gas flows gets affected significantly especially in low mass fluxes. The same is true for the void fraction models. Therefore, experimental modeling of the lubricant-refrigerant mixtures in channels is required.
- The impact of the expander lubricant oil on the mechanical and volumetric efficiencies is investigated. Nevertheless, the impact of the lubricant on the expander isentropic efficiency requires models for the entropy of the lubricant-refrigerant mixture that needs to be studied.
- The RFT studied in the thesis is the first design prototype. The internal leakages are found significantly detrimental for the turbine performance that should be minimized in next design efforts.
- The RFT is simulated numerically using R245fa for low-grade ORC systems. It shows a relatively reliable performance of the turbine especially in very low pressure ratios that is important for micro-scale ORC systems. Yet, experimental study of an RFT prototype is needed to develop a semi-empirical or a more deterministic model. The model can be used in the optimization of the different geometrical and flow parameters of the RFT to improve its performances.

# Appendices

Appendix (A): Properties of the diathermic oil (Texatherm HT22) and expander lubricant oil (PAG-SP10).

They are calculated for the diathermic oil using the table of properties provided by the manufacturer. Then, the following correlations were found to fit the tabular data.

$C_p = 3.658T + 827.4$ [J.kg$^{-1}$.K$^{-1}$] (A1)

$h = \int_0^T C_p dT = \frac{3.658}{2} T^2 + 827.4T$ [J/kg] (A2)

$\mu = 1.022 \times 10^{41} T^{-16.99}$ [Pa.s] (A3)

$\lambda = -7.253 \times 10^{-5} T + 0.1551$ [W.m$^{-1}$.K$^{-1}$] (A4)

$\rho = -0.6162T + 1066$ [kg.m$^{-3}$] (A5)

Enthalpy of the lubricant oil is adopted from [112] using the correlations similar to the diathermic oil.

$h_{lub} = \int_0^T C_p dT = \frac{0.0003}{2} T^2 + 0.48T$ [Btu/h] (A6)

Other lubricant-R134a mixture properties adopted from [209]:

Mixture kinematic viscosity:

$$ln\, \nu_{mix} = \left(1 - w_{ref}\right) ln\, \nu_{lub} + w_{ref} \cdot ln\, \nu_{ref} \quad (A7)$$

Mixture specific heat:

$$C_{p,mix} = w_{ref} \cdot C_{p,ref} + (1 - w_{ref}) C_{p,oil} \quad (A8)$$

Mixture thermal conductivity:

$$\lambda_{mix} = \lambda_{ref} \cdot w_{ref} + \lambda_{lub}\left(1 - w_{ref}\right) - 0.72(1 - w_{ref}) w_{ref} (\lambda_{lub} - \lambda_{ref}) \quad (A9)$$

Appendix (B): uncertainty analysis

Two types of standard uncertainty are presented by Jianfeng Yu et al. [210]: the standard uncertainty of measurement sensors (type A) and the standard uncertainty of testing data (Type B). The standard deviation of each uncertainty component is calculated using Eq. (B1):

$$u_{i,A} = \frac{\delta}{\sqrt{3}} \quad \text{(B1)}$$

where $\delta$ is the accuracy of the measurement tool.

Moreover, the repetition of the experiment reveals that another source of uncertainty exists in the results originated from any valid method for testing data:

$$u_{i,B} = \frac{s}{\sqrt{n}} \quad \text{(B2)}$$

where $u_i$ is the standard uncertainty of the data $x_i$, $n$ is the number of the repetitions of the measurement of the parameter "$i$", and $s$ is the total standard deviation of the mean:

$$s = \sqrt{\frac{\Sigma(x_i - \bar{x})^2}{n-1}} \quad \text{(B3)}$$

where $x_i$ indicates each measurement and $\bar{x}$ is the mean value of the measurement of the parameter "$i$".

Eventually, the total standard uncertainty of the measurement of the parameter "$i$" is calculated as the following:

$$u_{i,tot} = \sqrt{{u_{i,A}}^2 + {u_{i,B}}^2} \quad \text{(B4)}$$

Furthermore, if a parameter is a function of several independent parameters as Eq. (B5), the combined uncertainty of the parameter "y" is calculated using Eq. (B6).

$$y = f(x_1, x_2, \dots, x_n) \quad \text{(B5)}$$

$$u_{y,c}{}^2 = \sum_{i=1}^{n} \left(\frac{\partial f}{\partial x_i}\right)^2 u^2(x_i) \quad \text{(B6)}$$

In this work, the expanded uncertainty of the combined parameter is considered by adopting a coverage factor of "$K = 2$" associating with the confidence level of 95%:

$$U_y = K \cdot u_{y,c} \quad \text{(B7)}$$

Appendix (C): geometry-dependent correlations of HTCs

For different heat transfer mechanisms used for the modeling of the evaporator and the condenser of the ORC system in this study.

- Boiling in BPHEs (Amalfi et al. [146])

This correlation is obtained using 1903 heat transfer and 1513 pressure drop data points of PHEs from the literature. Depending on Bond number ($Bd$), two correlations for micro ($Bd < 4$) and macro ($Bd \geq 4$) boiling HTC are suggested:

$$Nu = 982\left(\frac{\beta}{\beta_{max}}\right)^{1.101} We_m^{0.315} \cdot Bo^{0.320} \left(\frac{\rho_l}{\rho_v}\right)^{-0.224} \qquad Bd < 4 \quad \text{(C1)}$$

$$Nu = 18.495\left(\frac{\beta}{\beta_{max}}\right)^{0.248} \cdot Re_v^{0.135} \cdot Re_{lo}^{0.351} \cdot Bd^{0.235} \cdot Bo^{0.198} \left(\frac{\rho_l}{\rho_v}\right)^{-0.223} \; Bd \geq 4 \quad \text{(C2)}$$

where $\beta$ and $\beta_{max}$ are the plate chevron angle and its maximum value in the experimental database (70 degree), $We_m$ is the Weber number using mean fluid properties, Bo and Bd are the Boiling and Bond numbers respectively. $Re_v$ is the Reynolds number using saturated vapor properties, and $Re_{lo}$ is the Reynolds number using saturated liquid properties.

- Single Phase flow in BPHEs

➢ Yang et al. [147] (used for diathermic oil, and R245fa liquid, $2 \leq Pr \leq 290$)

This correlation is obtained based on experiments of 22 PHEs and 25 empirical correlations.

$$Nu = (-1.342 \times 10^{-4}\beta^2 + 1.808 \times 10^{-2}\beta - 0.0075)Re^{(-7.956\times10^{-5}\beta^2+9.687\times10^{-3}\beta+0.3155)} \cdot Re^{\Phi/\beta} \cdot Re^{\gamma/\beta} \cdot Pr^{1/3}(\frac{\mu}{\mu_w})^{0.14} \quad \text{(C3)}$$

where $\beta$, $\Phi$, and $\gamma$, are the plate chevron angle, surface enlargement factor, and the corrugation aspect ratio respectively. $Re$ and $Pr$ are the Reynolds and Prandtl numbers respectively calculated using local fluid properties. The term $(\frac{\mu}{\mu_w})$ indicates the ratio of the fluid dynamic viscosity at the bulk temperature over its viscosity at the wall temperature.

- Khan et al. [149] (used for water single-phase flow in the condenser)

For water flow in the condenser, a specific correlation that was obtained using water in PHEs with different chevron angles is used instead of the general single-phase correlation to ensure higher accuracy of the model.

$$Nu = \left(0.0161\frac{\beta}{\beta_{max}} + 0.1298\right) Re^{(0.198\frac{\beta}{\beta_{max}}+0.6398)} \cdot Pr^{0.35}(\frac{\mu}{\mu_w})^{0.14} \quad \text{(C4)}$$

where $\beta_{max}$ is the maximum chevron angle of the PHEs in their experiments that was 60 degree.

- Gas turbulent flow in tubes [54] (used for R245fa gas, 0.5 ≤ Pr ≤ 1)

This is a simplified correlation suggested for turbulent flows of low Pr fluids (gases) in tubes.

$$Nu = 0.022Pr^{0.5} \cdot Re^{0.8} \quad \text{(C5)}$$

- Condensation (Longo et al. [148])

Depending on the *Re* number, two correlations for gravity-controlled condensation ($Re \leq 1600$) and forced condensation ($Re > 1600$) are suggested that was able to predict the experimental database of 1141 data points with relatively good accuracy.

$$Nu = 0.943\Phi[(\lambda_l{}^3 \cdot \rho_l{}^2 \cdot g \cdot h_{lg})/(\lambda_l \cdot \Delta T \cdot L)]^{1/4} \qquad Re \leq 1600 \qquad \text{(C6)}$$

$$Nu = 1.875\Phi(\lambda_l/d_h)Re_{eq}^{0.445} \cdot Pr_l^{1/3} \qquad Re > 1600 \qquad \text{(C7)}$$

where $d_h$ is the hydraulic diameter of one channel of the PHE considered equal to twice of the corrugation depth in their work. The parameters $g$, $h_{lg}$, $\Delta T$, and $L$ are the gravitational acceleration, phase change latent heat, the difference between the wall temperature and saturation temperature, and length of the plate respectively. $Re_{eq}$ is the equivalent Reynolds number calculated using the following equation:

$$Re_{eq} = G\left[(1-x) + x\left(\frac{\rho_L}{\rho_G}\right)^{0.5}\right]\frac{d_h}{\mu_L} \qquad \text{(C8)}$$

where $x$ is the vapor quality, and $G$ is the mass flux [kg/m²·s].

Appendix (D): geometry-independent correlations of HTCs

Single-phase:

- Dittus-Boelter [52] (it was originally introduced for single-phase turbulent flows in tubes)

$$Nu_D = a \cdot Re_D{}^b \cdot Pr^c \qquad \text{(D1)}$$

- Sieder-Tate [53] (it was originally introduced for single-phase turbulent flows in tubes)

$$Nu_D = a \cdot Re_D{}^b \cdot Pr^c \left(\frac{\mu}{\mu_w}\right)^{0.14} \qquad \text{(D2)}$$

- Bogaert-Bolcs [39] (it was originally introduced for mineral oil in PHEs)

$$Nu_D = a \cdot {Re_D}^b \cdot Pr^{\left(\frac{1}{3}e^{\left(\frac{6.4}{Pr+30}\right)}\right)} \left(\frac{\mu}{\mu_w}\right)^{\frac{0.3}{(Re+6)^{0.125}}} \quad \text{(D3)}$$

- Kays-Crawford [54] (it was originally introduced for single-phase turbulent flows in tubes)

$$Nu_D = \frac{a \cdot {Re_D}^{0.8} \cdot Pr}{0.88+2.03(Pr^{\frac{2}{3}}-0.78){Re_D}^{-0.1}} \quad \text{(D4)}$$

Condensation:

- Kuo et al. [57] (it was originally introduced for R410 in PHEs)

$$h_L = a\left(\frac{\lambda_L}{D_h}\right) {Re_L}^{0.78} \cdot {Pr_L}^{\frac{1}{3}} \left(\frac{\mu}{\mu_w}\right)^{0.14} \quad \text{(D5)}$$

$$h_{tp} = \left(0.25Co^{-0.45} \cdot {Fr_L}^{0.25} + 75Bo^{0.75}\right) \quad \text{(D6)}$$

where *Co*, $Fr_L$, and *Bo* are Convection number, Froud number and Boiling number respectively represented in the following equations:

$$Co = \left(\frac{\rho_g}{\rho_L}\right)\left(\frac{1-x_m}{x_m}\right)^{0.8} \quad \text{(D7)}$$

$$Fr_L = \frac{G^2}{{\rho_L}^2 \cdot g \cdot D_h} \quad \text{(D8)}$$

$$Bo = \frac{q}{G \cdot i_{fg}} \quad \text{(D9)}$$

- Claesson et al. [56] (it was originally introduced for R134a in PHEs)

$$h_{Nu} = a \cdot \lambda_L \left(\frac{Re \cdot \mu_L}{\rho_L(\rho_L-\rho_g)g}\right)^{\frac{-1}{3}} \quad \text{(D10)}$$

$$h_{tp} = \sqrt{{h_{Nu}}^2 + {h_{Bogaert}}^2} \quad \text{(D11)}$$

Boiling HTC correlations:

- Hsieh et al. I [58] (it was originally introduced for R134a in PHEs)

$$h_L = a\left(\frac{\lambda_L}{D_h}\right) Re_L^{0.78} \cdot Pr^{1/3} \left(\frac{\mu_{avg}}{\mu_{wall}}\right)^{0.14} \quad \text{(D12)}$$

$$h_{tp} = h_L\left[1.2Fr^{0.75} + 13.5Bo^{1/3} \cdot Ja^{0.25}\right] \quad \text{(D13)}$$

where $Fr$ and $Bo$ are calculated as Eqs. (D8) & (D9) respectively, and $Ja$ number using the following equation:

$$Ja = \frac{\rho_L \cdot C_p\left(T_{wall,avg} - T_{sat}\right)}{\rho_g \cdot i_{fg}} \quad \text{(D14)}$$

The HTC of the single-phase liquid zone used with this boiling model was the same as Eq. (D12).

- Hsieh et al. II [59] (it was originally introduced for R410 in PHEs)

$$h_L = 0.023 Re_L^{0.8} \cdot Pr^{0.4} \left(\frac{\lambda_L}{D_h}\right) \quad \text{(D15)}$$

$$h_{pool} = 55 P_r^{0.12} (-\ln P_r)^{-0.55} M^{-0.5} \cdot q^{0.67} \quad \text{(D16)}$$

$$E = 1 + 24{,}000 Bo^{1.16} + 1.37\left(\frac{1}{X_{tt}}\right)^{0.86} \quad \text{(D17)}$$

$$S = \left(1 + 1.15 \times 10^{-6} E^2 \cdot Re_L^{1.17}\right)^{-1} \quad \text{(D18)}$$

$$h_{tp} = a \cdot E \cdot h_L + b \cdot S \cdot h_{pool} \quad \text{(D19)}$$

Where $M$, $q$, $X_{tt}$, $P_r$ are molecular weight, heat flux, Martinelli parameter, and reduced pressure respectively defined as the following:

$$X_{tt} = \left(\frac{1-x_m}{x_m}\right)^{0.9} \left(\frac{\rho_g}{\rho_L}\right)^{0.5} \left(\frac{\mu_L}{\mu_g}\right)^{0.1} \quad \text{(D20)}$$

$$P_r = \frac{P}{P_{critical}} \quad \text{(D21)}$$

- Desideri et al. [51] (it was originally introduced for R245fa and R1233ZD in PHEs)

$$h_{tp} = a \cdot We^{-0.0322} \left(\frac{\rho_L}{\rho_g}\right)^{-0.338} {Re_L}^{0.451} \cdot Bd^{-0.469} \quad \text{(D22)}$$

where *We*, *Bo*, and *Bd* are Weber, Boiling (Eq. (D9)) and Bond numbers respectively defined as follows:

$$We = \frac{G^2 \cdot D_h}{\rho_m \cdot \sigma} \quad \text{(D23)}$$

$$Bd = \frac{(\rho_L - \rho_g) g \cdot {d_h}^2}{\sigma} \quad \text{(D24)}$$

where *G* and $\sigma$ are the mass flux and the surface tension respectively.

- Yan et al. [60] (it was originally introduced for R134a in PHEs)

$$Nu_{tp} = a \cdot {Re_L}^{0.5} \cdot {Pr_L}^{1/3} \cdot {Bo_{eq}}^{0.3} \frac{G_{eq}}{G} \quad \text{(D25)}$$

$$G_{eq} = G\left[(1 - x_m) + x_m \left(\frac{\rho_L}{\rho_g}\right)^{0.5}\right] \quad \text{(D26)}$$

$$Bo_{eq} = \frac{q}{G_{eq} \cdot i_{fg}} \quad \text{(D27)}$$

Appendix (E): Void fraction (*VF*) correlations.

- Rouhani and Axelsson [90]

$$VF = \frac{x}{\rho_g}\left[C\left(\frac{x}{\rho_g} + \frac{1-x}{\rho_l}\right) + \frac{1.18}{G}\left(\frac{\sigma \cdot g(\rho_l - \rho_g)}{{\rho_l}^2}\right)^{0.25}\right]^{-1} \quad \text{(E1)}$$

Rouhani I [91]: $C = 1 + 0.2(1 - x)$ (E2)

Rouhani II [91]: $C = 1 + 0.2(1 - x)\left(gD_h\left(\frac{\rho_l}{G}\right)^2\right)^{0.25}$ (E3)

where $\sigma$ is the surface tension.

- Zivi [93]

$$S = \left(\frac{\rho_l}{\rho_g}\right)^{\frac{1}{3}} \quad \text{(E4)}$$

- Premoli et al. [94]

$$S = 1 + F_1\left(\frac{y}{1+y\cdot F_2} - y\cdot F_2\right)^{0.5} \quad \text{(E5)}$$

$$y = \frac{VF_{hom}}{1-VF_{hom}} \quad \text{(E6)}$$

$$F_1 = 1.7{Re_l}^{-0.019}\left(\frac{\rho_l}{\rho_g}\right)^{0.22} \quad \text{(E7)}$$

$$F_2 = 0.0273We_l\cdot{Re_l}^{-0.51}\left(\frac{\rho_l}{\rho_g}\right)^{0.08} \quad \text{(E8)}$$

$$Re_l = \frac{G\cdot d_h}{\mu_l} \quad \text{(E9)}$$

$$We_l = \frac{G^2\cdot d_h}{\sigma\cdot g\cdot\rho_l} \quad \text{(E10)}$$

Where $VF_{hom}$ is the homogeneous void fraction and $\sigma$ is the surface tension.

- Sun et al. [96]

$$VF = \frac{x}{C_0\left[x+(1-x)\frac{\rho_g}{\rho_l}\right]+v_g\cdot v_l\left(\frac{\rho_g}{\rho_l}\right)} \quad \text{(E11)}$$

$$C_0 = \frac{1}{0.82+0.18\frac{P}{P_{cr}}} \quad \text{(E12)}$$

$$v_g = 1.41\left[\frac{\sigma\cdot g(\rho_l-\rho_g)}{{\rho_l}^2}\right]^{0.25} \quad \text{(E13)}$$

$$v_l = \frac{G}{\rho_l} \quad \text{(E14)}$$

where $v_l$ and $v_g$ are liquid and gas velocities, $\sigma$ is the surface tension, and $P_{cr}$ is the critical pressure.

- Graham et al. [98]

$$VF = \begin{cases} 1 - exp[-1 - 0.3\ln(F_t) - 0.0328(\ln(F_t))^2] & F_t > 0.01032 \\ 0 & F_t < 0.01032 \end{cases} \quad \text{(E15)}$$

$$F_t = \left(\frac{x^3 \cdot G^2}{\rho_g{}^2 \cdot d(1-x)}\right)^{0.5} \quad \text{(E16)}$$

where $F_t$ is the Froud rate number.

- Woldesemayat and Ghajar [91]

$$VF = \frac{U_{SG}}{U_{SG}\left(1+\left(\frac{U_{SL}}{U_{SG}}\right)\left(\frac{\rho_g}{\rho_l}\right)^{0.1}\right)+2.9\left[\frac{g \cdot D_h \cdot \sigma(1+\cos\theta)(\rho_l-\rho_g)}{\rho_l{}^2}\right]^{0.25}(1.22+1.22\sin\theta)^{\frac{P_{atm}}{P_{system}}}} \quad \text{(E17)}$$

$$U_{SG} = \frac{G.x}{\rho_g} \quad \text{(E18)}$$

$$U_{SL} = \frac{G(1-x)}{\rho_l} \quad \text{(E19)}$$

where $\theta$ is the inclination of the channel, $U_{SG}$ is the gas superficial velocity, and $U_{SL}$ is the superficial liquid velocity.

Appendix (F): Other mixture properties adopted from [209]:

Mixture kinematic viscosity:

$$ln\,\nu_{mix} = \left(1 - w_{ref}\right) ln\,\nu_{lub} + w_{ref} \cdot ln\,\nu_{ref} \quad \text{(F1)}$$

Mixture specific heat:

$$C_{p,mix} = w_{ref} \cdot C_{p,ref} + (1 - w_{ref})C_{p,oil} \quad \text{(F2)}$$

Mixture thermal conductivity:

$$\lambda_{mix} = \lambda_{ref} \cdot w_{ref} + \lambda_{lub}\left(1 - w_{ref}\right) - 0.72(1 - w_{ref})w_{ref}(\lambda_{lub} - \lambda_{ref}) \quad \text{(F3)}$$

Table A1. The calculated empirical coefficients of the hydraulic model of the PHEs of the ORC system

| The empirical coefficient in Eq. (3-4) | Evaporator | Condenser |
|---|---|---|
| $a$ | 9772.82 | 14,660.75 |

Table A2. The calculated empirical coefficients of the thermal model of the condenser

| | Water single-phase in Eq. (D4) | Liquid single-phase, R134a in Eq. (D4) | Gas single-phase, R134a in Eq. (D4) | Condensing R134a in Eq. (D10) |
|---|---|---|---|---|
| $a$ | 0.191 | 0.568 | 0.067 | 58.550 |

Table A3. The calculated empirical coefficients of the thermal model of the evaporator

| | Oil single-phase in Eq. (D3) | Liquid single-phase, R134a in Eq. (D4) | Gas single-phase, R134a in Eq. (D4) | Boiling R134a in Eq. (D25) |
|---|---|---|---|---|
| $a$ | 0.34641 | 0.023 | 0.023 | $f(Re_{oil}, Pr_{oil}, Re_{ref}, Pr_{ref})$ |
| b | 0.6636 | n.a. | n.a. | n.a. |

Table A4. Identified empirical coefficients of the Polytropic expansion model

| | | |
|---|---|---|
| Polytropic multiplier coefficient [-] | $a_{pol}$ | 0.85 |
| Leakage area [mm$^2$] | $A_{leak}$ | 4.45 |
| Expansion coefficient [-] | $K_{exp}$ | 30.2 |
| Suction overall heat transfer coefficient [W/K] | $AU_{su,n}$ | 59.77 |
| Discharge overall heat transfer coefficient [W/K] | $AU_{ex,n}$ | 105.95 |
| Overall heat transfer coefficient with ambient [W/K] | $AU_{amb}$ | 1.44 |
| Nominal mass flow rate [g/s] | $\dot{m}_{nom}$ | 111.19 |
| Suction cross-sectional area [mm$^2$] | $A_{su}$ | 22.40 |
| Coefficient of the mechanical loss torque correlation [-] | $C_1$ | 0.97 |
| Coefficient of the mechanical loss torque correlation [-] | $C_2$ | 2.64 |
| Coefficient of the mechanical loss torque correlation [-] | $C_3$ | 0.15 |

Table A5. Experimental database (measurement point numbers are referring to Figure 2-1)

| Row | P1 [bar] | T1 [°C] | P2 [bar] | T2 [°C] | P3 [bar] | T3 [°C] | P4 [bar] | T4 [°C] | P5 [bar] | T5 [°C] | T6 [°C] | T7 [°C] | T8 [°C] | T9 [°C] | P6 [bar] | P7 [bar] | τ [N.m] | $\dot{V}_{ref}$ [l/h] | $N_{exp}$ [rpm] | $N_{p,HF}$ [rpm] | $N_{p,WF}$ [rpm] |
|---|---|---|---|---|---|---|---|---|---|---|---|---|---|---|---|---|---|---|---|---|---|
| 1 | 11.74 | 11.83 | 11.34 | 46.47 | 1.05 | 16.10 | 5.40 | 25.01 | 4.82 | 9.93 | 120.01 | 107.04 | 9.84 | 12.53 | 4.83 | 4.85 | -2.91 | 155.00 | 832.05 | 1400.00 | 280.00 |
| 2 | 11.90 | 11.91 | 11.52 | 62.00 | 1.05 | 16.20 | 5.32 | 41.37 | 4.76 | 9.87 | 119.76 | 106.72 | 9.69 | 12.40 | 4.77 | 4.80 | -3.15 | 143.32 | 968.55 | 1400.00 | 260.00 |
| 3 | 12.19 | 11.70 | 11.78 | 47.72 | 1.06 | 14.09 | 5.52 | 23.51 | 4.88 | 10.09 | 124.39 | 110.92 | 9.79 | 12.66 | 4.89 | 4.92 | -2.92 | 166.39 | 836.74 | 1400.00 | 300.00 |
| 4 | 12.20 | 11.75 | 11.77 | 52.97 | 1.06 | 14.48 | 5.45 | 31.85 | 4.83 | 9.87 | 124.55 | 111.11 | 9.68 | 12.47 | 4.84 | 4.86 | -3.07 | 154.55 | 932.50 | 1400.00 | 280.00 |
| 5 | 11.81 | 11.77 | 11.43 | 57.64 | 1.06 | 14.77 | 5.32 | 37.14 | 4.76 | 9.83 | 124.93 | 110.16 | 9.76 | 12.41 | 4.77 | 4.80 | -3.07 | 143.42 | 938.96 | 1200.00 | 260.00 |
| 6 | 12.58 | 11.89 | 12.18 | 53.06 | 1.05 | 16.24 | 5.63 | 32.83 | 4.93 | 9.95 | 129.44 | 114.96 | 9.83 | 12.86 | 4.94 | 4.96 | -3.10 | 165.45 | 957.57 | 1400.00 | 300.00 |
| 7 | 12.12 | 11.97 | 11.71 | 59.79 | 1.05 | 16.40 | 5.40 | 39.58 | 4.81 | 9.86 | 129.51 | 114.03 | 9.67 | 12.46 | 4.82 | 4.85 | -3.11 | 148.82 | 973.47 | 1200.00 | 270.00 |
| 8 | 13.67 | 11.92 | 13.16 | 52.65 | 1.04 | 16.25 | 5.88 | 28.38 | 5.06 | 10.10 | 133.61 | 117.12 | 9.68 | 13.16 | 5.06 | 5.09 | -3.04 | 193.88 | 983.38 | 1400.00 | 350.00 |
| 9 | 13.26 | 11.94 | 12.80 | 55.67 | 1.04 | 16.44 | 5.71 | 33.83 | 4.99 | 9.97 | 133.89 | 118.24 | 9.67 | 12.94 | 4.99 | 5.02 | -3.10 | 178.17 | 1022.39 | 1400.00 | 320.00 |
| 10 | 12.53 | 11.88 | 12.08 | 50.78 | 1.04 | 16.59 | 5.55 | 29.35 | 4.92 | 9.92 | 134.45 | 119.09 | 9.82 | 12.79 | 4.93 | 4.96 | -2.95 | 165.45 | 929.87 | 1300.00 | 300.00 |
| 11 | 12.34 | 11.95 | 11.92 | 62.51 | 1.04 | 16.72 | 5.42 | 41.83 | 4.85 | 9.92 | 134.77 | 118.69 | 9.84 | 12.74 | 4.86 | 4.88 | -3.07 | 152.42 | 1001.50 | 1200.00 | 275.00 |
| 12 | 11.77 | 12.08 | 11.40 | 55.79 | 1.04 | 16.92 | 5.38 | 36.16 | 4.80 | 9.86 | 135.66 | 117.84 | 9.81 | 12.42 | 4.82 | 4.84 | -2.95 | 143.42 | 920.73 | 1000.00 | 260.00 |
| 13 | 14.27 | 12.04 | 13.73 | 57.86 | 1.05 | 15.45 | 6.03 | 35.30 | 5.07 | 10.03 | 138.11 | 120.36 | 9.26 | 12.97 | 5.07 | 5.10 | -3.26 | 197.48 | 1088.77 | 1400.00 | 360.00 |
| 14 | 13.43 | 12.21 | 12.85 | 57.98 | 1.05 | 17.59 | 6.08 | 39.27 | 5.10 | 10.16 | 137.78 | 119.83 | 9.32 | 13.16 | 5.10 | 5.12 | -2.08 | 197.90 | 1344.45 | 1400.00 | 360.00 |
| 15 | 13.76 | 11.97 | 13.32 | 63.68 | 1.05 | 15.29 | 5.86 | 42.02 | 5.04 | 10.05 | 138.67 | 121.79 | 9.66 | 13.16 | 5.04 | 5.07 | -3.31 | 181.04 | 1098.17 | 1400.00 | 330.00 |
| 16 | 12.98 | 12.19 | 12.45 | 63.52 | 1.05 | 17.82 | 5.94 | 45.06 | 5.07 | 10.23 | 138.11 | 121.11 | 9.80 | 13.44 | 5.08 | 5.10 | -2.28 | 181.45 | 1305.93 | 1400.00 | 330.00 |
| 17 | 12.42 | 11.92 | 12.00 | 53.75 | 1.05 | 15.56 | 5.55 | 33.19 | 4.87 | 9.96 | 139.64 | 123.22 | 9.79 | 12.72 | 4.88 | 4.90 | -3.06 | 160.44 | 963.99 | 1200.00 | 290.00 |
| 18 | 15.31 | 12.35 | 14.86 | 62.61 | 1.05 | 15.76 | 6.40 | 39.45 | 5.29 | 10.41 | 147.36 | 127.34 | 9.56 | 13.81 | 5.28 | 5.31 | -3.37 | 218.01 | 1158.91 | 1400.00 | 400.00 |
| 19 | 14.93 | 11.52 | 14.27 | 67.79 | 1.05 | 16.04 | 6.43 | 47.78 | 5.25 | 9.71 | 147.99 | 126.95 | 8.72 | 13.23 | 5.24 | 5.27 | -2.39 | 218.59 | 1415.86 | 1400.00 | 400.00 |
| 20 | 14.78 | 12.18 | 14.22 | 63.15 | 1.05 | 16.13 | 6.11 | 40.87 | 5.12 | 10.15 | 147.56 | 127.76 | 9.25 | 13.21 | 5.12 | 5.15 | -3.34 | 204.08 | 1150.91 | 1300.00 | 370.00 |
| 21 | 14.21 | 12.16 | 13.59 | 67.02 | 1.05 | 17.43 | 6.18 | 47.39 | 5.19 | 10.16 | 147.91 | 127.24 | 9.33 | 13.44 | 5.19 | 5.21 | -2.38 | 204.34 | 1371.48 | 1300.00 | 370.00 |
| 22 | 14.07 | 12.17 | 13.50 | 56.65 | 1.05 | 17.13 | 5.97 | 34.28 | 5.07 | 10.07 | 148.38 | 128.33 | 9.39 | 13.00 | 5.07 | 5.10 | -3.24 | 193.88 | 1082.04 | 1200.00 | 350.00 |
| 23 | 13.38 | 12.27 | 12.86 | 60.00 | 1.05 | 17.55 | 6.01 | 40.77 | 5.06 | 10.18 | 147.89 | 127.39 | 9.37 | 13.13 | 5.07 | 5.09 | -2.29 | 193.95 | 1321.84 | 1200.00 | 350.00 |
| 24 | 12.80 | 12.11 | 12.34 | 51.51 | 1.05 | 17.57 | 5.71 | 29.92 | 4.94 | 10.07 | 149.46 | 130.52 | 9.77 | 12.87 | 4.95 | 4.97 | -3.06 | 172.77 | 969.43 | 1100.00 | 310.00 |
| 25 | 12.12 | 12.06 | 11.62 | 56.23 | 1.05 | 17.55 | 5.79 | 38.47 | 4.98 | 10.04 | 148.80 | 129.32 | 9.75 | 13.03 | 4.99 | 5.01 | -1.98 | 172.53 | 1283.10 | 1100.00 | 310.00 |
| 26 | 11.94 | 12.07 | 11.56 | 49.80 | 1.05 | 17.48 | 5.50 | 29.11 | 4.81 | 9.98 | 150.10 | 130.45 | 9.79 | 12.55 | 4.82 | 4.84 | -2.95 | 154.89 | 906.95 | 950.00 | 280.00 |
| 27 | 11.56 | 12.12 | 11.20 | 58.28 | 1.05 | 17.50 | 5.34 | 38.36 | 4.74 | 9.94 | 150.66 | 130.06 | 9.87 | 12.44 | 4.75 | 4.78 | -3.01 | 137.60 | 933.91 | 850.00 | 250.00 |
| 28 | 12.00 | 16.20 | 11.65 | 54.11 | 1.05 | 16.01 | 5.97 | 36.07 | 5.55 | 14.86 | 120.36 | 106.44 | 14.70 | 17.18 | 5.56 | 5.59 | -2.79 | 144.60 | 815.66 | 1200.00 | 260.00 |
| 29 | 12.54 | 16.08 | 12.16 | 55.67 | 1.05 | 15.27 | 6.09 | 36.67 | 5.63 | 14.85 | 119.78 | 106.64 | 14.66 | 17.35 | 5.64 | 5.67 | -2.90 | 155.37 | 864.26 | 1400.00 | 280.00 |
| 30 | 11.98 | 16.43 | 11.61 | 52.24 | 1.04 | 18.01 | 6.06 | 34.51 | 5.55 | 14.95 | 125.11 | 109.92 | 14.77 | 17.25 | 5.56 | 5.59 | -2.83 | 144.60 | 831.60 | 1100.00 | 260.00 |
| 31 | 12.77 | 16.38 | 12.36 | 58.92 | 1.04 | 17.11 | 6.21 | 39.65 | 5.62 | 14.93 | 124.83 | 110.39 | 14.66 | 17.44 | 5.65 | 5.67 | -3.04 | 155.37 | 927.14 | 1300.00 | 280.00 |
| 32 | 13.01 | 16.27 | 12.57 | 53.11 | 1.04 | 16.51 | 6.32 | 33.13 | 5.72 | 15.00 | 124.50 | 110.60 | 14.70 | 17.58 | 5.73 | 5.76 | -3.00 | 166.80 | 894.46 | 1400.00 | 300.00 |
| 33 | 11.72 | 16.31 | 11.38 | 53.24 | 1.05 | 16.70 | 5.86 | 35.63 | 5.50 | 14.91 | 130.38 | 114.36 | 14.69 | 17.08 | 5.51 | 5.54 | -2.74 | 138.48 | 810.93 | 1000.00 | 250.00 |
| 34 | 12.68 | 16.31 | 12.29 | 59.67 | 1.05 | 16.70 | 6.11 | 40.61 | 5.64 | 14.56 | 130.10 | 114.44 | 14.52 | 17.29 | 5.65 | 5.67 | -2.93 | 155.37 | 921.24 | 1200.00 | 280.00 |

| Row | P1 [bar] | T1 [°C] | P2 [bar] | T2 [°C] | P3 [bar] | T3 [°C] | P4 [bar] | T4 [°C] | P5 [bar] | T5 [°C] | T6 [°C] | T7 [°C] | T8 [°C] | T9 [°C] | P6 [bar] | P7 [bar] | τ [N.m] | $\dot{V}_{ref}$ [l/h] | $N_{exp}$ [rpm] | $N_{p,HF}$ [rpm] | $N_{p,WF}$ [rpm] |
|---|---|---|---|---|---|---|---|---|---|---|---|---|---|---|---|---|---|---|---|---|---|
| 35 | 12.81 | 16.29 | 12.38 | 51.65 | 1.05 | 16.60 | 6.24 | 31.76 | 5.68 | 14.73 | 129.54 | 114.94 | 14.64 | 17.50 | 5.70 | 5.73 | -2.84 | 166.80 | 866.36 | 1300.00 | 300.00 |
| 36 | 13.60 | 16.31 | 13.12 | 53.85 | 1.05 | 16.44 | 6.43 | 33.02 | 5.84 | 14.69 | 129.06 | 113.89 | 14.62 | 17.75 | 5.79 | 5.81 | -2.96 | 183.05 | 927.67 | 1400.00 | 330.00 |
| 37 | 11.78 | 16.59 | 11.45 | 54.35 | 1.04 | 18.40 | 5.97 | 36.62 | 5.51 | 14.70 | 135.23 | 117.34 | 14.68 | 17.06 | 5.53 | 5.56 | -2.82 | 138.48 | 831.42 | 900.00 | 250.00 |
| 38 | 12.49 | 16.53 | 12.11 | 56.83 | 1.03 | 18.30 | 6.16 | 37.98 | 5.62 | 14.65 | 135.02 | 118.49 | 14.62 | 17.30 | 5.63 | 5.65 | -2.94 | 152.42 | 903.02 | 1100.00 | 275.00 |
| 39 | 13.07 | 16.58 | 12.62 | 51.74 | 1.04 | 18.42 | 6.33 | 31.26 | 5.72 | 14.70 | 134.81 | 118.14 | 14.49 | 17.43 | 5.72 | 5.75 | -2.93 | 172.70 | 899.42 | 1200.00 | 310.00 |
| 40 | 13.75 | 16.60 | 13.26 | 55.88 | 1.04 | 18.61 | 6.49 | 35.43 | 5.81 | 14.81 | 133.92 | 117.45 | 14.53 | 17.78 | 5.76 | 5.78 | -3.07 | 183.05 | 974.85 | 1300.00 | 330.00 |
| 41 | 14.33 | 16.60 | 13.82 | 58.09 | 1.04 | 18.20 | 6.66 | 37.17 | 5.90 | 14.85 | 133.72 | 116.99 | 14.50 | 17.98 | 5.79 | 5.81 | -3.15 | 193.77 | 1026.48 | 1400.00 | 350.00 |
| 42 | 12.23 | 16.24 | 11.86 | 53.17 | 1.05 | 16.46 | 6.01 | 34.89 | 5.61 | 14.83 | 140.27 | 120.74 | 14.72 | 17.29 | 5.61 | 5.64 | -2.78 | 149.18 | 842.15 | 900.00 | 270.00 |
| 43 | 13.03 | 16.23 | 12.60 | 55.91 | 1.05 | 16.67 | 6.22 | 36.27 | 5.72 | 14.70 | 139.38 | 122.94 | 14.61 | 17.51 | 5.74 | 5.76 | -2.93 | 166.80 | 918.65 | 1200.00 | 300.00 |
| 44 | 14.54 | 16.37 | 14.02 | 63.65 | 1.05 | 16.70 | 6.58 | 43.03 | 5.92 | 14.67 | 138.28 | 121.14 | 14.36 | 17.95 | 5.81 | 5.84 | -3.16 | 193.88 | 1071.19 | 1400.00 | 350.00 |
| 45 | 14.91 | 16.53 | 14.51 | 55.89 | 1.05 | 16.70 | 6.86 | 31.41 | 6.09 | 14.93 | 138.04 | 119.81 | 14.47 | 18.28 | 5.86 | 5.88 | -3.07 | 217.62 | 1003.88 | 1400.00 | 400.00 |
| 46 | 15.47 | 17.04 | 15.38 | 70.10 | 1.04 | 18.98 | 7.05 | 48.73 | 6.09 | 15.08 | 147.68 | 127.63 | 14.16 | 18.41 | 6.00 | 6.00 | -3.36 | 217.62 | 1182.00 | 1400.00 | 400.00 |
| 47 | 14.93 | 16.79 | 14.67 | 75.36 | 1.04 | 19.19 | 7.20 | 57.41 | 6.24 | 14.99 | 147.41 | 126.46 | 14.30 | 18.77 | 6.00 | 6.00 | -2.25 | 218.38 | 1398.28 | 1400.00 | 400.00 |
| 48 | 14.83 | 16.91 | 14.31 | 58.96 | 1.03 | 19.33 | 6.81 | 37.90 | 5.97 | 15.01 | 147.86 | 127.48 | 14.35 | 18.09 | 5.83 | 5.85 | -3.17 | 206.46 | 1062.34 | 1200.00 | 375.00 |
| 49 | 14.28 | 16.87 | 13.68 | 62.24 | 1.03 | 19.36 | 6.86 | 43.89 | 5.99 | 14.99 | 147.66 | 126.48 | 14.27 | 18.18 | 5.83 | 5.86 | -2.17 | 206.35 | 1296.06 | 1200.00 | 375.00 |
| 50 | 14.38 | 16.79 | 13.86 | 59.47 | 1.04 | 19.38 | 6.67 | 38.48 | 5.89 | 14.91 | 148.27 | 128.05 | 14.47 | 17.98 | 5.78 | 5.80 | -3.16 | 193.88 | 1053.97 | 1150.00 | 350.00 |
| 51 | 13.71 | 16.74 | 13.15 | 63.33 | 1.03 | 19.48 | 6.74 | 45.94 | 5.95 | 14.89 | 147.89 | 127.07 | 14.47 | 18.14 | 5.80 | 5.82 | -2.17 | 194.20 | 1268.46 | 1150.00 | 350.00 |
| 52 | 13.60 | 16.68 | 13.15 | 60.12 | 1.03 | 19.48 | 6.50 | 40.50 | 5.81 | 14.84 | 149.16 | 129.67 | 14.73 | 17.89 | 5.76 | 5.79 | -3.09 | 175.50 | 1007.76 | 1100.00 | 315.00 |
| 53 | 12.57 | 16.61 | 12.18 | 65.58 | 1.03 | 19.39 | 6.18 | 47.06 | 5.64 | 14.75 | 149.67 | 129.07 | 14.73 | 17.46 | 5.66 | 5.69 | -3.00 | 149.18 | 945.57 | 900.00 | 270.00 |
| 54 | 11.71 | 16.61 | 11.38 | 53.63 | 1.03 | 19.13 | 5.98 | 36.19 | 5.50 | 14.75 | 149.48 | 128.23 | 14.72 | 17.08 | 5.52 | 5.54 | -2.80 | 138.25 | 833.69 | 750.00 | 250.00 |
| 55 | 12.87 | 20.60 | 12.50 | 51.66 | 1.05 | 16.10 | 7.02 | 34.28 | 6.47 | 19.53 | 119.67 | 107.16 | 19.44 | 22.07 | 6.00 | 6.00 | -2.72 | 161.30 | 780.36 | 1400.00 | 290.00 |
| 56 | 12.63 | 20.62 | 12.26 | 53.92 | 1.05 | 16.10 | 6.85 | 36.80 | 6.41 | 19.50 | 120.59 | 106.48 | 19.46 | 21.92 | 6.00 | 6.00 | -2.76 | 149.93 | 792.02 | 1200.00 | 270.00 |
| 57 | 12.18 | 20.67 | 11.85 | 54.62 | 1.05 | 16.10 | 6.74 | 38.22 | 6.33 | 19.58 | 120.31 | 106.32 | 19.56 | 21.83 | 6.00 | 6.00 | -2.69 | 137.97 | 752.73 | 1100.00 | 250.00 |
| 58 | 13.50 | 20.67 | 13.08 | 57.72 | 1.05 | 15.91 | 7.16 | 40.09 | 6.58 | 19.43 | 124.98 | 111.15 | 19.32 | 22.11 | 6.00 | 6.00 | -2.91 | 166.55 | 873.97 | 1400.00 | 300.00 |
| 59 | 12.72 | 20.62 | 12.35 | 52.49 | 1.05 | 16.02 | 6.95 | 35.46 | 6.42 | 19.45 | 125.34 | 111.01 | 19.29 | 21.81 | 6.00 | 6.00 | -2.75 | 155.77 | 784.99 | 1200.00 | 280.00 |
| 60 | 12.34 | 20.65 | 11.99 | 52.95 | 1.05 | 16.06 | 6.83 | 36.58 | 6.36 | 19.53 | 125.31 | 109.38 | 19.46 | 21.81 | 6.00 | 6.00 | -2.69 | 144.80 | 758.29 | 1000.00 | 260.00 |
| 61 | 14.24 | 20.64 | 13.78 | 59.82 | 1.05 | 15.03 | 7.28 | 41.14 | 6.67 | 19.15 | 129.17 | 114.06 | 19.08 | 22.19 | 6.00 | 6.00 | -3.03 | 183.34 | 934.58 | 1400.00 | 330.00 |
| 62 | 13.21 | 20.57 | 12.81 | 52.97 | 1.05 | 15.20 | 7.06 | 35.03 | 6.55 | 19.47 | 129.75 | 114.45 | 19.40 | 22.10 | 6.00 | 6.00 | -2.81 | 166.57 | 807.74 | 1200.00 | 300.00 |
| 63 | 12.63 | 20.56 | 12.26 | 54.26 | 1.05 | 15.57 | 6.85 | 37.35 | 6.41 | 19.46 | 130.02 | 113.51 | 19.44 | 21.90 | 6.00 | 6.00 | -2.77 | 149.36 | 785.76 | 1000.00 | 270.00 |
| 64 | 14.93 | 20.70 | 14.58 | 56.79 | 1.06 | 14.22 | 7.55 | 35.64 | 6.87 | 19.33 | 133.33 | 116.45 | 19.17 | 22.64 | 6.00 | 6.00 | -3.06 | 208.24 | 936.41 | 1400.00 | 380.00 |
| 65 | 14.88 | 20.51 | 14.35 | 62.93 | 1.06 | 13.84 | 7.42 | 43.37 | 6.78 | 19.07 | 133.62 | 117.16 | 19.05 | 22.39 | 6.00 | 6.00 | -3.15 | 193.44 | 968.74 | 1400.00 | 350.00 |
| 66 | 13.85 | 20.54 | 13.40 | 55.63 | 1.05 | 14.46 | 7.17 | 36.70 | 6.62 | 19.30 | 134.52 | 117.66 | 19.21 | 22.15 | 6.00 | 6.00 | -2.97 | 178.17 | 876.27 | 1200.00 | 320.00 |
| 67 | 13.03 | 20.51 | 12.64 | 52.54 | 1.05 | 14.68 | 6.97 | 34.80 | 6.49 | 19.44 | 135.48 | 119.09 | 19.34 | 21.93 | 6.00 | 6.00 | -2.80 | 161.30 | 797.13 | 1100.00 | 290.00 |
| 68 | 12.79 | 20.49 | 12.44 | 66.55 | 1.05 | 14.83 | 6.87 | 48.64 | 6.43 | 19.38 | 135.68 | 118.11 | 19.36 | 21.85 | 6.00 | 6.00 | -2.84 | 144.59 | 836.70 | 1000.00 | 260.00 |
| 69 | 15.03 | 20.87 | 14.66 | 65.96 | 1.05 | 15.86 | 7.82 | 48.85 | 7.07 | 19.32 | 138.01 | 118.81 | 18.92 | 22.88 | 6.00 | 6.00 | -2.09 | 218.50 | 1257.79 | 1400.00 | 400.00 |
| 70 | 15.23 | 20.90 | 14.79 | 64.77 | 1.05 | 15.81 | 7.60 | 45.15 | 6.84 | 19.31 | 137.96 | 120.60 | 18.97 | 22.61 | 6.00 | 6.00 | -3.14 | 202.71 | 1034.79 | 1400.00 | 370.00 |

| Row | P1 [bar] | T1 [°C] | P2 [bar] | T2 [°C] | P3 [bar] | T3 [°C] | P4 [bar] | T4 [°C] | P5 [bar] | T5 [°C] | T6 [°C] | T7 [°C] | T8 [°C] | T9 [°C] | P6 [bar] | P7 [bar] | τ [N.m] | $\dot{V}_{ref}$ [l/h] | $N_{exp}$ [rpm] | $N_{p,HF}$ [rpm] | $N_{p,WF}$ [rpm] |
|---|---|---|---|---|---|---|---|---|---|---|---|---|---|---|---|---|---|---|---|---|---|
| 71 | 14.49 | 20.69 | 13.91 | 73.10 | 1.05 | 15.43 | 7.60 | 58.31 | 6.96 | 19.18 | 137.77 | 119.36 | 18.96 | 22.80 | 6.00 | 6.00 | -1.80 | 202.94 | 1308.77 | 1400.00 | 370.00 |
| 72 | 14.40 | 20.71 | 13.90 | 58.17 | 1.05 | 15.93 | 7.28 | 39.49 | 6.71 | 19.24 | 139.05 | 121.00 | 19.22 | 22.39 | 6.00 | 6.00 | -3.03 | 188.45 | 931.29 | 1200.00 | 340.00 |
| 73 | 13.63 | 20.69 | 13.15 | 62.06 | 1.05 | 16.10 | 7.34 | 46.54 | 6.77 | 19.17 | 138.20 | 119.79 | 19.09 | 22.41 | 6.00 | 6.00 | -1.99 | 188.70 | 1156.55 | 1200.00 | 340.00 |
| 74 | 13.40 | 20.68 | 12.99 | 56.89 | 1.05 | 16.10 | 7.01 | 39.49 | 6.54 | 19.50 | 139.58 | 122.23 | 19.34 | 22.11 | 6.00 | 6.00 | -2.92 | 165.92 | 867.42 | 1100.00 | 300.00 |
| 75 | 12.91 | 20.64 | 12.54 | 62.67 | 1.05 | 16.15 | 6.93 | 45.59 | 6.48 | 19.40 | 140.49 | 121.97 | 19.38 | 21.89 | 6.00 | 6.00 | -2.88 | 149.12 | 840.33 | 950.00 | 270.00 |
| 76 | 15.23 | 20.89 | 14.92 | 62.74 | 1.05 | 16.39 | 7.66 | 43.19 | 6.95 | 19.39 | 147.83 | 127.67 | 19.22 | 22.81 | 6.00 | 6.00 | -3.18 | 207.10 | 1020.34 | 1200.00 | 380.00 |
| 77 | 14.68 | 20.88 | 14.13 | 69.11 | 1.05 | 16.51 | 7.76 | 53.18 | 7.00 | 19.29 | 147.67 | 126.33 | 18.96 | 22.81 | 6.00 | 6.00 | -1.94 | 208.05 | 1283.85 | 1200.00 | 380.00 |
| 78 | 14.64 | 20.83 | 14.17 | 59.44 | 1.04 | 16.66 | 7.42 | 40.34 | 6.79 | 19.27 | 148.72 | 128.56 | 19.21 | 22.47 | 6.00 | 6.00 | -3.07 | 193.27 | 959.54 | 1100.00 | 350.00 |
| 79 | 14.06 | 20.73 | 13.53 | 62.47 | 1.04 | 16.86 | 7.51 | 46.37 | 6.85 | 19.19 | 148.08 | 127.36 | 19.17 | 22.55 | 6.00 | 6.00 | -2.22 | 193.39 | 1143.36 | 1100.00 | 350.00 |
| 80 | 13.76 | 20.75 | 13.32 | 55.04 | 1.05 | 16.80 | 7.29 | 36.51 | 6.62 | 19.30 | 149.65 | 129.67 | 19.27 | 22.18 | 6.00 | 6.00 | -2.96 | 178.03 | 876.70 | 1000.00 | 320.00 |
| 81 | 12.90 | 20.64 | 12.43 | 59.90 | 1.04 | 16.75 | 7.42 | 45.77 | 6.72 | 19.47 | 149.11 | 128.20 | 19.28 | 22.37 | 6.00 | 6.00 | -1.64 | 178.00 | 1160.53 | 1000.00 | 320.00 |
| 82 | 13.16 | 20.65 | 12.75 | 56.08 | 1.04 | 16.69 | 7.10 | 38.94 | 6.49 | 19.46 | 150.19 | 130.82 | 19.30 | 21.94 | 6.00 | 6.00 | -2.89 | 161.24 | 845.60 | 950.00 | 290.00 |
| 83 | 12.24 | 20.58 | 11.78 | 69.66 | 1.04 | 16.45 | 7.26 | 56.16 | 6.62 | 19.35 | 149.82 | 128.61 | 19.18 | 22.10 | 6.00 | 6.00 | -1.44 | 161.45 | 1182.66 | 950.00 | 290.00 |
| 84 | 12.46 | 20.67 | 12.14 | 57.38 | 1.04 | 16.47 | 6.98 | 41.28 | 6.41 | 19.50 | 149.90 | 128.22 | 19.47 | 21.81 | 6.00 | 6.00 | -2.78 | 143.53 | 784.95 | 750.00 | 260.00 |

## Bibliography

[1] Bronicki LY. Short Review of the Long History of ORC Power Systems. Keynote Lect. 2nd Int. Semin. ORC power Syst. - ASME-ORC 2013. Rotterdam, 2013.

[2] Tartière T, Astolfi M. A World Overview of the Organic Rankine Cycle Market. vol. 129. Elsevier Ltd; 2017. https://doi.org/10.1016/j.egypro.2017.09.159.

[3] Waste Heat Recovery: Technology and Opportunities in U.S. Industry. 2008.

[4] Jouhara H, Khordehgah N, Almahmoud S, Delpech B, Chauhan A, Tassou SA. Waste heat recovery technologies and applications. Therm Sci Eng Prog 2018;6:268–89. https://doi.org/10.1016/j.tsep.2018.04.017.

[5] van de Bor DM, Infante Ferreira CA, Kiss AA. Low grade waste heat recovery using heat pumps and power cycles. Energy 2015;89:864–73. https://doi.org/10.1016/j.energy.2015.06.030.

[6] Industrial excess heat recovery technologies and applications. 2019.

[7] Haddad C, Périlhon C, Danlos A, François MX, Descombes G. Some efficient solutions to recover low and medium waste heat: Competitiveness of the thermoacoustic technology. Energy Procedia, vol. 50, Elsevier Ltd; 2014, p. 1056–69. https://doi.org/10.1016/j.egypro.2014.06.125.

[8] Shi L, Shu G, Tian H, Deng S. A review of modified Organic Rankine cycles (ORCs) for internal combustion engine waste heat recovery (ICE-WHR). Renew Sustain Energy Rev 2018;92:95–110. https://doi.org/10.1016/j.rser.2018.04.023.

[9] Cioccolanti L, Tascioni R, Bocci E, Villarini M. Parametric analysis of a solar Organic Rankine Cycle trigeneration system for residential applications.

Energy Convers Manag 2018;163:407–19. https://doi.org/10.1016/j.enconman.2018.02.043.

[10] Colantoni A, Villarini M, Marcantonio V, Gallucci F, Cecchini M. Performance analysis of a small-scale ORC trigeneration system powered by the combustion of olive pomace. Energies 2019;12:2279. https://doi.org/10.3390/en12122279.

[11] Altun AF, Kilic M. Thermodynamic performance evaluation of a geothermal ORC power plant. Renew Energy 2020;148:261–74. https://doi.org/10.1016/j.renene.2019.12.034.

[12] Pereira, J. S., Ribeiro, J. B., Mendes, R., Vaz, G. C., André JC. ORC based micro-cogeneration systems for residential application – A state of the art review and current challenges. Renew Sustain Energy Rev 2018;92:728–43.

[13] Li J, Ge Z, Duan Y, Yang Z, Liu Q. Parametric optimization and thermodynamic performance comparison of single-pressure and dual-pressure evaporation organic Rankine cycles. Appl Energy 2018;217:409–21. https://doi.org/10.1016/j.apenergy.2018.02.096.

[14] Mahmoudi A, Fazli M, Morad MR. A recent review of waste heat recovery by Organic Rankine Cycle. Appl Therm Eng 2018. https://doi.org/10.1016/j.applthermaleng.2018.07.136.

[15] Ennio Macchi. Theoretical basis of the Organic Rankine Cycle. Org. Rank. Cycle Power Syst., 2017.

[16] Park BS, Usman M, Imran M, Pesyridis A. Review of Organic Rankine Cycle experimental data trends. Energy Convers Manag 2018;173:679–91. https://doi.org/10.1016/j.enconman.2018.07.097.

[17] Moradi R, Tascioni R, Habib E, Cioccolanti L, Villarini M, EnricoBocci, et al.

Thermodynamic simulation of a small-scale organic Rankine cycle testing facility using R245fa. Energy Procedia 2018;148:66–73. https://doi.org/10.1016/j.egypro.2018.08.020.

[18] Astolfi M. Technical options for Organic Rankine Cycle systems. Org. Rank. Cycle Power Syst., 2017.

[19] Rahbar K, Mahmoud S, Al-Dadah RK, Moazami N, Mirhadizadeh SA. Review of organic Rankine cycle for small-scale applications. Energy Convers Manag 2017;134:135–55. https://doi.org/10.1016/j.enconman.2016.12.023.

[20] Campana C, Cioccolanti L, Renzi M, Caresana F. Experimental analysis of a small-scale scroll expander for low-temperature waste heat recovery in Organic Rankine Cycle. Energy 2019;187:115929.

[21] Imran M, Haglind F, Asim M, Zeb Alvi J. Recent research trends in organic Rankine cycle technology: A bibliometric approach. Renew Sustain Energy Rev 2018;81:552–62. https://doi.org/10.1016/j.rser.2017.08.028.

[22] Jiménez-Arreola M, Pili R, Dal Magro F, Wieland C, Rajoo S, Romagnoli A. Thermal power fluctuations in waste heat to power systems: An overview on the challenges and current solutions. Appl Therm Eng 2018;134:576–84. https://doi.org/10.1016/j.applthermaleng.2018.02.033.

[23] Liu L, Zhu T, Gao N, Gan Z. A Review of Modeling Approaches and Tools for the Off-design Simulation of Organic Rankine Cycle. J Therm Sci 2018;27:305–20. https://doi.org/10.1007/s11630-018-1023-2.

[24] Freeman J, Guarracino I, Kalogirou SA, Markides CN. A small-scale solar organic Rankine cycle combined heat and power system with integrated thermal energy storage. Appl Therm Eng 2017;127:1543–54. https://doi.org/10.1016/j.applthermaleng.2017.07.163.

[25] Villarini M, Tascioni R, Arteconi A, Cioccolanti L. Influence of the incident radiation on the energy performance of two small-scale solar Organic Rankine Cycle trigenerative systems: A simulation analysis. Appl Energy 2019;242:1176–88. https://doi.org/10.1016/j.apenergy.2019.03.066.

[26] Hu D, Zheng Y, Wu Y, Li S, Dai Y. Off-design performance comparison of an organic Rankine cycle under different control strategies. Appl Energy 2015;156:268–79. https://doi.org/10.1016/j.apenergy.2015.07.029.

[27] Ibarra M, Rovira A, Alarcón-Padilla DC, Blanco J. Performance of a 5kWe Organic Rankine Cycle at part-load operation. Appl Energy 2014;120:147–58. https://doi.org/10.1016/j.apenergy.2014.01.057.

[28] Dickes R, Dumont O, Guillaume L, Quoilin S, Lemort V. Charge-sensitive modelling of organic Rankine cycle power systems for off-design performance simulation. Appl Energy 2018;212:1262–81. https://doi.org/10.1016/j.apenergy.2018.01.004.

[29] Dickes R. Charge-sensitive methods for the off-design performance characterization of organic Rankine cycle (ORC) power systems. University of Liege, 2019.

[30] Yousefzadeh M, Uzgoren E. Mass-conserving dynamic organic Rankine cycle model to investigate the link between mass distribution and system state. Energy 2015;93:1128–39. https://doi.org/10.1016/j.energy.2015.09.102.

[31] Ziviani D, Woodland BJ, Georges E, Groll EA, Braun JE, Horton WT, et al. Development and a validation of a charge sensitive organic Rankine cycle (ORC) simulation tool. Energies 2016;9. https://doi.org/10.3390/en9060389.

[32] Liu L, Zhu T, Ma J. Working fluid charge oriented off-design modeling of a small scale Organic Rankine Cycle system. Energy Convers Manag 2017;148:944–53. https://doi.org/10.1016/j.enconman.2017.06.009.

[33] Santos M, André J, Francisco S, Mendes R, Ribeiro J. Off-design modelling of an organic Rankine cycle micro-CHP: Modular framework, calibration and validation. Appl Therm Eng 2018;137:848–67. https://doi.org/10.1016/j.applthermaleng.2018.04.009.

[34] Woodland BJ, Braun JE, Groll EA, Horton WT. Experimental Testing of an Organic Rankine Cycle with Scroll-type Expander. Int. Refrig. air Cond. Conf. Purdue, No. 2505, 2012.

[35] Ziviani D, James NA, Accorsi FA, Braun JE, Groll EA. Experimental and numerical analyses of a 5 kWe oil-free open-drive scroll expander for small-scale organic Rankine cycle (ORC) applications. Appl Energy 2018;230:1140–56. https://doi.org/10.1016/J.APENERGY.2018.09.025.

[36] Michael PW, Khalid H, Wanke T. An investigation of external gear pump efficiency and stribeck values. SAE Tech. Pap., vol. 8, SAE International; 2012. https://doi.org/10.4271/2012-01-2041.

[37] Stribeck R. Kugellager fur beliebige Belastungen. Zeitschrift Des Vereines Dtsch Ingenieure 1901;45:73–9 & 118–25.

[38] Colebrook CF, White CM. Experiments with Fluid Friction Factor in Roughened Pipes. Proc R Soc London Ser A Math Phys Sci n.d. https://www.scirp.org/(S(lz5mqp453edsnp55rrgjct55))/reference/ReferencesPapers.aspx?ReferenceID=1764185 (accessed August 14, 2020).

[39] Bogaert R, Böles A. Global performance of a prototype brazed plate heat exchanger in a large reynolds number range. Exp Heat Transf 1995;8:293–311. https://doi.org/10.1080/08916159508946508.

[40] Landelle A, Tauveron N, Revellin R, Haberschill P, Colasson S, Roussel V. Performance investigation of reciprocating pump running with organic fluid for organic Rankine cycle. Appl Therm Eng 2017;113:962–9.

https://doi.org/10.1016/j.applthermaleng.2016.11.096.

[41] Borsukiewicz-Gozdur A. Pumping work in the organic Rankine cycle. Appl Therm Eng 2013;51:781–6. https://doi.org/10.1016/j.applthermaleng.2012.10.033.

[42] Yamada N, Watanabe M, Hoshi A. Experiment on pumpless Rankine-type cycle with scroll expander. Energy 2013;49:137–45. https://doi.org/10.1016/j.energy.2012.10.027.

[43] Yang X, Xu J, Miao Z, Zou J, Yu C. Operation of an organic Rankine cycle dependent on pumping flow rates and expander torques. Energy 2015;90:864–78. https://doi.org/10.1016/j.energy.2015.07.121.

[44] Dumont O, Quoilin S, Lemort V. Experimental investigation of a reversible heat pump/organic Rankine cycle unit designed to be coupled with a passive house to get a Net Zero Energy Building. Int J Refrig 2015;54:190–203. https://doi.org/10.1016/j.ijrefrig.2015.03.008.

[45] Chang JC, Hung TC, He YL, Zhang W. Experimental study on low-temperature organic Rankine cycle utilizing scroll type expander. Appl Energy 2015;155:150–9. https://doi.org/10.1016/j.apenergy.2015.05.118.

[46] Declaye S. Design, optimization and modeling of an organic Rankine cycle for waste heat recovery. University of Liege, Belgium, 2009.

[47] Galindo J, Ruiz S, Dolz V, Royo-Pascual L, Haller R, Nicolas B, et al. Experimental and thermodynamic analysis of a bottoming Organic Rankine Cycle (ORC) of gasoline engine using swash-plate expander. Energy Convers Manag 2015;103:519–32. https://doi.org/10.1016/j.enconman.2015.06.085.

[48] Miao Z, Xu J, Yang X, Zou J. Operation and performance of a low temperature organic Rankine cycle. Appl Therm Eng 2015;75:1065–75.

https://doi.org/10.1016/j.applthermaleng.2014.10.065.

[49] Quoilin S, Broek M Van Den, Declaye S, Dewallef P, Lemort V. Techno-economic survey of organic rankine cycle (ORC) systems. Renew Sustain Energy Rev 2013;22:168–86. https://doi.org/10.1016/j.rser.2013.01.028.

[50] Shah RK, Focke WW. Plate heat exchangers and their design theory. Heat Transf Equip Des 1988:227–54.

[51] Desideri A, Zhang J, Kærn MR, Ommen TS, Wronski J, Lemort V, et al. An experimental analysis of flow boiling and pressure drop in a brazed plate heat exchanger for organic Rankine cycle power systems. Int J Heat Mass Transf 2017;113:6–21. https://doi.org/10.1016/j.ijheatmasstransfer.2017.05.063.

[52] Dittus FW, Boelter LMK. Heat transfer in automobile radiators of the tubular type. Univ Calif Publ Eng Repr Int Commun Heat Mass 1930:443–61.

[53] Sieder EN, Tate GE. Heat Transfer and Pressure Drop of Liquids in Tubes. Ind Eng Chem 1936;28:1429–35. https://doi.org/10.1021/ie50324a027.

[54] Kays WMM, Crawford ME. Convective heat and mass transfer. 3 rd. McGraw-Hill Series in Mechanical Engineering; 1993.

[55] Claesson J. Thermal and hydraulic performance of compact brazed plate heat exchangers operating as evaporators in domestic heat pumps. 2004.

[56] Claesson J. Performance of compact brazed plate heat exchanger operating as condenser in domestic heat pump system : An experimental investigation. 8th IEA Heat Pump Conf., International Energy Agency Heat Pump Conference: Global Advances in Heat Pump Technology, Applications, and Market; 2005.

[57] Kuo WS, Lie YM, Hsieh YY, Lin TF. Condensation heat transfer and pressure drop of refrigerant R-410A flow in a vertical plate heat exchanger. Int J Heat Mass Transf 2005;48:5205–20.

https://doi.org/10.1016/j.ijheatmasstransfer.2005.07.023.

[58] Hsieh YY, Chiang LJ, Lin TF. Subcooled flow boiling heat transfer of R-134a and the associated bubble characteristics in a vertical plate heat exchanger. Int J Heat Mass Transf 2002;45:1791–806. https://doi.org/10.1016/S0017-9310(01)00294-0.

[59] Hsieh YY, Lin TF. Evaporation heat transfer and pressure drop of refrigerant R-410A flow in a vertical plate heat exchanger. J Heat Transfer 2003;125:852–7. https://doi.org/10.1115/1.1518498.

[60] Yan YY, Lin TF. Evaporation heat transfer and pressure drop of refrigerant r-134a in a plate heat exchanger. J Heat Transfer 1999;121:118–27. https://doi.org/10.1115/1.2825924.

[61] Aboelwafa, O; Fateen, S.E.K.; Soliman, A.; Ismail IM. A review on solar Rankine cycles: Working fluids, applications and cycle modifications. Renew Sustain Energy Rev 2018;82:868–85.

[62] Moradi R, Habib E, Bocci E, Cioccolanti L. Investigation on the use of a novel regenerative flow turbine in a micro-scale Organic Rankine Cycle unit. Energy 2020;210:118519. https://doi.org/10.1016/j.energy.2020.118519.

[63] Imran M, Usman M, Park B-S, Lee D-H. Volumetric expanders for low grade heat and waste heat recovery applications. Renew Sustain Energy Rev 2016;57:1090–109. https://doi.org/10.1016/J.RSER.2015.12.139.

[64] Dumont O, Parthoens A, Dickes R, Lemort V. Experimental investigation and optimal performance assessment of four volumetric expanders (scroll, screw, piston and roots) tested in a small-scale organic Rankine cycle system. Energy 2018. https://doi.org/10.1016/j.energy.2018.06.182.

[65] Yanagisawa T, Shimizu T, Fukuta M, Handa T. Study on Fundamental

Performance of Scroll Expander. Trans Japan Soc Mech Eng Ser B 1988;54:2798–803. https://doi.org/10.1299/kikaib.54.2798.

[66] Song P, Wei M, Shi L, Danish SN, Ma C. A review of scroll expanders for organic Rankine cycle systems. Appl Therm Eng 2015;75:54–64. https://doi.org/10.1016/j.applthermaleng.2014.05.094.

[67] Dickes R, Dumont O, Legros A, Quoilin S, Lemort V. Analysis and comparison of different modeling approaches for the simulation of a micro-scale organic Rankine cycle power plant. 3rd Int. Semin. ORC Power Syst., Brussels, Belgium: 2015.

[68] Wu Z, Pan D, Gao N, Zhu T, Xie F. Experimental testing and numerical simulation of scroll expander in a small scale organic Rankine cycle system. Appl Therm Eng 2015;87:529–37. https://doi.org/10.1016/j.applthermaleng.2015.05.040.

[69] Emhardt S, Song P, Tian G, Chew J, Wei M. CFD analysis of variable wall thickness scroll expander integrated into small scale ORC systems. Energy Procedia, vol. 158, Elsevier Ltd; 2019, p. 2272–7. https://doi.org/10.1016/j.egypro.2019.01.241.

[70] Song P, Zhuge W, Zhang Y, Zhang L, Duan H. Unsteady Leakage Flow Through Axial Clearance of an ORC Scroll Expander. Energy Procedia, vol. 129, Elsevier Ltd; 2017, p. 355–62. https://doi.org/10.1016/j.egypro.2017.09.221.

[71] Chang JC, Chang CW, Hung TC, Lin JR, Huang KC. Experimental study and CFD approach for scroll type expander used in low-temperature organic Rankine cycle. Appl Therm Eng 2014;73:1444–52. https://doi.org/10.1016/j.applthermaleng.2014.08.050.

[72] Winandy E, Saavedra O CS, Lebrun J. Experimental analysis and simplified modelling of a hermetic scroll refrigeration compressor. Appl Therm Eng

2002;22:107–20. https://doi.org/10.1016/S1359-4311(01)00083-7.

[73] Lemort V, Quoilin S, Cuevas C, Lebrun J. Testing and modeling a scroll expander integrated into an Organic Rankine Cycle. Appl Therm Eng 2009;29:3094–102. https://doi.org/10.1016/J.APPLTHERMALENG.2009.04.013.

[74] Quoilin S, Lemort V, Lebrun J. Experimental study and modeling of an Organic Rankine Cycle using scroll expander. Appl Energy 2010;87:1260–8. https://doi.org/10.1016/j.apenergy.2009.06.026.

[75] Lemort V, Declaye S, Quoilin S. Experimental characterization of a hermetic scroll expander for use in a micro-scale Rankine cycle. Proc Inst Mech Eng Part A J Power Energy 2012;226:126–36. https://doi.org/10.1177/0957650911413840.

[76] Yang J, Sun Z, Yu B, Chen J. Modeling and optimization criteria of scroll expander integrated into organic Rankine cycle for comparison of R1233zd(E) as an alternative to R245fa. Appl Therm Eng 2018;141:386–93. https://doi.org/10.1016/j.applthermaleng.2018.06.001.

[77] Dardenne L, Fraccari E, Maggioni A, Molinaroli L, Proserpio L, Winandy E. Semi-empirical modelling of a variable speed scroll compressor with vapour injection. Int J Refrig 2015;54:76–87. https://doi.org/10.1016/j.ijrefrig.2015.03.004.

[78] Ziviani D, Gusev S, Lecompte S, Groll EA, Braun JE, Horton WT, et al. Characterizing the performance of a single-screw expander in a small-scale organic Rankine cycle for waste heat recovery. Appl Energy 2016;181:155–70. https://doi.org/10.1016/j.apenergy.2016.08.048.

[79] Ayachi F, Ksayer EB, Neveu P, Zoughaib A. Experimental investigation and modeling of a hermetic scroll expander. Appl Energy 2016;181:256–67.

https://doi.org/10.1016/j.apenergy.2016.08.030.

[80] Declaye S, Quoilin S, Guillaume L, Lemort V. Experimental study on an open-drive scroll expander integrated into an ORC (Organic Rankine Cycle) system with R245fa as working fluid. Energy 2013;55:173–83.

[81] Giuffrida A. Modelling the performance of a scroll expander for small organic Rankine cycles when changing the working fluid. Appl Therm Eng 2014;70:1040–9. https://doi.org/10.1016/j.applthermaleng.2014.06.004.

[82] MATLAB R2020a. Natick, Massachusetts: The MathWorks Inc. n.d.

[83] Dumont O, Dickes R, Lemort V. Extrapolability and limitations of a semi-empirical model for the simulation of volumetric expanders. Energy Procedia, vol. 129, Elsevier Ltd; 2017, p. 315–22. https://doi.org/10.1016/j.egypro.2017.09.198.

[84] Byrne P, Ghoubali R, Miriel J. Scroll compressor modelling for heat pumps using hydrocarbons as refrigerants. Int J Refrig 2014;41:1–13. https://doi.org/10.1016/j.ijrefrig.2013.06.003.

[85] Duprez ME, Dumont E, Frère M. Modelling of reciprocating and scroll compressors. Int J Refrig 2007;30:873–86. https://doi.org/10.1016/j.ijrefrig.2006.11.014.

[86] Mendoza LC, Navarro-Esbrí J, Bruno JC, Lemort V, Coronas A. Characterization and modeling of a scroll expander with air and ammonia as working fluid. Appl Therm Eng 2014;70:630–40. https://doi.org/10.1016/j.applthermaleng.2014.05.069.

[87] Chen Y, Halm NP, Groll EA, Braun JE. Mathematical modeling of scroll compressors - Part I: Compression process modeling. Int J Refrig 2002;25:731–50. https://doi.org/10.1016/S0140-7007(01)00071-8.

[88] Thome JR. Encyclopedia of Two-Phase Heat Transfer and Flow I. vol. 3. WORLD SCIENTIFIC; 2015. https://doi.org/10.1142/9310-vol3.

[89] SWEP brazed plate heat exchangers - SWEP n.d. https://www.swep.net/ (accessed November 17, 2020).

[90] Rouhani SZ, Axelsson E. Calculation of void volume fraction in the subcooled and quality boiling regions. Int J Heat Mass Transf 1970;13:383–93. https://doi.org/10.1016/0017-9310(70)90114-6.

[91] Woldesemayat MA, Ghajar AJ. Comparison of void fraction correlations for different flow patterns in horizontal and upward inclined pipes. Int J Multiph Flow 2007;33:347–70. https://doi.org/10.1016/j.ijmultiphaseflow.2006.09.004.

[92] Qian H, Hrnjak P. Void Fraction and Flow Regimes of R134a In Horizontal and Vertical Round Tubes in Developed Adiabatic Conditions. Int Refrig Air Cond Conf 2018.

[93] Zivi SM. Estimation of steady-state steam void-fraction by means of the principle of minimum entropy production. J Heat Transfer 1964;86:247–51. https://doi.org/10.1115/1.3687113.

[94] Premoli A, Francesco D., Prina A. A dimensional correlation for evaluating two-phase mixture density. La Termotec 1971;25:17–26.

[95] Pan Y, Liu L, Zhu T. Simulation of working fluid mass distribution in small-scale Organic Rankine Cycle system under sub-critical conditions. Appl Therm Eng 2018;131:884–96. https://doi.org/10.1016/j.applthermaleng.2017.12.017.

[96] Sun KH, Duffey RB, Peng CM. The prediction of two-phase mixture level and hydrodynamically-controlled dryout under low flow conditions. Int J Multiph Flow 1981;7:521–43. https://doi.org/10.1016/0301-9322(81)90056-2.

[97] Godbole P V., Tang CC, Ghajar AJ. Comparison of void fraction correlations for different flow patterns in upward vertical two-phase flow. Heat Transf Eng 2011;32:843–60. https://doi.org/10.1080/01457632.2011.548285.

[98] Graham DM, Newell TA, Chato JC. Experimental Investigation of Void Fraction During Refrigerant Condensation. Air Conditioning and Refrigeration Center. College of Engineering. University of Illinois at Urbana-Champaign.; 1997.

[99] Sarntichartsak P, Monyakul V, Thepa S, Nathakaranakule A. Simulation and experimental evaluation of the effects of oil circulation in an inverter air conditioning system using R-22 and R-407C. Appl Therm Eng 2006;26:1481–91. https://doi.org/10.1016/j.applthermaleng.2006.01.002.

[100] Popovic P, Shimon RL, Pate M, Schnur NE. Effects of lubricant miscibility and viscosity on the performance of an R-134a refrigerating system. ASHRAE Trans 2000;106:1–13.

[101] Kruse HH, Schroeder M. Fundamentals of lubrication in refrigerating systems and heat pumps. Int J Refrig 1985;8:347–55. https://doi.org/10.1016/0140-7007(85)90030-1.

[102] McMullan JT, Murphy N, Hughes DW. The effect of oil on the performance of heat pumps and refrigerators-II. Experimental results. Heat Recover Syst CHP 1988;8:95–124. https://doi.org/10.1016/0890-4332(88)90004-X.

[103] Navarro E, Urchueguía JF, Gonzálvez J, Corberán JM. Test results of performance and oil circulation rate of commercial reciprocating compressors of different capacities working with propane (R290) as refrigerant. Int J Refrig 2005;28:881–8. https://doi.org/10.1016/j.ijrefrig.2005.01.010.

[104] Biancardi FR, Michels HH, Sienel TH, Pandy DR. STUDY OF LUBRICANT CIRCULATION IN HVAC SYSTEMS Volume I-Description of Technical

Effort and Results Final Technical Report. 1996.

[105] Landelle A, Tauveron N, Haberschill P, Revellin R, Colasson S. Organic Rankine cycle design and performance comparison based on experimental database. Appl Energy 2017;204:1172–87. https://doi.org/10.1016/j.apenergy.2017.04.012.

[106] Desideri A, Gusev S, van den Broek M, Lemort V, Quoilin S. Experimental comparison of organic fluids for low temperature ORC (organic Rankine cycle) systems for waste heat recovery applications. Energy 2016;97:460–9. https://doi.org/10.1016/j.energy.2015.12.012.

[107] Feng Y qiang, Hung TC, He YL, Wang Q, Chen SC, Wu SL, et al. Experimental investigation of lubricant oil on a 3 kW organic Rankine cycle (ORC) using R123. Energy Convers Manag 2019;182:340–50. https://doi.org/10.1016/j.enconman.2018.12.021.

[108] Yang J, Yu B, Ye Z, Shi J, Chen J. Experimental investigation of the impact of lubricant oil ratio on subcritical organic Rankine cycle for low-temperature waste heat recovery. Energy 2019;188:116099. https://doi.org/10.1016/j.energy.2019.116099.

[109] Dawo F, Fleischmann J, Kaufmann F, Schifflechner C, Eyerer S, Wieland C, et al. R1224yd(Z), R1233zd(E) and R1336mzz(Z) as replacements for R245fa: Experimental performance, interaction with lubricants and environmental impact. Appl Energy 2021;288:116661. https://doi.org/10.1016/j.apenergy.2021.116661.

[110] Bell IH, Wronski J, Quoilin S, Lemort V. Pure and pseudo-pure fluid thermophysical property evaluation and the open-source thermophysical property library coolprop. Ind Eng Chem Res 2014;53:2498–508. https://doi.org/10.1021/ie4033999.

[111] Grebner JJ, Crawford RR, Conditioning A. The Effects of Oil on the Thermodynamic Properties of Dichlorodifluoromethane ( R-12 ) and Tetrafluoroethane ( R-134a ) Acustar Division of Chrysler Bergstrom Manufacturing Co . Ford Motor Company General Electric Company Harrison Division of GM ICI Ameri. Ind Eng 1992;61801.

[112] Grebner JJ, Crawford RR. The Effects of Oil on the Thermodynamic Properties of Dichlorodifluoromethane (R-12) and Tetrafluoroethane (R-134a). Air Conditioning and Refrigeration Center. College of Engineering. University of Illinois at Urbana-Champaign.; 1992.

[113] Dickes R, Dumont O, Lemort V. Experimental assessment of the fluid charge distribution in an organic Rankine cycle (ORC) power system. Appl Therm Eng 2020;179:115689. https://doi.org/10.1016/j.applthermaleng.2020.115689.

[114] Pantano F, Capata R. Expander selection for an on board ORC energy recovery system. Energy 2017;141:1084–96. https://doi.org/10.1016/j.energy.2017.09.142.

[115] Galloni E, Fontana G, Staccone S. Design and experimental analysis of a mini ORC (organic Rankine cycle)power plant based on R245fa working fluid. Energy 2015;90:768–75.

[116] Gao P, Jiang L, Wang LW, Wang RZ, Song FP. Simulation and experiments on an ORC system with different scroll expanders based on energy and exergy analysis. Appl Therm Eng 2015;75:880–8. https://doi.org/10.1016/j.applthermaleng.2014.10.044.

[117] Manfrida G, Pacini L, Talluri L. An upgraded Tesla turbine concept for ORC applications. Energy 2018;158:33–40. https://doi.org/10.1016/J.ENERGY.2018.05.181.

[118] Talluri L, Dumont O, Manfrida G, Lemort V, Fiaschi D. Experimental

investigation of an Organic Rankine Cycle Tesla turbine working with R1233zd(E). Appl Therm Eng 2020;174:115293. https://doi.org/10.1016/j.applthermaleng.2020.115293.

[119] Lemort V, Legros A. Positive displacement expanders for Organic Rankine Cycle systems. Org Rank Cycle Power Syst 2017:361–96. https://doi.org/10.1016/B978-0-08-100510-1.00012-0.

[120] Zhao Y, Liu G, Li L, Yang Q, Tang B, Liu Y. Expansion devices for organic Rankine cycle (ORC) using in low temperature heat recovery: A review. Energy Convers Manag 2019. https://doi.org/10.1016/j.enconman.2019.111944.

[121] Nejad J, Riasi A, Nourbakhsh A. Performance improvement and parametric study of regenerative flow pump considering the modification in blade and casing geometry. Int J Numer Methods Heat Fluid Flow 2017;27:1887–906.

[122] Karlsen-Davies ND, Aggidis GA. Regenerative Liquid Ring Pumps Review and Advances on Design and Performance. Appl Energy 2016;164:815–25.

[123] Quail F, Scanlon T, Baumgartner A. Design study of a regenerative pump using one-dimensional and three-dimensional numerical techniques. Eur J Mech B/Fluids 2012;31:181–7.

[124] Meakhail T, Park SO. An improved theory for regenerative pump performance. Proc Inst Mech Eng Part A J Power Energy 2005;219:213–22.

[125] Quail F, Stickland M, Baumgartner A. A one-dimensional numerical model for the momentum exchange in regenerative pumps. J Eng Gas Turbines Power 2011;133.

[126] Song JW, Engeda A, Chung MK. A modified theory for the flow mechanism in a regenerative flow pump. Proc Inst Mech Eng Part A J Power Energy

2003;217:311–21.

[127] Yoo IS, Park MR, Chung MK. Improved momentum exchange theory for incompressible regenerative turbomachines. Proc Inst Mech Eng Part A J Power Energy 2005;219:567–81.

[128] Badami M, Mura M. Theoretical model with experimental validation of a regenerative blower for hydrogen recirculation in a PEM fuel cell system. Energy Convers Manag 2010;51:553–60.

[129] Engeda A, Raheel M. Theory and design of the regenerative flow compressor. Proc. Int. Gas Turbine Congr., Tokyo: 2003.

[130] Karlsen-Davies ND, Aggidis GA. Computational and experimental analysis of the effects of manufacturing tolerances on the performance of a regenerative liquid ring pump. Lancaster University, 2017.

[131] Raheel M, Engeda A. Current status, design and performance trends for the regenerative flow compressors and pumps. ASME Int Mech Eng Congr Expo New Orleans, Louisiana 2002:17–22.

[132] Quail FJ, Scanlon T, Strickland M. Development of a regenerative pump impeller using rapid manufacturing techniques. Rapid Prototyp J 2010;16:337–44.

[133] Balducci F, Bartolini CM. INDAGINE SPERIMENTALE SUL CAMPO FLUIDODINAMICO INTERNO ALLE TURBINE A CANALE PERIFERICO TT - Experimental survey on the dynamics of the peripheral channel turbines. University of Ancona, 1992.

[134] Bartolini CM, Salvi D. Experimental analysis of a small prototype of peripheral turbine for decompression of natural gas. ASME Int Gas Turbine Aeroengine Congr Exhib Birmingham, UK 1996.

[135] Denton JD. Some limitations of turbomachinery CFD. ASME Turbo Expo 2010 Power Land, Sea, Air 2010;7:735–45.

[136] ANSYS® Academic Research CFD, Release 18.0 n.d.

[137] Muhammad U, Imran M, Lee DH, Park BS. Design and experimental investigation of a 1 kW organic Rankine cycle system using R245fa as working fluid for low-grade waste heat recovery from steam. Energy Convers Manag 2015;103:1089–100.

[138] Academic Research CFD, Release 18.0, ANSYS FLUENT User's Guide n.d.

[139] ANSYS® Academic Research CFD, Release 18.0, ANSYS Fluent Theory Guide n.d.:1571.

[140] Griffini D, Salvadori S, Carnevale M, Cappelletti A, Ottanelli L, Martelli F. On the Development of an Efficient Regenerative Compressor. Energy Procedia, 70th Conf ATI Eng Assoc 2015;82:252–7.

[141] Badami M, Mura M. Comparison between 3D and 1D simulations of a regenerative blower for fuel cell applications. Energy Convers Manag 2012;55:93–100.

[142] Quail FJ, Stickland M, Scanlon T. Numerical and Experimental Design Study of a Regenerative Pump. AIP Conf Proc 2010;1220.

[143] Dixon SL, Hall CA. Fluid Mechanics and Thermodynamics of Turbomachinery. 6th ed. University of Cambridge, Cambridge, UK: Elsevier Inc; 2010.

[144] Denton JD. Loss mechanisms in turbomachines. Proc ASME 1993 Int Gas Turbine Aeroengine Congr Expo Cincinnati, OH, USA 1993:24–27.

[145] Ramin Moradi, Cioccolanti L, Bocci E, Villarini M, Renzi M. Numerical

Investigation on the Performance of a Regenerative Flow Turbine for Small-Scale Organic Rankine Cycle Systems. J Eng Gas Turbines Power 2019;141. https://doi.org/10.1115/1.4044062.

[146] Amalfi RL, Vakili-Farahani F, Thome JR. Flow boiling and frictional pressure gradients in plate heat exchangers. Part 2: Comparison of literature methods to database and new prediction methods. Int J Refrig 2016;61:185–203. https://doi.org/10.1016/J.IJREFRIG.2015.07.009.

[147] Yang J, Jacobi A, Liu W. Heat transfer correlations for single-phase flow in plate heat exchangers based on experimental data. Appl Therm Eng 2017;113:1547–57. https://doi.org/10.1016/J.APPLTHERMALENG.2016.10.147.

[148] Longo GA, Righetti G, Zilio C. A new computational procedure for refrigerant condensation inside herringbone-type Brazed Plate Heat Exchangers. Int J Heat Mass Transf 2015;82:530–6. https://doi.org/10.1016/J.IJHEATMASSTRANSFER.2014.11.032.

[149] Khan TS, Khan MS, Chyu M-C, Ayub ZH. Experimental investigation of single phase convective heat transfer coefficient in a corrugated plate heat exchanger for multiple plate configurations. Appl Therm Eng 2010;30:1058–65. https://doi.org/10.1016/J.APPLTHERMALENG.2010.01.021.

[150] consortium PEUSE. Sustainable and optimal use of biomass for energy in the EU beyond 2020. European Commission; 2017.

[151] Bauen A, Berndes G, Junginger M, Londo M, Vuille F. Bioenergy: a sustainable and reliable energy source. a review of status and prospects. IEA Bioenergy 2009.

[152] World Energy Outlook. Int Energy Agency 2012.

[153] Bocci E, Di Carlo A, McPhail SJ, Gallucci K, Foscolo PU, Moneti M, et al. Biomass to fuel cells state of the art: A review of the most innovative technology solutions. Int J Hydrogen Energy 2014;39:21876–95.

[154] Bocci E, Sisinni M, Moneti M, Vecchione L, Carlo A Di, Villarini M. State of art of small scale biomass gasification power systems: a review of the different typologies. Energy Procedia 2014;45:247–56.

[155] Ruiz JA, Juarez MC, Morales MP, Munoz P, Mendivil MA. Biomass gasification for electricity generation: Review of current technology barriers. Renew Sustain Energy Rev 2013;18:174–83.

[156] Din ZU, Zainal ZA. Biomass integrated gasification-SOFC systems: Technology overview. Renew Sustain Energy Rev 2016;53:1356–76.

[157] Lahijani P, Zainal ZA, Mohamed AR, Mohammadi M. Microwave-enhanced CO2 gasification ofoilpalmshellchar. Bioresour Technol 2014;158:193–200.

[158] Vera D, Jurado F, Carpio J, Kamel S. Biomass gasification coupled to an EFGT-ORC combined system to maximize the electrical energy generation: A case applied to the olive oil industry. Energy 2018;144:41–53.

[159] Wang W, Cai R, Zhang N. General characteristics of single shaft microturbine set at variable speed operation and its optimization. Appl Therm Eng 2004;24:1851–63.

[160] Boyce MP. Gas Turbine Engineering Handbook. Second. Butterworth_Heinemann; 2002.

[161] Renzi M, Patuzzi F, Baratieri M. Syngas feed of micro gas turbines with steam injection: Effects on performance, combustion and pollutants formation. Appl Energy 2017;206:697–707.

[162] Ward De Paepe, Delattin F, Bram S, DeRuyck J. Steam injection experiments

in a microturbine – A thermodynamic performance analysis. Appl Energy 2012;97:569–76.

[163] Ferrari ML, Pascenti M, Traverso AN, Massardo AF. Hybrid system test rig: Chemical composition emulation with steam injection. Appl Energy 2012;97:809–15.

[164] Stathopoulos P, Paschereit CO. Retrofitting micro gas turbines for wet operation. A way to increase operational flexibility in distributed CHP plants. Appl Energy 2015;154:438–46.

[165] Invernizzi C, Iora P, PaoloSilva. Bottoming micro-Rankine cycles for micro-gas turbines. Appl Therm Eng 2007;27:100–10.

[166] Camporeale SM, Pantaleo AM, Ciliberti PD, Fortunato B. Cycle configuration analysis and techno-economic sensitivity of biomass externally fired gas turbine with bottoming ORC. Energy Convers Manag 2015;105:1239–50.

[167] Klimantos P, Koukouzas N, Katsiadakis A, Kakaras E. Air-blown biomass gasification combined cycles (BGCC): System analysis and economic assessment. Energy Convers Manag 2009;34:708–14.

[168] Dogru M, Howarth CR, Akay G, Keskinler B, Malik AA. Gasification of hazelnut shells in a downdraft gasifier. Energy 2002;27:415–27.

[169] Carlo A Di, Borello D, Sisinni M, Savuto E, Venturini P, Bocci E, et al. Reforming of tar contained in a raw fuel gas from biomass gasification using nickel-mayenite catalyst. Int J Hydrogen Energy 2015;40:9088–95.

[170] Marcantonio V, Bocci E, Monarca D. Development of a Chemical Quasi-Equilibrium Model of Biomass Waste Gasification in a Fluidized-Bed Reactor by Using Aspen Plus. Energies 2019;13:53. https://doi.org/10.3390/en13010053.

[171] Swierczynski D, Courson C, Kiennemann A. Study of steam reforming of toluene used as model compound of tar produced by biomass gasification. Chem Eng Process Process Intensif 2008;47:508–13. https://doi.org/10.1016/J.CEP.2007.01.012.

[172] Marcantonio V, Bocci E, Ouweltjes JP, DelZotto L, Monarca D. Evaluation of sorbents for high temperature removal of tars, hydrogen sulphide, hydrogen chloride and ammonia from biomass-derived syngas by using Aspen Plus. Int J Hydrogen Energy 2020;45:6651–62. https://doi.org/https://doi.org/10.1016/j.ijhydene.2019.12.142.

[173] Wan W, Engvall K, Yang W. Model investigation of condensation behaviors of alkalis during syngas treatment of pressurized biomass gasification. Chem Eng Process - Process Intensif 2018;129:28–36. https://doi.org/10.1016/J.CEP.2018.05.001.

[174] Narváez I, Orío A, Aznar MP, Corella J. Biomass Gasification with Air in an Atmospheric Bubbling Fluidized Bed. Effect of Six Operational Variables on the Quality of the Produced Raw Gas. Ind Eng Chem Res 1996;35:2110–20.

[175] Savuto E, Carlo A Di, Steele A, Heidenreich S, Gallucci K, Rapagnà S. Syngas conditioning by ceramic filter candles filled with catalyst pellets and placed inside the freeboard of a fluidized bed steam gasifier. Fuel Process Technol 2019;191:44–53.

[176] Fremaux S, Beheshti S-M, Ghassemi H, Shahsavan-Markadeh R. An experimental study on hydrogen-rich gas production via steam gasification of biomass in a research-scale fluidized bed. Energy Convers Manag 2015;91:427–32.

[177] Herguido J, Corella J, González-Saiz J. Steam Gasification of Lignocellulosic Residues in a Fluidized Bed at a Small Pilot Scale. Effect of the Type of

Feedstock. Ind Eng Chem Res 1992;31:1274–82. https://doi.org/10.1021/ie00005a006.

[178] Loha C, Chatterjee PK, Chattopadhyay H. Performance of fluidized bed steam gasification of biomass – Modeling and experiment. Energy Convers Manag 2011;52:1583–8.

[179] Mayerhofer M, Mitsakis P, Meng X, Jong W de, Spliethoff H, Gaderer M. Influence of pressure, temperature and steam on tar and gas in allothermal fluidized bed gasification. Fuel 2012;99:204–9.

[180] Villarini M, Marcantonio V, Colantoni A, Bocci E, Villarini M, Marcantonio V, et al. Sensitivity Analysis of Different Parameters on the Performance of a CHP Internal Combustion Engine System Fed by a Biomass Waste Gasifier. Energies 2019;12:688. https://doi.org/10.3390/en12040688.

[181] Serigio R, Ajmal L. Steam gasification of almond shells in a fluidised bed reactor: the influence of temperature and particle size on product yield and distribution. Biomass and Bioenergy 1997;12:281–8.

[182] Corella J, Toledo JM, Molina G. Performance of CaO and MgO for the hot gas clean up in gasification of a chlorine-containing (RDF) feedstock. Bioresour Technol 2008;99:7539–44. https://doi.org/10.1016/J.BIORTECH.2008.02.018.

[183] Pallozzi V, Di Carlo A, Bocci E, Carlini M. Combined gas conditioning and cleaning for reduction of tars in biomass gasification. Biomass and Bioenergy 2018;109:85–90. https://doi.org/10.1016/j.biombioe.2017.12.023.

[184] Meng X, De Jong W, Pal R, Verkooijen AHM. In bed and downstream hot gas desulphurization during solid fuel gasification: A review. Fuel Process Technol 2010;91:964–81. https://doi.org/10.1016/j.fuproc.2010.02.005.

[185] Dou B, Wang C, Chen H, Song Y, Xie B, Xu Y, et al. Research progress of hot

gas filtration, desulphurization and HCl removal in coal-derived fuel gas: A review. Chem Eng Res Des 2012;90:1901–17. https://doi.org/10.1016/J.CHERD.2012.04.009.

[186] Xu C (Charles), Donald J, Byambajav E, Ohtsuka Y. Recent advances in catalysts for hot-gas removal of tar and NH3 from biomass gasification. Fuel 2010;89:1784–95. https://doi.org/10.1016/J.FUEL.2010.02.014.

[187] Bjoerkman E, Sjoestroem K. Decomposition of ammonia over dolomite and related compounds. Energy & Fuels 1991;5:753–60. https://doi.org/10.1021/ef00029a023.

[188] Cheah S, Carpenter DL, Magrini-Bair KA. Review of mid- to high-temperature sulfur sorbents for desulfurization of biomass- and coal-derived syngas. Energy and Fuels 2009;23:5291–307. https://doi.org/10.1021/ef900714q.

[189] Tran KQ, Iisa K, Steenari BM, Lindqvist O. A kinetic study of gaseous alkali capture by kaolin in the fixed bed reactor equipped with an alkali detector. Fuel 2005;84:169–75. https://doi.org/10.1016/j.fuel.2004.08.019.

[190] Aravind P V, De Jong W. Review Evaluation of high temperature gas cleaning options for biomass gasification product gas for Solid Oxide Fuel Cells. Prog Energy Combust Sci 2012;38:737–64. https://doi.org/10.1016/j.pecs.2012.03.006.

[191] Yu Q, Brage C, Chen G, Sjöström K. Temperature impact on the formation of tar from biomass pyrolysis in a free-fall reactor. J Anal Appl Pyrolysis 1997;40–41:481–9. https://doi.org/10.1016/S0165-2370(97)00017-X.

[192] Izumi Y, Ogawa M, Urabe K. Alkali metal salts and ammonium salts of Keggin-type heteropolyacids as solid acid catalysts for liquid-phase Friedel-Crafts reactions. Appl Catal A Gen 1995;132:127–40.

https://doi.org/10.1016/0926-860X(95)00167-0.

[193] Kautz M, Hansen U. The externally-fired gas-turbine (EFGT-Cycle) for decentralized use of biomass. Appl Energy 2007;84:795–805.

[194] Caresana F, Comodi G, Pelagalli L, Renzi M, Vagni S. Use of a test-bed to study the performance of micro gas turbines for cogeneration applications. Appl Therm Eng 2011;31:3552–8.

[195] Di Carlo A, Borello D, Bocci E. Process simulation of a hybrid SOFC/mGT and enriched air/steam fluidized bed gasifier power plant. Int J Hydrogen Energy 2013;38:5857–74.

[196] Orecchini F, Bocci E, Carlo A Di. MCFC and microturbine power plant simulation. J Power Sources 2006;160:835–41.

[197] Clemente S, Micheli D, Reini M, Taccani R. Bottoming organic Rankine cycle for a small scale gas turbine: A comparison of different solutions. Appl Energy 2013;106:355–64.

[198] Pallozzi V, Carlo A Di, Bocci E, Villarini M, Foscolo PU, Carlini M. Performance evaluation at different process parameters of an innovative prototype of biomass gasification system aimed to hydrogen production. Energy Convers Manag 2016;130:34–43.

[199] Hermann H, Reinhard R, Klaus B, Reinhard K. Biomass CHP Plant Güssing – A Success Story. Strasbourg, France: 2002.

[200] Carlo A Di, Bocci E, Naso V. Process simulation of a SOFC and double bubbling fluidized bed gasifier power plant. Int J Hydrogen Energy 2013;38:532–42.

[201] Florin NH, Harris AT. Hydrogen production from biomass coupled with carbon dioxide capture: The implications of thermodynamic equilibrium. Int

J Hydrogen Energy 2007;32:4119–34. https://doi.org/10.1016/J.IJHYDENE.2007.06.016.

[202] Inayat A, Ahmad MM, Yusup S, Mutalib MIA, Inayat A, Ahmad MM, et al. Biomass Steam Gasification with In-Situ CO2 Capture for Enriched Hydrogen Gas Production: A Reaction Kinetics Modelling Approach. Energies 2010;3:1472–84. https://doi.org/10.3390/en3081472.

[203] Rapagna S, Jand N, Foscolo P. Catalytic gasification of biomass to produce hydrogen rich gas. Int J Hydrogen Energy 1998.

[204] Wang Y, Kinoshita CM. Experimental analysis of biomass gasification with steam and oxygen. Sol Energy 1992;49:153–8. https://doi.org/10.1016/0038-092X(92)90066-J.

[205] Hofbauer H, Rauch R, Loeffler G, Kaiser S, Fercher E, Tremmel H. Six years experience with the FICFB-gasification process. 12th Eur Conf Technol Exhib Biomass Energy, Ind Clim Prot 2002:982–985.

[206] Torres W, Pansare SS, Goodwin JG. Hot Gas Removal of Tars, Ammonia, and Hydrogen Sulfide from Biomass Gasification Gas. Catal Rev 2007;49:407–56. https://doi.org/10.1080/01614940701375134.

[207] Husmann M, Hochenauer C, Meng X, Jong W De, Kienberger T. Evaluation of sorbents for high temperature in situ desulfurization of biomass-derived syngas. Energy and Fuels 2014;28:2523–34. https://doi.org/10.1021/ef402254x.

[208] Kalina J. Integrated biomass gasification combined cycle distributed generation plant with reciprocating gas engine and ORC. Appl Therm Eng 2011;31:2829–40.

[209] Conde MR. Estimation of thermophysical properties of lubricating oils and their solutions with refrigerants: an appraisal of existing methods. Appl

Therm Eng 1996;16:51–61. https://doi.org/10.1016/1359-4311(95)00011-2.

[210] Yu J, Zhang T, Qian J. Electrical motor products: International energy-efficiency standards and testing methods. Woodhead Publishing Limited; 2011. https://doi.org/10.1533/9780857093813.